

# **Frictional and transport properties of faults in the Opalinus Clay formation**

THÈSE N° 9002 (2018)

PRÉSENTÉE LE 16 NOVEMBRE 2018

À LA FACULTÉ DE L'ENVIRONNEMENT NATUREL, ARCHITECTURAL ET CONSTRUIT  
LABORATOIRE EXPÉRIMENTAL DE MÉCANIQUE DES ROCHES  
PROGRAMME DOCTORAL EN MÉCANIQUE

ÉCOLE POLYTECHNIQUE FÉDÉRALE DE LAUSANNE

POUR L'OBTENTION DU GRADE DE DOCTEUR ÈS SCIENCES

PAR

**Luis Felipe ORELLANA ESPINOZA**

acceptée sur proposition du jury:

Dr M. Farhat, président du jury  
Prof. M. E. S. Violay, Prof. J.-F. Molinari, directeurs de thèse  
Prof. Y. Guglielmi, rapporteur  
Prof. N. De Paola, rapporteur  
Prof. B. Lecampion, rapporteur



ÉCOLE POLYTECHNIQUE  
FÉDÉRALE DE LAUSANNE

Suisse  
2018









Me gustaría ser un nido si fueras un pajarito  
me gustaría ser una bufanda si fueras un cuello y tuvieras frío  
si fueras música yo sería un oído  
si fueras agua yo sería un vaso  
si fueras luz yo sería un ojo  
si fueras pie yo sería un calcetín  
si fueras el mar yo sería una playa  
y si fueras todavía el mar yo sería un pez  
y nadaría por ti  
y si fueras el mar yo sería sal  
y si yo fuera sal  
tú serías una lechuga  
una palta o al menos un huevo frito  
y si tú fueras un huevo frito  
yo sería un pedazo de pan  
y si yo fuera un pedazo de pan  
tú serías mantequilla o mermelada  
y si tú fueras mermelada  
yo sería el durazno de la mermelada  
y si yo fuera un durazno  
tú serías un árbol  
y si tú fueras un árbol  
yo sería tu savia y correría  
por tus brazos como sangre  
y si yo fuera sangre  
viviría en tu corazón

Claudio Bertoni



# ACKNOWLEDGMENTS

There were moments during these years I thought this point will never arrive. Yet, it just happened. I finished my thesis, and here I am with many feelings. There is one emotion, however, that comes to my mind often while I am writing: I am truly thankful. Thankful to many people who from one way to another contributed to this moment.

First, I would like to express my deep gratitude to Professor Marie Violay, my research supervisor, for her patient guidance and enthusiastic encouragement. It is difficult to imagine a better supervisor and I will always be grateful of you having me accepted as Ph.D. student. You have turned me from an engineer into a geologist while I pretended I was not. Thanks for introducing me to the world of geoscience research. It has been an exciting opportunity to work next to you.

I would like to offer my special thanks to all the members of the committee, Prof. Jean Francois Molinari, Prof. Yves Guglielmi, Prof. Nicola De Paola, and Prof. Brice Lecampion, and to the President of the jury Dr. Mohamed Farhat for having the time and consideration to evaluate my research. Thank you all for the constructive discussion, criticism, and comments.

I want to thank the financial support coming from Swisstopo and Nagra. I would like to express my profound gratitude to Dr. Cristophe Nussbaum and Dr. Silvio Gigier for their help on collecting samples and the fruitful discussions we have about fault zones and soil mechanics.

My grateful thanks are also extended to Prof. Cristiano Collettini, Dr. Marco Scuderi and Dr. Carolina Giorgetti from La Sapienza University in Rome. Thank you all for your patience and guidance during the first steps of my research. I am honored you are my co-authors.

I want to express my gratitude to Dr. Thierry Adatte, Dr. Luiz Grafulha, and Dr. Pierre Henry for the help and collaboration on sample characterization and discussion. Your work and help were very important to this research.

Finally, I would like to thank the people of the Department of Mining Engineering at the University of Chile, for encouraging and supporting me in my research career.

During these years I have been lucky to be surrounded by fantastic friends and colleagues. There is no way to express how much it meant to me to have been part of this amazing group. It will be very difficult to thank you all in the way you deserve. It is actually very difficult to write but you will hear it. No doubt. Anyway, here I go (and I am really sorry If I forget to mention one of you... Ups!).

I want to start with Donni, Francesco, Alberto, and Eleonora. Since the first day we met, I have enjoyed every moment we have spent together. Thanks to all the LMS and LMR (R.I.P) members, in particular to Alessandro and Valentina, and Erika and Yang (the last survivors!),

I have had the pleasure to share fraternal moments, morning coffees, early lunches and beers during these years.

To the LEMR crew. These brilliant friends who inspired me over these years: Mateo (and Michelle!), Chiara, Corentin, Barnaby, Carolina, François, and Lucas. I will never forget the nice moments we spend together, the infinite coffees and the endless discussions we had. Federica, thanks for those cheerful words. They meant a lot to me. Rosana thanks a lot for your warm welcome, your charisma and all your invaluable work. More than thanks, I would like to say sorry now. I am sorry Laurent, Benjamin, and Aurelien for forcing you to work with the Opalinus Clay. Never again...

Guys, I'll miss you so much, but I'll come back. And come to Chile! I'll be waiting for you.

Chileans are everywhere they say.

There are no proper words to say thank you to Lorenzo and Dayana (and Agustin and Mateo), my family here in Switzerland. To those old friends which fortune brought us together Bernardo, Angela, Trini, Alida, and Gato. To those new friends I have met Romina, Camila, Tomas, Lucia, Oscar, Hugo, Xime and all the ICES group. To all of you, thank you for listening and supporting me through this entire process.

To my family and friends in Chile who have also been supportive despite the long distance between us. To my dad and mom. To my sister and brother. I love you.

Finally, there is a group of invisible people who I need to say something. To those who have fought and are still fighting for the rights of people like me. Thanks, thank a lot. I am speechless.

It has been a fantastic journey. But none of this could not have happened without you, Domingo. My best friend, my boyfriend, my husband, the love of my life. We are not doing this again, promise.

# ABSTRACT

Deep geological repositories in clay formations are a promising option to ensure the long-term isolation of nuclear waste from the population and the environment. In Switzerland, the Opalinus Clay (OPA) formation is a shale whose favorable barrier properties have been characterized in the framework of the Mont Terri Laboratory project. Yet, faults intersecting the formation brings the integrity of future repositories into question. Faults, indeed, might reactivate upon any physical hydro-mechanical perturbation resulting in induced seismicity or creation of preferential paths for fluid leakage. How these fault arrays will reactivate, i.e., aseismic or seismic, and whether dilatancy or compaction will accompany reactivation are far from being well established, yet are of paramount importance to furthering any predictive capabilities.

In this context, the objective of this research is to study, through laboratory experiments, the frictional and transport properties of the fault zones intersecting the OPA formation at relevant conditions for nuclear waste storage.

The first section of this study reveals a fault gouge that has a pore network dominated by nanopores, yet a higher porosity, and slightly higher permeability with respect to the surrounding non-deformed rock. Furthermore, analyses show a lack of calcite content within the fault gouge, in agreement with recent evidence suggesting pore fluids flowing throughout it. Based on these results, the fault gouge does not act as a barrier; rather it can act as preferential but localized and narrow fluid flow channel favoring fluid transportation.

The second part of this research reveals 1) a weak frictional strength of the OPA fault gouge, however extremely weaker under wet conditions, 2) a clear aseismic stable behavior for wet and partially saturated samples, yet a transition from unstable to stable behavior with increasing sliding velocity for dry samples, 3) almost null frictional healing, i.e., a lack of re-strengthening during interseismic periods, 4) cataclastic deformation processes and, 5) on wet experiments, shear-enhanced dilation and a small increase in permeability after shearing. All these results indicate that OPA fault gouge could be easily reactivated via aseismic creep, possibly acting as weak fluid conduits. However, if temporarily dried, they could become potentially unstable.

A final section of this work presents the frictional response of simulated scaly clays. Simulated and natural scaly clay fabrics present significant similarities, notably mirror-like surfaces which are formed at sub-seismic velocities and low normal stresses in the laboratory. The simulated scaly fabrics exhibit 1) a lower frictional strength than the fault gouge at same partially saturated conditions, 2) both stable and unstable behavior, i.e., the co-existence of velocity-strengthening and weakening slip patches, and 3) low frictional healing. These observations suggest that the scaly clay fabrics are prone to host earthquakes, yet they might be small and rare over time.

This Ph.D. work finds direct implications for the concept of deep geological repositories in clays. In spite of favorable barrier properties of non-deformed OPA, faults cannot be ignored. Hence, this study might be the starting point for the long-term risk mitigation strategies.

**Keywords:** Opalinus Clay, faults, friction, fault gouge, scaly clays, nuclear waste storage, porosity, permeability, dilatancy, fault stability

# RÉSUMÉ

Utiliser les formations argileuses profondes est une option prometteuse pour isoler les déchets nucléaires sur le long terme. En Suisse, les argiles à Opalinus (OPA) sont des schistes argileux dont les propriétés hydromécaniques sont favorables à cette fin. Des failles recoupant la formation remettent en question l'intégrité des futures zones de stockage. En effet, une perturbation hydromécanique peut réactiver les failles, entraînant de la sismicité ou la création de chenaux préférentiels pour la circulation de fluide. La façon dont ces failles se réactiveront (i.e. sismique vs aséismique) et si la réactivation sera accompagnée de dilatation ou de compaction n'est pas encore compris, mais reste une question capitale pour une conception optimale de ces zones de stockage.

L'objectif de cette thèse est d'étudier, grâce à des expériences en laboratoire, les propriétés de frottement et de transport des failles intersectant les OPA, sous des conditions représentatives des zones de stockage.

La première partie de cette étude révèle que la gouge présente au cœur des failles possède une porosité plus élevée et une perméabilité légèrement supérieure à celle de la roche environnante non déformée. De plus, des analyses chimiques montrent un déficit en calcite dans cette gouge, suggérant la circulation de fluides réactifs au cœur de faille. Ainsi, la gouge agirait comme un canal d'écoulement préférentiel, localisé et étroit favorisant le transport fluide.

La deuxième partie de cette recherche révèle 1) une faible résistance au frottement des gouges de faille, d'autant plus faible en présence d'eau, 2) un comportement frictionnel aséismique pour les échantillons partiellement et complètement saturés, mais un comportement à la fois instable à stable, pour les échantillons secs, 3) une cicatrisation presque nulle entre les épisodes de glissement, 4) des processus de déformation cataclastiques et 5) une déformation accompagnée par de la dilatance et une faible augmentation de perméabilité. Ces résultats indiquent que les gouges de failles dans l'OPA pourraient être réactivées par fluage asismique, et agir comme conduits préférentiels pour les fluides. Néanmoins, en conditions sèches, la gouge pourrait se comporter de manière instable.

La dernière partie de ce travail décrit le comportement frictionnel des argiles de type «scaly clay». Sur le terrain comme en laboratoire, ces structures présentent des surfaces de glissement de type poli miroir, formées à des vitesses sub-sismiques et à faible contrainte normale. Les scaly clays montrent 1) une résistance au frottement inférieure à celle de la gouge, 2) un comportement frictionnel à la fois stable et instable et 3) une faible cicatrisation entre les épisodes de glissement. Ces observations suggèrent qu'au niveau des zones à scaly clay, des tremblements de terre peuvent nucléer, mais seront sûrement petits et rares dans le temps.

Ce travail a des implications directes pour les futurs projets de stockage des déchets nucléaires dans les schistes argileux profonds. Malgré les propriétés favorables de l'OPA intacte, les failles

ne peuvent être ignorées. Par conséquent, cette étude est un point de départ pour l'optimisation de la conception des dépôts afin d'atténuer les risques à long terme.

**Mots-clés :** Argiles à Opalinus, failles, frottement, gouge de faille, scaly clay, stockage des déchets nucléaires, porosité, perméabilité, dilatation, stabilité des failles



# TABLE OF CONTENTS

## Chapter 1: Introduction

1.1.	General framework: Nuclear waste disposal.....	1
1.1.1.	The Opalinus Clay formation, the Mont Terri Laboratory and the Main Fault...2	
1.2.	Fault-related issues affecting nuclear waste repositories. ....	6
1.3.	Faults and friction.....	7
1.3.1.	Fault structure .....	7
1.3.2.	Fluid-flow in fault zones.....	9
1.3.3.	Friction of rocks.....	10
1.3.4.	The earthquake cycle .....	15
1.3.5.	Earthquake nucleation.....	17
1.4.	The objective of the thesis.....	23
1.5.	Organization of the thesis.....	23
1.6.	References .....	25

## Chapter 2: Clay-rich fault gouges can act as discrete fluid-flow channels: The case of the Opalinus Clay formation

2.1.	Abstract .....	38
2.2.	Introduction .....	39
2.2.1.	Geological context .....	39
2.3.	Methods.....	41
2.3.1.	Sample composition and microstructures .....	42
2.3.2.	Transport properties .....	43
2.4.	Results .....	45
2.4.1.	Samples composition .....	45
2.4.2.	The microstructure of the fault gouge.....	46
2.4.3.	Transport properties of the fault gouge.....	48
2.5.	Discussion .....	49
2.5.1.	Comparison of results with previous studies .....	49

2.5.2.	Sample composition.....	50
2.5.3.	Porosity and grain density.....	50
2.5.4.	The permeability of non-deformed Opalinus Clay .....	50
2.5.5.	Microstructural evidence of fluid-flow in the fault gouge.....	51
2.5.6.	A conceptual schema for the Main Fault-related fluid-flow.....	51
2.5.7.	Implications for fluid flow in OPA fault zones. ....	53
2.6.	Conclusions .....	55
2.7.	References .....	56

## **Chapter 3: Frictional properties of the fault zones intersecting the Opalinus Clay formation**

3.1.	Abstract .....	64
3.2.	Introduction .....	65
3.2.1.	The Opalinus clay – fault gouge .....	67
3.3.	Materials and Methods.....	68
3.3.1.	Experimental Samples .....	68
3.3.2.	Experimental Procedure.....	69
3.3.3.	Microstructural Analysis.....	73
3.4.	Results .....	73
3.4.1.	Mechanical Data .....	73
3.4.2.	Microstructural Observations.....	80
3.5.	Discussion .....	82
3.5.1.	Fault strength .....	82
3.5.2.	Variation of friction with normal stress. ....	82
3.5.3.	Influence of water on frictional strength.....	84
3.5.4.	Fault Stability.....	84
3.5.5.	Fault Healing.....	85
3.5.6.	Implications for nuclear waste storage .....	88
3.6.	Conclusions .....	88
3.7.	References .....	90

## **Chapter 4: Frictional properties and permeability variations of fault zones in the Opalinus Clay formation, a host-rock for deep nuclear waste storage**

4.1.	Abstract .....	98
4.2.	Introduction .....	99
4.3.	Methods .....	101
4.3.1.	Samples .....	101
4.3.2.	Experimental setup.....	101
4.3.3.	Testing procedure.....	102
4.3.4.	Data processing.....	104
4.4.	Results .....	106
4.5.	Discussion .....	110
4.5.1.	Frictional strength .....	110
4.5.2.	Frictional stability .....	110
4.5.3.	Permeability evolution and shear-enhanced dilation .....	112
4.5.4.	Implications for nuclear waste repository.....	112
4.6.	Conclusion.....	113
4.7.	References .....	115

## **Chapter 5: Do scaly clays control seismicity in shales?**

5.1.	Abstract .....	122
5.2.	Introduction .....	123
5.3.	Material and methods .....	125
5.4.	Results .....	129
5.4.1.	Mechanical results .....	129
5.4.2.	Microstructural results .....	133
5.5.	Discussion .....	136
5.6.	Conclusions .....	141
5.7.	References .....	142

## Chapter 6: Conclusions and perspectives

6.1. Summary and main findings .....	147
6.1.1. Transport properties of the fault gouge.....	147
6.1.2. Frictional properties of simulated fault gouge.....	148
6.1.3. Frictional properties of simulated scaly clays.....	149
6.1.4. Deformation mechanism of simulated fault gouges and scaly clays .....	150
6.1.5. Dilatancy and permeability evolution of fault gouge .....	150
6.2. Future research .....	151
6.3. References .....	153
Appendix A: Chapter 2 .....	157
Appendix B: Chapter 4 .....	161
Curriculum Vitae .....	162

# LIST OF FIGURES

<b>Figure 1-1:</b> Nuclear plants in Switzerland and electricity production from 1960 to 2015. Source: The World Bank Group, (2018) and the Swiss Federal Nuclear Safety Inspectorate (2018). .....	1
<b>Figure 1-2:</b> Schematic illustration of the concept of deep geological disposal of nuclear waste ( <i>Norris, 2017</i> ) .....	2
<b>Figure 1-3:</b> The Mont Terri Laboratory. A) Cross-section of the Opalinus Clay formation showing the location of the Mont Terri Laboratory and the Main Fault crosscutting the laboratory. Inlet shows the site of the MTL in the northern part of Switzerland. B) Plan view of the laboratory showing the different facies of the Opalinus Clay formation and the Main Fault intersection galleries 08 and 98. Figure modified after Nussbaum et al. (2011). Locations of the boreholes BFS-1(blue), BFS-2 (red) and BGC-1 (green) is indicated in the figure. ....	3
<b>Figure 1-4:</b> Photographs of borehole BGC-1 samples courtesy of Mr. Senecio Schefer (Swisstopo, October 2016). A) Sandy and carbonate-rich facies samples. B) Shaly facies sample. ....	3
<b>Figure 1-5:</b> The Main Fault structure. A) View of the Main Fault intersecting gallery 98 at the Mont Terri Laboratory. The Main Fault figure reveals a complex fault geometry of scaly clays, secondary shear planes, non-deformed rock and fault gouge. The figure A) is modified after <i>Nussbaum et al. (2011)</i> . Samples of B) Non-deformed rock, C) Scaly-clays, and D) Fault gouge collected from borehole BFS-2.....	4
<b>Figure 1-6:</b> Photograph of the Main Fault intersecting the Opalinus Clay formation at the Mont Terri Laboratory ( <a href="http://www.mont-terri.ch">www.mont-terri.ch</a> ). Within the Main Fault damage zone linked shear surfaces and arrays of scaly clays are present. The fault core, where the majority of slip appears accommodated i.e. the fault gouge, is narrow, millimetre-thick slip zone which appears discontinuous at meter scale. Red lines with arrows are main shear planes. Others corresponds to secondary shear panes. ....	5
<b>Figure 1-7:</b> Schematic representation of nuclear waste storage risks. Risk includes release of radionuclides from the canister and fault reactivation. Based on Rutqvist et al. (2014). ....	6
<b>Figure 1-8:</b> Diagram showing the complex the interaction between the structure, mechanics, and fluid-transport properties of faults ( <i>Faulkner et al., 2010</i> ). For instance, the fault architecture and its associated permeability structure can control whether the fault is a barrier, a conduit or a barrier-conduit system ( <i>Caine et al., 1996</i> ). Also fault roughness might condition the onset of unstable sliding ( <i>Brodsky et al., 2016; Candela et al., 2012; Harbord et al., 2017</i> ). The architecture of faults is therefore fundamental to understand their mechanical, hydrological and seismological properties. ....	8
<b>Figure 1-9:</b> Typical fault structures. A) Model of a single high-strain core fault surrounded by a distributed zone of fractures and faulting in the damage zone. B) Model of high strain multi-branched fault and damaged zones ( <i>Faulkner et al., 2010</i> ). ....	8

<b>Figure 1-10:</b> Fault zone structure and permeability distribution. A) A fault zone is usually described by a narrow fault core that contains a principal sliding zone (PSZ). The fault core is bounded by a damage zone and a non-deformed host rock. B) The figure shows the resulting complexity of a multiple core fault zone with respect to the idealized structure of a fault zone with a single fault core. Figure modified after Chester and Logan (1986), Faulkner et al. (2010) and Yamashita and Tsutsumi, (2017).	10
<b>Figure 1-11:</b> Friction of rocks. Shear stress versus normal stress at the maximum friction for a variety of rocks. The static coefficient of friction is equal to $\mu = 0.85$ at low normal stress $< 200$ MPa and $\mu \approx 0.6$ at normal stress up to 2000 MPa. Figure has been taken from Byerlee (1978).	12
<b>Figure 1-12:</b> Scanning Electron Micrograph (SEM) pictures of a non-deformed Opalinus Clay sample. Figure a) and b) show the sheet structure of the constituent clay minerals at different scales.	13
<b>Figure 1-13:</b> Friction ( $\mu = \tau / \sigma'_n$ ) for different clay and synthetic clay-rich mixtures. Figure shows an apparent effect of normal stress. A second observation corresponds to an effect of clay content where generally, the higher the clay content (%), the lower the friction value.	13
<b>Figure 1-14:</b> Mohr-Coulomb diagram showing fault reactivation conditions as fluid pressures modifies the stress field. Figure modified after Scuderi et al. (2017).	14
<b>Figure 1-15:</b> Simplified flow diagram of an earthquake cycle after Ohnaka (2013).	16
<b>Figure 1-16:</b> Schematic illustration of the spring slider model showing the origin of sliding instabilities. A) Geometry of the system. B) Fault frictional strength as function of slip. The fault instability occurs when the frictional strength of the fault ( $k_c$ ) is released faster than the imposed strength of the loading system i.e., the spring in the spring slider model ( $k$ ).	17
<b>Figure 1-17:</b> A) Schematic illustration of the slip-dependent law for shear strength. B) A more simple representation of the slip-dependent law assuming a linear decay of the shear strength with displacement (Ohnaka, 2013).	18
<b>Figure 1-18:</b> A physical shear rupture model (Ohnaka, 2003).	19
<b>Figure 1-19:</b> Schematic illustration of the frictional response to velocity-stepping. A) Velocity-strengthening behaviour. B) Velocity weakening behaviour.	20
<b>Figure 1-20:</b> Frictional parameter versus effective normal stress and clay content (%).	22
<b>Figure 2-1:</b> A) Schema of the Main Fault intersecting Gallery 08 at the Mont Terri Laboratory. Schematic location (not to scale) of the boreholes BFS-2 intersecting the Main Fault at a depth of $\sim 44$ m from the gallery floor. We have modified the figure after Nussbaum et al., (2011) and Kneuker et al., (2017). B). Borehole BFS-2. Lithology and structures of BFS-2 are based on detailed observations of the core. Samples discussed in this study are from borehole BFS-2 and are indicated by a star symbol in the figure. Examples of c) non-deformed d) scaly clays, and e) fault gouge recovered from borehole BFS-2.	40

<b>Figure 2-2:</b> Permeability measurements. A) Setup used in this study. B) Calculation of $Q$ ( $\text{mm}^3/\text{s}$ ) following Darcy's law for test at 4 MPa effective confining stress. C) Following the transient step method of Brace et. al (1968), the pressure $P_1$ and $P_2$ evolved exponentially in time until they approached a final pressure $P_f$ . Figure show an example of measurement at 5 MPa effective confining stress. ....	44
<b>Figure 2-3:</b> Microstructures of the fault gouge. A) A cm-scale photograph of the fault gouge (black) recovered from borehole BFS-2. The thickness of the gouge varies from 3 to 10 mm, and it is surrounded by calcite-enriched scaly clays. On the right, three graphs showing the different mineralogical composition of the gouge and its surrounding. B) FIB-SEM image of the fault gouge showing micropores. White box shows the position of figures (d) and (g). The image also shows rounded quartz minerals, isolated pyrite grains and rare presence of calcite. C) FIB-SEM image of the fault gouge showing sub-rounded and sub-angular nanopores aligned the direction of shearing. Isolated rounded pores are also present D) Thin and elongated micropore connected in 3D by pore throats. E) SEM images of a framboid pyrite with porosity in between the single pyrite grains. F) FIB-SEM image of an angular or jagged micropore connected in 3D by pore throats. G) Nanopores possible connected by pore throats situated near a calcite grain boundary i.e. pore-grain bridge complex. ....	47
<b>Figure 2-4:</b> A) HP and FD porosity, b) grain density, c) MIP pore throat sizes and d) PSD measurements of the non-deformed and fault-related rocks of borehole BFS2. The MF is highlighted in red in b) and c). ....	48
<b>Figure 2-5:</b> Permeability results for samples cored parallel to the bedding planes. ....	49
<b>Figure 3-1:</b> A) Simplified geological plan-view map of the Mont Terri Laboratory (MTUL) modified after Nussbaum et al. (2011). Figure 1a shows the distribution of the different facies within the Opalinus Clay Formation (see legend) and location of boreholes BFS -1 and BFS-2. Inset is a scheme not to scale of the boreholes drilled through the Main fault zone. B) Scheme of the Main Fault intersected in gallery 98 at MTUL modified after Nussbaum et al. (2011) and Jaeggi et al. (2017). The “Main Fault” zone is about 0.8-0.9 to 3 m thick. The lower and upper fault boundaries have a dip of 55-60° to the SSE. Bedding planes dips in the same direction with a 15° angular difference (Nussbaum et al., 2011). ....	66
<b>Figure 3-2:</b> A cm-scale sample (recovered from borehole BFS2) and BSE images of Opalinus clay gouge. A) Hand sample of Opalinus clay gouge. Gouge thickness is about 1 cm. B) The homogenous clay matrix has fine grain size ( $\sim 7 \mu\text{m}$ ). We observe the ubiquitous presence of quartz (Qtz), smaller proportions of pyrite and calcite minerals, and sub-horizontal sets of interconnected shear planes. White box indicates the position of Figure 2c. C) A sub-horizontal shear plane underlined by the orientation of clay platelets. D) Clay matrix flowing around rigid, sub-rounded calcite crystal forming an eye-shape flow pattern perturbation (Passchier & Trouw, 2005). In this case, several pyrite framboids are on the surface of the calcite mineral. ....	67
<b>Figure 3-3:</b> Material and shear configuration. A) Particle Size Distribution (PSD) for Opalinus gouge. 90% of the particles are finer than $60 \mu\text{m}$ while the	

- average size is 7  $\mu\text{m}$ . B) Double direct shear configuration used in these experiments. C) Opalinus clay samples employed in the experiments on sample holder before shearing ..... 69
- Figure 3-4:** Friction experiments performed on simulated gouge samples of Opalinus Clay at different normal stress (from 4 MPa to 30 MPa). The curves show the evolution of the shear stress ( $\tau$ ) with slip. Experiments show a peak strength followed by a residual value. Curves indicate a low to moderate slip weakening. The weakening is higher at lower normal stress (4,7,10 MPa). Velocity step and slide-hold-slide tests start after shear stress reach a steady value. Inset: Double direct shear configuration used in these experiments. .... 70
- Figure 3-5:** Friction parameter analysis. A) The coefficient of friction versus displacement during the velocity step sequence. B) The coefficient of friction versus displacement during the slide hold slide sequence. C) An example of frictional parameter (a-b) measurement. The parameter a, also known as the direct effect, is proportional to the instantaneous change in friction. The friction parameter b, also known as the evolution effect, is proportional to the subsequent drop to a new steady-state. The black line shows the modelled output of Ruina's slip dependent evolution law. D) An example of frictional healing ( $\Delta\mu$ ) measurement for experiment i443 (normal stress equal to 10 MPa). The sequence corresponds to 100 s holding time. Frictional healing  $\Delta\mu$  is defined as the difference between peak static friction  $\mu_s$  and the pre-hold steady-state friction  $\mu_{ss}$ . .... 72
- Figure 3-6:** A) Amonton's friction  $\mu$  (Equation 3-1) versus normal stress. In black: peak friction  $\mu_{\text{peak}}$ . In red: steady-state friction  $\mu_{ss}$ . Filled symbols correspond to experiments performed on dry samples. B) Shear stress versus normal stress. We have linearized both peak and steady-state shear strength following the linear fit  $\tau = \mu_f \sigma_n + S_0$  as shown in the graph. At the peak,  $\mu_{f,\text{peak}} = 0.30$  and  $S_0 = 1.16$ . At steady state,  $\mu_{f,ss} = 0.29$  and  $S_0 = 0.40$ . For comparison, we display  $\tau = 0.6 \cdot \sigma_n$  and  $\tau = 0.1 \cdot \sigma_n$  on the chart. C) The coefficient of friction for coherent surfaces  $\mu_f$  (Equation 3-2) at both peak and steady state shear stress. .... 74
- Figure 3-7:** Friction rate parameters for simulated Opalinus clay gouge. A) Stability friction parameter (a-b) versus normal stress. Gouge samples are characterized by a velocity-strengthening behavior meaning  $a-b > 0$ . The parameter (a-b) decreased as normal stress increased and (a-b) values are nearly close to 0. B) Evolution of the individual parameters a and b with normal stress. Parameters a and b are represented by a circle and a square respectively. Parameter b increased when normal stress increased. C) Critical slip distance  $D_c$  versus normal stress. D) The frictional healing parameter  $\Delta\mu$  versus hold time. Experiments were carried out at sliding velocity of 10  $\mu\text{m/s}$  and at different normal stress. Error bars denote the standard deviation of multiple tests and non-filled symbols referred to results on the dry sample. .... 76
- Figure 3-8:** Evolution of porosity. A) Porosity ( $\phi_t$ ) versus shear displacement. On shearing,  $\phi_t$  monotonically decreases for all samples. The total porosity  $\phi_t$  decreases from  $\sim 27$  to  $\sim 17\%$  for sample sheared at 4MPa, and from



~22% to ~16% for sample sheared at 30 MPa. B) Total and corrected porosity versus displacement during velocity-step tests for sample sheared at 7 MPa normal stress. C) Total and corrected porosity versus elapsed time since the beginning of slide-hold-slide tests (in logarithmic scale) for samples sheared at 4 and 30 MPa normal stress. Values of corrected porosity $\phi_c$ were treated by removing the linear trend. ....	79
<b>Figure 3-9:</b> BSE images of post-mortem OPA samples. Shear direction is at the top of figures (a) and (b). The orientation of typical brittle fault zone is included. Images (a), (c), and (e) show sample sheared at 7 MPa normal stress. Images (b), (d), and (f) show sample sheared at 30 MPa normal stress. A) R-shear plane, weak foliation, development of cracks often aligned sub-parallel to the shear direction. B) R-shear plane on sample sheared at 30 MPa. Significant grain-size reduction within the entire experimental fault. C) Close-up of a Riedel shear plane. Note the clay alignment parallel to the R-shear plane. D) Detailed R-shear plane on sample sheared at 30 MPa. We observe a band of grain size reduction. Pictures (e) and (f) show intragranular cracks in calcite minerals. The penetrative clays in the cracks suggest that microcracking occurred during deformation. Photos also show how clays flow around stiffer fragments such as calcite and quartz.....	81
<b>Figure 3-10:</b> Comparison of the peak coefficient of friction as a function of effective normal stress for different kaolinite-rich clay gouges. ....	82
<b>Figure 4-1:</b> A) Cross-section of the Opalinus Clay formation showing the location of the Mont Terri Laboratory (MTL) and the Main Fault crosscutting the laboratory. Inlet shows the site of the MTL in the northern part of Switzerland. B) A schematic representation of nuclear waste storage risks including potential seismicity and creation of preferential fluid-flow paths.....	99
<b>Figure 4-2:</b> Experimental setup, frictional tests, and quantification of frictional properties. A) Saw-cut and pore pressure pumps configuration. B) Wet and dry test. Friction is calculated before velocity-steps started. Run-in velocity is of 1 $\mu\text{m/s}$ . Blue squares show the position of figures C) and D). C). Model inversion of the experimental data with slip law resulting in rate and state values of a, b, and a-b. D) Stress drop and recurrence time of the stick-slip events. ....	102
<b>Figure 4-3:</b> Frictional results. A) Friction at 2 mm displacement (axial) and B) Shear stress versus effective normal stress for wet and dry samples. For comparison, we have included the Byerlee's rule (Byerlee, 1978) and previous results of frictional experiments carried out at 100% room humidity condition (Orellana et al., 2018b). Frictional parameter versus axial velocity for C) wet and D) dry samples. E) Stress drops for selected experiments (t015, t005, t018, t023).....	109
<b>Figure 4-4:</b> A) Permeability measurements before and after shearing. B) The change in pore volume during shearing for selected samples (t010, t008, t016, t009). Compaction corresponds to negative pore volume change. ....	110
<b>Figure 5-1:</b> The Main Fault. A) A cross-section of the Main Fault that intersects the Mont Terri Laboratory (MTL) in the clay-rich facies of the OPA formation (shaly OPA). Gray lines are bedding planes oriented 15° on average from the fault zone. The red box indicates the position of the	

samples used in this study. Black semicircle in gallery 08 indicates the position of Figure 1B. The inset shows the location of the MTL, in the north part of Switzerland. B) Scheme of the Main Fault intersecting the gallery 08 at the MTL modified from Nussbaum et al., (2011).....	123
<b>Figure 5-2:</b> Experimental setup. A) The double-direct shear configuration in BRAVA modified after Colletini et al. (2014). Dashed red box shows the position of the samples and orientation of stresses. B) Experimental samples. Samples have a nominal contact area of $\sim 25 \text{ cm}^2$ and are 1 cm thick. ....	126
<b>Figure 5-3:</b> A) Representative friction experiment (sample sheared perpendicular to bedding at 4 MPa normal stress). The curve shows the evolution of shear stress with displacement, the velocity-step, and the slide-hold-tests. During shearing, friction reaches a peak value ( $\mu_{\text{peak}}$ ) and then evolves to a steady-state ( $\mu_{\text{ss}}$ ) condition. B) Example of frictional parameter ( $a$ - $b$ ) modelling using the Ruina's empirical law in sample sheared parallel to bedding at 20 MPa. C) Example of frictional healing during hold time of 10 s in sample sheared perpendicular to bedding at 10 MPa normal stress indicating almost null re-strengthening on time. ....	128
<b>Figure 5-4:</b> Results. A) Friction versus normal stress. B) Frictional parameter ( $a$ - $b$ ) versus normal stress (MPa). C) Critical slip distance (mm) versus normal stress (MPa). D) Frictional healing values versus hold time (s).....	130
<b>Figure 5-5:</b> Natural and experimental samples. Photographs of A) non-deformed sample, B) experimental samples sheared parallel to bedding after 0.5 cm and C) 1.5 cm of displacement showing mirror-like slip surfaces under natural light, and D) a deformed hand sample exhibiting natural scaly clays. Scanning electron microscope images of E) a non-deformed, F) experimental samples sheared parallel to bedding after 0.5 cm and G) 1.5 cm of displacement, and H) natural scaly clays. Optical contactless profilometer model (area of $0.7 \text{ mm}^2$ ) showing mean roughness amplitude of about I) $\sim 24 \mu\text{m}$ for non-deformed samples and L) $\sim 7.5 \mu\text{m}$ for natural scaly clays. For samples sheared after J) 0.5 and H) 1.5 cm, the mean surface roughness range between $\sim 10 \mu\text{m}$ and $\sim 15 \mu\text{m}$ . ....	134
<b>Figure 5-6:</b> Microstructures of experimental samples tested at 7 MPa, 10 MPa and 20 MPa normal stress. A) Optical image of sample sheared parallel to bedding at 7 MPa showing incipient R-shear planes, microfractures parallel to the R-direction, and the accommodation of shearing within bedding planes (yellow dashed lines). B) BSE image of sample sheared parallel to bedding at 10 MPa showing a smooth surface associated with a zone of intense grain size reduction in which deformation is localised (R-plane). C) BSE image of sample sheared parallel to bedding at 10 MPa showing a truncated carbonate mineral. D) Optical image of sample sheared perpendicular to bedding at 7 MPa reveals the formation of R-shear planes (red dashed lines) and rotation of the bedding planes ( $\sim 45^\circ$ ) parallel to the P-direction (yellow dashed lines). E) BSE image of sample sheared perpendicular to bedding at E) 20 MPa and F) showing mirror-like surface associated with a zone of intense grain size reduction where deformation is localised. ....	135

<b>Figure 5-7:</b> Friction $\mu = \tau/\sigma_n$ values for intact samples sheared parallel and perpendicular to bedding, and simulated fault gouges samples from Chapter 3.....	137
<b>Figure 5-8:</b> Friction parameter (a-b) for intact samples sheared parallel and perpendicular to bedding, and simulated fault gouges samples from Chapter 3. Figure is showing that simulated fault gouges have a velocity-strengthening behaviour (Orellana et al., 2018), while on the other hand, intact samples sheared parallel and perpendicular to bedding planes exhibit both velocity-weakening and -strengthening behaviour at the same range of normal stresses (up to 20 MPa) .....	138
<b>Figure 5-9:</b> Contour plot of the stability parameter $\xi = \sigma_n \cdot a-b$ (Scholz, 1998) as a function of depth and sliding velocity for samples sheared A) parallel and B) perpendicular to bedding planes. Parameter $\xi$ is obtained from experimental values of (a-b) and assuming a gradient in vertical stress of 24 MPa/km (corresponding to the lithostatic pressure at the MTL). The critical nucleation length $L_c(m)$ is calculated based on the elliptical crack approach (Scholz, 2002). In the figure, the numbers within the unstable areas represent the values of $L_c(m)$ . $L_c$ has not been estimated for velocity strengthening regions. ....	140
<b>Figure 6-1:</b> Shear stress versus effective normal stress for the simulated fault gouge.....	148
<b>Figure 6-2:</b> Shear stress versus effective normal stress for the simulated fault gouge and scaly clays. ....	150



# 1.

## INTRODUCTION

### 1.1. GENERAL FRAMEWORK: NUCLEAR WASTE DISPOSAL

The World Nuclear Association estimates that by 2050, 25 % of the total worldwide energy production will come from nuclear sources as a consequence of the increasing demand for electricity (World Nuclear Association, 2018). Today, nuclear power generation corresponds to the 11% of world electricity and is used by more than 30 countries. Among them, Switzerland operates five nuclear plants (Figure 1-1) that generate about 40% of the total electricity generation within the country (The World Bank Group, 2018). However, following a decision of the Swiss authorities, Switzerland is introducing a progressive withdrawal from nuclear energy to be completed by 2034 (Swiss Federal Nuclear Safety Inspectorate, 2018; World Nuclear Association, 2018).

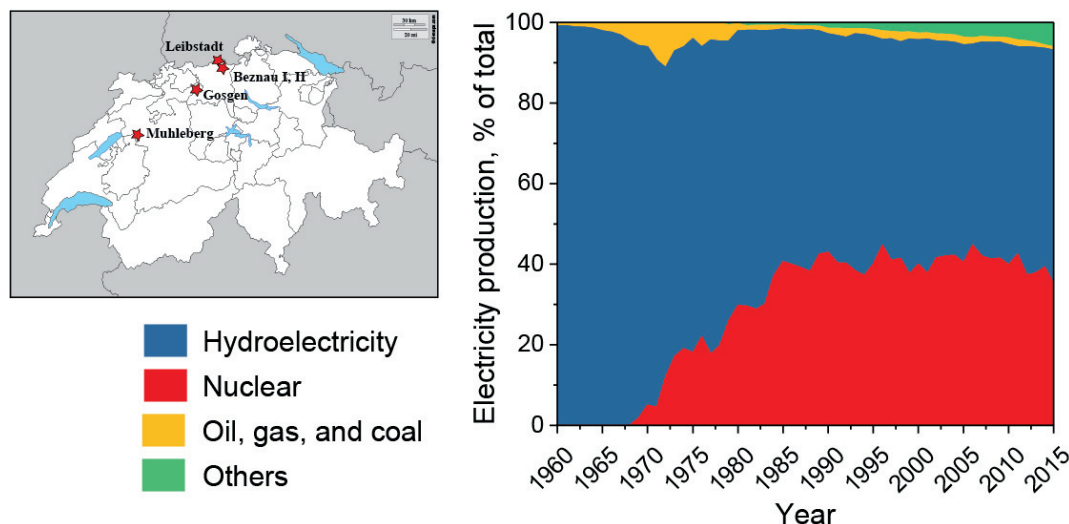


**Figure 1-1:** Nuclear plants in Switzerland and electricity production from 1960 to 2015. Source: The World Bank Group, (2018) and the Swiss Federal Nuclear Safety Inspectorate (2018).

The total shutdown of the five nuclear plants imposes complex challenges regarding the management of high-level radioactive waste (HLW). HLW corresponds to large volumes of a type of highly radioactive waste coming from spent fuel assemblies mainly from nuclear power plants (Swiss Federal Nuclear Safety Inspectorate, 2018). HLW requires complete isolation as it presents a serious hazard to human health and the environment.

Among today's available options for the long-term safe storage of HLW, there is a generalized scientific consensus that deep geological disposal is one of the most suitable options (Figure 1-2) (Norris, 2017).

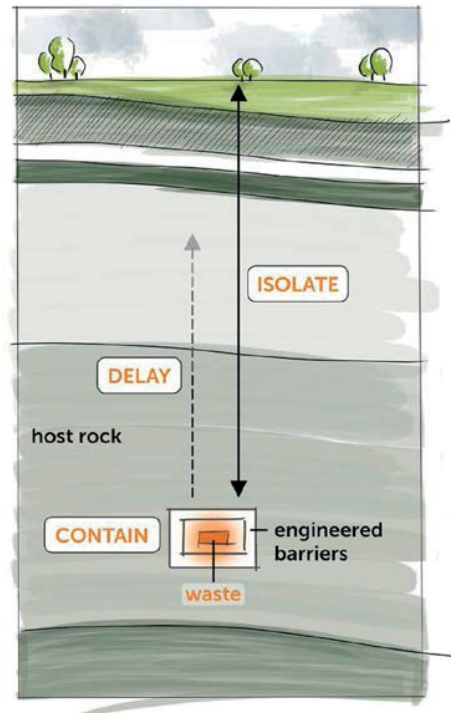


**Figure 1-2:** Schematic illustration of the concept of deep geological disposal of nuclear waste (Norris, 2017)

The general geological disposal concept is based on an Engineered (Multi-) Barrier Systems (EBS) that considers the nuclear waste and a host rock to prevent the migration of radionuclides towards the surface (Kim et al., 2011). An EBS consists of a metallic canister that contains the vitrified HLW and a buffer material (e.g., bentonite). It is surrounded by a host rock formation, usually of crystalline rocks, salt, or clays (Tsang et al., 2015). Because of the long average radioactive decay times of radionuclides, host formations need to be chemo-hydro-mechanically stable over geological time scales (more than hundred thousand years) (Norris, 2017), thus ensuring the long-term isolation of the nuclear waste.

### 1.1.1. THE OPALINUS CLAY FORMATION, THE MONT TERRI LABORATORY, AND THE MAIN FAULT

In Switzerland, the planned geological repository for HLW will be located at a depth of 400 to 900 m below the ground in the Opalinus Clay (OPA) formation (Giger et al., 2018). The Opalinus clay is an indurated shale that presents advantageous barrier properties including low permeability, fracture sealing and high retention capacity (Bossart et al., 2017). Current potential sitting regions includes Zürich Nordost, Nördlich Lägern and Jura Ost where the OPA formation thickness has an average of around 110 m (National Cooperative for the Disposal of Radioactive Waste, 2018).



To study and demonstrate the suitability of the Opalinus Clay formation as a host rock for nuclear waste storage, the Mont Terri Laboratory (MTL) Project started operation in 1996 (The Mont Terri Project, 2018). Situated to the north of St-Ursanne in the canton of Jura, the Mont Terri Laboratory is an underground research facility that runs site characterization and testing activities for the hydrogeological, geochemical and geotechnical characterization of the OPA formation. The laboratory will not host nuclear waste and serves only as a research facility. The MTL is emplaced in the northern part of Switzerland, Canton de Jura and it was built at a depth between 250 – 300 m (Figure 1-3).

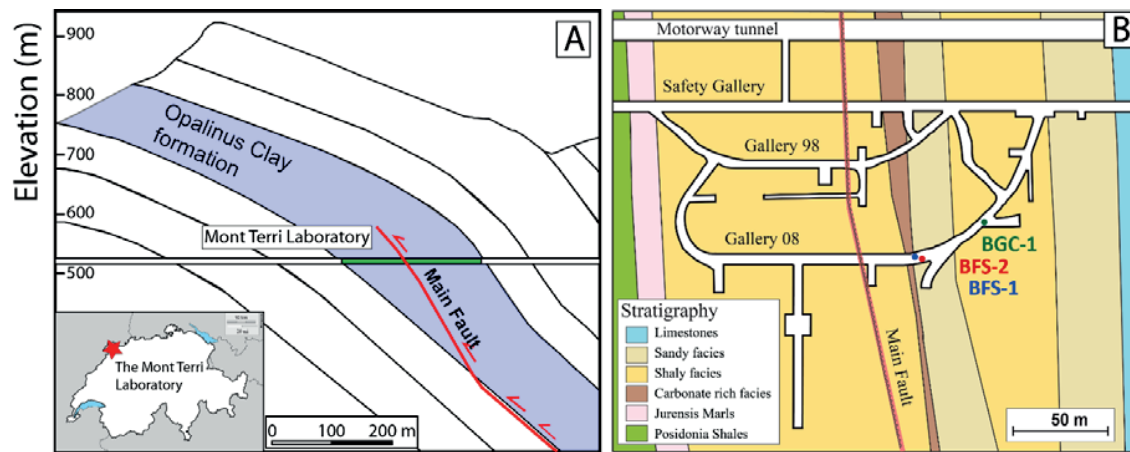


**Figure 1-3:** The Mont Terri Laboratory. A) Cross-section of the Opalinus Clay formation showing the location of the Mont Terri Laboratory and the Main Fault crosscutting the laboratory. Inlet shows the site of the MTL in the northern part of Switzerland. B) Plan view of the laboratory showing the different facies of the Opalinus Clay formation and the Main Fault intersection galleries 08 and 98. Figure modified after Nussbaum et al. (2011). Locations of the boreholes BFS-1(blue), BFS-2 (red) and BGC-1 (green) is indicated in the figure.

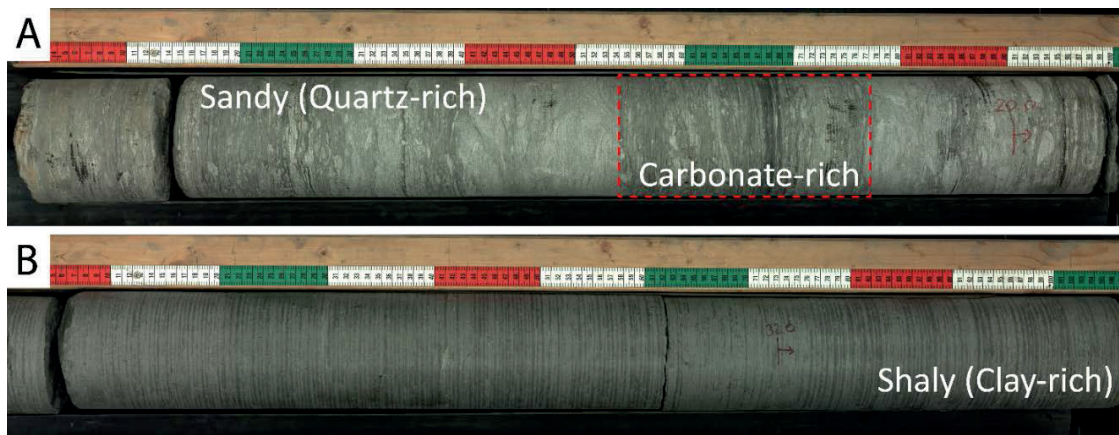


**Figure 1-4:** Photographs of borehole BGC-1 samples courtesy of Mr. Senecio Schefer (Swisstopo, October 2016). A) Sandy and carbonate-rich facies samples. B) Shaly facies sample.

Mineralogy of the Opalinus Clay facies (%wt)			
Facies	Shaly (n=3)	Sandy (n=3)	Carbonate-rich (n=3)
Borehole	BFS-2	BGC-1	BGC-1
Phyllosilicates	49.89 ± 0.40	26.29 ± 2.55	18.63 ± 1.08
Quartz	23.26 ± 0.70	49.98 ± 3.27	35.58 ± 6.39
Calcite	14.68 ± 0.80	8.66 ± 0.92	36.04 ± 9.32
Others	2.91 ± 0.39	16.07 ± 4.51	9.75 ± 1.77

**Table 1-1:** Bulk (% weight) mineralogical composition the three Opalinus Clay facies at the MTL. Samples correspond to non-deformed (intact) rock of the different facies. Samples from the carbonate-rich and the sandy facies were collected from borehole BGC-1. Samples of the shaly facies were collected from boreholes BFS-2. We present results as  $X \pm S$ , where X is the mean and S the standard deviation; “n” corresponds to the number of samples.

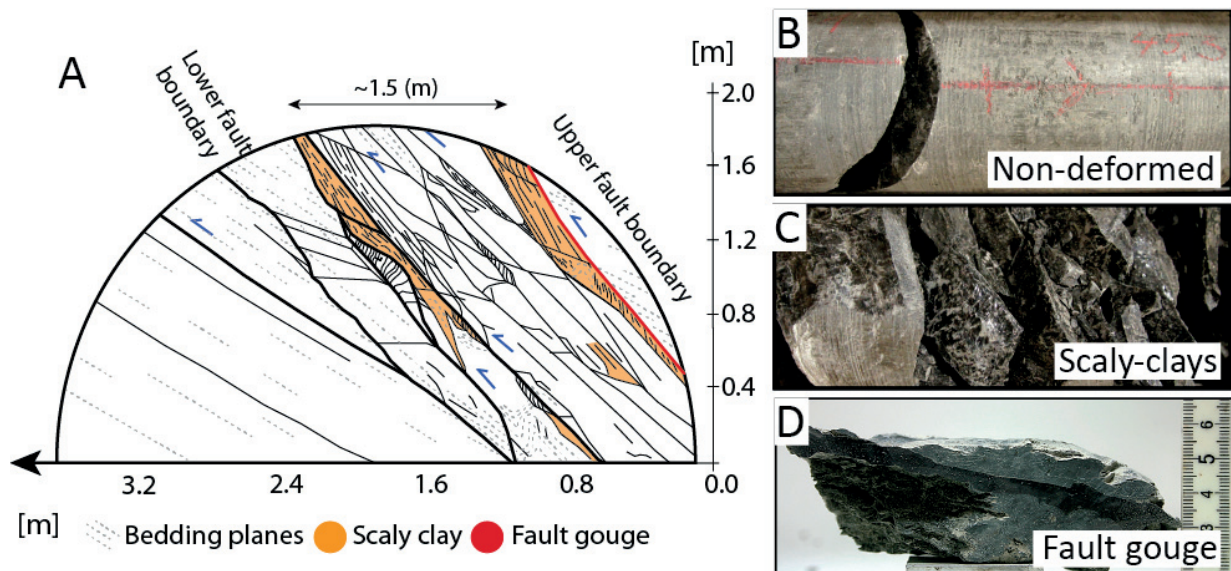


**Figure 1-5:** The Main Fault structure. A) View of the Main Fault intersecting gallery 98 at the Mont Terri Laboratory. The Main Fault figure reveals a complex fault geometry of scaly clays, secondary shear planes, non-deformed rock and fault gouge. The figure A) is modified after *Nussbaum et al. (2011)*. Samples of B) Non-deformed rock, C) Scaly-clays, and D) Fault gouge collected from borehole BFS-2.

Three main subunits of facies in the Opalinus Clay formation can be recognized at the MTL (Figure 1-3, Figure 1-4): 1) the shaly, 2) the sandy, and 3) the carbonate-rich facies (Hostettler et al., 2017; Nussbaum et al., 2011). X-Ray analysis (Table 1-1) performed at the University of Lausanne have revealed that the shaly facies corresponds to a dark clay-rich shale with approximately ~50% of clays, ~25% of quartz, and ~15% of calcite. The sandy facies is a dark grey quartz-rich shale which characteristic mineralogical content is ~25% of clay, ~50% of quartz and ~10% of calcite. Finally, the carbonate-rich facies is a thin portion of dark light grey shale with ~20% of clays, ~35% of quartz and ~35% of calcite.

At the Mont Terri Laboratory, the Opalinus Clay formation is intersected by faults of different scales. The major structure is called Main Fault (MF). It is a large tectonic structure in the



shaly facies of the OPA formation (Figure 1-3, Figure 1-5, Figure 1-6). The Main Fault is a thrust fault of about 1 to 3 m in thickness that has a dip of  $55 - 60^\circ$  to the SSE (Nussbaum et al., 2011). The Main Fault zone has a single but discontinuous fault core, and it bounds a non-symmetrical damage zone where the upper part is more deformed than the bottom section (Figure 1-5) (Nussbaum et al., 2011). The surrounding rock corresponds to a relatively intact shale which anisotropic hydro-mechanical behavior depends on the orientation of bedding planes (Favero et al., 2016; Giger et al., 2018; Van Loon et al., 2004).

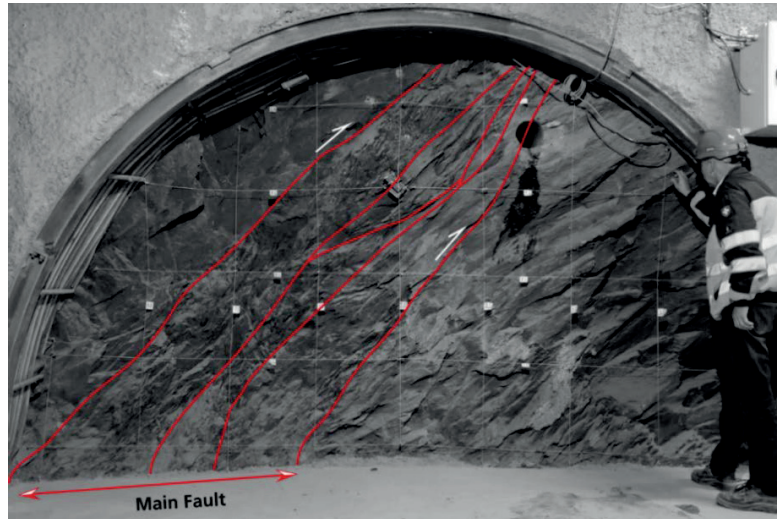


**Figure 1-6:** Photograph of the Main Fault intersecting the Opalinus Clay formation at the Mont Terri Laboratory ([www.mont-terri.ch](http://www.mont-terri.ch)). Within the damaged zone of the Main Fault, linked shear surfaces and arrays of scaly clays are present. The fault core, where the majority of slip appears accommodated, i.e. the fault gouge, is narrow, millimeter-thick slip zone which appears discontinuous at meter scale. Red lines with arrows are main shear planes. Others correspond to secondary shear panes.

As part of this study, the boreholes BFS-1 and BFS-2 were drilled intersecting the Main Fault at a depth of about 36 and 44 m respectively (Figure 1-3). Samples collected from the mentioned boreholes and field observations at the MTL reveal different fault structural elements that belong to the fault assemblage. Indeed, within the MF boundaries it is possible to recognize ubiquitous fractures, secondary shear planes, volumes of non-deformed rock (Figure 1-5b), a complex array of scaly clays (Figure 1-5c) and a spatially discontinuous mm-thick fault gouge (Figure 1-5d) (Kneuker et al., 2017; Laurich et al., 2014; Nussbaum et al., 2011, 2017, Orellana et al., 2018a, 2018b).

Within the fault core, the narrow clay-rich fault gouge (millimeter-thick) shows some typical elements of brittle fault rock fabrics. These include aligned phyllosilicates following Riedel shear plane structure (Logan et al., 1992), fragmented quartz and calcite clasts, and dismantled framboid pyrites (Laurich et al., 2014; Nussbaum et al., 2011; Orellana et al., 2018b).

Furthermore, secondary fractures and shear planes, and ubiquitous portions of scaly clays are contained within the Main Fault damage zone. The scaly clays are highly deformed intact rocks characterized by a scaly fabric, i.e. striated and polished mirror-like surfaces (Laurich et al.,

2014; Orellana et al., 2018a; Vannucchi et al., 2003). The presence of these two structural elements suggests that the Main Fault underwent both distributed (scaly clays) and localized (fault gouge) deformation. This arrangement provides not just a number of fluid flow possibilities within the fault zone, but also mechanical fault behaviors.

## 1.2. FAULT-RELATED ISSUES AFFECTING NUCLEAR WASTE REPOSITORIES.

Despite extensive research, there are still hydrogeological, geochemical and geotechnical concerns regarding clay formations in the context of nuclear waste storage. Among them, a major issue is the presence of faults nearby of the host formations. While it is most likely that underground nuclear repositories will be placed far away from fault systems, the identification of them remains challenging. Therefore, risks associated to fault re-activation and induced-seismicity might result, not just from well-known fault arrays, but also from pre-existing faults that went undetected during the site characterization process of the project (Husen et al., 2012; Mazzoldi et al., 2012). This persists as a major concern for deep geological repositories that cannot be neglected.

In the context of nuclear waste storage in clay formations, two major concerns related to the presence of faults come into sight (Figure 1-7): 1) the potential fault reactivation resulting in diverse fault behaviors from destructive earthquakes to stable aseismic fault creep (Scholz, 2002) and 2) the generation of enhanced preferential hydraulic-pathways as consequence of shear slip (Caine et al., 1996).

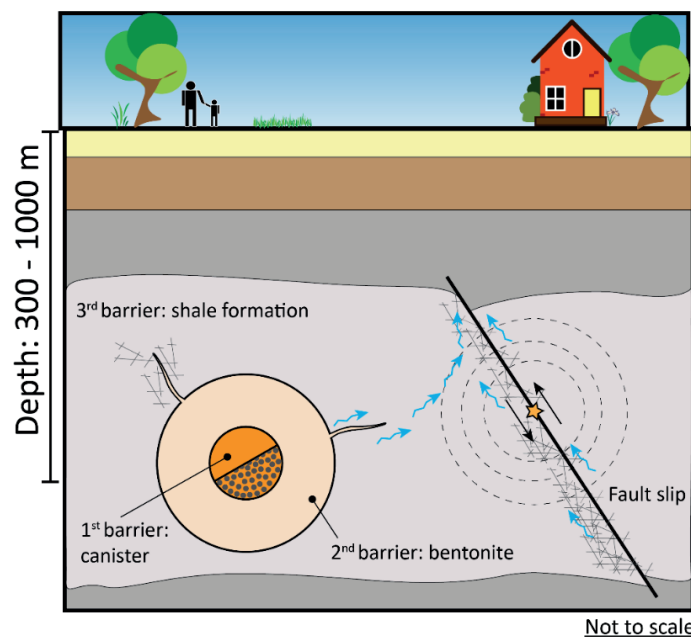


**Figure 1-7:** Schematic representation of nuclear waste storage risks. Risk includes the release of radionuclides from the canister and fault reactivation. Based on Rutqvist et al. (2014).

Faults might be disturbed by hydro-mechanical, thermal, chemical effects or a combination of them (Tsang et al., 2012, 2015). For instance, stress re-distribution due to tunneling, changes in the air relative humidity, pore-pressure changes due to stress-induced deformation or processes of heat-releasing radioactive waste including thermal expansion and changes in the mechanical properties of clays, etc. Under these circumstances, a consistent risk mitigation strategy must consider the investigation of the physical phenomena of fault reactivation and earthquakes nucleation in the Opalinus Clay formation. Up to now, far too little attention has been paid to this challenge, and a more comprehensive understanding of the fault system intersecting the shale formation is still lacking. Moreover, despite the recent advances, there are still many details that remain poorly understood regarding the phenomena of induced earthquakes, in particular, when referring to the mechanisms that control whether earthquakes are able to nucleate or not, and later propagate in clay-rich formations (Faulkner et al., 2011; Guglielmi et al., 2015; Jeanne et al., 2018; Kohli & Zoback, 2013; Lefèvre et al., 2016; Saffer et al., 2001; Ujiie et al., 2013).

In the next section, we review first, the distinct fault structural elements and hydrogeological aspects, both controlling the fluid-flow in the Earth's upper crust and second, the criteria and conditions for fault re-activation and earthquake nucleation. Because the Opalinus Clay shale is the main subject of this study, the review offers focused insights into the role of clays minerals in these processes.

## 1.3. FAULTS AND FRICTION

### 1.3.1. FAULT STRUCTURE

Based on laboratory experience, in the upper part of the Earth's crust where low-grade conditions are expected i.e., low temperature ( $<300^{\circ}\text{C}$ ), low pressures ( $<300\text{ MPa}$ ), rocks predominately develop in an elastic-brittle response to stresses (Cox & Scholz, 1988; Lockner & Beeler, 2002). Indeed, rocks deform in a nearly linear manner according to their elastic parameter until brittle failure occurs (Scholz, 2002).

Brittle failure of rocks can be described as the completion of a process of progressive development of cracks during loading, which may occur on all scales (Paterson & Wong, 2005; Scholz, 2002). When confining pressures are applied (even at low values), brittle failure takes place after a drastically, often catastrophically, increase of linked cracks oriented sub-parallel to the direction of maximum compressive stress (Jaeger et al., 2007). The coalescence of these cracks can lead to the formation of a fault, which corresponds to the significant shear strain concentration zone where the relative displacement of the two rock opposing surfaces has occurred (Jaeger et al., 2007; Scholz, 2002).

Geologic faults are generally complex systems showing an anastomosing distribution and geometry of fault-rocks, presenting different mineralogy, and consequently transport properties

and frictional behaviors (Figure 1-8)(Barros et al., 2016; Evans et al., 1997; Fagereng & Sibson, 2010; Faulkner et al., 2010; Sutherland et al., 2012).

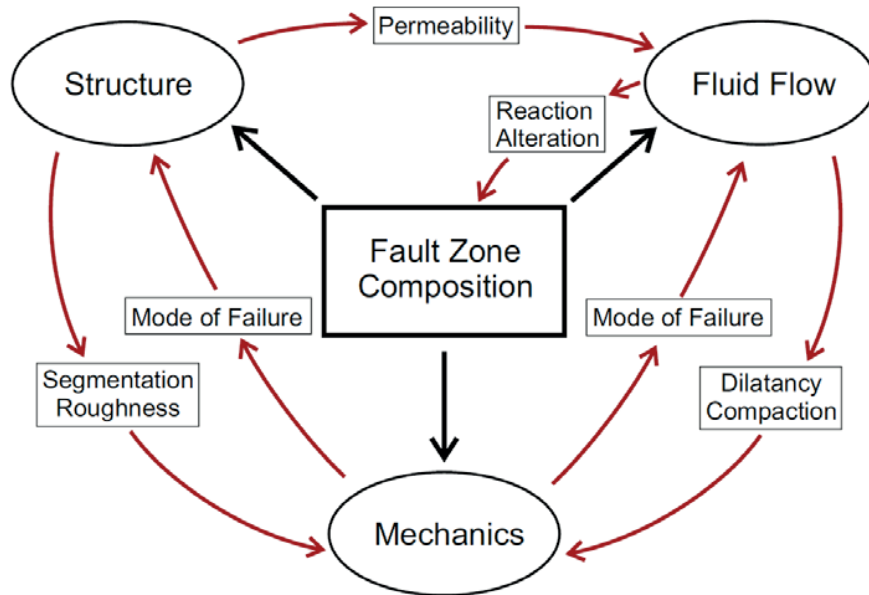


**Figure 1-8:** Diagram showing the complex the interaction between the structure, mechanics, and fluid-transport properties of faults (Faulkner et al., 2010). For instance, the fault architecture and its associated permeability structure can control whether the fault is a barrier, a conduit or a barrier-conduit system (Caine et al., 1996). Also, fault roughness might condition the onset of unstable sliding (Brodsky et al., 2016; Candela et al., 2012; Harbord et al., 2017). The architecture of faults is therefore fundamental to understand their mechanical, hydrological and seismological properties.

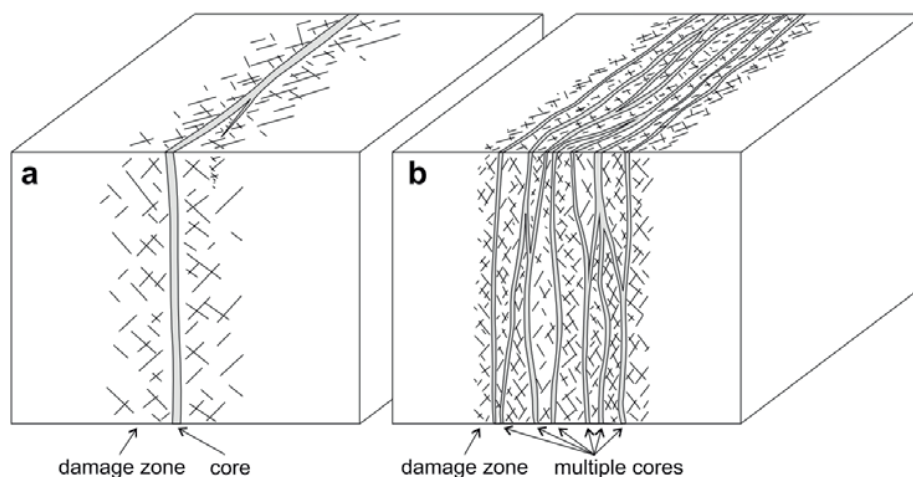


**Figure 1-9:** Typical fault structures. A) Model of a single high-strain core fault surrounded by a distributed zone of fractures and faulting in the damage zone. B) Model of high strain multi-branched fault and damaged zones (Faulkner et al., 2010).

A generalized and classical view of the structure of a fault is based on single-core surrounded by a damage zone of fractures and intense faulting and hosted by a non-damaged protolith

(**Figure 1-9a**) (Chester & Logan, 1986; Faulkner et al., 2010). A more realistic view, however, suggests that faults are composed of multiple, branched and linked fault cores (Faulkner et al., 2003; Mitchell & Faulkner, 2009) (**Figure 1-9b**). At shallow conditions, fault cores are often characterized by incohesive brittle fault rocks with different internal fabrics that define the through-going slip surfaces controlling fault slip. Following Sibson (1977), these brittle fault rocks can be subdivided into incohesive or cohesive rocks. Among incohesive fault rocks, we can find breccia (>30% visible fragments) and gouge (< 30% visible fragments). Among cohesive fault rocks, we can find cohesive breccia and cataclasites, which can also be sub-classified upon fragments size.

### 1.3.2. FLUID-FLOW IN FAULT ZONES

The fault architecture exerts a strong control on the fluid-flow behavior across a fault system. In the typical structure of a silicate-rich fault early described by *Caine et al.* [1996], the single fault core can act as a barrier while the damage zone as a preferential pathway for fluid migration (Figure 1-10a). However, how fluids will flow within a fault system is vastly more complex. A more realistic scheme suggests a fault structure with multiple, partially discontinuous, anisotropic and heterogeneous fluid channels (Figure 1-10b). For instance, in crystalline host rocks, fault-rocks are commonly rich in phyllosilicates showing barrier characteristics to fluid-flow. Earlier studies on the San Andreas Fault and the Alpine Fault indicates that the permeability of the foliated clay-rich gouge within the fault core is very low ( $10^{-21}$  -  $10^{-22}$  m<sup>2</sup>) compared to the damaged zone and host rock, suggesting that the fault core will act as a barrier to fluid-flow across the fault (Morrow et al., 2014). Same barrier feature has been attributed to the fault core of the Alpine Fault in New Zealand (Sutherland et al., 2012) and to the shallow plate boundary in the Japan Trench (Tanikawa et al., 2013). Low permeability values ( $10^{-18}$  -  $10^{-21}$  m<sup>2</sup>) have also been measured on clay-rich fault core samples from the Carboneras fault (Faulkner & Rutter, 2000), the Median Tectonic Line strike-slip fault zones (Wibberley & Shimamoto, 2002), the Mozumi fault (Forster et al., 2003), and the Nojima Fault (Lockner et al., 2009). All these fault systems have been classified as conduit-barrier for fluid-flow.

Different researchers have shown the inherently low permeability of clay rocks with values in the order of  $\sim 10^{-17}$  to  $10^{-21}$  m<sup>2</sup> (e.g. Billiotte et al., 2008; Bourg, 2015; Bourg et al., 2015; Faulkner and Rutter, 2000; Neuzil, 1994; Yang and Aplin, 2010). The low permeability of clays is mainly controlled by the pore structure of the clay minerals, as a consequence of the poor pore connectivity through narrow pore throats (Farrokhrouz & Asef, 2013). For instance, although the non-deformed Opalinus Clay is characterized by a very high porosity 13 -22%, its permeability has been estimated in the range of  $\sim 10^{-19}$  to  $10^{-21}$  m<sup>2</sup>, (Giger et al., 2018; Houben et al., 2013; Keller et al., 2013).



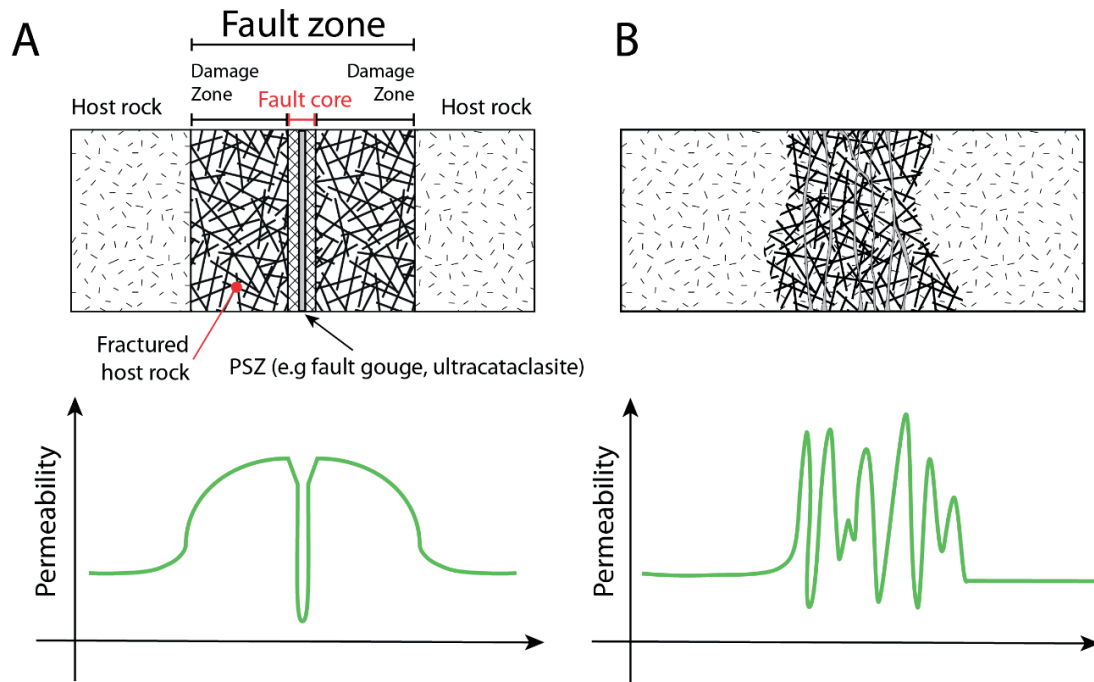


**Figure 1-10:** Fault zone structure and permeability distribution. A) A fault zone is usually described by a narrow fault core that contains a principal sliding zone (PSZ). The fault core is bounded by a damage zone and a non-deformed host rock. B) The figure shows the resulting complexity of a multiple core fault zone with respect to the idealized structure of a fault zone with a single fault core. Figure modified after Chester and Logan (1986), Faulkner et al. (2010) and Yamashita and Tsutsumi, (2017).

### 1.3.3. FRICTION OF ROCKS

A large body of evidence confirms that the motion of faults is controlled by friction (Scholz, 2002). Friction has been defined by Jaeger et al., (2007) as: “*the phenomenon by which a tangential shearing force is required in order to displace two contacting surfaces along a direction parallel to their nominal contact plane.*” The concept of friction, frictional resistance or frictional strength ( $\mu$ ) of two surfaces in contact was defined by Amontons (1699). Amontons’ law indicates that friction is the ratio of the shear resistance ( $\tau$ ) to the applied normal stress ( $\sigma_n$ ). Thus:

$$\mu = \tau / \sigma_n$$

Equation 1-1: Amontons’ law (Amontons, 1699)

Later, Coulomb, (1773) introduces the concept of a shear strength that has cohesive and frictional components in the form of:

$$\tau = S_o + \mu_f \sigma_n$$

Equation 1-2: Coulomb failure criterion (Coulomb, 1773)

Where  $S_o$  is an inherent shear strength at zero normal stress ( $\sigma_n$ ),  $\sigma_n$  is the given normal stress, and  $\mu_f$  is the coefficient of friction. Thus, for a wide range of rock cohesive surfaces, friction ( $\mu$ ) and the coefficient of friction ( $\mu_f$ ) are related as:

$$\mu = \frac{\tau}{\sigma_n} = \frac{S_o}{\sigma_n} + \mu_f$$

Equation 1-3: Relationship between friction and coefficient of friction (*Jaeger et al., 2007; Lockner & Beeler, 2002*)

In his work, Coulomb also differentiates the concept of static  $\mu_s$  and the kinetic (or dynamic)  $\mu_d$  friction (Popova & Popov, 2015). Static friction refers to a static frictional force that needs to be overcome to set in motion a body in a state of rest. After the static frictional force has been overcome, the body slides and a resisting frictional force is still necessary to keep the object in motion. This force is associated to kinetic friction (Popov, 2010).

Later, Bowden and Tabor, (1964, 1950) postulated the adhesion theory for friction between unlubricated surfaces based on experiments in metals. Two main factors were recognized in this modern theory. First, the adhesion occurs at the asperities level in regions of the real contact area  $A_r$ , which is generally much smaller than the apparent or geometric area of contact  $A$ . The second factor is associated to frictional interactions at the asperities level, including ploughing, grooving or cracking of one surface by asperities on the other (Bowden & Tabor, 1966). Under this conceptual framework,  $A_r$  is linearly proportional to the load regardless if the asperity deformation is elastic or plastic, and the shear stress required to allow frictional sliding is proportional to  $A_r$ .

Despite the fundamental basis of the theory, friction remains a complex phenomenon that responds to specific conditions and materials (Scholz, 2002). Therefore, when studying friction, and in particular when studying the friction of rocks and faults, friction needs to be considered as a system rather than material property.

As earlier introduced, faults are, indeed, complex systems whose behavior is based on the interactions of various components including the mechanics, their architecture, composition and fluid-transport properties (Faulkner et al., 2010) (Figure 1-8). During fault deformation, it is very likely that several competing processes take place, where various parameters, including normal and confining stress, mineralogy, porosity, permeability, temperature, sliding velocity, surface roughness, pore fluid pressures, fabric, and others, will affect the frictional strength of faults (Lockner & Beeler, 2002).

Based on a collection of laboratory experiments, Byerlee (1978) demonstrated that friction of crustal rocks does not depend on mineralogy or normal stress, at least to first order (Figure 1-11). The classic relation is known as the Byerlee's rule where:

$$\tau = 0.85 \cdot \sigma_n \quad \sigma_n < 200 \text{ MPa}$$

$$\tau = 0.5 + 0.6 \cdot \sigma_n \quad 200 < \sigma_n < 1700 \text{ MPa}$$

Equation 1-4: Byerlee's rule (Byerlee, 1978)

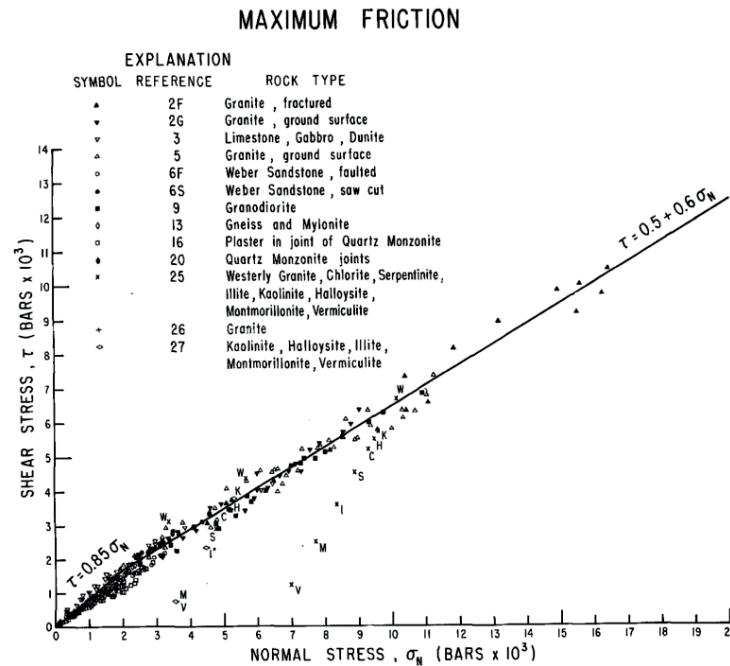


**Figure 1-11:** Friction of rocks. Shear stress versus normal stress at the maximum friction for a variety of rocks. The static coefficient of friction is equal to  $\mu = 0.85$  at low normal stress  $< 200 \text{ MPa}$  and  $\mu \approx 0.6$  at normal stress up to  $2000 \text{ MPa}$ . Figure has been taken from Byerlee (1978).

However, Byerlee (1978) also highlighted that exceptions need to be considered. While at low normal stress, friction strongly depends on surface roughness, at high normal stress, friction is non-linear. Similarly, if clay minerals are present, friction has proved to be consistently smaller at a broad range of normal stresses. Later, several authors have presented evidence of instances where the friction of rocks deviates from the Byerlee's law. Here we briefly refer to two of these cases: clay mineralogy and pore fluids.

### 1.3.3.1. CLAY MINERALOGY

A clay mineral corresponds to a sheet silicate (phyllosilicate) mineral forming sheet structures at the microscopic scale (Figure 1-12). The different forms of sheets bonding produce a variety of clay minerals, e.g. smectite, kaolinite, illite, etc. (Farrokhrouz & Asef, 2013). Because of its structure, clays can take a large amount of interlayer water upon their bonding affinity (e.g., surface charge, mineral composition) and environmental conditions (e.g., pressure, temperature) (Morrow et al., 2000).



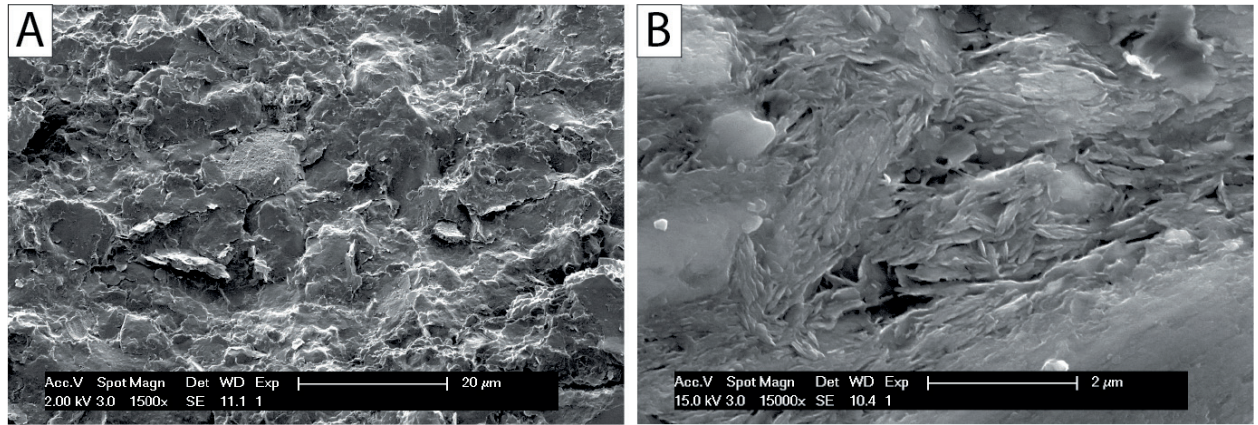


**Figure 1-12:** Scanning Electron Micrograph (SEM) pictures of a non-deformed Opalinus Clay sample. Figure a) and b) show the sheet structure of the constituent clay minerals at different scales.

As earlier envisioned by Byerlee (1978), clays play an important role in the friction of rocks, and therefore, in the mechanics of faulting and earthquakes. The presence of clay minerals within the fault architecture accounts for the weakness of faults and lower permeability than other crystalline and quartz-feldspathic rock gouges. Thus, their presence may exert a primary control of the fault hydro-mechanical behavior (Byerlee, 1978; Lockner et al., 2011).

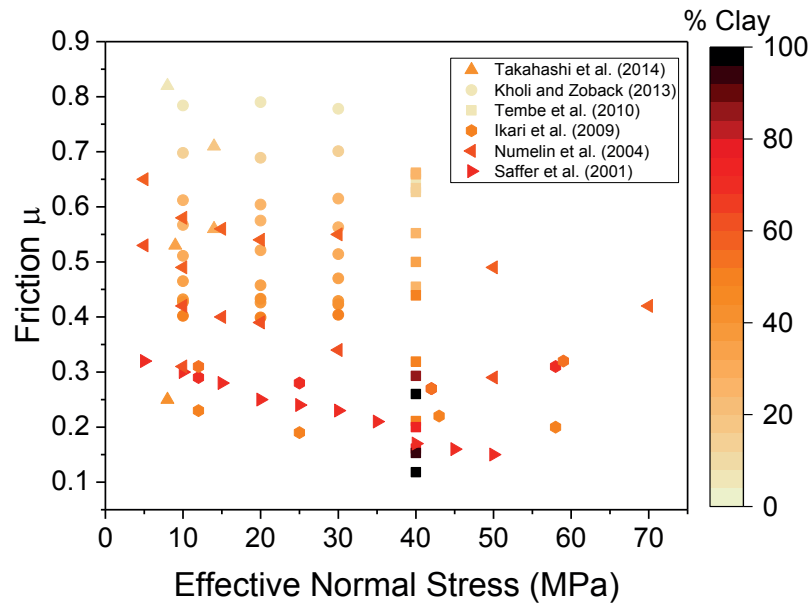


**Figure 1-13:** Friction ( $\mu = \tau/\sigma_{n\_eff}$ ) for different clay and synthetic clay-rich mixtures. Figure shows an apparent effect when increasing normal stress. This effect is commonly associated to cohesion (Equation 1-5). A second observation corresponds to an effect of clay content where generally, the higher the clay content (%), the lower the friction value. However, this is a first-order observation. A detailed description of the minerals is required.

Different laboratory frictional experiments have been carried out to measure dry and/or partially to fully saturated frictional strengths of clays minerals or synthetic clay-rich mixtures (e.g. Behnsen and Faulkner, 2012; Bullock et al., 2015; Carpenter et al., 2012; Lacroix et al., 2015; Moore and Lockner, 2011; Morrow et al., 2017; Numelin et al., 2007; Saffer et al., 2012;

Shimamoto and Logan, 1981; Takahashi et al., 2014; Tembe et al., 2010; Tesei et al., 2012). Figure 1-13 shows a compilation of friction data calculated as  $\mu = \tau / \sigma_{n\_eff}$  as a function of effective normal stress and clay content (%). Laboratory results show that at a given normal stress, the measured clay friction consistently departs from the Byerlee's law, showing in some cases, significantly lower values. The figure also suggests that, in general, friction decreases with normal stress and higher clay content. However, the latter observation might be associated to friction values been calculated without considering the effect of cohesion as in Equation 1-3 (Jaeger et al., 2007).

One hypothesis to the low frictional strength of clays has been related to the aligned relative weak layer bonds of the sheet structures, and to the capacity to attract water of the sheet minerals structures (Moore & Lockner, 2004; Morrow et al., 2000). However, still exists a great variability among studies in the literature as shown in Figure 1-13, highlighting the difficulties to account for idealized experimental procedures and conditions that are challenging to achieve when working with clays materials under shearing.

#### 1.3.3.2. PORE FLUIDS AND PORE PRESSURE

The presence of fluids can affect the fault frictional strength either by a direct mechanical reduction of normal stresses via the effective pressure law or by chemical reactions promoting chemo-mechanical weakening of the rocks by fluid-assisted mechanisms (Hubbert & Rubey, 1959; Ishikawa et al., 2008; Moreno et al., 2018; Scholz, 2002; Tenthorey et al., 2003; Wintsch et al., 1995). In particular, when pore pressures are present, the effective normal stress  $\sigma_{eff}$  is then calculated as:

$$\sigma_{eff} = \sigma_n - P_p$$

Equation 1-6: Effective normal stress

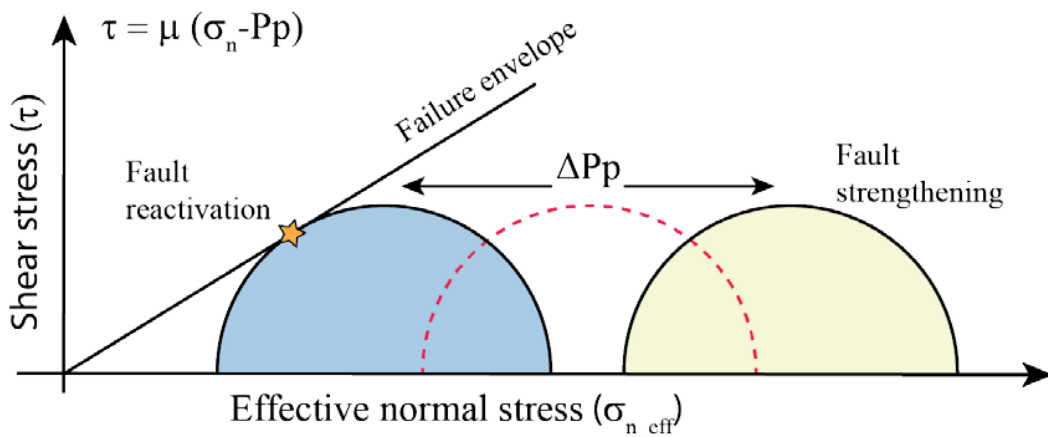


**Figure 1-14:** Mohr-Coulomb diagram showing fault reactivation conditions as fluid pressures modify the stress field. Figure modified after Scuderi et al. (2017).

Where  $\sigma_n$  corresponds to the total normal stress and  $P_p$  the pore fluid pressures. Pore pressure changes can lead to significant fault weakening or fault strengthening (Figure 1-14) (Duboeuf

et al., 2017; Ellsworth, 2013; Hirakawa et al., 2016; Leclère et al., 2015; Rice et al., 2014; Samuelson et al., 2009; Wintsch et al., 1995). For instance, fault weakening can be due to 1) sudden compaction generating elevated pore pressures, 2) via injection of water at high pressures i.e. fluid pressurization, or 3) thermal pressurization in impermeable formations. On the contrary, a fault strengthening effect (i.e. arrest nucleation of unstable slip) might occur thanks to shear-enhanced dilatancy, as long as shearing increases the pore space i.e. pore volume, inducing a decrease in pore pressure at a rate that is faster than the rate of fluid diffusion (Faulkner et al., 2018).

The development or not of pore pressures changes, as suggested before, will depend on the drainage rate of excess pore fluid pressures. Thus key factors in fault weakening or strengthening are the fluid-diffusion time-scales and the fluid-transport properties, i.e., porosity and permeability (Faulkner et al., 2018). Consequently, clays have here an important role. Because clays have inherently low permeability, they can retard fluid-flow and govern the evolution of overpressures within the fault structure leading to different fault responses.

### 1.3.4. THE EARTHQUAKE CYCLE

Earthquakes are a mechanism for accommodating motion in the Earth's upper crust. Most of them occur at shallow conditions ( $< 30$  km depth) where brittle regime dominates (Brace & Kohlstedt, 1980). Under this regime, earthquakes occur, given the right combination of stored energy release and spatial homogeneity of fault strength, because of the sudden slip on a pre-existing inhomogeneous fault.

In Figure 1-15 we show a flow diagram of the Earthquake cycle divided into five stages (Ohnaka, 2013). Briefly, we explain each of them:

1. **Phase II:** Earthquakes take place first when external stress loads a pre-existing fault; elastic strain energy progressively is stored in the rock medium surrounding the fault. When stresses start to reach critical levels i.e., critically close to fault strength, the fault zone starts to behave in a quasi-in-elastically manner leading to the beginning of the seismic activity. This initial activity is due to the heterogeneous nature of the rock where secondary small-to-medium fault patches activate.
2. **Phase III:** Then, as deformation localizes along the fault zone, the external loads overcome the fault strength at the weakest point of the fault. Fault nucleation begins as stresses are suddenly released (stress drop) with increasing slip and slip velocity.
3. **Phase IV:** Then, the elastic strain energy is partially converted into kinetic frictional heat and seismic waves that control the instability (Lockner & Beeler, 2002; Nielsen et al., 2016; Ohnaka, 2013). Next, the instability rupture dynamically extends at high velocity, and the seismic fault slip can accelerate into an earthquake.
4. **Phase V:** The arrest of an earthquake includes relaxation and re-distribution of stresses in the surroundings of the fault area, leading to aftershock activity.
5. **Phase I:** The fault might then remain locked (interseismic period) and fault healing, and re-strengthening process happen. Then, a new earthquake cycle begins.

This, however, is not the only mechanism of fault reactivation. Faults can also slowly release the stored elastic strain energy for long periods of times, through aseismic fault creep and so, producing many small and sometimes silent earthquakes (Harris, 2017).

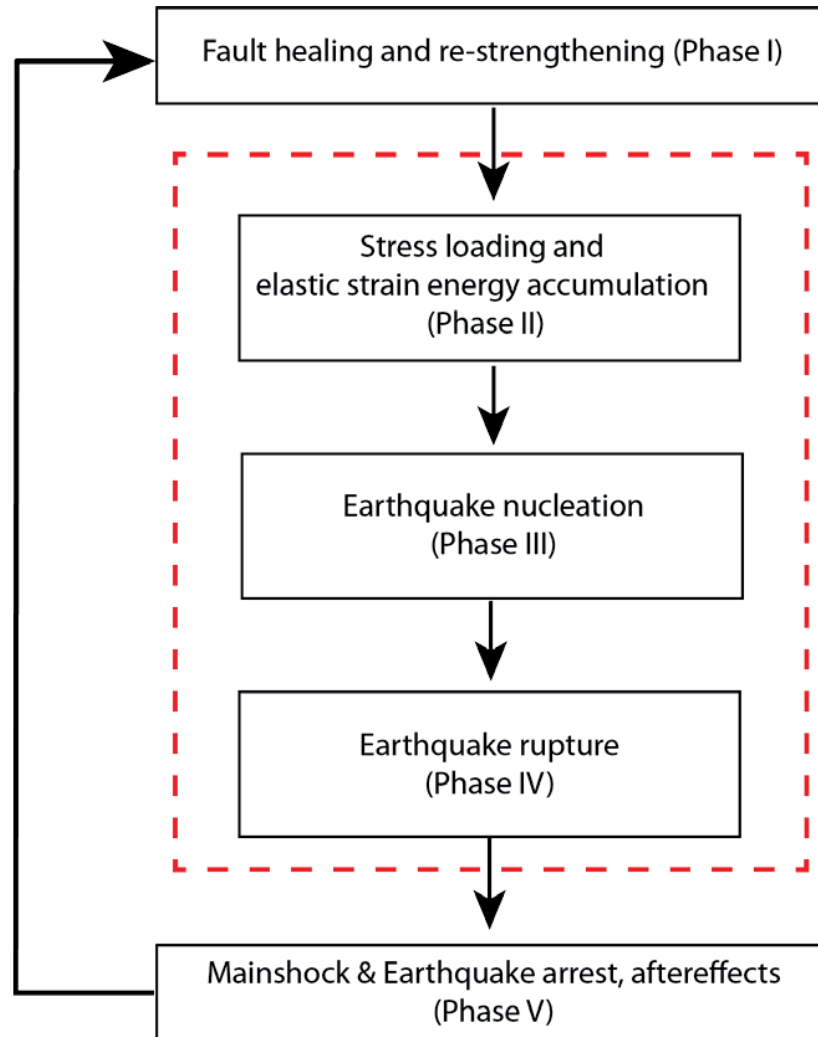


**Figure 1-15:** Simplified flow diagram of an earthquake cycle after Ohnaka (2013).

One explanation for fault creep can arise from rock frictional properties. Laboratory shearing experiments conducted on a wide range of wet clays at slow velocities has shown that clays can inhibit earthquake nucleation because fault frictional strength increases as slip accelerates (e.g., Haines et al., 2014; Ikari et al., 2009). However, under certain conditions, they appear to be favorable for unstable slip propagation (Faulkner et al., 2011; Noda & Lapusta, 2013).

Whether a fault follows an unstable or stable regime, will mostly depend on the evolution of friction during fault slip. Environmental conditions, fault geometry and a combination of these factors will also play an important role. In this research, we focus on the nucleation phase. This is the main scope of this research.

### 1.3.5. EARTHQUAKE NUCLEATION

The occurrence of shallow earthquakes has been explained by the analog idea of stick-slip (Brace & Byerlee, 1966; Byerlee, 1978; Byerlee & Brace, 1968). The mechanism of stick-slip can be illustrated by a spring-slider model (Figure 1-16a). In the model, a rider (simulating a rock mass) is free to slide on a frictional surface (reproducing a fault's surface), and a tangential force  $F$  is required to initiate its movement at constant velocity  $V$  through a spring of stiffness  $k$  (reproducing the elasticity of the rock mass surrounding the fault). After an initial increase in tangential force with slip,  $F$  will decrease in one of the two potential regimes (Figure 1-16b):

- Stable sliding, if the stiffness of the rock mass surrounding the fault ( $k$ ) is higher than the stiffness of the fault ( $k_c$ ), i.e.  $k_c < k$  and the frictional behavior of the fault is qualified as slip-strengthening at a relatively constant stress, or
- Unstable sliding, if  $k_c > k$ , following periods of “stick”, where the strength of the material evolves linearly with displacement, and later “slip” or sudden failure.

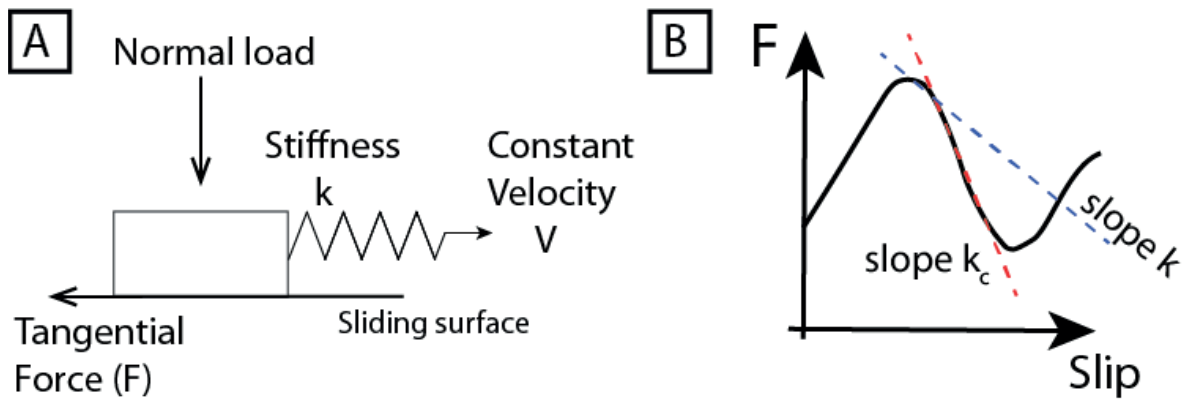


**Figure 1-16:** Schematic illustration of the spring slider model showing the origin of sliding instabilities. A) The geometry of the system. B) Fault frictional strength as a function of slip. The fault instability occurs when the frictional strength of the fault ( $k_c$ ) is released faster than the imposed strength of the loading system i.e., the spring in the spring slider model ( $k$ ).

As has been discussed, several factors will affect the stability of rock frictional sliding, fault structure, mineralogy, transport properties, etc. Nevertheless, based on the work of Brace and Byerlee (1966), two main laws (or visions) are generally considered to explain the nucleation of the fault instability; the transition from stable, i.e., strengthening to unstable, i.e., weakening behavior. We briefly discussed them now.

#### 1.3.5.1. SLIP-DEPENDENT LAW

In the slip-dependent model, frictional strength is termed solely on a slip-dependent relation (Ohnaka, 1992, 2003, 2013). The model is based on the evolution of shear strength as slip increases, where shear strength decreases to a residual value over a critical slip distance (Figure 1-17a). The model is defined by the initial stress on the verge of slip  $\tau_i$  i.e.,  $D = 0$ , the peak shear strength  $\tau_p$ , the residual shear strength  $\tau_r$ , the critical slip displacement at which  $\tau_p$  is observed  $D_a$ , the critical slip displacement or breakdown displacement  $D_c$ , and the slip

weakening displacement  $D_{wc} = D_c - D_a$  (Ohnaka, 2013). A simpler and common representation of the slip-dependent law (Figure 1-17b) assume a linear decay of shear strength from  $\tau_p$  to  $\tau_r$  over  $D_c$ , usually refers as the slip-weakening law.

The slip-dependent model is based on experimental observations, and it has been adopted with variations by several authors to described the earthquake generation process [e.g., *Abercrombie and Rice*, 2005; *Wibberley and Shimamoto*, 2005; *Sone and Shimamoto*, 2009; *Huang et al.*, 2013; *Ikari et al.*, 2013; *Brantut and Viesca*, 2015].

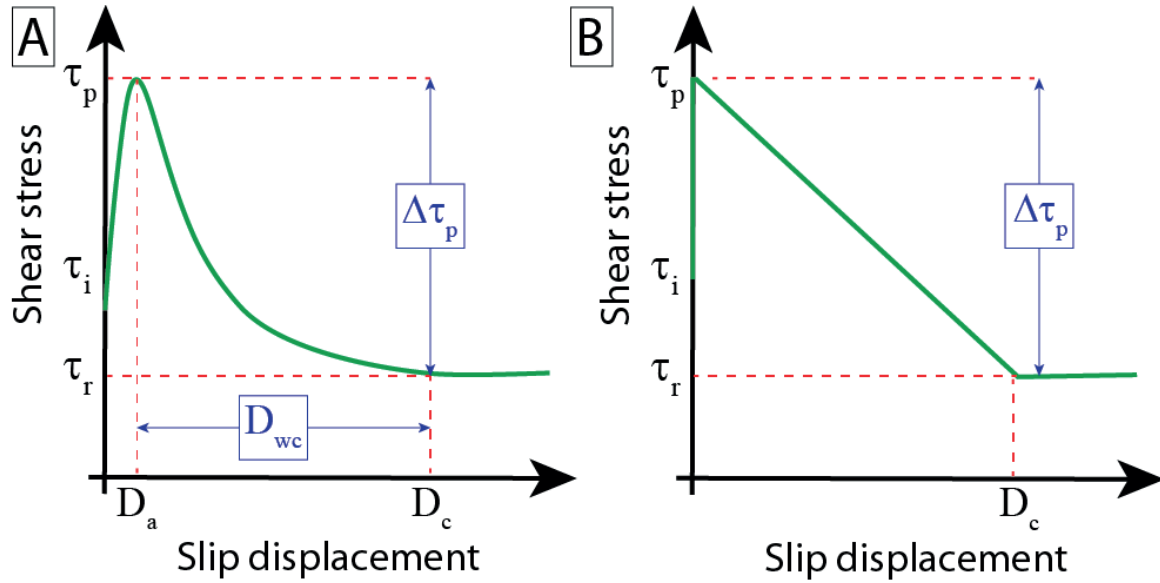


**Figure 1-17:** A) Schematic illustration of the slip-dependent law for shear strength. B) A more simple representation of the slip-dependent law assuming a linear decay of the shear strength with displacement (Ohnaka, 2013).

Based on the laboratory work of Ohnaka (2003), a shear rupture nucleation model has been proposed following the slip-dependent law (Figure 1-18). We briefly described it now:

1. **The quasi-static phase:** First, the rupture nucleation initiates in a stable or quasi-stable fashion at a steady speed  $V_{st}$ . Here, the rupture growth length  $L$  of the fault increases slowly up to a critical length  $L_{sc}$ .
2. **The acceleration phase:** Once the critical length  $L_{sc}$  is overcome, nucleation extends spontaneously up to a second critical nucleation length  $L_c$ . In this stage  $L$  increases more rapidly.
3. **The dynamic phase of constant high-speed rupture:** Finally, the rupture propagates at  $t = t_c$  at a constant high-speed velocity  $V_c$  inducing earthquakes.

The length  $L_{sc}$  might be then defined as the critical nucleation length that allows the transition from stable sliding to accelerated sliding, and  $L_c$  as the length at which rupture starts to propagate dynamically (Ohnaka, 2013). Thus fault asperities of size  $L$  can slip seismically only



if  $L > L_c$ , and aseismically if the contrary i.e.,  $L < L_c$ . The critical nucleation length  $L_c$  can be described in terms of  $D_c$  and  $\Delta\tau_p$  as:

$$L_c = \frac{1}{\alpha} \frac{\mu}{\Delta\tau_p} D_c$$

Where  $\mu$  is the rigidity of the host rock and  $\alpha$  is a dimensionless parameter (Ohnaka, 2003).

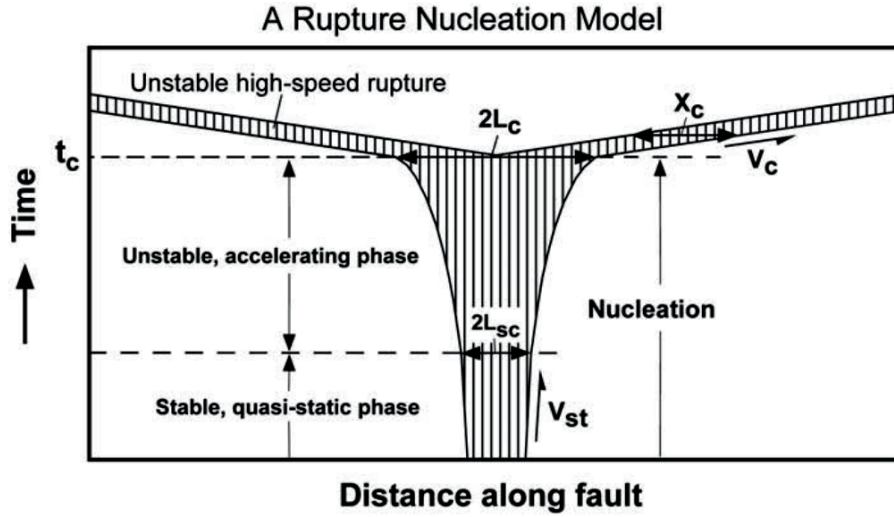


**Figure 1-18:** A physical shear rupture model (Ohnaka, 2003).

#### 1.3.5.2. RATE-AND-STATE FRICTION LAW

At moderate normal stresses ( $< 200$  MPa), the response of fault frictional strength to changes in velocity can be successfully described using the rate-and-state friction (RSF) constitutive equations (Lockner & Beeler, 2002; Marone, 1998; Scholz, 2002). The RSF laws are based on laboratory studies in rocks performed at low sliding velocities ( $10^{-9}$  to  $10^{-6}$  m/s) (Lockner & Beeler, 2002; Scholz, 1988). In this framework, friction depends on the slip rate and a state variable allowing the velocity-dependence of friction (Dieterich, 1979; Ruina, 1983). The empirical laws can be formulated as:

$$\mu = \mu_o + a \cdot \ln\left(\frac{V}{V_o}\right) + b \cdot \ln\left(\frac{V_o \cdot \theta}{D_c}\right),$$

Equation 1-7: Rate-and-state constitutive empirical law.

Where  $\mu_o$  is a constant that represents friction at steady-state for a reference velocity  $V_o$ ,  $\mu$  is the friction at the new steady-state velocity  $V$ , and “a” and “b” are empirical parameters, also named the direct and evolution effect respectively (Lockner & Beeler, 2002). The state variable  $\theta$  can be interpreted as the average lifetime of contacts, i.e., the average elapsed time since the contacts existing at a given time were first formed (Scholz, 2002). The critical slip distance  $D_c$ , at a constant velocity  $V$ , is often interpreted as the distance over which friction evolves from a local peak to a steady-state (Marone, 1998).

The two most common evolution laws correspond to Dieterich's (Dieterich, 1979) and Ruina's (Ruina, 1983) law. The empirical Ruina's law is defined as:

$$\frac{d\theta}{dt} = -\frac{V \cdot \theta}{D_c} \cdot \ln\left(\frac{V_0 \cdot \theta}{D_c}\right)$$

Equation 1-8: Ruina's evolution empirical law (Ruina, 1983).

Where the dominant physical process suggests that any change in friction, including strengthening during quasi-stationary contact, requires slip (Marone, 1998). The also empirical Dieterich's law is defined as:

$$\frac{d\theta}{dt} = 1 - \frac{V \cdot \theta}{D_c}$$

Equation 1-9: Dieterich's evolution empirical law (Dieterich, 1979).

In the Dieterich's model, friction primarily depends on the time-dependent microstructural evolution. Despite the initial microphysical assumptions, both laws successfully reproduced laboratory data in a similar manner and differences are difficult to distinguish in the laboratory (Marone, 1998).

The sliding stability is determined by the friction parameter (a-b), defined as:

$$a - b = \frac{\Delta\mu_{ss}}{\ln\left(\frac{V}{V_0}\right)}$$

Equation 1-10: Frictional stability parameter

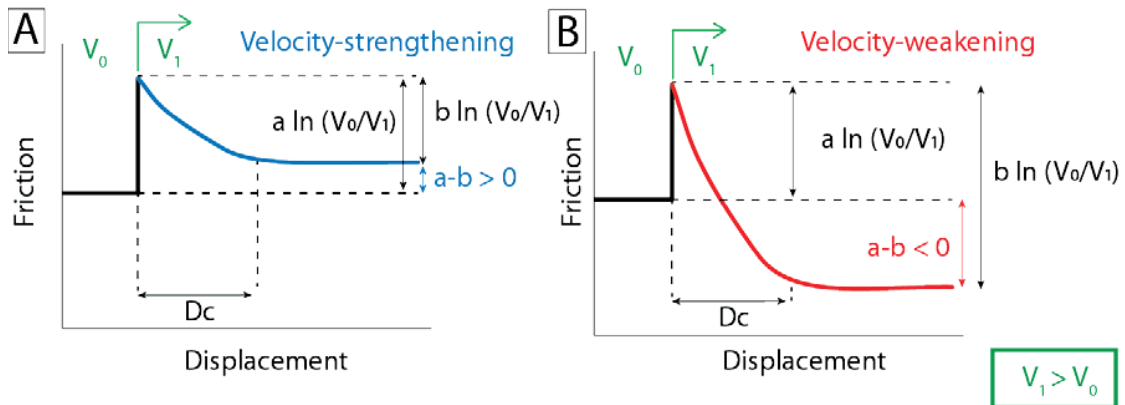


**Figure 1-19:** Schematic illustration of the frictional response to velocity-stepping .A) Velocity-strengthening behavior. B) Velocity weakening behavior.



Where  $\Delta\mu_{ss}$  is the change in the steady-state friction upon an immediate change in sliding velocity from  $V_0$  to  $V$  (Marone, 1998). For neutral or positive rate dependence,  $(a - b) \geq 0$ , sliding will tend to be stable, and the material will be described as velocity-strengthening (Figure 1-19a). Conversely, if the frictional strength decreases upon an increase in sliding velocity,  $(a - b) < 0$ , any perturbation on the fault will potentially promote slip acceleration. Thus, the system will be considered as potentially unstable, and the material will be described as velocity- weakening (Figure 1-19b) (Scholz, 2002).

However, the condition for instability to occur does not just depend on the velocity-weakening characteristic of the material. Stick-slip instabilities in the RSF framework will occur when the system elastic stiffness  $k$  is smaller than the critical fault rheologic stiffness  $k_c$  (Gu et al., 1984; Scholz, 1998; Scuderi, Collettini, Viti, et al., 2017). Thus, in addition to velocity-weakening, the nucleation condition at low sliding velocities is given by:

$$k < k_c = \frac{(\sigma_n - Pp) \cdot (b - a)}{D_c}$$

Equation 1-11: Stiffness instability condition

It is still difficult to account for the physics supporting the empirical rate- and – state frictional (RSF) approach. Nevertheless, the RSF theory has been widely adopted in the literature (Marone, 1998). It has successfully described fault friction and the resulting slip behavior at low sliding velocities for several rocks and conditions. However, results also show remarkable discrepancies upon mineralogy (Carpenter et al., 2011; Giorgetti et al., 2015; Kohli & Zoback, 2013; Logan & Rauenzahn, 1987; Moore & Lockner, 2011), fault fabric (Ikari et al., 2011; Tesei et al., 2012), surface roughness (Harbord et al., 2017), temperature (Den Hartog & Spiers, 2013; Lu & He, 2018; Niemeijer & Collettini, 2013; Verberne et al., 2013), the presence of fluids (Faulkner et al., 2018; Morrow et al., 2017), and others.

For example, in terms of mineralogy, clay-rich rocks are usually described as velocity-strengthening materials, while crystalline rocks velocity-weakening at low-grade conditions (Dieterich, 1979; Scholz, 2002). However, mixtures of clays and crystalline minerals suggest the velocity-dependence of frictional sliding might transit from unstable to stable fault slip and vice-versa (Tembe et al., 2010) (Figure 1-20). Pre-existing fault fabric can also modify the velocity-dependence of rocks, can induce a strong reduction in the frictional strength, and affect the evolution of the rock microstructures (Collettini et al., 2009; Ikari et al., 2015; Tesei et al., 2014). Finally, the presence of pore fluids can lower the frictional strength (Morrow et al., 2017) and promote velocity-strengthening behavior in clays (Ikari et al., 2007). For other types of rocks, pore fluid pressures can promote a transition from velocity-strengthening to velocity-weakening (Scuderi, Collettini, & Marone, 2017; Scuderi & Collettini, 2016) or can assist a fault strengthening process under favorable hydrothermal conditions during interseismic periods (Tenthorey et al., 2003).

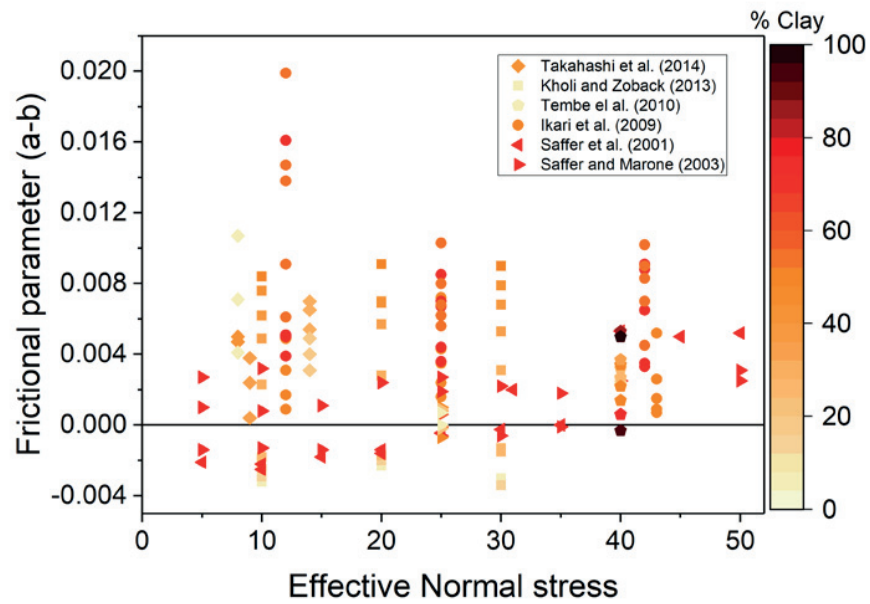


**Figure 1-20:** Frictional parameter versus effective normal stress and clay content (%).

As we have seen, both the fault heterogeneity and environmental conditions puzzle how fault behaves raising significant questions about a general pattern or mechanism that can explain, for instance, the fault behavior of the Main Fault (MF) in the Opalinus Clay formation. In this thesis, we used this approach to study the frictional properties of the MF.

## 1.4. THE OBJECTIVE OF THE THESIS

Extensive research has been carried out to characterize the mechanical behavior of the Opalinus Clay formation (e.g., Favero et al., 2016; Giger et al., 2017; Minardi et al., 2016; Parisio et al., 2015). However little is still known about the architecture, mechanics and the fluid-transport properties of the OPA fault zones and how these properties are coupled between them. Therefore, there is a need for the study of clay-bearing faults to overcome safety, operational, and constructability issues that put into question the long-term suitability of deep geological repositories.

In this thesis, we study the frictional and the transport properties of fault systems within the Opalinus Clay formation. We have integrated datasets of microstructural observations, petrophysical measurements, and mechanical results from frictional experiments to provide a qualitative and quantitative characterization of the clay-bearing fault systems within the Opalinus Clay formation. By doing that, we have investigated the heterogeneous fault behaviors of a clay-rich fault; we provide new constraints of the fluid-transport properties and the evolution of permeability during fault slip. We finally contribute to a better understanding of faulting and fault systems in shales and to the risk assessment process for nuclear waste storage.

In this doctoral research, we have addressed three main aspects:

- i. Microstructural characterization of the pore structure and fluid-transport properties of the fault gouge.
- ii. Frictional properties of fault-related rocks in relation to fault stability and earthquakes generation and fault microstructure at low slip rates ( $< 300 \mu\text{m/s}$ ): the fault gouge and scaly clays of the Opalinus Clay formation.
- iii. The evolution of dilatancy and permeability during deformation of the Opalinus Clay fault gouge.

## 1.5. ORGANIZATION OF THE THESIS

This thesis has been written in a compilation of articles format following EPFL guidelines. The articles are published or submitted for publication in peer-reviewed journals. As a result, in the introduction section of each chapter, the literature review may be repeated. The thesis is structured as follows:

- Chapter 2 is under review in *Geophysical Journal International*. The chapter investigates the fluid-transport properties and mineralogy of the related-fault rocks of the Opalinus Clay formation. Results include porosity measurements across the borehole BFS-2 intersecting the Main Fault in the Mont Terri Laboratory, mineralogy analysis of the fault-related rocks, and FIB-SEM observations of the fault gouge. The

chapter concludes that the fault gouge in the Opalinus Clay formation can act as a spatially-discrete however discontinuous preferential fluid-flow pathway.

- Chapter 3 has been published in the *Journal of Geophysical Research: Solid Earth* in December 2017. The chapter provides results on frictional strength, frictional stability, and frictional healing of simulated Opalinus Clay fault gouge. Experiments were carried out using a double-direct shear configuration. Together with microstructure observations, the chapter discussed the dominant deformation mechanism responsible for accommodating fault slip displacements. The chapter concludes the low frictional strength, the velocity-strengthening behavior and the extremely low healing capacity of the fault gouge.
  - **Reference:** Orellana, L.F., Scuderi, M.M., Collettini, C., Violay, M., 2018. Frictional Properties of Opalinus Clay: Implications for nuclear waste storage. *J. Geophys. Res. Solid Earth* 123, 157–175. doi:10.1002/2017JB014931
- Chapter 4 is under review in *Geophysical Research Letters*. The chapter presents the results of frictional strength, permeability and dilatancy variation during shear deformation of simulated Opalinus Clay fault gouge samples. Experiments have been performed in a saw-cut triaxial configuration. The chapter discusses the evolution of permeability with fault slip and provides stress-dilatancy and stress-compaction relations for simulated fault gouge.
- Chapter 5 has been published in *Earth and Planetary Science Letters* on April 2018. The chapter examines the role of the scaly clays in the fault stability behavior of major faults in the Opalinus Clay formation. Frictional tests were performed in a double-direct shear configuration on intact samples sheared parallel and perpendicular to the bedding. The research finally reports laboratory and microstructural evidence indicating that first, scaly clays can be generated on intact shale rock at sub-seismic rates and low-pressure conditions; and second, once scaly clay fabric forms, its presence can reduce fault strength and might facilitate earthquake generation.
  - **Reference:** Orellana, L.F., Scuderi, M.M., Collettini, C., Violay, M., 2018. Do scaly clays control seismicity on faulted shale rocks? *Earth Planet. Sci. Lett.* 488, 59–67. doi: 10.1016/j.epsl.2018.01.027
- Chapter 6 corresponds to the Conclusion chapter. It summarizes the major outcomes of this research and presents possibilities for future development of the work presented in the thesis.

This work has been carried out under the supervision of Prof. Marie Violay, the co-supervision of Prof. Jean-François Molinari, and in collaboration with Prof. Cristiano Collettini, Dr. Marco Scuderi, Dr. Carolina Giorgetti, Dr. Christophe Nussbaum, Dr. Luiz Grafalha, Dr. Pierre Henry, and Dr. Thierry Adatte.

## 1.6. REFERENCES

- Abercrombie, R. E., & Rice, J. R. (2005). Can observations of earthquake scaling constrain slip weakening? *Geophysical Journal International*, 162(2), 406–424. <https://doi.org/10.1111/j.1365-246X.2005.02579.x>
- Amontons, M. (1699). De la resistance cause'e dans les machines. *Memoires de l'Academie Royale Des Frances*, A, 206–227.
- Barros, L. De, Daniel, G., Guglielmi, Y., Rivet, D., Caron, H., Payre, X., et al. (2016). Fault structure, stress, or pressure control of the seismicity in shale? Insights from a controlled experiment of fluid-induced fault reactivation. *Journal of Geophysical Research: Solid Earth*, 121(6), 4506–4522. <https://doi.org/10.1002/2015JB012633>
- Behnsen, J., & Faulkner, D. (2012). The effect of mineralogy and effective normal stress on frictional strength of sheet silicates. *Journal of Structural Geology*, 42, 49–61. <https://doi.org/10.1016/j.jsg.2012.06.015>
- Billiotte, J., Yang, D., & Su, K. (2008). Experimental study on gas permeability of mudstones. *Physics and Chemistry of the Earth*, 33(SUPPL. 1), 231–236. <https://doi.org/10.1016/j.pce.2008.10.040>
- Bossart, P., Bernier, F., Birkholzer, J., Bruggeman, C., Connolly, P., Dewonck, S., et al. (2017). Mont Terri rock laboratory, 20 years of research: introduction, site characteristics and overview of experiments. *Swiss Journal of Geosciences*, 110(1), 3–22. <https://doi.org/10.1007/s00015-016-0236-1>
- Bourg, I. C. (2015). Sealing Shales versus Brittle Shales: A Sharp Threshold in the Material Properties and Energy Technology Uses of Fine-Grained Sedimentary Rocks. *Environmental Science and Technology Letters*, 2(10), 255–259. <https://doi.org/10.1021/acs.estlett.5b00233>
- Bourg, I. C., Beckingham, L. E., & DePaolo, D. J. (2015). The Nanoscale Basis of CO<sub>2</sub> Trapping for Geologic Storage. *Environmental Science & Technology*, 49(17), 10265–10284. <https://doi.org/10.1021/acs.est.5b03003>
- Bowden, F. P., & Tabor, D. (1950). *The friction and lubrication of solids, Part I*. Oxford: Clarendon Press.
- Bowden, F. P., & Tabor, D. (1964). *The friction and lubrication of solids, Part II*. Oxford: Clarendon Press.
- Bowden, F. P., & Tabor, D. (1966). Friction, lubrication and wear: a survey of work during the last decade. *British Journal of Applied Physics*, 17(1521–1544), 1521–1544. <https://doi.org/10.1088/0508-3443/17/12/301>
- Brace, W. F., & Byerlee, J. D. (1966). Stick Slip as a Mechanism for Earthquakes. *Science*, 153(3739), 990–992.
- Brace, W. F., & Kohlstedt, D. L. (1980). Limits on lithospheric stress imposed by laboratory experiments. *Journal of Geophysical Research: Solid Earth*, 85(B11), 6248–6252.

<https://doi.org/10.1029/JB085iB11p06248>

- Brantut, N., & Viesca, R. C. (2015). Earthquake nucleation in intact or healed rocks. *Journal of Geophysical Research: Solid Earth*, 120(1), 191–209. <https://doi.org/10.1002/2014JB011518>
- Brodsky, E. E., Kirkpatrick, J., & Candela, T. (2016). Constraints from fault roughness on the scale-dependent strength of rocks. *Geology*, 44(1), 19–22. <https://doi.org/10.1130/G37206.1>
- Bullock, R., De Paola, N., & Holdsworth, R. (2015). An experimental investigation into the role of phyllosilicate content on earthquake propagation during seismic slip in carbonate faults. *Journal of Geophysical Research: Solid Earth*, 120(5), 3187–3207. <https://doi.org/10.1002/2015JB011914>
- Byerlee, J. D. (1978). Friction of rocks. *Pure and Applied Geophysics*, 116(4–5), 615–626. <https://doi.org/10.1007/BF00876528>
- Byerlee, J. D., & Brace, W. F. (1968). Stick slip, stable sliding, and earthquakes-Effect of rock type, pressure, strain rate, and stiffness. *Journal of Geophysical Research*, 73(18), 6031–6037. <https://doi.org/10.1029/JB073i018p06031>
- Caine, J. S., Evans, J. P., & Forster, C. B. (1996). Fault zone architecture and permeability structure. *Geology*, 24(11), 1025–1028. [https://doi.org/10.1130/0091-7613\(1996\)024<1025](https://doi.org/10.1130/0091-7613(1996)024<1025)
- Candela, T., Renard, F., Klinger, Y., Mair, K., Schmittbuhl, J., & Brodsky, E. E. (2012). Roughness of fault surfaces over nine decades of length scales. *Journal of Geophysical Research: Solid Earth*, 117(8), 1–30. <https://doi.org/10.1029/2011JB009041>
- Carpenter, B., Marone, C., & Saffer, D. (2011). Weakness of the San Andreas Fault revealed by samples from the active fault zone. *Nature Geoscience*, 4(4), 251–254. <https://doi.org/10.1038/ngeo1089>
- Carpenter, B., Saffer, D., & Marone, C. (2012). Frictional properties and sliding stability of the San Andreas fault from deep drill core. *Geology*, 40(8), 759–762. <https://doi.org/10.1130/G33007.1>
- Chester, F. M., & Logan, J. M. (1986). Implications for mechanical properties of brittle faults from observations of the Punchbowl fault zone, California. *Pure and Applied Geophysics*, 124(1), 79–106. <https://doi.org/10.1007/BF00875720>
- Collettini, C., Niemeijer, A., Viti, C., & Marone, C. (2009). Fault zone fabric and fault weakness. *Nature*, 462(7275), 907–910. <https://doi.org/10.1038/nature08585>
- Coulomb, C. A. (1773). Essai sur une application des règles de Maximis & Minimis à quelques Problèmes de Statique, relatifs à l'Architecture. *Mémoires de Mathématique et de Physique, Présentés à l'Académie Royale Des Sciences, Par Divers Savans, & Lûs Dans Ses Assemblées*, 7, 343–382.
- Cox, S., & Scholz, C. H. (1988). On the formation and growth of faults: an experimental study. *Journal of Structural Geology*, 10(4), 413–430. <https://doi.org/10.1016/0191->



8141(88)90019-3

- Dieterich, J. H. (1979). Modeling of rock friction: 1. Experimental results and constitutive equations. *Journal of Geophysical Research*, 84(9), 2161–2168. <https://doi.org/10.1007/BF00876539>
- Duboeuf, L., De Barros, L., Cappa, F., Guglielmi, Y., Deschamps, A., & Seguy, S. (2017). Aseismic Motions Drive a Sparse Seismicity During Fluid Injections Into a Fractured Zone in a Carbonate Reservoir. *Journal of Geophysical Research: Solid Earth*, 122(10), 8285–8304. <https://doi.org/10.1002/2017JB014535>
- Ellsworth, W. L. (2013). Injection-Induced Earthquakes. *Science*, 341(6142), 1225942–1225942. <https://doi.org/10.1126/science.1225942>
- Evans, J. P., Forster, C. B., & Goddard, J. V. (1997). Permeability of fault-related rocks, and implications for hydraulic structure of fault zones. *Journal of Structural Geology*, 19(11), 1393–1404. [https://doi.org/10.1016/S0191-8141\(97\)00057-6](https://doi.org/10.1016/S0191-8141(97)00057-6)
- Fagereng, Å., & Sibson, R. H. (2010). Mélange rheology and seismic style. *Geology*, 38(8), 751–754. <https://doi.org/10.1130/G30868.1>
- Farrokhrouz, M., & Asef, M. R. (2013). *Shale Engineering Mechanics and Mechanisms*. CRC Press. <https://doi.org/10.1007/s13398-014-0173-7.2>
- Faulkner, D., & Rutter, E. (2000). Comparisons of water and argon permeability in natural clay-bearing fault gouge under high pressure at 20°C. *Journal of Geophysical Research*, 105(B7), 16415. <https://doi.org/10.1029/2000JB900134>
- Faulkner, D., Lewis, A. C., & Rutter, E. (2003). On the internal structure and mechanics of large strike-slip fault zones: Field observations of the Carboneras fault in southeastern Spain. *Tectonophysics*, 367(3–4), 235–251. [https://doi.org/10.1016/S0040-1951\(03\)00134-3](https://doi.org/10.1016/S0040-1951(03)00134-3)
- Faulkner, D., Jackson, C. A. L., Lunn, R. J., Schlische, R. W., Shipton, Z. K., Wibberley, C. A. J., & Withjack, M. O. (2010). A review of recent developments concerning the structure, mechanics and fluid flow properties of fault zones. *Journal of Structural Geology*, 32(11), 1557–1575. <https://doi.org/10.1016/j.jsg.2010.06.009>
- Faulkner, D., Mitchell, T. M., Behnson, J., Hirose, T., & Shimamoto, T. (2011). Stuck in the mud? Earthquake nucleation and propagation through accretionary forearcs. *Geophysical Research Letters*, 38(18), 1–5. <https://doi.org/10.1029/2011GL048552>
- Faulkner, D., Sanchez-Roa, C., Boulton, C., & Den Hartog, S. A. M. (2018). Pore Fluid Pressure Development in Compacting Fault Gouge in Theory, Experiments, and Nature. *Journal of Geophysical Research: Solid Earth*, 123(1), 226–241. <https://doi.org/10.1002/2017JB015130>
- Favero, V., Ferrari, A., & Laloui, L. (2016). Thermo-mechanical volume change behaviour of Opalinus Clay. *International Journal of Rock Mechanics and Mining Sciences*, 90(November 2015), 15–25. <https://doi.org/10.1016/j.ijrmms.2016.09.013>
- Forster, C. B., Evans, J. P., Tanaka, H., Jeffreys, R., & Nohara, T. (2003). Hydrologic

- properties and structure of the Mozumi Fault, central Japan. *Geophysical Research Letters*, 30(6), 1–4. <https://doi.org/10.1029/2002GL014904>
- Giger, S. B., Ewy, R., Favero, V., Stankovic, R., & Keller, L. M. (2018). Consolidated-undrained triaxial testing of Opalinus Clay: Results and method validation. *Geomechanics for Energy and the Environment*, 1–13. <https://doi.org/10.1016/j.gete.2018.01.003>
- Giorgetti, C., Carpenter, B., & Collettini, C. (2015). Frictional behavior of talc-calcite mixtures. *Journal of Geophysical Research: Solid Earth*, 120(9), 6614–6633. <https://doi.org/10.1002/2015JB011970>
- Gu, J.-C., Rice, J. R., Ruina, A., & Tse, S. T. (1984). Slip motion and stability of a single degree of freedom elastic system with rate and state dependent friction. *Journal of the Mechanics and Physics of Solids*, 32(3), 167–196. [https://doi.org/https://doi.org/10.1016/0022-5096\(84\)90007-3](https://doi.org/https://doi.org/10.1016/0022-5096(84)90007-3)
- Guglielmi, Y., Cappa, F., Avouac, J. P., Henry, P., & Elsworth, D. (2015). Seismicity triggered by fluid injection – induced aseismic slip. *Science*, 348(6240), 1224–1227. <https://doi.org/10.1126/science.aab0476>
- Haines, S., Marone, C., & Saffer, D. (2014). Frictional properties of low-angle normal fault gouges and implications for low-angle normal fault slip. *Earth and Planetary Science Letters*, 408, 57–65. <https://doi.org/10.1016/j.epsl.2014.09.034>
- Harbord, C. W. A., Nielsen, S., De Paola, N., & Holdsworth, R. (2017). Earthquake nucleation on rough faults. *Geology*, 45(10), 931–934. <https://doi.org/10.1130/G39181.1>
- Harris, R. A. (2017). Large earthquakes and creeping faults. *Reviews of Geophysics*, 55(1), 169–198. <https://doi.org/10.1002/2016RG000539>
- Den Hartog, S. A. M., & Spiers, C. J. (2013). Influence of subduction zone conditions and gouge composition on frictional slip stability of megathrust faults. *Tectonophysics*, 600, 75–90. <https://doi.org/10.1016/j.tecto.2012.11.006>
- Hirakawa, E., Ma, S., Evan, H., & Shuo, M. (2016). Dynamic fault weakening and strengthening by gouge compaction and dilatancy in a fluid-saturated fault zone. *Journal of Geophysical Research: Solid Earth*, 121(8), 5988–6008. <https://doi.org/10.1002/2015JB012509>
- Hostettler, B., Reisdorf, A. G., Jaeggi, D., Deplazes, G., Bläsi, H., Morard, A., et al. (2017). Litho- and biostratigraphy of the Opalinus Clay and bounding formations in the Mont Terri rock laboratory (Switzerland). *Swiss Journal of Geosciences*, 110(1), 23–37. <https://doi.org/10.1007/s00015-016-0250-3>
- Houben, M. E., Desbois, G., & Urai, J. L. (2013). Pore morphology and distribution in the Shaly facies of Opalinus Clay (Mont Terri, Switzerland): Insights from representative 2D BIB-SEM investigations on mm to nm scale. *Applied Clay Science*, 71, 82–97. <https://doi.org/10.1016/j.clay.2012.11.006>
- Huang, Y., Ampuero, J. P., & Kanamori, H. (2013). Slip-Weakening Models of the 2011 Tohoku-Oki Earthquake and Constraints on Stress Drop and Fracture Energy. *Pure and Applied Geophysics*, 171(10), 2555–2568. <https://doi.org/10.1007/s00024-013-0718-2>



- Hubbert, M. K., & Rubey, W. W. (1959). Role of fluid pressure in mechanics of overthrust faulting: I. Mechanics of fluid-filled porous solids and its application to overthrust faulting. *GSA Bulletin*, 70(2), 115–166. Retrieved from [http://dx.doi.org/10.1130/0016-7606\(1959\)70\[115:ROFPIM\]2.0.CO](http://dx.doi.org/10.1130/0016-7606(1959)70[115:ROFPIM]2.0.CO)
- Husen, S., Kissling, E., & von Deschanden, A. (2012). Induced seismicity during the construction of the Gotthard Base Tunnel, Switzerland: Hypocenter locations and source dimensions. *Journal of Seismology*, 17(1), 63–81. <https://doi.org/10.1007/s10950-012-9313-8>
- Ikari, M. J., Saffer, D., & Marone, C. (2007). Effect of hydration state on the frictional properties of montmorillonite-based fault gouge. *Journal of Geophysical Research: Solid Earth*, 112(6), 1–12. <https://doi.org/10.1029/2006JB004748>
- Ikari, M. J., Saffer, D., & Marone, C. (2009). Frictional and hydrologic properties of clay-rich fault gouge. *Journal of Geophysical Research: Solid Earth*, 114(5), 1–18. <https://doi.org/10.1029/2008JB006089>
- Ikari, M. J., Niemeijer, A., & Marone, C. (2011). The role of fault zone fabric and lithification state on frictional strength, constitutive behavior, and deformation microstructure. *Journal of Geophysical Research: Solid Earth*, 116(8), 1–25. <https://doi.org/10.1029/2011JB008264>
- Ikari, M. J., Marone, C., Saffer, D., & Kopf, A. J. (2013). Slip weakening as a mechanism for slow earthquakes. *Nature Geoscience*, 6(6), 468–472. <https://doi.org/10.1038/ngeo1818>
- Ikari, M. J., Niemeijer, A., & Marone, C. (2015). Experimental investigation of incipient shear failure in foliated rock. *Journal of Structural Geology*, 77, 82–91. <https://doi.org/10.1016/j.jsg.2015.05.012>
- Ishikawa, T., Tanimizu, M., Nagaishi, K., Matsuoka, J., Tadai, O., Sakaguchi, M., et al. (2008). Coseismic fluid-rock interactions at high temperatures in the Chelungpu fault. *Nature Geoscience*, 1(10), 679–683. <https://doi.org/10.1038/ngeo308>
- Jaeger, J., Cook, N. G., & Zimmerman, R. (2007). *Fundamentals of Rock Mechanics*, 4th Edition (4th Editio). Blackwell Publishing.
- Jeanne, P., Guglielmi, Y., Rutqvist, J., Nussbaum, C., & Birkholzer, J. (2018). Permeability Variations Associated With Fault Reactivation in a Claystone Formation Investigated by Field Experiments and Numerical Simulations. *Journal of Geophysical Research: Solid Earth*, 123(2), 1694–1710. <https://doi.org/10.1002/2017JB015149>
- Keller, L. M., Schuetz, P., Erni, R., Rossell, M. D., Lucas, F., Gasser, P., & Holzer, L. (2013). Characterization of multi-scale microstructural features in Opalinus Clay. *Microporous and Mesoporous Materials*, 170, 83–94. <https://doi.org/10.1016/j.micromeso.2012.11.029>
- Kim, J.-S., Kwon, S.-K., Sanchez, M., & Cho, G.-C. (2011). Geological storage of high level nuclear waste. *KSCE Journal of Civil Engineering*, 15(4), 721–737. <https://doi.org/10.1007/s12205-011-0012-8>
- Kneuker, T., Hammer, J., Shao, H., Schuster, K., Furche, M., & Zulauf, G. (2017).

- Microstructure and composition of brittle faults in claystones of the Mont Terri rock laboratory (Switzerland): New data from petrographic studies, geophysical borehole logging and permeability tests. *Engineering Geology*, 231(October), 139–156. <https://doi.org/10.1016/j.enggeo.2017.10.016>
- Kohli, A. H., & Zoback, M. D. (2013). Frictional properties of shale reservoir rocks. *Journal of Geophysical Research: Solid Earth*, 118(9), 5109–5125. <https://doi.org/10.1002/jgrb.50346>
- Lacroix, B., Tesei, T., Oliot, E., Lahfid, A., & Collettini, C. (2015). Early weakening processes inside thrust fault. *Tectonics*, 34(7), 1396–1411. <https://doi.org/10.1002/2014TC003716>
- Laurich, B., Urai, J. L., Desbois, G., Vollmer, C., & Nussbaum, C. (2014). Microstructural evolution of an incipient fault zone in Opalinus Clay: Insights from an optical and electron microscopic study of ion-beam polished samples from the Main Fault in the Mt-Terri Underground Research Laboratory. *Journal of Structural Geology*, 67(PA), 107–128. <https://doi.org/10.1016/j.jsg.2014.07.014>
- Leclère, H., Cappa, F., Faulkner, D., Fabbri, O., Armitage, P., & Blake, O. (2015). Development and maintenance of fluid overpressures in crustal fault zones by elastic compaction and implications for earthquake swarms. *Journal of Geophysical Research: Solid Earth*, 120(6), 4450–4473. <https://doi.org/10.1002/2014JB011759>
- Lefèvre, M., Guglielmi, Y., Henry, P., Dick, P., & Gout, C. (2016). Calcite veins as an indicator of fracture dilatancy and connectivity during strike-slip faulting in Toarcian shale (Tournemire tunnel, Southern France). *Journal of Structural Geology*, 83, 73–84. <https://doi.org/10.1016/j.jsg.2016.01.002>
- Lockner, D. A., & Beeler, N. M. (2002). *Rock failure and earthquakes*. *International Geophysics* (Vol. 81). [https://doi.org/10.1016/S0074-6142\(02\)80235-2](https://doi.org/10.1016/S0074-6142(02)80235-2)
- Lockner, D. A., Tanaka, H., Ito, H., Ikeda, R., Omura, K., & Naka, H. (2009). Geometry of the Nojima fault at Nojima-Hirabayashi, Japan - I. A simple damage structure inferred from borehole core permeability. *Pure and Applied Geophysics*, 166(10–11), 1649–1667. <https://doi.org/10.1007/s00024-009-0515-0>
- Lockner, D. A., Morrow, C., Moore, D., & Hickman, S. (2011). Low strength of deep San Andreas fault gouge from SAFOD core. *Nature*, 472(7341), 82–86. <https://doi.org/10.1038/nature09927>
- Logan, J. M., & Rauenzahn, K. A. (1987). Frictional dependence of gouge mixtures of quartz and montmorillonite on velocity, composition and fabric. *Tectonophysics*, 144(1–3), 87–108. [https://doi.org/10.1016/0040-1951\(87\)90010-2](https://doi.org/10.1016/0040-1951(87)90010-2)
- Logan, J. M., Dengo, C. A., Higgs, N. G., & Wang, Z. Z. (1992). Fabrics of Experimental Fault Zones: Their Development and Relationship to Mechanical Behavior. In *International Geophysics* (Vol. 51, pp. 33–67). [https://doi.org/10.1016/S0074-6142\(08\)62814-4](https://doi.org/10.1016/S0074-6142(08)62814-4)
- Van Loon, L. R., Soler, J. M., Müller, W., & Bradbury, M. H. (2004). Anisotropic diffusion in layered argillaceous rocks: A case study with Opalinus Clay. *Environmental Science and Technology*, 38(21), 5721–5728. <https://doi.org/10.1021/es049937g>

- Lu, Z., & He, C. (2018). Friction of foliated fault gouge with a biotite interlayer at hydrothermal conditions. *Tectonophysics*, 740–741(May), 72–92. <https://doi.org/10.1016/j.tecto.2018.05.003>
- Marone, C. (1998). Laboratory-Derived Friction Laws and Their Application To Seismic Faulting. *Annual Review of Earth and Planetary Sciences*, 26(1), 643–696. <https://doi.org/10.1146/annurev.earth.26.1.643>
- Mazzoldi, A., Rinaldi, A. P., Borgia, A., & Rutqvist, J. (2012). Induced seismicity within geological carbon sequestration projects: Maximum earthquake magnitude and leakage potential from undetected faults. *International Journal of Greenhouse Gas Control*, 10, 434–442. <https://doi.org/10.1016/j.ijggc.2012.07.012>
- Minardi, A., Crisci, E., Ferrari, A., & Laloui, L. (2016). Anisotropic volumetric behaviour of Opalinus clay shale upon suction variation. *Géotechnique Letters*, 6(2), 144–148. <https://doi.org/10.1680/jgele.16.00023>
- Mitchell, T. M., & Faulkner, D. (2009). The nature and origin of off-fault damage surrounding strike-slip fault zones with a wide range of displacements: A field study from the Atacama fault system, northern Chile. *Journal of Structural Geology*, 31(8), 802–816. <https://doi.org/10.1016/j.jsg.2009.05.002>
- Moore, D., & Lockner, D. A. (2004). Crystallographic controls on the frictional behavior of dry and water-saturated sheet structure minerals. *Journal of Geophysical Research*, 109(B3), B03401. <https://doi.org/10.1029/2003JB002582>
- Moore, D., & Lockner, D. A. (2011). Frictional strengths of talc-serpentine and talc-quartz mixtures. *Journal of Geophysical Research: Solid Earth*, 116(1), 1–17. <https://doi.org/10.1029/2010JB007881>
- Moreno, M., Li, S., Melnick, D., Bedford, J. R., Baez, J. C., Motagh, M., et al. (2018). Chilean megathrust earthquake recurrence linked to frictional contrast at depth. *Nature Geoscience*, 11(4), 285–290. <https://doi.org/10.1038/s41561-018-0089-5>
- Morrow, C., Moore, D., & Lockner, D. A. (2000). The effect of mineral bond strength and adsorbed water on fault gouge frictional strength. *Geophysical Research Letters*, 27(6), 815–818. <https://doi.org/10.1029/1999GL008401>
- Morrow, C., Lockner, D. A., Moore, D., & Hickman, S. (2014). Deep permeability of the San Andreas Fault from San Andreas Fault Observatory at Depth (SAFOD) core samples. *Journal of Structural Geology*, 64, 99–114. <https://doi.org/10.1016/j.jsg.2013.09.009>
- Morrow, C., Moore, D., & Lockner, D. A. (2017). Frictional strength of wet and dry montmorillonite. *Journal of Geophysical Research: Solid Earth*, 122(5), 3392–3409. <https://doi.org/10.1002/2016JB013658>
- National Cooperative for the Disposal of Radioactive Waste. (2018). HLW siting regions.
- Neuzil, C. E. (1994). How permeable are clays and shales? *Water Resources*, 30(2), 145–150.
- Nielsen, S., Spagnuolo, E., Violay, M., Smith, S. A. F., Di Toro, G., & Bistacchi, A. (2016). G: Fracture energy, friction and dissipation in earthquakes. *Journal of Seismology*, 20(4),

- 1187–1205. <https://doi.org/10.1007/s10950-016-9560-1>
- Niemeijer, A., & Collettini, C. (2013). Frictional Properties of a Low-Angle Normal Fault Under In Situ Conditions: Thermally-Activated Velocity Weakening. *Pure and Applied Geophysics*, 171(10), 2641–2664. <https://doi.org/10.1007/s00024-013-0759-6>
- Noda, H., & Lapusta, N. (2013). Stable creeping fault segments can become destructive as a result of dynamic weakening. *Nature*, 493(7433), 518–521. <https://doi.org/10.1038/nature11703>
- Norris, S. (2017). Radioactive waste confinement: Clays in natural and engineered barriers - introduction. *Geological Society Special Publication*, 443(1), 1–8. <https://doi.org/10.1144/SP443.26>
- Numelin, T., Marone, C., & Kirby, E. (2007). Frictional properties of natural fault gouge from a low-angle normal fault, Panamint Valley, California. *Tectonics*, 26(2), n/a-n/a. <https://doi.org/10.1029/2005TC001916>
- Nussbaum, C., Bossart, P., Amann, F., & Aubourg, C. (2011). Analysis of tectonic structures and excavation induced fractures in the Opalinus Clay, Mont Terri underground rock laboratory (Switzerland). *Swiss Journal of Geosciences*, 104(2), 187–210. <https://doi.org/10.1007/s00015-011-0070-4>
- Nussbaum, C., Kloppenburg, A., Caër, T., & Bossart, P. (2017). Tectonic evolution around the Mont Terri rock laboratory, northwestern Swiss Jura: constraints from kinematic forward modelling. *Swiss Journal of Geosciences*, 110(1), 39–66. <https://doi.org/10.1007/s00015-016-0248-x>
- Ohnaka, M. (1992). Earthquake source nucleation: A physical model for short-term precursors. *Tectonophysics*, 211(1), 149–178. [https://doi.org/10.1016/0040-1951\(92\)90057-D](https://doi.org/10.1016/0040-1951(92)90057-D)
- Ohnaka, M. (2003). A constitutive scaling law and a unified comprehension for frictional slip failure, shear fracture of intact rock, and earthquake rupture. *Journal of Geophysical Research: Solid Earth*, 108(B2), 1–21. <https://doi.org/10.1029/2000JB000123>
- Ohnaka, M. (2013). *The Physics of Rock Failure and Earthquakes*. Cambridge: Cambridge University Press. <https://doi.org/10.1017/CBO9781139342865>
- Orellana, L. F., Scuderi, M. M., Collettini, C., & Violay, M. (2018a). Do scaly clays control seismicity on faulted shale rocks? *Earth and Planetary Science Letters*, 488, 59–67. <https://doi.org/10.1016/j.epsl.2018.01.027>
- Orellana, L. F., Scuderi, M. M., Collettini, C., & Violay, M. (2018b). Frictional Properties of Opalinus Clay: Implications for Nuclear Waste Storage. *Journal of Geophysical Research: Solid Earth*, 123(1), 157–175. <https://doi.org/10.1002/2017JB014931>
- Parisio, F., Samat, S., & Laloui, L. (2015). Constitutive analysis of shale: A coupled damage plasticity approach. *International Journal of Solids and Structures*, 75–76, 88–98. <https://doi.org/10.1016/j.ijsolstr.2015.08.003>
- Paterson, M. S., & Wong, T. F. (2005). *Experimental rock deformation - The brittle field* (2nd

- ed.). Springer-Verlag Berlin Heidelberg. <https://doi.org/10.1007/b137431>
- Popov, V. (2010). *Contact Mechanics and Friction: Physical Principles and Applications*. Springer Berlin Heidelberg. Retrieved from <https://books.google.ch/books?id=-I8qtcJN1VIC>
- Popova, E., & Popov, V. (2015). The research works of Coulomb and Amontons and generalized laws of friction. *Friction*, 3(2), 183–190. <https://doi.org/10.1007/s40544-015-0074-6>
- Rice, J. R., Rudnicki, J. W., & Platt, J. D. (2014). Stability and localization of rapid shear in fluid-saturated fault gouge: 1. Linearized stability analysis. *Journal of Geophysical Research: Solid Earth*, 119(5), 4311–4333. <https://doi.org/10.1002/2013JB010710>
- Ruina, A. (1983). Slip instability and state variable friction laws. *Journal of Geophysical Research*, 88(B12), 10359. <https://doi.org/10.1029/JB088iB12p10359>
- Rutqvist, J., Cappa, F., Rinaldi, A. P., & Godano, M. (2014). Modeling of induced seismicity and ground vibrations associated with geologic CO<sub>2</sub> storage, and assessing their effects on surface structures and human perception. *International Journal of Greenhouse Gas Control*, 24, 64–77. <https://doi.org/10.1016/j.ijggc.2014.02.017>
- Saffer, D., Frye, K. M., Marone, C., & Mair, K. (2001). Laboratory results indicating complex and potentially unstable frictional behavior of smectite clay. *Geophysical Research Letters*, 28(12), 2297–2300. <https://doi.org/10.1029/2001GL012869>
- Saffer, D., Lockner, D. A., & McKiernan, A. (2012). Effects of smectite to illite transformation on the frictional strength and sliding stability of intact marine mudstones. *Geophysical Research Letters*, 39(11), 2–7. <https://doi.org/10.1029/2012GL051761>
- Samuelson, J., Elsworth, D., & Marone, C. (2009). Shear-induced dilatancy of fluid-saturated faults: Experiment and theory. *Journal of Geophysical Research: Solid Earth*, 114(12), 1–15. <https://doi.org/10.1029/2008JB006273>
- Scholz, C. H. (1988). The critical slip distance for seismic faulting. *Nature*, 336(6201), 761–763. <https://doi.org/10.1038/336761a0>
- Scholz, C. H. (1998). Earthquakes and friction laws. *Nature*, 391(6662), 37–42. <https://doi.org/10.1038/34097>
- Scholz, C. H. (2002). *The Mechanics of Earthquakes and Faulting*. Cambridge University Press. Retrieved from <https://books.google.ch/books?id=JL1VM5wMbrQC>
- Scuderi, M. M., & Collettini, C. (2016). The role of fluid pressure in induced vs. triggered seismicity: Insights from rock deformation experiments on carbonates. *Scientific Reports*, 6(January), 1–9. <https://doi.org/10.1038/srep24852>
- Scuderi, M. M., Collettini, C., Viti, C., Tinti, E., & Marone, C. (2017). Evolution of shear fabric in granular fault gouge from stable sliding to stick slip and implications for fault slip mode. *Geology*, 45(8), 731–734. <https://doi.org/10.1130/G39033.1>
- Scuderi, M. M., Collettini, C., & Marone, C. (2017). Frictional stability and earthquake



- triggering during fluid pressure stimulation of an experimental fault. *Earth and Planetary Science Letters*, 477, 84–96. <https://doi.org/10.1016/j.epsl.2017.08.009>
- Shimamoto, T., & Logan, J. M. (1981). Effects of simulated clay gouges on the sliding behavior of Tennessee sandstone. *Tectonophysics*, 75(3–4), 243–255. [https://doi.org/10.1016/0040-1951\(81\)90276-6](https://doi.org/10.1016/0040-1951(81)90276-6)
- Sibson, R. H. (1977). Fault rocks and fault mechanisms. *Journal of the Geological Society*, 133(3), 191–213. <https://doi.org/10.1144/gsjgs.133.3.0191>
- Sone, H., & Shimamoto, T. (2009). Frictional resistance of faults during accelerating and decelerating earthquake slip. *Nature Geoscience*, 2(10), 705–708. <https://doi.org/10.1038/ngeo637>
- Sutherland, R., Toy, V., Townend, J., Cox, S., Eccles, J., Faulkner, D., et al. (2012). Drilling reveals fluid control on architecture and rupture of the Alpine fault, New Zealand. *Geology*, 40(12), 1143–1146. <https://doi.org/10.1130/G33614.1>
- Swiss Federal Nuclear Safety Inspectorate. (2018). Nuclear Power Plants.
- Takahashi, M., Azuma, S., Ito, H., Kanagawa, K., & Inoue, A. (2014). Frictional properties of the shallow Nankai Trough accretionary sediments dependent on the content of clay minerals. *Earth, Planets and Space*, 66(1), 1–13. <https://doi.org/10.1186/1880-5981-66-75>
- Tanikawa, W., Hirose, T., Mukoyoshi, H., Tadai, O., & Lin, W. (2013). Fluid transport properties in sediments and their role in large slip near the surface of the plate boundary fault in the Japan Trench. *Earth and Planetary Science Letters*, 382, 150–160. <https://doi.org/10.1016/j.epsl.2013.08.052>
- Tembe, S., Lockner, D. A., & Wong, T. F. (2010). Effect of clay content and mineralogy on frictional sliding behavior of simulated gouges: Binary and ternary mixtures of quartz, illite, and montmorillonite. *Journal of Geophysical Research: Solid Earth*, 115(3), 1–22. <https://doi.org/10.1029/2009JB006383>
- Tenthorey, E., Cox, S. F., & Todd, H. F. (2003). Evolution of strength recovery and permeability during fluid-rock reaction in experimental fault zones. *Earth and Planetary Science Letters*, 206(1–2), 161–172. [https://doi.org/10.1016/S0012-821X\(02\)01082-8](https://doi.org/10.1016/S0012-821X(02)01082-8)
- Tesei, T., Collettini, C., Carpenter, B., Viti, C., & Marone, C. (2012). Frictional strength and healing behavior of phyllosilicate-rich faults. *Journal of Geophysical Research: Solid Earth*, 117(9), 1–13. <https://doi.org/10.1029/2012JB009204>
- Tesei, T., Collettini, C., Barchi, M. R., Carpenter, B., & Di Stefano, G. (2014). Heterogeneous strength and fault zone complexity of carbonate-bearing thrusts with possible implications for seismicity. *Earth and Planetary Science Letters*, 408, 307–318. <https://doi.org/10.1016/j.epsl.2014.10.021>
- The Mont Terri Project. (2018). Rock laboratory.
- The World Bank Group. (2018). Electricity production from nuclear sources (% of total).

- Tsang, C.-F., Barnichon, J. D., Birkholzer, J., Li, X. L., Liu, H. H., & Sillen, X. (2012). Coupled thermo-hydro-mechanical processes in the near field of a high-level radioactive waste repository in clay formations. *International Journal of Rock Mechanics and Mining Sciences*, 49, 31–44. <https://doi.org/10.1016/j.ijrmms.2011.09.015>
- Tsang, C.-F., Neretnieks, I., & Tsang, Y. (2015). Hydrologic issues associated with nuclear waste repositories. *Water Resources Research*, 51(9), 6923–6972. <https://doi.org/10.1002/2015WR017641>
- Ujiie, K., Tanaka, H., Saito, T., Tsutsumi, A., Mori, J., & Toczko, S. (2013). Low Coseismic Shear Stress on the Tohoku-Oki Megathrust Determined from Laboratory Experiments. *Science*, 342(December), 1211–1214. <https://doi.org/10.1126/science.1243485>
- Vannucchi, P., Maltman, A., Bettelli, G., & Clennell, B. (2003). On the nature of scaly fabric and scaly clay. *Journal of Structural Geology*, 25(5), 673–688. [https://doi.org/10.1016/S0191-8141\(02\)00066-4](https://doi.org/10.1016/S0191-8141(02)00066-4)
- Verberne, B., Spiers, C., Niemeijer, A., De Bresser, J., De Winter, D. A. M., & Plümpner, O. (2013). Frictional Properties and Microstructure of Calcite-Rich Fault Gouges Sheared at Sub-Seismic Sliding Velocities. *Pure and Applied Geophysics*, 171(10), 2617–2640. <https://doi.org/10.1007/s00024-013-0760-0>
- Wibberley, C. A. J., & Shimamoto, T. (2002). Internal structure and permeability of major strike-slip fault zones: The Median Tectonic Line in Mie Prefecture, Southwest Japan. *Journal of Structural Geology*, 25(1), 59–78. [https://doi.org/10.1016/S0191-8141\(02\)00014-7](https://doi.org/10.1016/S0191-8141(02)00014-7)
- Wibberley, C. A. J., & Shimamoto, T. (2005). Earthquake slip weakening and asperities explained by thermal pressurization. *Nature*, 436(7051), 689–692. <https://doi.org/10.1038/nature03901>
- Wintsch, R. P., Christoffersen, R., & Kronenberg, A. K. (1995). Fluid-rock reaction weakening of fault zones. *Journal of Geophysical Research: Solid Earth*, 100(B7), 13021–13032. <https://doi.org/10.1029/94JB02622>
- World Nuclear Association. (2018). Nuclear Power in Switzerland.
- Yamashita, T., & Tsutsumi, A. (2017). *Involvement of Fluids in Earthquake Ruptures: Field/Experimental Data and Modeling*. Springer Japan. Retrieved from <https://books.google.ch/books?id=VxsuDwAAQBAJ>
- Yang, Y., & Aplin, A. C. (2010). A permeability-porosity relationship for mudstones. *Marine and Petroleum Geology*, 27(8), 1692–1697. <https://doi.org/10.1016/j.marpetgeo.2009.07.001>





## 2.

# CLAY-RICH FAULT GOUGES CAN ACT AS DISCRETE FLUID-FLOW CHANNELS: THE CASE OF THE OPALINUS CLAY FORMATION

**Authors:** Luis Felipe Orellana<sup>1\*</sup>, Christophe Nussbaum<sup>2</sup>, Luiz Grafulha<sup>3</sup>, Pierre Henry<sup>4</sup>, Marie Violay<sup>1</sup>

<sup>1</sup> Laboratory of Experimental Rock Mechanics (LEMR), ENAC, EPFL, Switzerland;

<sup>2</sup> Federal Office of Topography (Swisstopo), Wabern, Switzerland.

<sup>3</sup> Scientific Centre of Optical and Electron Microscopy, ETH Zürich, Zürich, Switzerland

<sup>4</sup> Centre Européen de Recherche et d'Enseignement des Géosciences de l'Environnement, Aix-Marseille Université, France.

**Status:** under review in *Geophysical Journal International*

**Contributions:** L. F. Orellana has collected, prepared and characterized samples used in this study. P. Henry, L.F. Orellana, and M. Violay have contributed to the testing strategy and methodology. C. Nussbaum has supervised samples collection. L.F. Orellana has performed permeability and porosity tests. L.F. Orellana and L. Grafulha have carried out microstructural observations. L. F. Orellana has written the manuscript. C. Nussbaum, L. Grafulha, P. Henry and M. Violay have edited and guided discussions of the manuscript. M. Violay has acted as a supervisor and main responsible author of the publication.

### Highlights:

- Study of the transport properties and microstructure of a clay-bearing fault gouge.
- Higher porosity in the fault gouge with respect to the clay rock matrix.
- Clay-bearing fault gouges might act as discrete fluid-flow channels.

## 2.1. ABSTRACT

Near-surface disposal of radioactive waste in shales is a promising option to safeguard the population and environment. However, natural fault arrays intersecting these geological formations can potentially enhance contaminants mobilization putting into question the long-term isolation of the repositories. This paper investigates the fluid-transport properties and mineralogy of a fault zone intersecting the Opalinus Clay (OPA) formation, a host rock under investigation for nuclear waste storage at the Mont Terri Laboratory (MTL, Switzerland). The MTL will not be the final location for nuclear waste, yet it provides a unique opportunity to foresee potential hazards. We have performed laboratory porosity measurements, and microstructural and mineralogical analysis to describe, model and quantify the fault structure, mineralogy, permeability, and connected porosity in different sections of the fault, including non-deformed and fault-related rocks (scaly clays and fault gouge). Laboratory analysis and permeability models reveal a fault gouge that has a pore network dominated by nanopores of less than 10 nm, yet a high-porosity (21%), and high-permeability (up to three times higher) with respect to the surrounding non-deformed rock. In addition, the mineralogical analysis shows a strong reduction in calcite content within the fault gouge, in agreement with recent microstructural evidence. Based on our study, the fault gouge does not act as a barrier. Further, we describe the OPA fault gouge at the MTL as a preferential but localized, discontinuous and narrow fluid flow channel that can potentially favor the transportation of radionuclides.

**Keywords:** Fault gouge, Opalinus Clay formation, nuclear waste storage, clay-bearing fault, fluid-flow conduit system.

## 2.2. INTRODUCTION

Fault zones are complex, anisotropic and heterogeneous discontinuities cutting the upper Earth's crust (Faulkner et al., 2010). Extensive research has shown that the architecture (e.g. lithology, fault zone geometry, spatial variability), the mechanics (e.g. fault displacement, fluid-rock interactions), and the fluid-transport properties (e.g. permeability, porosity) are inter-related parameters governing the fault deformation processes (Caine et al., 1996; Chester et al., 1993; Evans et al., 1997; Faulkner et al., 2010). For instance, a classical yet not general model for faults in crystalline rocks usually illustrates a low-permeability ( $10^{-18}$  -  $10^{-22}$  m<sup>2</sup>) clay-rich fault gouge core surrounded by a higher-permeability damage zone (Caine et al., 1996; Chester & Logan, 1986; Walker et al., 2013). In this configuration, fault cores can then act as a barrier (Morrow et al., 2014; Sutherland et al., 2012; Tanikawa et al., 2013) or as mixed conduit-barrier for fluids (Faulkner & Rutter, 2000; Forster et al., 2003; Wibberley & Shimamoto, 2002). Therefore, faults can exert a strong control on the pore pressures and effective stresses, but also the migration of fluids in geological formations (Evans et al., 1997).

This natural fluid-flow barrier feature is also important for engineering activities. Indeed, thanks to the low permeability of shales (Bourg, 2015; Crawford et al., 2008; Neuzil, 1994), they have been recognized in several countries as one of the most suitable candidates for the storage of nuclear waste in deep geological repositories (Tsang et al., 2015). However, due to the presence of faults, it remains unclear how they might weaken the isolation of radioactive contamination from the environment and population.

This paper investigates the transport properties and the fluid-flow regime governing faults in shales. As the capacity for fluid transport is related to the connected pore structure and faults, the research herein comprises a study of the pore structure of clay-bearing fault-rocks within the Opalinus Clay formation, a potential host rock for nuclear waste storage in Switzerland (Bossart et al., 2017; Nussbaum et al., 2011, 2017). For this purpose, we have conducted mineralogical and microstructural analysis; we have characterized the pore structure to comprehend the transport capabilities of the clay-bearing fault system. To investigate the flow distribution and to clarify the prevalence of rapid-flow paths within the fault structures in the Opalinus Clay formation, we have used the porosity characterization and permeability models to infer and quantify the fluid permeability of fault rocks. From these data and field observations, we show that clay-rich fault gouges might potentially act as a localized, discontinuous and discrete pathway for fluid flow.

### 2.2.1. GEOLOGICAL CONTEXT

The Mont Terri Laboratory (MTL) is the underground research infrastructure devoted to the study – thus not meant to be the final location – of deep-nuclear waste storage repositories in the Opalinus Clay (OPA) formation in Switzerland (Nussbaum et al., 2011, 2017).

At a depth of about 300 m, the MTL is intersected by a 1.0 to 4.2 m thick thrust fault dipping 50°–60° SSE named “Main Fault” (MF) (Nussbaum et al., 2011, 2017) (Figure 2-1a). As part of this study, the borehole BFS-2 (Figure 2-1b) was cored intersecting part of non-deformed rock (Figure 2-1c) and the Main Fault at a depth of about ~44 m. Within the MF, we recognize two main structural elements: a complex array of scaly clays (Figure 2-1d) and a discrete fault gouge (Figure 2-1e). Below we briefly describe these three units following their fabric and not their lithologies.

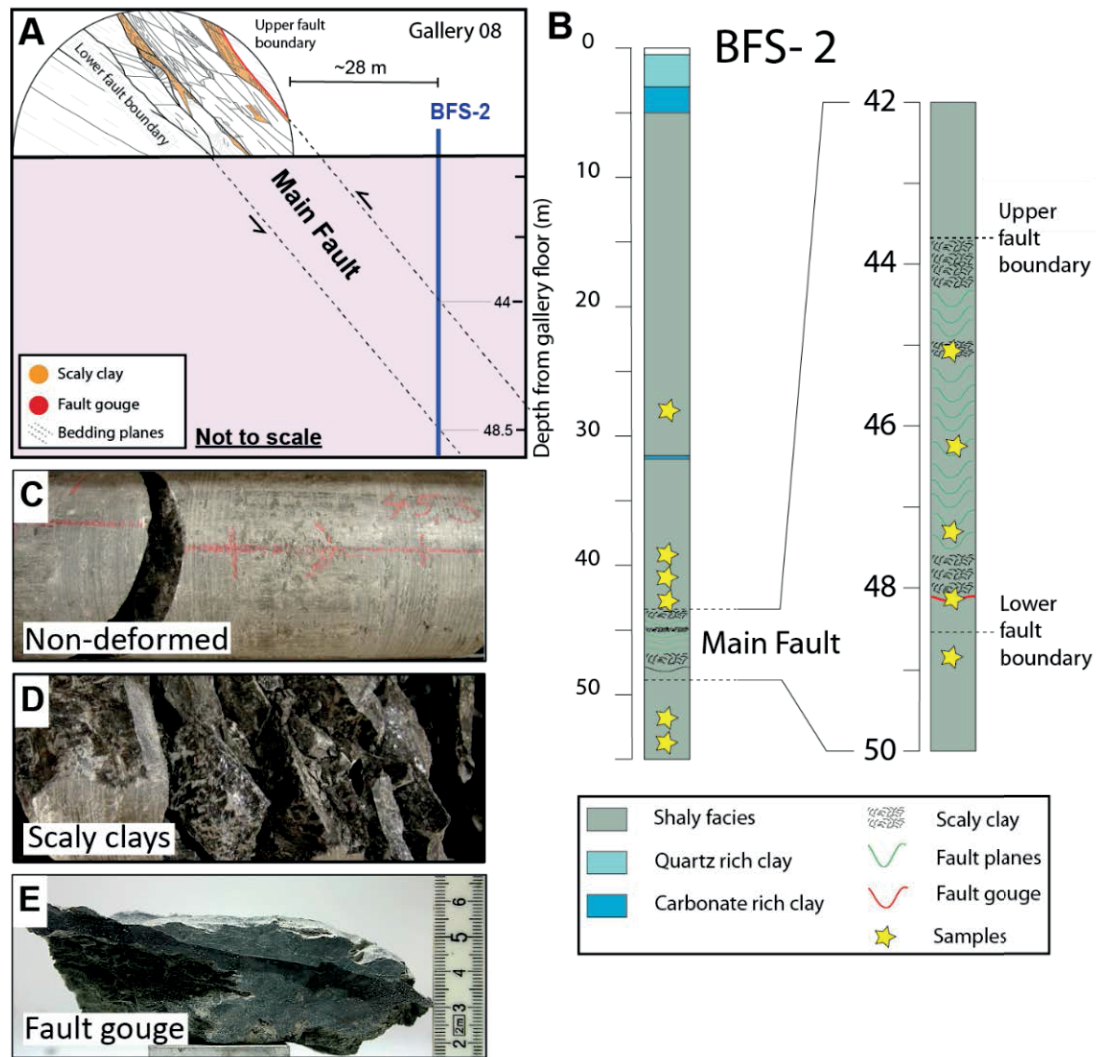


**Figure 2-1:** A) Schema of the Main Fault intersecting Gallery 08 at the Mont Terri Laboratory. Schematic location (not to scale) of the boreholes BFS-2 intersecting the Main Fault at a depth of ~44 m from the gallery floor. We have modified the figure after Nussbaum et al., (2011) and Kneuker et al., (2017). B) Borehole BFS-2. Lithology and structures of BFS-2 are based on detailed observations of the core. Samples discussed in this study are from borehole BFS-2 and are indicated by a star symbol in the figure. Examples of c) non-deformed d) scaly clays, and e) fault gouge recovered from borehole BFS-2.

The non-deformed OPA is a stiff, hydro-mechanically anisotropic (bedding planes) and overconsolidated shale (Favero et al., 2016; Van Loon et al., 2004). Previous mineralogical analyses have revealed that non-deformed samples of OPA have, in average, ~55 to 60% of phyllosilicates, ~15 to 20% of calcite, and ~13 to 17% of quartz (Fang et al., 2017; Klinkenberg

et al., 2009). The non-deformed OPA is characterized by a low permeability, i.e.,  $\sim 10^{-19}$  to  $10^{-21}$  m<sup>2</sup> upon the bedding planes orientation (Monfared et al., 2014; Philipp et al., 2017; Senger et al., 2018; Yu et al., 2017) and good fracture sealing properties (Bossart et al., 2017; Cuss et al., 2011). Depending upon the method, the porosity of the non-deformed OPA usually ranges from  $\sim 12$  to  $\sim 20\%$  (e.g., Busch et al., 2017; Houben et al., 2014, 2013; Keller and Holzer, 2018; Mazurek et al., 2011; Minardi et al., 2016). Nanopores, intragranular pores (e.g., framboid pyrites) and aggregates of micro-cracks (Houben et al., 2013; Keller et al., 2011, 2013) constitute the pore structure. The pore structure is preferentially oriented parallel to the bedding planes and can be considered as fully connected at the nanometer scale by pore throats smaller than 10 nm (Houben et al., 2013; Keller et al., 2011, 2013). Following the work of Yu et al., (2017), more than 70 % of the connected porous network is constituted by pore diameters between 2 and 50 nm with an average pore diameter size of 13 nm.

The scaly clays in the OPA formation are zones of dense shear strain characterized by complex arrangements of anastomosing slickensides enclosing apparent lentil-shape inclusions of non-deformed rock. Calcite veins can be recognized in scaly clays (Laurich et al., 2014, 2017; Orellana et al., 2018a; Vannucchi et al., 2003).

The fault gouge corresponds to a spatially discrete mm-thick and apparently continuous tectonite. Earlier studies on its microstructure unveil sub-horizontal interconnected shear planes, comminution of minerals (e.g., quartz, calcite, and pyrite framboid complexes), sub-rounded grain minerals, and a strong reduction in the calcite content (Laurich et al., 2014, 2018; Orellana et al., 2018b). The absence of calcite has been related to the dissolution of calcite minerals by reactive fluids flowing through the fault gouges during tectonic activity (Clauer et al., 2017).

Surprisingly, few studies have focused on the transport properties of the MF. Based on the SEM-image analysis technique, the fault gouge has been described as a very low porous fault-rock ( $< 2\%$ ) (Laurich et al., 2014, 2018) compared to the surrounding non-deformed material. Finally, recent *in-situ* tests have revealed contradictory results. Permeability values of the non-deformed rock and the Main Fault have been estimated around  $\sim 1 \times 10^{-20}$  m<sup>2</sup> with no significant difference (Marschall et al., 2005). A second study, however, measured two orders of magnitude higher permeability values around  $\sim 10^{-18}$  to  $10^{-19}$  m<sup>2</sup> for the Main Fault (Kneuker et al., 2017). Thus, much uncertainty still exists about the transport properties of the MF and how they might impact the barrier condition of the Opalinus Clay formation.

## 2.3. METHODS

At the Mont Terri Laboratory, we selected a group of samples from the borehole BFS-2 (Figure 2-1b) to perform porosity, permeability, microstructural and mineralogical analysis in order to assess the pore structure of the OPA fault gouge. Determining transport properties in shales has always been challenging. Samples that are not well stored or handled can be affected by non-controlled dehydration processes or mechanical stress unloading (Busch et al.,

2017). To minimize uncertainties due to possible artifacts, we have carefully followed standard procedures both on-site and in the laboratory (Mazurek et al., 2009, 2011). Thus, we have ensured (as much as it was possible) the mechanical integrity and natural humidity of the natural samples. The on-site treatment of the samples includes, reducing contact times of the fresh core with the atmosphere, wrapping the cores in PVC bags, and then, vacuum-packing into aluminum barrier foils. Once drill core samples were at the laboratory, the fresh cores were stored, while vacuum-sealed, in a humidity controlled room and carefully unpacked just before testing. Samples were taken from the inner part of the drill cores by hand or by dry sawing (when necessary) to avoid desaturation and chemical contamination.

### 2.3.1. SAMPLE COMPOSITION AND MICROSTRUCTURES

To determine the bulk mineral composition (% weight) of our samples, we have carried out X-Ray diffraction (XRD) analysis at the University of Lausanne (UNIL). The sample preparation has followed the procedure described by Kübler (1987) and Adate et al., (1996). The procedure has included: a) the disaggregation of the rock sample and mixing with de-ionized water, b) the subtraction of the carbonate portion by the addition of HCl 10% c) the separation of the different grain size fractions ( $< 2\mu\text{m}$  and  $2\text{--}16\mu\text{m}$ ) using the timed settling method (Stokes law), d) the application of ethylene-glycol onto clays already placed on glass-slide, and finally, e) the recognition of characteristic XRD peaks of each clay mineral.

To get insights into the pore structure microstructure, we have acquired a set of nanoscale images of the OPA fault gouge using a Zeiss Nvision 40 FIB-SEM microscopy combined with the Zeiss Atlas software at the Scientific Centre of Optical and Electron Microscopy (ScopeM) of ETH Zürich. Before imaging, we have dried the sample using a laboratory glass vacuum desiccator at room temperature until a constant weight was achieved. Then, we have epoxied the sample, and we have cut a cross-section perpendicular to the shear direction. We have polished this surface using a broad ion beam (BIB) equipment (IM4000 Hitachi). After, we have coated the sample with a 30 nm film of 80/20 - Pt/Pd alloy using a CCU-010 sputter coater equipment. Before FIB-SEM nano-tomography imaging process initiates, we have selected a region of interest (ROI) ( $\sim 15\mu\text{m} \times 15\mu\text{m} \times 15\mu\text{m}$ ) using the Zeiss Atlas software. Next, we have covered the ROI with a  $2\mu\text{m}$  layer of Pt for protection, and fiducial marks were delineated for auto-drift correction and auto-focus. Later, a layer of carbon (C) is deposited to enhance image contrast. Both layers were deposited using the FIB operated at 30 kV and 150 pA beam current. After that, an initial trench was milled at an accelerating voltage of 30 kV and beam current of 10 nA in the front part of the ROI, creating a flat surface perpendicular to the sample surface. This cross section is then polished with the FIB operating at a same accelerating voltage, but using a beam current of 1.5 nA. The nanotomography was then performed by progressively sputtering thin layers of material out of the sample ( $\sim 150\text{ nm}$ ) with the FIB, followed by imaging with the SEM. During image acquisition, accelerating voltage and beam current were, respectively, 30 kV and 1.5 nA for the FIB, and 3 kV and  $\sim 80\text{ pA}$  for the SEM.



## 2.3.2. TRANSPORT PROPERTIES

### 2.3.2.1. POROSITY STRUCTURE AND GRAIN DENSITY

Because of the complexity of determining porosity in shales, we have used 60 samples (7 fault gouge, 8 scaly clays and 45 non-deformed) and two different methods on the same group of samples ( $< 2 \text{ cm}^3$  in size): The Helium Pycnometry (HP) and the Fluid displacement (FD) methods. In particular, the HP technique uses the gas displacement method, i.e., Boyle's law allowing the measurements of very small pores less than 0.5 nm.

In what follows, we describe step-by-step our experimental protocol. First, we have measured the weight of the saturated samples  $W_{sat}$ . Then, we immersed the samples into paraffin, thus preventing the mechanical damage of the sample because of clay swelling due to absorption of water. After, we have measured the weight of the saturated samples immerse in paraffin  $W_{wet}$ . The weight of the paraffin displaced is  $W_{sub} = W_{sat} - W_{wet}$ . Considering the value of the density of paraffin is equal to  $\rho_p = 0.7895 \text{ gr/cm}^3$ , we have calculated the bulk volume of the sample  $V_b = W_{sub}/\rho_p$ .

To compute the dried volume of the samples  $V_s$ , we have placed the samples into a glass vacuum desiccator until a constant weight was achieved. Once the weight was stable ( $\sim 7$  days), we have measured the dried weight  $W_{dry}$ . The average water content of the samples was  $\sim 6\%$ . At this point, we have performed the HP measurements (Micromeritics Accupyc II 1340) to obtain both the HP porosity, but also the values of grain density. We have obtained the values of grain volume  $V_{skel}$  and we have calculated the He-porosity ( $\phi_{He}$ ) as  $\phi_{He} = (V_b - V_{skel})/V_b$ . Later, we have crushed the samples, and we have measured the grain density  $\rho_g$ . The latter has allowed us to calculate the dry volume  $V_s$  of the sample by dividing the dried weight by the grain density i.e.  $W_{dry}/\rho_g$ . Finally, we have calculated the values of FD-porosity as  $\phi_{3w} = (V_b - V_s)/V_b$ .

We have measured pore throat sizes and the pore size distribution (PSD) by mercury intrusion porosimetry (MIP) at the Laboratory of Construction Materials at EPFL. The MIP is a useful technique that allows the description of pore throat sizes (Abell et al., 1999; Giesche, 2006; Romero & Simms, 2008). However, because it has limitations, such as the lack of direct access to the pore volume (Diamond, 2000), we have restricted our discussion of the MIP results mostly to a qualitative interpretation. Thus, we have not computed porosity from this technique. The throat size distribution might not exactly match the pore size distribution (PSD), but can be considered as a first order approximation (Abell et al., 1999; Romero & Simms, 2008). The MIP procedure is as follows. First, we have dehydrated the samples ( $< 1 \text{ cm}^3$ ) for about 24 hours using a freeze-drying technique (Minardi et al., 2018). Then, we have placed the samples in a sample-cell holder who was filled with mercury at low pressure (up to 400 kPa) to penetrate the largest pores in the sample. After, we emplaced the sample holder in a high-pressure system where pressures of up to 440 MPa were applied. Both the isostatic pressure  $P$  and the intruded

volume of mercury  $V_m$  were recorded continuously. We have processed the MIP data using the Washburn's equation:

$$\Delta P = - \frac{4\gamma \cdot \cos \theta}{d}$$

**Equation 2-1:** Washburn's equation

Where  $P$  is pressure,  $\gamma$  is the surface tension of mercury, and  $\theta$  the contact angle between the solid and mercury. We used  $\gamma = 0.486 \text{ N/m}$  and  $\theta = 142^\circ$  (Minardi et al., 2018). Assuming non-intersecting cylindrical pores geometries, we were able to determine the diameter of the pore throat  $d$ .

### 2.3.2.2. PERMEABILITY

To measure the permeability of the OPA fault gouge and scaly clays is very challenging. Because of their geometry and mechanical properties (Orellana et al., 2018a, 2018b), it is not possible to core a well-defined sample suitable for testing. Hence, as fluid-flow through pores parallel to the bedding direction is the most favorable scenario (Van Loon et al., 2004), we have decided to measure the permeability on a non-deformed OPA sample cored parallel to bedding. This data is then used to model the permeability of fault-related rocks based on porosity-permeability relationships (see discussion later).

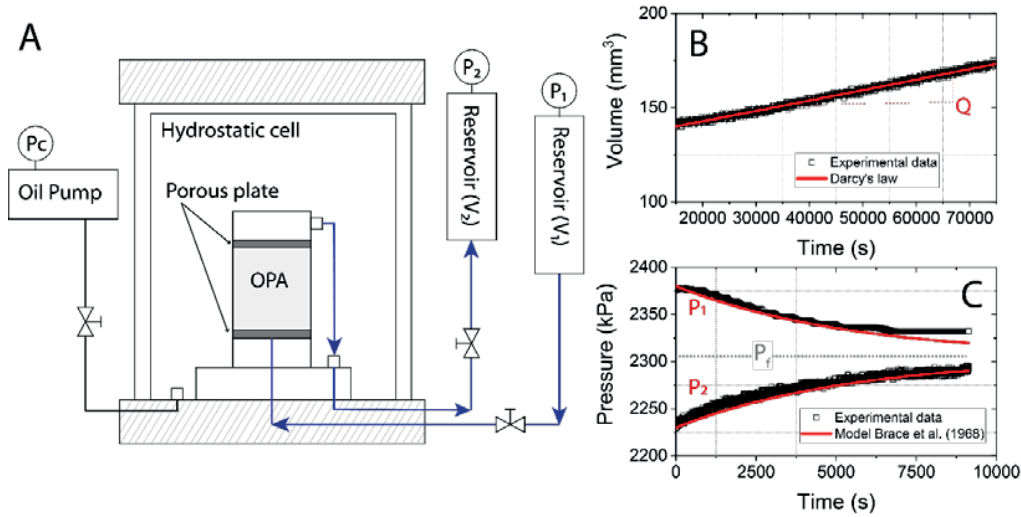


**Figure 2-2:** Permeability measurements. A) The setup used in this study. B) Calculation of  $Q$  ( $\text{mm}^3/\text{s}$ ) following Darcy's law for the test at 4 MPa effective confining stress. C) Following the transient step method of Brace et al. (1968), pressures  $P_1$  and  $P_2$  evolved exponentially over time until they approached a final pressure  $P_f$ . Figure shows an example of measurement at 5 MPa effective confining stress.

We have carried out permeability measurements at ambient temperature on a hydrostatic cell (Figure 2-2a) using the steady-state method and the pulse decay method (Brace et al., 1968). Two cylindrical samples of diameter and height of 38 mm were cored parallel to the direction of bedding. Using Darcy's law equation (Figure 2-2b), we have calculated permeability  $k$  as:



$$k = \frac{Q}{A} \left( \frac{\mu \cdot L}{P_1 - P_2} \right)$$

**Equation 2-2:** Darcy's law

Where  $P_1$  and  $P_2$  corresponds to the pore pressures of reservoir 1 and 2 respectively,  $Q$  is the flux or total discharge ( $\text{mm}^3/\text{s}$ ),  $A$  is the area and  $L$  the length of the sample. The viscosity of water ( $T=25^\circ \text{C}$ ) =  $8.9 \times 10^{-4} \text{ Pa s}$ . Following the pulse decay method (Figure 2-2c), we have estimated permeability  $k$  as:

$$k = \frac{\alpha \cdot \mu \cdot \beta \cdot L}{A \cdot \left( \frac{1}{V_1} + \frac{1}{V_2} \right)}$$

$$P_1 - P_f = \Delta P \cdot \left( \frac{V_2}{V_1 + V_2} \right) \cdot e^{-\alpha t}$$

**Equation 2-3:** Pulse decay equation (Brace et al., 1968)

Where  $V_1$  and  $V_2$  are the volume of the reservoirs (including the volume of the connecting tubes),  $\beta = 4.6 \times 10^{-10} \text{ Pa}^{-1}$  is water compressibility,  $t$  is time,  $\Delta P$  is the initial change in pore pressure and  $P_f$  is the constant final pressure when the pore pressure equilibrium is reached.

## 2.4. RESULTS

### 2.4.1. SAMPLES COMPOSITION

From the X-Ray diffraction measurements, we have identified phyllosilicates, quartz, calcite, and pyrite as the main constituents of the samples (Table 2-1). The mineral composition of the non-deformed rock consists of phyllosilicates (~51%), quartz (~23%), calcite (~14%), and pyrite (~1.4%). We observe a higher amount of calcite content (~17%) in the scaly clays, in particular, in the calcite-rich scaly clays near the fault gouge (>17%) (Figure 2-3a). Here, we refer to calcite-enriched scaly clay to the scaly clays samples that are 5% higher in calcite content (thanks to calcite veins) than the most common scaly clay samples which are collected far from the fault gouge.

We recognize a proportion of calcite minerals significantly smaller (~2%) in the fault gouge compared to the non-deformed and scaly clay rocks. We also observe different phyllosilicates including illite-smectite, kaolinite, mica, and chlorite. Among them, kaolinite is the dominant constituent in all samples.

Mineralogy (wt %)	Fault gouge (n=4)	Scaly Clays (n=3)	Ca-rich veins Scaly clays (n=4)	Non-deformed (n=6)
<b>Quartz</b>	26.5 ± 1.4	20.6 ± 0.9	22.7 ± 1.7	23.0 ± 0.9
<b>Feldspath-K</b>	3.3 ± 0.2	2.2 ± 0.2	2.9 ± 0.4	2.3 ± 0.4
<b>Plagioclase-Na</b>	3.0 ± 0.7	3.8 ± 2.5	2.5 ± 0.5	2.3 ± 0.2
<b>Calcite</b>	2.1 ± 0.4	17.5 ± 4.6	19.9 ± 3.0	14.2 ± 1.3
<b>Dolomite</b>	0.7 ± 0.4	1.4 ± 0.4	0.0 ± 0.0	1.3 ± 0.3
<b>Pyrite</b>	2.5 ± 0.3	1.4 ± 0.5	1.1 ± 0.3	1.4 ± 0.3
<b>Goethite</b>	1.4 ± 1.4	1.4 ± 1.0	1.8 ± 1.1	2.1 ± 0.3
<b>Illite-Smectite</b>	11.7 ± 5.5	3.0 ± 0.9	2.7 ± 0.6	4.0 ± 2.3
<b>Mica</b>	11.8 ± 4.9	8.8 ± 1.4	7.0 ± 1.3	10.3 ± 3.6
<b>Chlorite</b>	9.9 ± 4.3	9.3 ± 1.0	10.5 ± 3.3	8.5 ± 2.4
<b>Kaolinite</b>	23.4 ± 6.2	28.2 ± 2.1	26.9 ± 1.2	28.0 ± 2.9
<b>Others</b>	3.6	2.4	1.9	2.7

**Table 2-1:** Bulk (% weight) mineralogical composition of Opalinus Clay samples. We present results as  $X \pm S$ , where X is the mean and S the standard deviation; “n” corresponds to the number of samples.

## 2.4.2. THE MICROSTRUCTURE OF THE FAULT GOUGE

The fault gouge is a black layer of about 3 to 10 mm thickness (Figure 2-3a). It contains clay lamellae following the direction of shearing, sub-rounded quartz and isolated pyrites minerals with angular edges (Figure 2-3b, Figure 2-3c). The fault gouge is surrounded by calcite-enriched scaly clays and calcite veins as revealed by the mineralogical composition (Figure 2-3a). Here, we refer to calcite-enriched scaly clay to the scaly clays that is 5% higher in calcite content (thanks to calcite veins) than the most common scaly clay samples which are collected far from the fault gouge. The top fault gouge-scaly boundary appears as a wavy or non-regular surface, and the associated calcite-enriched scaly clay reveals a complex pattern as suggested by the ubiquitous orientation of the calcite minerals. In contrast, the bottom boundary is fairly regular or flat. The bottom scaly clays appear aligned parallel to the fault gouge, dominated by a laminar (sheet-like) flow as highlighted by the orientation of calcite minerals (Figure 2-3a).

Following the FIB-SEM observations, we recognize an apparent low –porosity matrix, with nano and micro-pores with a radius of about  $<100$  nm and lengths  $<3$   $\mu\text{m}$  respectively, that appear aligned parallel to the direction of shearing and partly interconnected in 3D (More images in the Appendix). While nanopores are of sub-rounded shapes of typically  $<30$  nm (Figure 2-3b, Figure 2-3c), micropores show thin, elongated and sub-angular shapes and are connected in 3D by pore throats that follow the direction of shearing (Figure 2-3d, Figure 2-3f). Also, we observe intragranular nanopores in framboid pyrites (Figure 2-3e) and intergranular pores in sub-rounded shapes (diameter  $<30$  nm) forming a pore-grain bridge complex (Figure 2-3g).

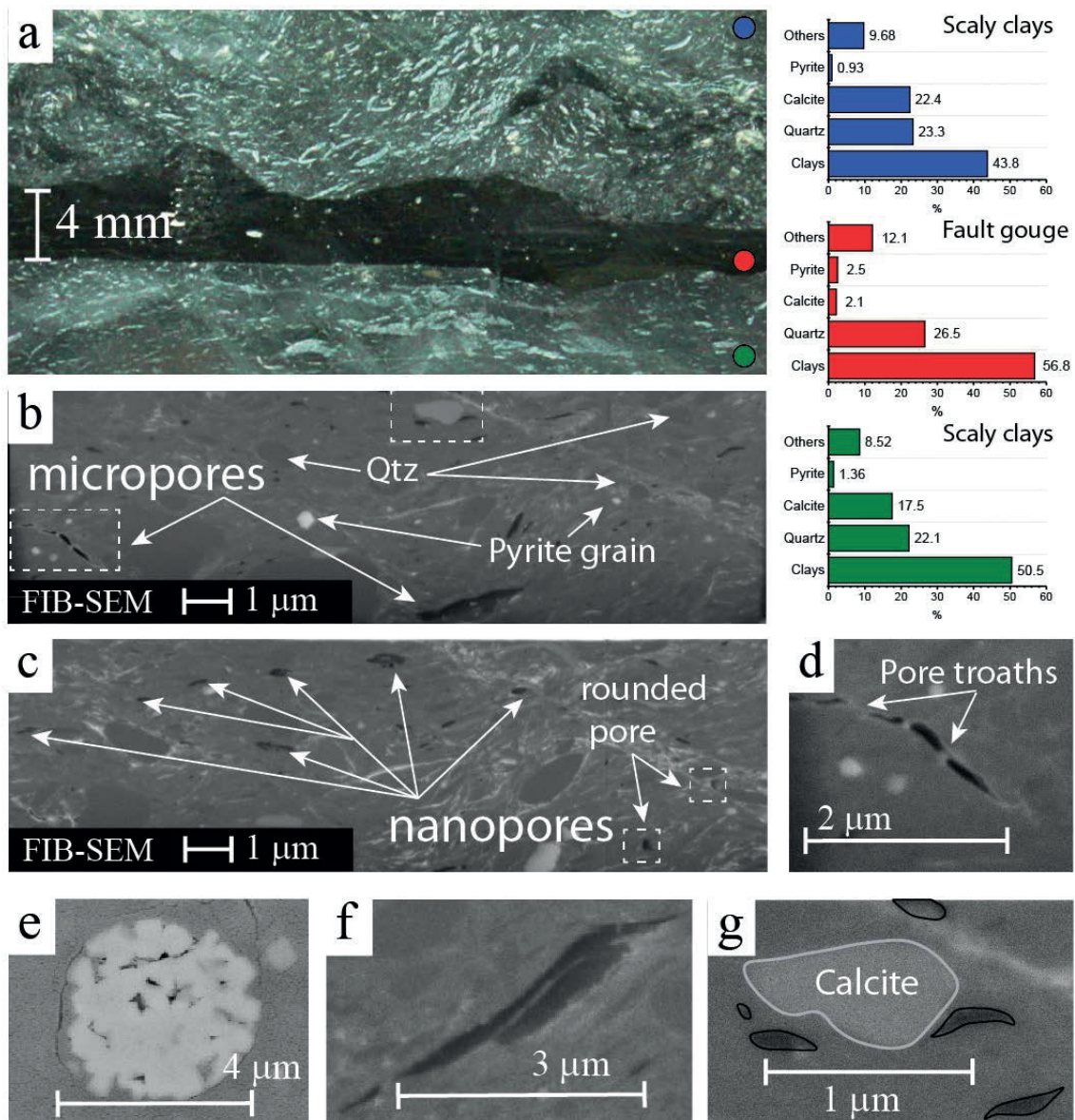


**Figure 2-3:** Microstructures of the fault gouge. A) A cm-scale photograph of the fault gouge (black) recovered from borehole BFS-2. The thickness of the gouge varies from 3 to 10 mm, and it is surrounded by calcite-enriched scaly clays. On the right, three graphs showing the different mineralogical composition of the gouge and its surrounding. B) FIB-SEM image of the fault gouge showing micropores. White boxes show the position of figures (d) and (g). The image also shows rounded quartz minerals, isolated pyrite grains and rare presence of calcite. C) FIB-SEM image of the fault gouge showing sub-rounded and sub-angular nanopores aligned in the direction of shearing. Isolated rounded pores are also present D) Thin and elongated micropores connected in 3D by pore throats. E) SEM images of a framboid pyrite with porosity in the single pyrite grains. F) FIB-SEM image of angular or jagged micropores connected in 3D by pore throats. G) Nanopores possibly connected by pore throats situated near a calcite grain boundary, i.e. pore-grain bridge complex.

### 2.4.3. TRANSPORT PROPERTIES OF THE FAULT GOUGE

The HP-porosity (Figure 2-4a) is  $14.3 \pm 1.1$  % (average  $\pm$  standard deviation) for non-deformed samples,  $13.6 \pm 1.2$  % for scaly clays, and  $21.5 \pm 1.5$  % for the fault gouge. Similarly, FD-porosity (Figure 2-4a) shows values of  $14.0 \pm 1.1$  % for non-deformed,  $12.8 \pm 0.7$  % for scaly clays, and  $21.1 \pm 1.2$  % for fault gouge samples. The grain density results (Figure 2-4b) indicate values of  $2.69 \pm 0.02$  g/cm<sup>3</sup> for the non-deformed,  $2.69 \pm 0.01$  g/cm<sup>3</sup> for scaly clays, and  $2.62 \pm 0.05$  g/cm<sup>3</sup> for the fault gouge samples.

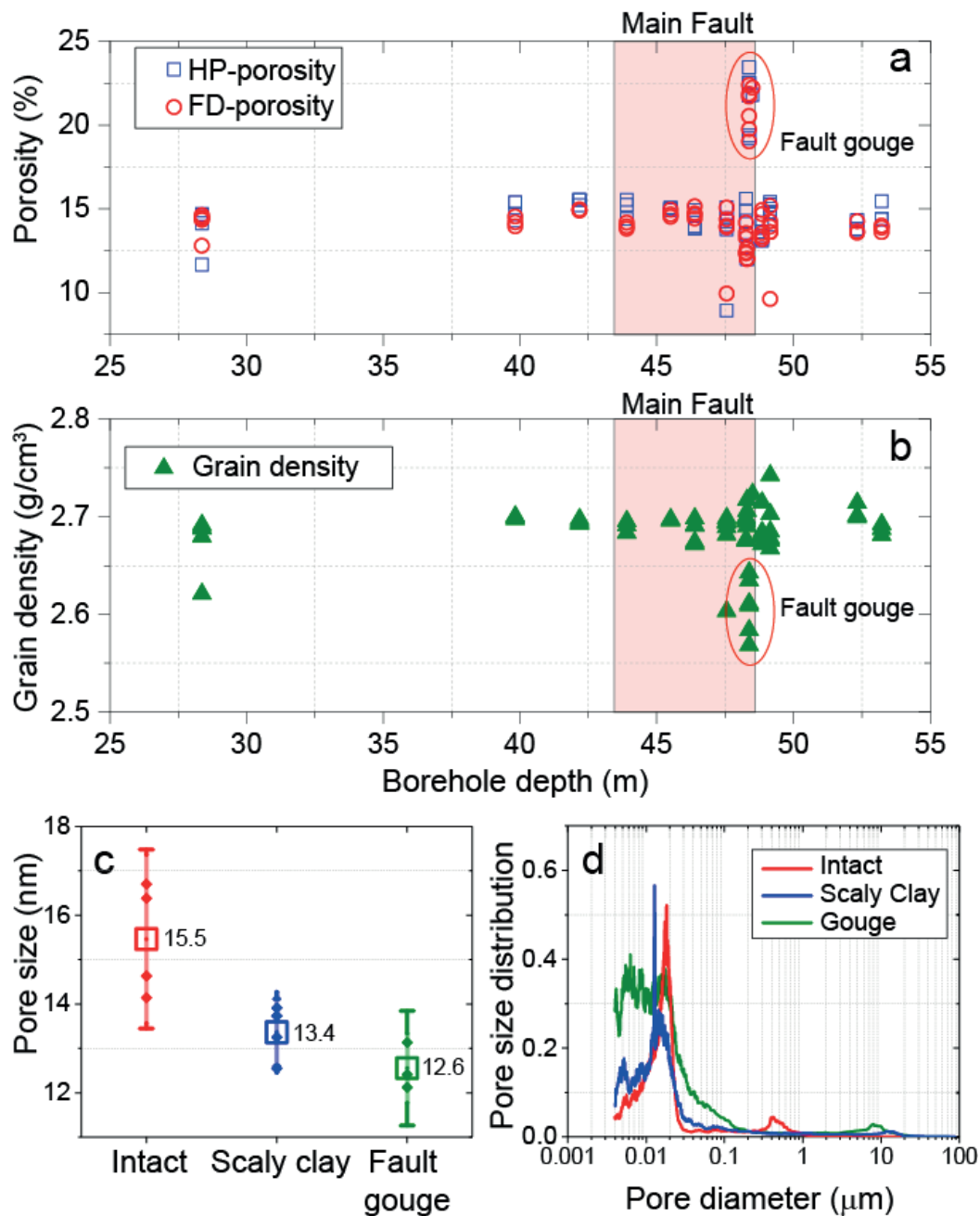


**Figure 2-4:** A) HP and FD porosity, b) grain density, c) MIP pore throat sizes and d) PSD measurements of the non-deformed and fault-related rocks of borehole BFS2. The MF is highlighted in red in b) and c).

The MIP measurements indicate an average pore throat diameter of  $15.5 \pm 1.1$  nm for non-deformed samples,  $13.4 \pm 0.5$  nm for scaly clays and  $12.6 \pm 0.4$  nm for fault gouge (Figure 2-4c). The PSD curves show that dominant pore throat size ranges are in between  $\sim 4$  and  $\sim 20$  nm for all the tested samples (Figure 2-4d). In particular, the PSD shows that pores throats of less than  $\sim 10$  nm exert an important control on the pore structure of fault gouges. In contrast, the dominant spectrum of pore throat diameter is higher and around  $\sim 12$  and  $\sim 20$  nm for scaly clays and non-deformed rocks respectively.

The permeability of the non-deformed samples cored parallel to the bedding planes decreases from  $\sim 3 \times 10^{-19}$  to  $\sim 4 \times 10^{-20}$  when the effective pressures increase from 2 to 12 MPa respectively (Figure 2-5). The permeability of the samples varied up to  $\sim 1$  order of magnitude according to  $\log k = -0.07\sigma'_c - 18.3$ , where  $\sigma'_c$  is the effective confining stress.

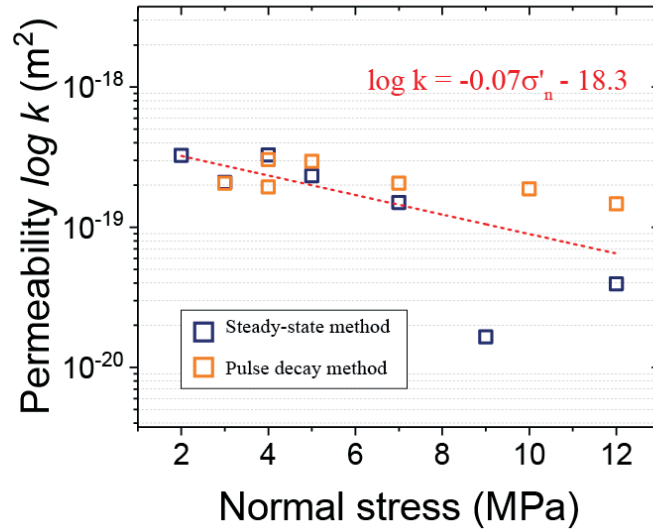


**Figure 2-5:** Permeability results from steady-state and pulse decay methods of two non-deformed samples cored parallel to bedding.

## 2.5. DISCUSSION

### 2.5.1. COMPARISON OF RESULTS WITH PREVIOUS STUDIES

Previous studies have mostly focused on the characterization, and the mechanical and transport properties of non-deformed samples of the OPA formation. Yet, less attention has been paid to its faulted zones and their properties (e.g. Clauer et al., 2017; Kneuker et al., 2017; Laurich et al., 2014, 2017, 2018; Marschall et al., 2005; Nussbaum et al., 2011; Orellana et al., 2018a, 2018b). In this experimental work, we present one of the first investigations into the transport properties of the faulted rocks intersecting the OPA formation by studying their pore structure through physical laboratory measurements. We essentially discuss our results by comparing them with earlier studies of non-deformed samples.



## 2.5.2. SAMPLE COMPOSITION

For the non-deformed samples, our results indicate a dominant proportion of phyllosilicates (~51%) followed by quartz (~23%) and calcite (~14%) as main constitutive minerals (Table 2-1). These results are consistent with data obtained in earlier studies (Fang et al., 2017; Klinkenberg et al., 2009). Our XRD measurements show 1) an important reduction in calcite (~2 %) in the fault gouge with respect to non-deformed OPA (~14%), and 2) calcite-enrichment of scaly clays (~22 -18%) thanks to calcite veins, in particular in the immediate surroundings of the fault gouge (Figure 2-3a). Previous microstructural observations (Laurich et al., 2014, 2018; Nussbaum et al., 2011) have qualitatively described a similar lack of calcite within the mineralogical composition of the fault gouge.

## 2.5.3. POROSITY AND GRAIN DENSITY

We have collected and tested 60 OPA samples to ensure the reproducibility of our measurements at different positions from the borehole BFS-2 (Figure 2-1), including i) 45 non-deformed OPA, ii) 8 scaly clays, and iii) 7 fault gouges. For non-deformed samples, our porosity data agree with those of various authors who have reported values of around 12 to 15% (Houben et al., 2013, 2014, Keller et al., 2011, 2013; Keller & Holzer, 2018; Yu et al., 2017). For scaly clays, our porosity results are consistent with previous ones based on the SEM-image analysis technique ( $\phi \sim 19\%$ ) (Laurich et al., 2014). For the fault gouges, values of porosity less than 2% were recorded from SEM-based images (Laurich et al., 2014, 2018). Thanks to both independent physical laboratory methods, HP and FD, a fault gouge of ~21 % was measured. These discrepancies could be related to the high spatial variability of the microstructural properties within the whole formation, but also to different technical capabilities. Indeed Figure 2-4d shows that an important portion of the pores throats sizes is below 10 nm, thus necessarily being out of the measurement space of the SEM-image technique (Desbois et al., 2009; Laurich et al., 2018).

Finally, small pore throat diameters of about ~15 nm and a grain density of 2.69 g/cm<sup>3</sup> also characterize the non-deformed Opalinus clay samples (Figure 2-4b, Figure 2-4d). Similarly, earlier results have reported comparable values of ~13 nm and 2.74 g/cm<sup>3</sup> for pore throat diameter and grain density respectively (Yu et al., 2017).

## 2.5.4. THE PERMEABILITY OF NON-DEFORMED OPALINUS CLAY

The permeability values of non-deformed OPA samples cored parallel to the bedding planes ( $10^{-19}$  to  $10^{-20}$  m<sup>2</sup>) are in agreement with measured values in earlier laboratory studies (e.g., Monfared et al., 2014; Philipp et al., 2017; Senger et al., 2018; Yu et al., 2017). We have not measured permeability perpendicular to bedding as we have focused on the capacity for fluid flow parallel to the direction of shearing. Permeability perpendicular to bedding is

expected to be lower than permeability parallel to bedding as shown by the same earlier studies cited in this section.

### 2.5.5. MICROSTRUCTURAL EVIDENCE OF FLUID-FLOW IN THE FAULT GOUGE

A closer look at the fault gouge and the fault gouge – scaly clay boundary (Figure 2-3a) reveals an assorted distribution of the calcite content, calcite grain sizes, and their shapes. As described before, the OPA fault gouge microstructure displays a notorious absence of calcite (Table 2-1, Figure 2-3a) which is consistent with the reduction in grain density (Figure 2-4b). The bottom fault gouge-scaly clay boundary predominantly presents elongated calcite veins and small calcite minerals mostly oriented parallel to the fault gouge direction. In Figure 3a, the calcite content of the bottom fault gouge-scaly clay is lower than in the top boundary (17.5 versus 22.4%) but higher than in the fault gouge (~2%) and the non-deformed samples (~14%). On the other hand, the top scaly-gouge boundary evidences a higher concentration of blocky calcite grains and calcite veins, and no clear spatial pattern.

An explanation for the absence of calcite and the inhomogeneous distribution of calcite grains and veins in the surroundings of the fault gouge is that carbonate-reactive fluids have played an important role during the tectonic activity of the Main Fault as explained by Clauer et al., (2017). As calcite minerals can deform by fracturing and cataclastic flow even at low-grade conditions, i.e., increasing the area of contact (Passchier & Trouw, 2005), reactive fluids flowing throughout the fault gouge could have easily dissolved, and later transported the comminuted calcite outside the fault gouge limits where they recrystallize. This process can only occur if the fault gouge acts as a preferential path for fluid-flow. In our study, we have shown that the fault gouge has a relative higher porosity with respect to the surrounding rock mass (21% vs. 14%), thus pairing the field evidence and supporting this hypothesis. Because water is present, pressure solution may have also played an important deformation role (Passchier & Trouw, 2005). However, it is difficult to differentiate their relative contributions to the total calcite dissolution process.

### 2.5.6. A CONCEPTUAL MODEL FOR THE MAIN FAULT-RELATED FLUID-FLOW

Porosity and permeability are related transport parameters that are vastly used to characterize the capacity for fluids circulation in fault zones. Unfortunately, we have strong limitations to collect and directly test permeability on OPA fault gouges and scaly clays samples. Thus, in this section, we attempt to provide a conceptual model of the Main Fault-related fluid-flow based mainly on our porosity data and different permeability models following the approaches of different authors. There are no obvious porosity-permeability relationships that can allow us to estimate the permeability of the mentioned fault rocks effectively. Yet, their fluid permeability might be assessed with some models we describe below. By doing so, these models allow us to provide an estimation of the fluid permeability



magnitudes of the Main Fault. Note that all models are first compared with the permeability tests we have performed on non-deformed OPA (Figure 2-5).

#### 2.5.6.1. ESTIMATION OF PERMEABILITY BASED ON TUBE AND CRACK MODELS

In this section, we follow Guéguen & Dienes (1989), and Guéguen & Palciauskas (1994) approaches to estimate permeability ( $k$ ). We then simplify the permeability by assuming that the pore network of the OPA fault rocks is either characterized by a network of interconnected crack-like pores (i.e., interconnect sheets) or interconnected tube- and sphere-like pores. These models represent two end members of possible pore structure constructions.

Assuming that the permeability and porosity are such that can be represented by tubes, then  $k_{tubes} \cong \frac{r^2}{8} \emptyset$ , where  $r$  is the pore radii and  $\emptyset$  is the porosity. Following the porosity results of section 2.4.3, the tube model provides values of permeability of  $\sim 1 \times 10^{-18} \text{ m}^2$  for the non-deformed rock,  $\sim 7 \times 10^{-19} \text{ m}^2$  for the scaly clays, and  $\sim 1 \times 10^{-18} \text{ m}^2$  for the fault gouge. The measured permeability for non-deformed OPA is in the order of  $\sim 2.5 \times 10^{-19} \text{ m}^2$  at 5 MPa confining stress, i.e., one order of magnitude lower than the estimated value from the tube/sphere model. This suggests that the characteristic pore size for fluid transport should be smaller than 15.5 nm in order to match the modelled and the estimated value of permeability. Indeed, it requires pore diameters of less than 7 nm. These appears least consistent with the dominant spectrum of pore throat diameter of  $\sim 12$  and  $\sim 20$  nm (Figure 2-4d) and with the earlier description of a connected porous network of mesoporous (13 nm mean size) within the non-deformed OPA (Yu et al., 2017). However, we have shown that the fault gouge contains a large portion of pore throats of less than 10 nm (Figure 2-4d) and nanopores of sub-rounded shapes (Figure 2-3c) matching some of the geometrical characteristics of this pore network model.

Alternatively, if permeability is the result of straight interconnected crack-like pores, then  $k_{cracks} \cong \frac{w^2}{3} \emptyset$ , where  $2w$  corresponds to the aperture of the cracks. We assume  $2w$  to be equivalent to pore throat size entry. Again, following the average of porosity and pore size throats sizes for each rock type, the crack model provides values of permeability of  $\sim 3 \times 10^{-20} \text{ m}^2$  for the non-deformed rock,  $\sim 2 \times 10^{-20} \text{ m}^2$  for the scaly clays, and  $\sim 3 \times 10^{-20} \text{ m}^2$  for the fault gouge. In this scenario, measured permeability is one order of magnitude lower than measured permeability ( $\sim 1 \times 10^{-19} \text{ m}^2$  at 5 MPa confining stress), however, is consistent with permeability values at higher confining stresses (e.g.,  $\geq 9$  MPa) and other studies in non-deformed OPA (Monfared et al., 2014; Philipp et al., 2017; Senger et al., 2018; Yu et al., 2017). Measured permeability in samples cored parallel to bedding decreases up to one order of magnitude when the effective pressure increases from 2 to 12 MPa (Figure 2-5). This suggests a control by interconnected sheet or crack-like pores (Guéguen et al., 2009; Ougier-Simonin et al., 2011), which in turn is consistent with pores more or less oriented along clay particles interfaces in the non-deformed rock (Houben et al., 2013; Keller et al., 2011, 2013; Yu et al., 2017). The preferential orientation of the pore network, including sheet-like pores is also observed in the FIB-SEM images of fault gouge (Figure 2-3). Thus, if we extrapolate the

permeability dependence of the non-deformed rock to the fault gouge, we might infer that the pore structure of the fault gouge is also like a crack-like pore network.

Obviously, none of this two end-member models can represent the complex nature of porous shales. Indeed, we have seen that none of these two models can explain the permeability of the non-deformed rock by itself. Thus, when characterizing the pore network of the non-deformed and the OPA fault rocks, we should expect a combination of both, where a heterogeneous network of crack-like and tubes/sphere-likes pores coexist.

#### 2.5.6.2. ESTIMATION OF PERMEABILITY BASED ON HYDRAULIC RADIUS MODELS

We have tested the classical semi-empirical relationship of Kozeny-Cartman (KC) (Carman, 1997; Kozeny, 1927). The KC is based on a geometrical approach where the pores are modeled as a group of capillary tubes. Permeability from the KC can be calculated as  $k = \frac{d^2 \phi^3}{180 (1-\phi^2)}$  where  $d$  corresponds to the mean pore diameter. The KC model predicts values of permeability of  $\sim 4 \times 10^{-21} \text{ m}^2$  for the non-deformed rock,  $\sim 2 \times 10^{-21} \text{ m}^2$  for the scaly clays, and  $\sim 9 \times 10^{-21} \text{ m}^2$  for the fault gouge. These values are two orders of magnitudes lower than the values measures on non-deformed OPA.

#### 2.5.6.3. ESTIMATION OF PERMEABILITY BASED ON EMPIRICAL MODELS

Finally, we have used two empirical relationships, one of them constructed for shales that includes the clay content as a parameter, and the second specifically for non-deformed OPA. Based on a large dataset of shale properties, Yang and Aplin, (2010) have introduced a permeability-porosity ( $\phi$ ) of the form  $\ln(k) = a(\delta) + b(\delta) \cdot \frac{\phi}{1-\phi} + c(\delta) \cdot \left(\frac{\phi}{1-\phi}\right)^{0.5}$ , where  $a$ ,  $b$ , and  $c$  are constants that depends on the clay content (for details, see Appendix). Muñoz et al., (2009) have presented a laboratory-based model for non-deformed OPA in the form  $k = 1.05 \times 10^{-17} \cdot \frac{\phi^3}{(1-\phi)^2}$ .

The Muñoz et al. (2009) model predicts values of permeability of  $\sim 3 \times 10^{-20} \text{ m}^2$  for the non-deformed rock,  $\sim 2 \times 10^{-20} \text{ m}^2$  for the scaly clays, and  $\sim 1 \times 10^{-19} \text{ m}^2$  for the fault gouge. The Yang et al. (2010) model predicts values of permeability of  $\sim 9 \times 10^{-21} \text{ m}^2$  for the non-deformed rock,  $\sim 8 \times 10^{-21} \text{ m}^2$  for the scaly clays, and  $\sim 3 \times 10^{-20} \text{ m}^2$  for the fault gouge. These values are not consistent with the permeability measured on non-deformed OPA. Others empirical relationships might be found in the literature; our objective is not testing them all but rather illustrate different approaches.

### 2.5.7. IMPLICATIONS FOR FLUID FLOW IN OPA FAULT ZONES.

We have presented empirical (Muñoz et al., 2009; Yang & Aplin, 2010), statistical (tubes/spheres and cracks, Guéguen & Palciauskas, (1994)), and hydraulic (Carman, 1997;

Kozeny, 1927) permeability models to account for a hypothetical model of the Main Fault fluid flow. A summary of the results is presented in Table 2-2.

Although the models can be considered simplistic, they provide useful insights into the fluid flow distribution and locations of preferential pathways in the Main Fault. The tube and crack models indicate a null increase in the fluid permeability of the fault gouge with respect to non-deformed rock, yet reveal that the scaly clays are less permeable. The rest of the models suggest an increase up to 3 times in the magnitude of OPA fault gouge permeability with respect to scaly clay and non-deformed material. This permeability increase is more pronounced when the porosity-permeability model is a function of either porosity (Muñoz et al., 2009) or porosity and clay content (Yang & Aplin, 2010). The permeability increase is smaller in the KC relationship with respect to the latter two empirical models, as it depends on the diameter of the pores (Carman, 1997; Kozeny, 1927).

Sample	Mean Ø (%)	Modeled Permeability (m <sup>2</sup> )				
		Tubes	Crack-like pores	Kozeny- Cartman (1927)	Muñoz et al. (2009)	Yang et al. (2010)
<b>Non-deformed</b>	14.2	1E-18	3E-20	4E-21	3E-20	9E-21
<b>Scaly clay</b>	13.2	7E-19	2E-20	2E-21	2E-20	8E-21
<b>Gouge</b>	21.3	1E-18	3E-20	9E-21	1E-19	2E-20

**Table 2-2:** Mean experimental porosity (%) and modeled permeability (m<sup>2</sup>) of non-deformed, scaly clay, and fault gouge samples.

As we have shown, different permeability models lead to different scenarios of fluid permeability within the fault gouge, yet none of them leads to a fault gouge acting as an active barrier. In addition, the microstructural observations evidence of dissolution and transport of calcite near the surrounding of the fault gouge, as shown here and by other authors (Clauer et al., 2017; Laurich et al., 2014, 2018), favors the scenario of the fault gouge acting as a potential conduit structure. The conduit hypothesis, however, cannot be supported if the porosity within the fault gouge is 2%, as has been early described (Laurich et al., 2014, 2018) in spite of the porosity values reported in this manuscript and field observations.

Finally, a note of attention is due to the scaly clays samples. In this study, the tested scaly clay samples are less than 2 cm<sup>3</sup> in size. Thus they might not represent the complexities of long fractures with scaly clay fabrics as observed in the Main Fault, and therefore some larger scale features are possibly missing (Vannucchi et al., 2003). In addition, self-sealing mechanisms such as clay-swelling acting on fractures can also be argued as an effective mechanism against a less favorable conduit pathway for fluid flow when the content of mixed layers of illite/smectite is high enough to be efficient (Bock et al., 2010; Bossart et al., 2017; Mazurek & de Haller, 2017). Apparently, this is not the case in our samples.

Following our results, a Main Fault fluid transport schema based on a higher-porosity higher-permeability fault gouge is in general agreement with previous studies of fault gouge samples collected along natural faults (e.g., Leclère et al., 2015; Tanikawa & Shimamoto, 2009). However, it differs from those typically reported in classical models referring to clay-rich low-permeability fault cores (e.g., Chester & Logan, 1986; Evans et al., 1997; Walker et al., 2013). If this interpretation is correct, the higher permeability and porosity of the OPA fault gouge compared to its rock mass surroundings is consistent with a localized conduit permeability structure (Caine et al., 1996).

## 2.6. CONCLUSIONS

Because of the low permeability of non-deformed shales, hydrological concerns in the context of nuclear waste storage have been focused on disturbances caused by mechanical and thermal effects during excavation and operation respectively. As we have shown, fault settings, however, impose new restrictions on the very long-term operation of these repositories.

Through microstructural and pore network characterization, we present an analysis of the hydrological behavior of the clay-rich fault gouge within a major fault system (MF) intersecting the Opalinus Clay (OPA) formation at the Mont Terri Laboratory (MTL), a host-rock candidate for deep nuclear waste storage in Switzerland.

In this study, we have shown 1) the absence of calcite within the fault gouge suggesting that calcite might have been dissolved by a reactive fluid flowing throughout the fault gouge, 2) a recrystallization of calcite veins and blocky grains in the surrounding of the calcite-enriched scaly clays thanks to precipitations of the dissolved calcite in the vicinity, 3) a high porous fault gouge (~21%) when compared to the non-deformed rock (~14%) and finally, 4) a non-homogenous distribution of fluid-flow in the Main Fault as a consequence of the architecture and the related spatial variability of the transport properties.

Based on this evidence, we suggest, in agreement with the field and laboratory observations that the OPA fault gouge might act as a preferential path for fluid-flow. However, if this occurs, it will be limited to a narrow (millimeters-thick) and tortuous fluid-channel.

Because the OPA formation is a potential host rock for nuclear waste storage, the implication of the fluid-flow governing behavior is of critical importance. While the OPA formation at the MTL is not meant to be the final repository, if fluid-flow of radionuclides occurs within a fault system in the OPA formation, it will take place following an uneven competition, between a relatively high permeability but spatially discrete fault gouge, versus a more extensive low permeability non-deformed rock.

## 2.7. REFERENCES

- Abell, A. B., Willis, K. L., & Lange, D. A. (1999). Mercury intrusion porosimetry and image analysis of cement-based materials. *Journal of Colloid and Interface Science*, 211(1), 39–44. <https://doi.org/10.1006/jcis.1998.5986>
- Adatte, T., Stinnesbeck, W., & Keller, G. (1996). Lithostratigraphic and mineralogic correlations of near K/T boundary clastic sediments in northeastern Mexico: Implications for origin and nature of deposition. In G. Ryder, D. E. Fastovsky, & S. Gartner (Eds.), *The Cretaceous-Tertiary Event and Other Catastrophes in Earth History*. Geological Society of America.
- Bock, H., Dehandschutter, B., Martin, C. D., Mazurek, M., De Haller, A., Skoczylas, F., & Davy, C. (2010). Seal-sealing of fractures in argillaceous formations in the context of geological disposal of radioactive waste: Review and Synthesis. *Nuclear Waste Management*.
- Bossart, P., Bernier, F., Birkholzer, J., Bruggeman, C., Connolly, P., Dewonck, S., et al. (2017). Mont Terri rock laboratory, 20 years of research: introduction, site characteristics and overview of experiments. *Swiss Journal of Geosciences*, 110(1), 3–22. <https://doi.org/10.1007/s00015-016-0236-1>
- Bourg, I. C. (2015). Sealing Shales versus Brittle Shales: A Sharp Threshold in the Material Properties and Energy Technology Uses of Fine-Grained Sedimentary Rocks. *Environmental Science and Technology Letters*, 2(10), 255–259. <https://doi.org/10.1021/acs.estlett.5b00233>
- Brace, W. F., Walsh, J. B., & Frangos, W. T. (1968). Permeability of granite under high pressure. *Journal of Geophysical Research*, 73(6), 2225–2236. <https://doi.org/10.1029/JB073i006p02225>
- Busch, A., Schweinar, K., Kampman, N., Coorn, A., Pipich, V., Feoktystov, A., et al. (2017). Determining the porosity of mudrocks using methodological pluralism. *Geological Society, London, Special Publications*, 454(1), 15–38. <https://doi.org/10.1144/SP454.1>
- Caine, J. S., Evans, J. P., & Forster, C. B. (1996). Fault zone architecture and permeability structure. *Geology*, 24(11), 1025–1028. [https://doi.org/10.1130/0091-7613\(1996\)024<1025](https://doi.org/10.1130/0091-7613(1996)024<1025)
- Carman, P. C. (1997). Fluid flow through granular beds. *Chemical Engineering Research and Design*, 75, S32–S48. [https://doi.org/10.1016/S0263-8762\(97\)80003-2](https://doi.org/10.1016/S0263-8762(97)80003-2)
- Chester, F. M., & Logan, J. M. (1986). Implications for mechanical properties of brittle faults from observations of the Punchbowl fault zone, California. *Pure and Applied Geophysics*, 124(1), 79–106. <https://doi.org/10.1007/BF00875720>
- Chester, F. M., Evans, J. P., & Biegel, R. L. (1993). Internal structure and weakening mechanisms of the San Andreas Fault. *Journal of Geophysical Research*, 98(B1), 771–786. <https://doi.org/10.1029/92JB01866>
- Clauer, N., Techer, I., Nussbaum, C., & Laurich, B. (2017). Geochemical signature of



- paleofluids in microstructures from Main Fault in the Opalinus Clay of the Mont Terri rock laboratory, Switzerland. *Swiss Journal of Geosciences*, 110(1), 105–128. <https://doi.org/10.1007/s00015-016-0253-0>
- Crawford, B. R., Faulkner, D., & Rutter, E. (2008). Strength, porosity, and permeability development during hydrostatic and shear loading of synthetic quartz-clay fault gouge. *Journal of Geophysical Research: Solid Earth*, 113(3), 1–14. <https://doi.org/10.1029/2006JB004634>
- Cuss, R. J., Milodowski, A., & Harrington, J. F. (2011). Fracture transmissivity as a function of normal and shear stress: First results in Opalinus Clay. *Physics and Chemistry of the Earth*, 36(17–18), 1960–1971. <https://doi.org/10.1016/j.pce.2011.07.080>
- Desbois, G., Urai, J. L., & Kukla, P. A. (2009). Morphology of the pore space in claystones - Evidence from BIB/FIB ion beam sectioning and cryo-SEM observations. *EEarth*, 4(1), 15–22. <https://doi.org/10.5194/ee-4-15-2009>
- Diamond, S. (2000). Mercury porosimetry: an inappropriate method for the measurement of pore size distributions in cement-based material. *Cement and Concrete Research*, 30(10), 1517–1525. [https://doi.org/10.1016/S0008-8846\(00\)00370-7](https://doi.org/10.1016/S0008-8846(00)00370-7)
- Evans, J. P., Forster, C. B., & Goddard, J. V. (1997). Permeability of fault-related rocks, and implications for hydraulic structure of fault zones. *Journal of Structural Geology*, 19(11), 1393–1404. [https://doi.org/10.1016/S0191-8141\(97\)00057-6](https://doi.org/10.1016/S0191-8141(97)00057-6)
- Fang, Y., Elsworth, D., Wang, C., Ishibashi, T., & Fitts, J. P. (2017). Frictional stability-permeability relationships for fractures in shales. *Journal of Geophysical Research: Solid Earth*, 122(3), 1760–1776. <https://doi.org/10.1002/2016JB013435>
- Faulkner, D., & Rutter, E. (2000). Comparisons of water and argon permeability in natural clay-bearing fault gouge under high pressure at 20°C. *Journal of Geophysical Research*, 105(B7), 16415. <https://doi.org/10.1029/2000JB900134>
- Faulkner, D., Jackson, C. A. L., Lunn, R. J., Schlische, R. W., Shipton, Z. K., Wibberley, C. A. J., & Withjack, M. O. (2010). A review of recent developments concerning the structure, mechanics and fluid flow properties of fault zones. *Journal of Structural Geology*, 32(11), 1557–1575. <https://doi.org/10.1016/j.jsg.2010.06.009>
- Favero, V., Ferrari, A., & Laloui, L. (2016). On the hydro-mechanical behaviour of remoulded and natural Opalinus Clay shale. *Engineering Geology*, 208, 128–135. <https://doi.org/10.1016/j.enggeo.2016.04.030>
- Forster, C. B., Evans, J. P., Tanaka, H., Jeffreys, R., & Nohara, T. (2003). Hydrologic properties and structure of the Mozumi Fault, central Japan. *Geophysical Research Letters*, 30(6), 1–4. <https://doi.org/10.1029/2002GL014904>
- Giesche, H. (2006). Mercury porosimetry: A general (practical) overview. *Particle and Particle Systems Characterization*, 23(1), 9–19. <https://doi.org/10.1002/ppsc.200601009>
- Guéguen, Y., & Dienes, J. (1989). Transport properties of rocks from statistics and percolation. *Mathematical Geology*, 21(1), 1–13. <https://doi.org/10.1007/BF00897237>

- Guéguen, Y., & Palciauskas, V. (1994). *Introduction to the Physics of Rocks*. Princeton University Press. Retrieved from <https://books.google.ch/books?id=fCP5qyRyX-Oc>
- Guéguen, Y., Sarout, J., Fortin, J., & Schubnel, A. (2009). Cracks in porous rocks: Tiny defects, strong effects. *The Leading Edge*, 28(1), 40–47. <https://doi.org/10.1190/1.3064145>
- Houben, M. E., Desbois, G., & Urai, J. L. (2013). Pore morphology and distribution in the Shaly facies of Opalinus Clay (Mont Terri, Switzerland): Insights from representative 2D BIB-SEM investigations on mm to nm scale. *Applied Clay Science*, 71, 82–97. <https://doi.org/10.1016/j.clay.2012.11.006>
- Houben, M. E., Desbois, G., & Urai, J. L. (2014). A comparative study of representative 2D microstructures in Shaly and Sandy facies of Opalinus Clay (Mont Terri, Switzerland) inferred from BIB-SEM and MIP methods. *Marine and Petroleum Geology*, 49, 143–161. <https://doi.org/10.1016/j.marpetgeo.2013.10.009>
- Keller, L. M., & Holzer, L. (2018). Image based upscaling of permeability in Opalinus Clay. *Journal of Geophysical Research: Solid Earth*, 1–11. <https://doi.org/10.1002/2017JB014717>
- Keller, L. M., Holzer, L., Wepf, R., & Gasser, P. (2011). 3D geometry and topology of pore pathways in Opalinus clay: Implications for mass transport. *Applied Clay Science*, 52(1–2), 85–95. <https://doi.org/10.1016/j.clay.2011.02.003>
- Keller, L. M., Schuetz, P., Erni, R., Rossell, M. D., Lucas, F., Gasser, P., & Holzer, L. (2013). Characterization of multi-scale microstructural features in Opalinus Clay. *Microporous and Mesoporous Materials*, 170, 83–94. <https://doi.org/10.1016/j.micromeso.2012.11.029>
- Klinkenberg, M., Kaufhold, S., Dohrmann, R., & Siegesmund, S. (2009). Influence of carbonate microfabrics on the failure strength of claystones. *Engineering Geology*, 107(1–2), 42–54. <https://doi.org/10.1016/j.enggeo.2009.04.001>
- Kneuker, T., Hammer, J., Shao, H., Schuster, K., Furche, M., & Zulauf, G. (2017). Microstructure and composition of brittle faults in claystones of the Mont Terri rock laboratory (Switzerland): New data from petrographic studies, geophysical borehole logging and permeability tests. *Engineering Geology*, 231(October), 139–156. <https://doi.org/10.1016/j.enggeo.2017.10.016>
- Kozeny, J. (1927). Über kapillare Leitung des Wassers im Boden. *Sitzungsber. Akad. Wiss. Wien*, 136, 271–306.
- Kübler, B. (1987). Cristallinité de l'illite, méthodes normalisées de préparations, méthodes normalisées de mesures. In *Cahiers de l'Institut de Géologie de Neuchâtel, Série ADX* (Vol. 1, p. 13).
- Laurich, B., Urai, J. L., Desbois, G., Vollmer, C., & Nussbaum, C. (2014). Microstructural evolution of an incipient fault zone in Opalinus Clay: Insights from an optical and electron microscopic study of ion-beam polished samples from the Main Fault in the Mt-Terri Underground Research Laboratory. *Journal of Structural Geology*, 67(PA), 107–128. <https://doi.org/10.1016/j.jsg.2014.07.014>
- Laurich, B., Urai, J. L., & Nussbaum, C. (2017). Microstructures and deformation mechanisms



- in Opalinus Clay: Insights from scaly clay from the Main Fault in the Mont Terri Rock Laboratory (CH). *Solid Earth*, 8(1), 27–44. <https://doi.org/10.5194/se-8-27-2017>
- Laurich, B., Urai, J. L., Vollmer, C., & Nussbaum, C. (2018). Deformation mechanisms and evolution of the microstructure of gouge in the Main Fault in Opalinus Clay in the Mont Terri rock laboratory (CH). *Solid Earth*, 9(1), 1–24. <https://doi.org/10.5194/se-9-1-2018>
- Leclère, H., Cappa, F., Faulkner, D., Fabbri, O., Armitage, P., & Blake, O. (2015). Development and maintenance of fluid overpressures in crustal fault zones by elastic compaction and implications for earthquake swarms. *Journal of Geophysical Research: Solid Earth*, 120(6), 4450–4473. <https://doi.org/10.1002/2014JB011759>
- Van Loon, L. R., Soler, J. M., Müller, W., & Bradbury, M. H. (2004). Anisotropic diffusion in layered argillaceous rocks: A case study with Opalinus Clay. *Environmental Science and Technology*, 38(21), 5721–5728. <https://doi.org/10.1021/es049937g>
- Marschall, P., Horseman, S., & Gimmi, T. (2005). Characterisation of Gas Transport Properties of the Opalinus Clay, a Potential Host Rock Formation for Radioactive Waste Disposal. *Oil & Gas Science and Technology – Rev. IFP*, 60(1), 121–139. <https://doi.org/10.2516/ogst:2005008>
- Mazurek, M., & de Haller, A. (2017). Pore-water evolution and solute-transport mechanisms in Opalinus Clay at Mont Terri and Mont Russelin (Canton Jura, Switzerland). *Swiss Journal of Geosciences*, 110(1), 129–149. <https://doi.org/10.1007/s00015-016-0249-9>
- Mazurek, M., Alt-Epping, P., Bath, A., Gimmi, T., & Waber, N. (2009). Natural tracer profiles across argillaceous formations : the CLAYTRAC project.
- Mazurek, M., Alt-Epping, P., Bath, A., Gimmi, T., Niklaus Waber, H., Buschaert, S., et al. (2011). Natural tracer profiles across argillaceous formations. *Applied Geochemistry*, 26(7), 1035–1064. <https://doi.org/10.1016/j.apgeochem.2011.03.124>
- Minardi, A., Crisci, E., Ferrari, A., & Laloui, L. (2016). Anisotropic volumetric behaviour of Opalinus clay shale upon suction variation. *Géotechnique Letters*, 6(2), 144–148. <https://doi.org/10.1680/jgele.16.00023>
- Minardi, A., Ferrari, A., Ewy, R., & Laloui, L. (2018). The impact of the volumetric swelling behavior on the water uptake of gas shale. *Journal of Natural Gas Science and Engineering*, 49(May 2017), 132–144. <https://doi.org/10.1016/j.jngse.2017.11.001>
- Monfared, M., Sulem, J., Delage, P., & Mohajerani, M. (2014). Temperature and damage impact on the permeability of opalinus clay. *Rock Mechanics and Rock Engineering*, 47(1), 101–110. <https://doi.org/10.1007/s00603-013-0459-7>
- Morrow, C., Lockner, D. A., Moore, D., & Hickman, S. (2014). Deep permeability of the San Andreas Fault from San Andreas Fault Observatory at Depth (SAFOD) core samples. *Journal of Structural Geology*, 64, 99–114. <https://doi.org/10.1016/j.jsg.2013.09.009>
- Muñoz, J., Alonso, E. E., & Lloret, A. (2009). Thermo-hydraulic characterisation of soft rock by means of heating pulse tests. *Géotechnique*, 59(4), 293–306. <https://doi.org/10.1680/geot.2009.59.4.293>

- Neuzil, C. E. (1994). How permeable are clays and shales? *Water Resources*, 30(2), 145–150.
- Nussbaum, C., Bossart, P., Amann, F., & Aubourg, C. (2011). Analysis of tectonic structures and excavation induced fractures in the Opalinus Clay, Mont Terri underground rock laboratory (Switzerland). *Swiss Journal of Geosciences*, 104(2), 187–210. <https://doi.org/10.1007/s00015-011-0070-4>
- Nussbaum, C., Kloppenburg, A., Caër, T., & Bossart, P. (2017). Tectonic evolution around the Mont Terri rock laboratory, northwestern Swiss Jura: constraints from kinematic forward modelling. *Swiss Journal of Geosciences*, 110(1), 39–66. <https://doi.org/10.1007/s00015-016-0248-x>
- Orellana, L. F., Scuderi, M. M., Collettini, C., & Violay, M. (2018a). Do scaly clays control seismicity on faulted shale rocks? *Earth and Planetary Science Letters*, 488, 59–67. <https://doi.org/10.1016/j.epsl.2018.01.027>
- Orellana, L. F., Scuderi, M. M., Collettini, C., & Violay, M. (2018b). Frictional Properties of Opalinus Clay: Implications for Nuclear Waste Storage. *Journal of Geophysical Research: Solid Earth*, 123(1), 157–175. <https://doi.org/10.1002/2017JB014931>
- Ougier-Simonin, A., Guéguen, Y., Fortin, J., Schubnel, A., & Bouyer, F. (2011). Permeability and elastic properties of cracked glass under pressure. *Journal of Geophysical Research: Solid Earth*, 116(7), 1–12. <https://doi.org/10.1029/2010JB008077>
- Passchier, C. W., & Trouw, R. a J. (2005). *Microtectonics*. Springer, Berlin, Heidelberg. <https://doi.org/10.1007/3-540-29359-0>
- Philipp, T., Amann-Hildenbrand, A., Laurich, B., Desbois, G., Littke, R., & Urai, J. L. (2017). The effect of microstructural heterogeneity on pore size distribution and permeability in Opalinus Clay (Mont Terri, Switzerland): insights from an integrated study of laboratory fluid flow and pore morphology from BIB-SEM images. *Geological Society, London, Special Publications*, 454(1), 85 LP-106. Retrieved from <http://sp.lyellcollection.org/content/454/1/85.abstract>
- Romero, E., & Simms, P. H. (2008). Microstructure investigation in unsaturated soils: A review with special attention to contribution of mercury intrusion porosimetry and environmental scanning electron microscopy. *Geotechnical and Geological Engineering*, 26(6), 705–727. <https://doi.org/10.1007/s10706-008-9204-5>
- Senger, R., Romero, E., & Marschall, P. (2018). Modeling of Gas Migration Through Low-Permeability Clay Rock Using Information on Pressure and Deformation from Fast Air Injection Tests. *Transport in Porous Media*, 1–17. <https://doi.org/10.1007/s11242-017-0962-5>
- Sutherland, R., Toy, V., Townend, J., Cox, S., Eccles, J. D., Faulkner, D., et al. (2012). Drilling reveals fluid control on architecture and rupture of the Alpine fault, New Zealand. *Geology*, 40(12), 1143–1146. <https://doi.org/10.1130/G33614.1>
- Tanikawa, W., & Shimamoto, T. (2009). Frictional and transport properties of the Chelungpu fault from shallow borehole data and their correlation with seismic behavior during the 1999 Chi-Chi earthquake. *Journal of Geophysical Research: Solid Earth*, 114(1), 1–15. <https://doi.org/10.1029/2008JB005750>

- Tanikawa, W., Hirose, T., Mukoyoshi, H., Tadai, O., & Lin, W. (2013). Fluid transport properties in sediments and their role in large slip near the surface of the plate boundary fault in the Japan Trench. *Earth and Planetary Science Letters*, 382, 150–160. <https://doi.org/10.1016/j.epsl.2013.08.052>
- Tsang, C.-F., Neretnieks, I., & Tsang, Y. (2015). Hydrologic issues associated with nuclear waste repositories. *Water Resources Research*, 51(9), 6923–6972. <https://doi.org/10.1002/2015WR017641>
- Vannucchi, P., Maltman, A., Bettelli, G., & Clennell, B. (2003). On the nature of scaly fabric and scaly clay. *Journal of Structural Geology*, 25(5), 673–688. [https://doi.org/10.1016/S0191-8141\(02\)00066-4](https://doi.org/10.1016/S0191-8141(02)00066-4)
- Walker, R. J., Holdsworth, R., Armitage, P., & Faulkner, D. (2013). Fault zone permeability structure evolution in basalts. *Geology*, 41(1), 59–62. <https://doi.org/10.1130/G33508.1>
- Wibberley, C. A. J., & Shimamoto, T. (2002). Internal structure and permeability of major strike-slip fault zones: The Median Tectonic Line in Mie Prefecture, Southwest Japan. *Journal of Structural Geology*, 25(1), 59–78. [https://doi.org/10.1016/S0191-8141\(02\)00014-7](https://doi.org/10.1016/S0191-8141(02)00014-7)
- Yang, Y., & Aplin, A. C. (2010). A permeability-porosity relationship for mudstones. *Marine and Petroleum Geology*, 27(8), 1692–1697. <https://doi.org/10.1016/j.marpetgeo.2009.07.001>
- Yu, C., Matray, J. M., Gonçalves, J., Jaeggi, D., Gräsle, W., Wieczorek, K., et al. (2017). Comparative study of methods to estimate hydraulic parameters in the hydraulically undisturbed Opalinus Clay (Switzerland). *Swiss Journal of Geosciences*, 110(1), 85–104. <https://doi.org/10.1007/s00015-016-0257-9>



### 3.

## FRICITIONAL PROPERTIES OF THE FAULT ZONES INTERSECTING THE OPALINUS CLAY FORMATION

**Authors:** Luis Felipe Orellana<sup>1\*</sup>, Marco Maria Scuderi<sup>2,3</sup>, Cristiano Collettini<sup>2,3</sup>, and Marie Violay<sup>1</sup>

<sup>1</sup> Laboratory of Experimental Rock Mechanics (LEMR), ENAC, EPFL, Switzerland;

<sup>2</sup> Dipartimento di Scienze della Terra, Università degli Studi La Sapienza, Rome, Italy;

<sup>3</sup> Istituto Nazionale di Geofisica e Vulcanologia (INGV), Italy;

**Reference:** Orellana, L.F., Scuderi, M.M., Collettini, C., Violay, M., 2018. Frictional Properties of Opalinus Clay: Implications for nuclear waste storage. *J. Geophys. Res. Solid Earth* 123, 157–175. doi:10.1002/2017JB014931

**Contributions:** L. F. Orellana has collected, prepared and characterized samples used in this study. M.M. Scuderi and L. F. Orellana have run the experiments. All authors have contributed to the testing strategy and methodology. L. F. Orellana has carried out microstructural observations and modelled results. L. F. Orellana has written the manuscript. M. M. Scuderi, C. Collettini and M. Violay have edited and guided discussions of the manuscript. M. Violay has acted as a supervisor and main responsible author of the publication.

### Highlights:

- Laboratory study on the frictional properties of Opalinus Clay, a host rock for nuclear waste storage.
- Faults within the Opalinus Clay formation are mechanically weak.
- Velocity strengthening and lack of re-strengthening during inter-seismic periods predict aseismic fault-slip behavior.

### 3.1. ABSTRACT

The kaolinite-bearing Opalinus Clay (OPA) is the host-rock proposed in Switzerland for disposal of radioactive waste. However, the presence of tectonic faults intersecting the OPA formation put the long-term safety performance of the underground repository into question due to the possibility of earthquakes triggered by fault instability. In this paper, we study the frictional properties of the OPA shale. To do that, we have carried out biaxial direct shear experiments under conditions typical of nuclear waste storage. We have performed velocity-steps (1-300  $\mu\text{m/s}$ ) and slide-hold-slide tests (1-3000 s) on simulated fault gouge at different normal stresses (4-30 MPa). To establish the deformation mechanisms, we have analyzed the microstructures of the sheared samples through scanning electron microscopy. Our results show that peak ( $\mu_{peak}$ ) and steady-state friction ( $\mu_{ss}$ ) range from 0.21 to 0.52 and 0.14 to 0.39 respectively, thus suggesting that OPA fault gouges are weak. The velocity-dependence of friction indicates a velocity-strengthening regime, with the friction rate parameter ( $a-b$ ) that decreases with normal stress. Finally, the zero healing values imply a lack of re-strengthening during inter-seismic periods. Taken together, if OPA fault reactivates, our experimental evidence favors an aseismic slip behavior, making the nucleation of earthquakes difficult, and long-term weakness, resulting in stable fault creeping over geological times. Based on the results, our study confirms the seismic safety of the OPA formation for a nuclear waste repository.

**Keywords:** Friction, Opalinus clay, nuclear waste storage, earthquake nucleation, experimental rock deformation

## 3.2. INTRODUCTION

Based on its favorable hydro-mechanical properties, the kaolinite-bearing Opalinus Clay formation (OPA) has been selected as suitable candidate for the long-term underground storage of radioactive waste. Located in the northern part of Switzerland, this shale formation is characterized by a very low permeability ( $10^{-19}$  to  $10^{-21}$  m<sup>2</sup>), a self-sealing capacity (i.e. the spontaneous reduction of fracture permeability by hydro-mechanical, hydro-chemical, and/or hydro-bio-chemical processes (Bock et al., 2010)), and advantageous geochemical properties that allow the formation to prevent the migration of radionuclides (Bossart et al., 2017).

To ensure the safety of any deep geological repository, the host-rocks need to be seismically safe over geological time scales (~300.000 years, the time needed for radioactivity decay). However, within the OPA formation, various tectonic fault systems have been identified. Among them, the Main Fault is a major thrust fault that intersects the Mont Terri Underground Laboratory (MTL). The MTL an international research consortium devoted to the development of a better understanding for the concept of deep geological disposal of nuclear waste (**Figure 3-1**) (Bossart et al., 2017; Nussbaum et al., 2011).

Clearly, the presence of various tectonic fault systems put into question the suitability of the formation for the purpose of underground nuclear repository. Moreover, during the life of the deep geological repositories, changes of the surrounding stress field can modify the hydro-mechanical and geo-mechanical properties of the host formation (Popp et al., 2008; Tsang et al., 2012). Natural perturbations (e.g. earthquakes, hydrologic boundary conditions) or engineering activities (e.g. tunnel excavations) may perturb the local stress field, and hence, influence the response of a fault system by triggering natural or induced earthquakes that can potentially damage the underground storage facilities (Hashash et al., 2001; Perfettini & Ampuero, 2008; W. L. Wang et al., 2001). The infrastructure loss may be then followed by radionuclide leakages to the surface, contaminating aquifers, causing environmental harm, and posing a direct risk to the health of the nearby population.

In this paper, we present results of an experimental study on the frictional properties of the Opalinus Clay formation from borehole samples retrieved from the Main Fault. To do this, we performed friction experiments at low-slip velocities (3 to 300  $\mu\text{m/s}$ ) in a double shear direct configuration under representative nuclear waste repository conditions (4 to 30 MPa normal stress). Here, for the first time, we report a full collection of results regarding the frictional properties of the Opalinus Clay formation. By doing so, we discuss the potential for fault reactivation, the associated slip behavior, i.e. stable or unstable, and its implications on its use as a nuclear waste repository.

Previous work on friction have emphasized the role of mineralogy on the frictional behavior of rocks. In addition to the grain size and environmental conditions (temperature, surrounding stresses, presence and chemistry of water, and others), the mineralogy of the fault gouge has proved to be a critical parameter controlling the frictional behavior and slip stability of faults. Moreover, when fault gouges contain certain clay minerals, they exhibit a generally weak frictional strength relative to the Byerlee's rule (Byerlee, 1978; Shimamoto & Logan, 1981). Indeed, laboratory experiments on clay-rich gouges have shown a large variety of friction values ranging from 0.1 to 0.6 (Bird, 1984; Haines



et al., 2014; Ikari et al., 2011; Kohli & Zoback, 2013; Niemeijer & Collettini, 2013; Numelin et al., 2007; Saffer et al., 2001, 2012; Smith & Faulkner, 2010; Tembe et al., 2010; Tesei et al., 2012, 2014; Tsutsumi et al., 2011). In the context of the rate- and state constitutive laws (Dieterich, 1979; Marone, 1998; Ruina, 1983; Scholz, 1998), it has also been shown that the vast majority of clays show velocity-strengthening behavior at slow slip velocities (0.1-100  $\mu\text{m/s}$ ), and low frictional healing rates.

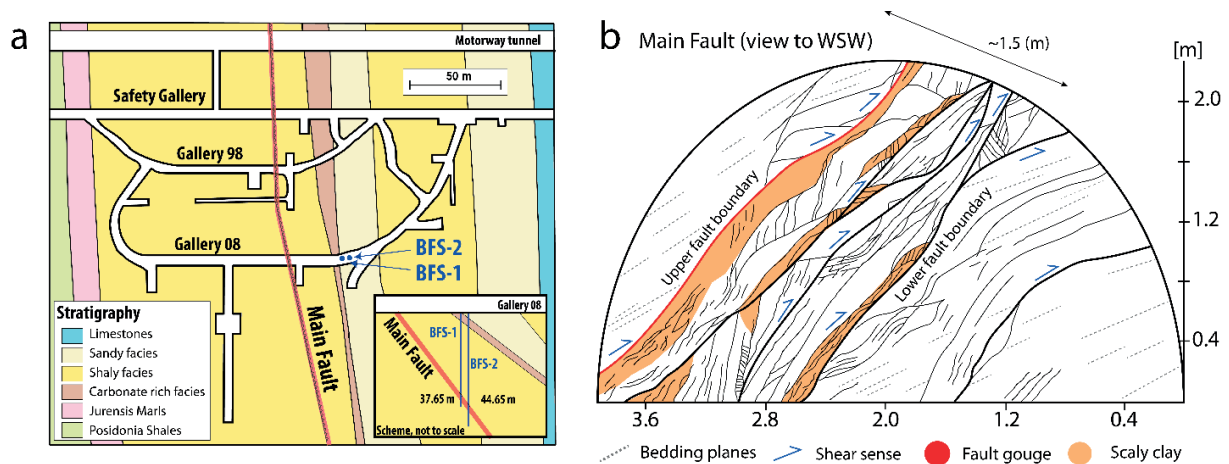


**Figure 3-1:** A) Simplified geological plan-view map of the Mont Terri Laboratory (MTUL) modified after Nussbaum et al. (2011). Figure 1a shows the distribution of the different facies within the Opalinus Clay Formation (see legend) and location of boreholes BFS -1 and BFS-2. Inset is a scheme not to scale of the boreholes drilled through the Main fault zone. B) Scheme of the Main Fault intersected in gallery 98 at MTUL modified after Nussbaum et al. (2011) and Jaeggi et al. (2017). The “Main Fault” zone is about 0.8-0.9 to 3 m thick. The lower and upper fault boundaries have a dip of 55-60° to the SSE. Bedding planes dips in the same direction with a 15° angular difference (Nussbaum et al., 2011).

Among clays, the number of experiments on the frictional properties of kaolinite –rich gouges are scarce in the literature, especially when compared to the extensive attention devoted to illite, smectite, or montmorillonite minerals. Moreover, whilst results on the frictional strength of kaolinite –rich gouges are more common, data on the velocity-dependence of friction and fault healing is limited. In terms of frictional strength, kaolinite –rich samples have shown diverse values ranging between 0.22 to 0.55 and 0.4 to 0.85 for wet and dry conditions respectively (Bos et al., 2000; Bos & Spiers, 2000; Brantut et al., 2008; Carpenter et al., 2015, 2016; Crawford et al., 2008; Fang et al., 2017; Moore & Lockner, 2004; Morrow et al., 2000).

Regarding the frictional stability and fault healing, the samples from the Northeast Boundary Fault composed of ~25% of kaolinite + chlorite exhibited an uniform velocity strengthening behavior and healing rates between 0.0035 and 0.007 (Carpenter et al., 2015). Frictional healing tests on kaolinite/halite mixtures have shown that the presence of kaolinite inhibited halite to halite contact, reducing the healing capacity of the gouge material to a very small re-strengthening rate (Bos & Spiers, 2000). Recently, in the context of CO<sub>2</sub> sequestration, one shear experiment where two blocks of intact Opalinus Clay slide against each other was carried out at 3 MPa effective normal stress and sliding velocities of 1 and 10  $\mu\text{m/s}$  (Fang et al., 2017). The authors have shown a velocity-strengthening regime and a steady-state friction value equal to 0.5.

Unfortunately, a more comprehensive work on the frictional properties of the OPA fault rocks is lacking so far. This is the focus of our study. We integrate mechanical data and observations of microstructural deformation to provide a thorough analysis of the frictional behavior of the OPA fault rocks. By doing so, we provide results on its frictional strength, stability, and healing behavior.

### 3.2.1. THE OPALINUS CLAY – FAULT GOUGE

At the MTUL, the BSF-1 and BSF-2 boreholes (**Figure 3-1a** inset) were drilled in gallery 08 intersecting the Main Fault. Both intact and faulted samples were recovered. Fault core samples contain an arrangement of different structural elements, including an anastomosing network of scaly clays and fractures, calcite veins, undisturbed blocks, shear zones, and a series of planes containing fault gouges (Laurich et al., 2014; Nussbaum et al., 2011).

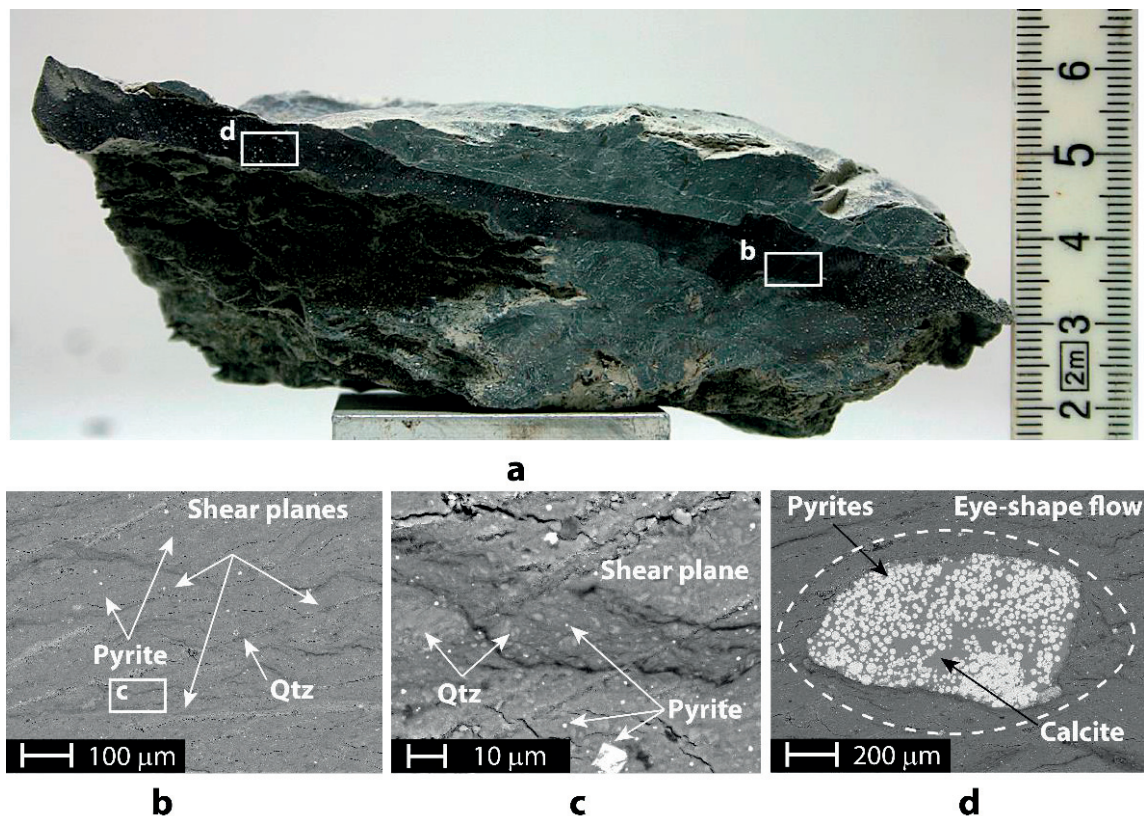


**Figure 3-2:** A cm-scale sample (recovered from borehole BFS2) and BSE images of Opalinus clay gouge. A) Hand sample of Opalinus clay gouge. Gouge thickness is about 1 cm. B) The homogenous clay matrix has fine grain size ( $\sim 7 \mu\text{m}$ ). We observe the ubiquitous presence of quartz (Qtz), smaller proportions of pyrite and calcite minerals, and sub-horizontal sets of interconnected shear planes. White box indicates the position of Figure 2c. C) A sub-horizontal shear plane underlined by the orientation of clay platelets. D) Clay matrix flowing around rigid, sub-rounded calcite crystal forming an eye-shape flow pattern perturbation (Passchier & Trouw, 2005). In this case, several pyrite framboids are on the surface of the calcite mineral.

Within the fault core, the Opalinus Clay – fault gouges (Figure 3-2) appear as dark and partially continuous bands of 8-15 mm in thickness, surrounded by deformed rock, including portions of scaly clay. The darker colour originates from the reduction of the particle size ( $\sim 7 \mu\text{m}$ ) and smaller calcite content compared to the protolith (Laurich et al., 2014). Some particular elements can be recognized within the fault gouge, including a texture of very fine and homogeneous grain size, and the

ubiquitous presence of quartz minerals and smaller proportions of pyrite and calcite minerals (Figure 3-2b). The fault gouge is layered through a regular and sub-horizontal fabric (Figure 3-2b) linked to interconnected shear planes underlined by the orientation of clay platelets (Figure 3-2c). We also observed isolated and relatively large, rigid, sub-rounded minerals, often quartz, but also calcite minerals inside the clay-rich gouge (Figure 3-2d). Their presence developed an eye-shape flow pattern perturbation (i.e. shear flow around a round object in simple shear flow (Passchier & Trouw, 2005)) highlighting the apparent movement of clay minerals around those large fragments.

### 3.3. MATERIALS AND METHODS

#### 3.3.1. EXPERIMENTAL SAMPLES

To study the frictional properties of the Opalinus Clay gouge, we have sheared pulverized samples of intact OPA, hereafter named simulated OPA gouge, at conditions representative of the environment targeted by nuclear waste repositories. We have used simulated OPA gouge because natural gouge is difficult to collect and the material recovered from borehole BFS-1 and BFS-2 was not sufficient for our experimental work.

We have prepared the simulated gouge sample by crushing and sieving ( $< 300 \mu\text{m}$ ) intact OPA retrieved from the same boreholes. An average grain size of about  $7 \mu\text{m}$  (Figure 3-3a) was measured using the particle size measurement equipment Malvern Mastersizer S, which is comparable to the gouge grain size of the main fault at MTUL (Laurich et al., 2014).

<b>Mineralogy of the simulated fault gouge Opalinus Clay (%wt)</b>	
<b>Phyllosilicates</b>	$49.89 \pm 0.40$
<i>Illite-Smectite IS 1</i>	$2.25 \pm 1.41$
<i>Illite-Smectite (2)</i>	$0.75 \pm 0.29$
<i>Mica</i>	$10.48 \pm 3.55$
<i>Chlorite</i>	$8.38 \pm 2.85$
<i>Kaolinite</i>	$28.04 \pm 0.99$
<b>Quartz</b>	$23.26 \pm 0.70$
<b>Feldspar-K</b>	$2.40 \pm 0.31$
<b>Plagioclase-Na</b>	$2.34 \pm 0.20$
<b>Calcite</b>	$14.68 \pm 0.80$
<b>Dolomite</b>	$1.19 \pm 0.34$
<b>Pyrite</b>	$1.43 \pm 0.30$
<b>Goethite</b>	$1.90 \pm 0.16$
<b>Others</b>	$2.91 \pm 0.39$

**Table 3-1:** Bulk mineral composition (% weight) of Opalinus clay. Four measurements were carried out for the simulated gouge (intact rock from the OPA formation). Results are presented as  $X \pm S$ , where X is the mean and S the standard deviation. The group Phyllosilicates corresponds to the sum of Illite-Smectite IS 1, Illite-Smectite (2), Mica, Chlorite, and Kaolinite.



X-Ray diffraction (XRD) analysis were performed at the Geological Institute of the University of Lausanne (UNIL), Switzerland. The clay mineral analyses were based on methods outlined by (Kübler, 1987). Sample preparation included, but were not limited to, a) the disaggregation of the rock, b) mixing the sample with de-ionize water, b) removal of the carbonate fraction by the addition of HCl 10% c) separation of different grain size fractions ( $< 2\mu\text{m}$  and  $2\text{--}16\mu\text{m}$ ) using the timed settling method based on Stokes law, d) application of ethylene-glycol onto clays already placed on glass-slide, and finally, d) the recognition of characteristic XRD peaks of each clay mineral presented in the size fraction.

The mineralogy of the simulated gouge (**Table 3-1**) consists of phyllosilicates ( $\sim 50\%$ ), quartz ( $\sim 23\%$ ), calcite ( $\sim 15\%$ ), and smaller proportions of less than 3% of plagioclase – Na, Feldspath – K, dolomite, goethite and pyrite. XRD analysis of intact Opalinus Clay have been reported by other authors where the content of illite-smectite is higher than reported in Table 3-1 (Fang et al., 2017; Klinkenberg et al., 2009).

### 3.3.2. EXPERIMENTAL PROCEDURE

We have carried out experiments on simulated gouge material to characterize the frictional behavior of the Opalinus Clay as a function of applied normal stress and slip velocity. In our tests, normal stress ranged between 4 and 30 MPa, which are the conditions of interest for nuclear waste repositories ( $\sim 100\text{--}1000$  m depth). We performed experiments using BRAVA installed at INGV Rome, Italy (Collettini et al., 2014), a biaxial rock deformation apparatus, in the double-direct shear configuration (Figure 3-3b). In this configuration, two layers of powdered gouge samples (Figure 3-3c) are sandwiched in a three steel block assembly, characterized by two side stationary blocks and a central block with a nominal frictional contact area of  $5\text{cm} \times 5\text{cm}$ .

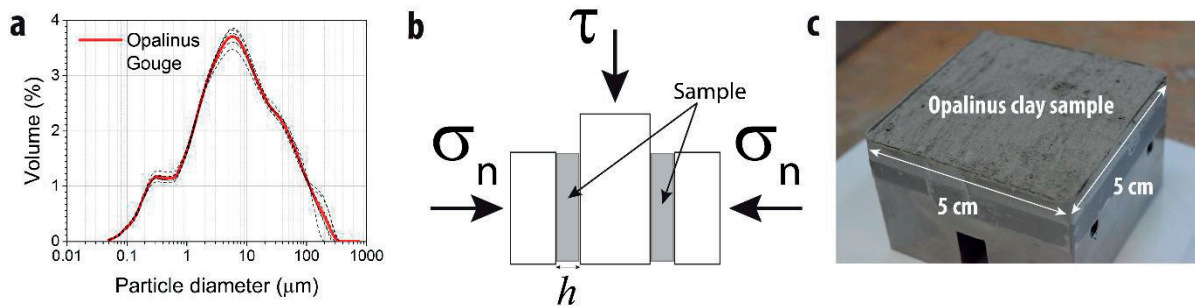


**Figure 3-3:** Material and shear configuration. A) Particle Size Distribution (PSD) for Opalinus gouge. 90% of the particles are finer than  $60\mu\text{m}$  while the average size is  $7\mu\text{m}$ . B) Double direct shear configuration used in these experiments. C) Opalinus clay samples employed in the experiments on sample holder before shearing

For all the experiments, the layers of simulated OPA gouge were constructed using precise leveling jigs to obtain a starting uniform layer thickness of 5 mm. We used two fast-acting servo-hydraulic rams to apply the horizontal and vertical loads. The applied load was measured via strain gauge load cells (accuracy  $\pm 0.03\text{kN}$ ) positioned at the extremity of the hydraulic rams in contact with the sample assembly. We measured the horizontal and vertical displacements by using Linear Variable Displacement Transformers (LVDTs), with an accuracy of  $\pm 0.1\mu\text{m}$ , referenced to the load frame and

the upper side of the ram. The displacement values were corrected by taking into account the machine stiffness for both vertical (928.5 kN/mm) and horizontal (1283 kN/mm) load frames.

Experiments were run at room temperature ( $\sim 25^\circ\text{C}$ ), on samples that were saturated overnight with vaporized fluids at constant 100% relative humidity conditions (RH). To this end, we have placed a humidifier inside the BRAVA apparatus to ensure a saturated environment for the samples during deformation. Thus, we have prevented them from dehydration, however, local pore pressures within the samples were not controlled during tests due to experimental constraints. Water humidity was measured with a hygrometer during the experiments. Also, we have ran one experiment on dry gouge material (RH=5%) to evaluate the effect of water saturation.

At the beginning of each test, we have applied the normal load and maintained it constant at the target normal stress value via a load feedback control mode. Before shear began, we have monitored the thickness of the gouge layer ( $h$ ) using the horizontal LVDTs (Figure 3-3b). We measured compaction of the gouge until a constant value of layer thickness was achieved. Then, we have started shearing. The initial thickness of the samples ( $h_o$ ) under load before shearing ranged from 2.7 to 2.3 mm. We have determined variation in porosity ( $\Delta\phi$ ) during shear via measurement of the change in layer thickness ( $\Delta h$ ) assuming that  $\Delta\phi \approx \frac{\Delta h}{h}$ , (Niemeijer et al., 2010; Samuelson et al., 2009).

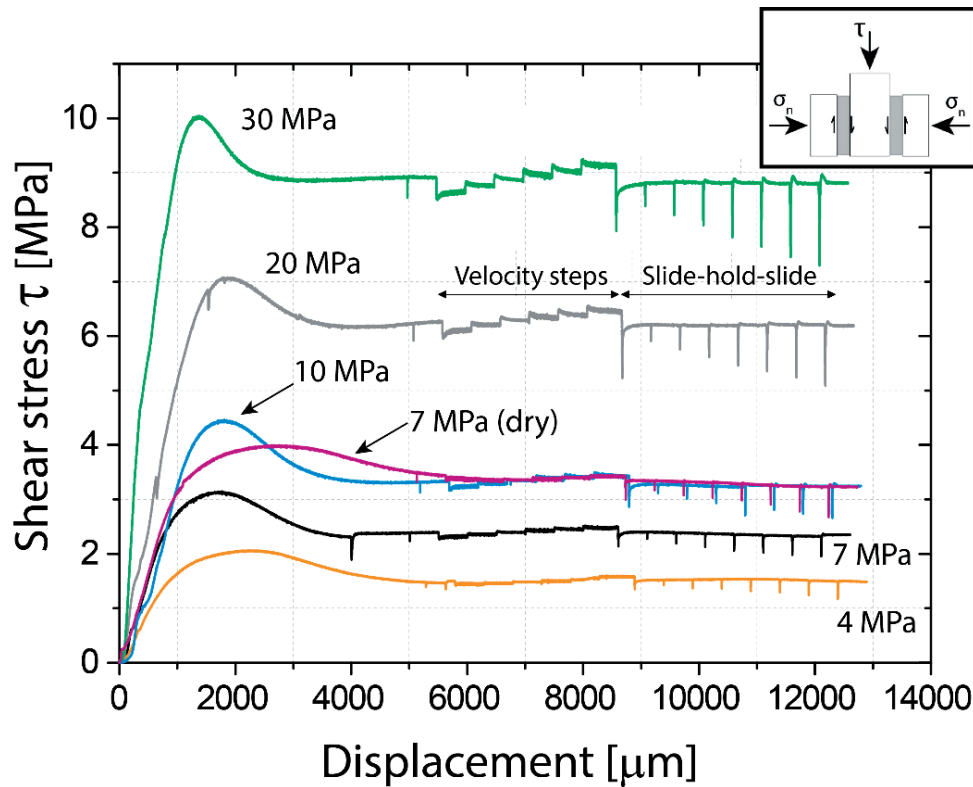


**Figure 3-4:** Friction experiments performed on simulated gouge samples of Opalinus Clay at different normal stress (from 4 MPa to 30 MPa). The curves show the evolution of the shear stress ( $\tau$ ) with slip. Experiments show a peak strength followed by a residual value. Curves indicate a low to moderate slip weakening. The weakening is higher at lower normal stress (4,7,10 MPa). Velocity step and slide-hold-slide tests start after shear stress reach a steady value. Inset: Double direct shear configuration used in these experiments.

Each experiment has followed a typical computer-controlled displacement history. Shear began with an initial stage at a constant displacement rate of 10  $\mu\text{m/s}$  for  $\sim 5.5$  mm. During this phase, the sample has deformed quasi-elastically until a peak friction value was reached followed by an evolution to a steady-state sliding friction (Figure 3-4).

We have calculated the shear stress ( $\tau$ ) dividing the vertical load by the sample surfaces (two gouge layers). Then, we determined the Amonton's friction  $\mu$  (or frictional resistance) as the ratio of the shear resistance,  $\tau$ , over the applied normal stress,  $\sigma_n$ .

$$\mu = \frac{\tau}{\sigma_n}$$

**Equation 3-1:** Friction

However, for a wide range of cohesive surfaces, shear strength might not completely vanish when normal stress is equal to zero, and therefore, a more accurate definition of the coefficient of friction (Lockner & Beeler, 2002) is given by:

$$\mu_f = \frac{\tau - S_o}{\sigma_n}$$

**Equation 3-2:** Coefficient of friction

Where  $S_o$  corresponds to an inherent shear strength. To provide a more wide-ranging and systemic analysis of our results, in this study we calculated both the Amonton's friction ( $\mu$ ) and the coefficient of friction for cohesive surface  $\mu_f$ . Here, in this study, when we mention friction, we refer to the Amonton's friction (Equation 3-1).

To get insight on fault stability, we have studied the velocity-dependence of friction by imposing different velocity steps (1-300  $\mu\text{m/s}$ ) as shown in Figure 3-5a. For each step, we have suddenly increased slip velocity inducing an immediate increase in friction followed by an exponential decay over some critical slip distance ( $D_c$ ), to a new steady-state value of the frictional resistance (Figure 3-5c) (Scholz, 2002). To retrieve the rate- and state- frictional constitutive parameters, we have modeled each velocity step using the Ruina's slip dependent evolution law (Ruina, 1983). The empirical Ruina's law is defined by the friction relation (Equation 3-3) and the state evolution law (Equation 3-4):

$$\mu = \mu_o + a \cdot \ln\left(\frac{V}{V_o}\right) + b \cdot \ln\left(\frac{V_o \cdot \theta}{D_c}\right),$$

**Equation 3-3:** Rate and state constitutive empirical law

$$\frac{d\theta}{dt} = -\frac{V \cdot \theta}{D_c} \cdot \ln\left(\frac{V_o \cdot \theta}{D_c}\right)$$

**Equation 3-4:** Ruina's evolution law (Ruina, 1983)

Where  $\mu_o$  is a constant that represents friction at steady-state for a reference velocity  $V_o$ ,  $\mu$  is the friction at the new steady-state velocity  $V$ , and  $a$  and  $b$  are empirical parameters, also named the direct and evolution effect respectively (Marone, 1998).

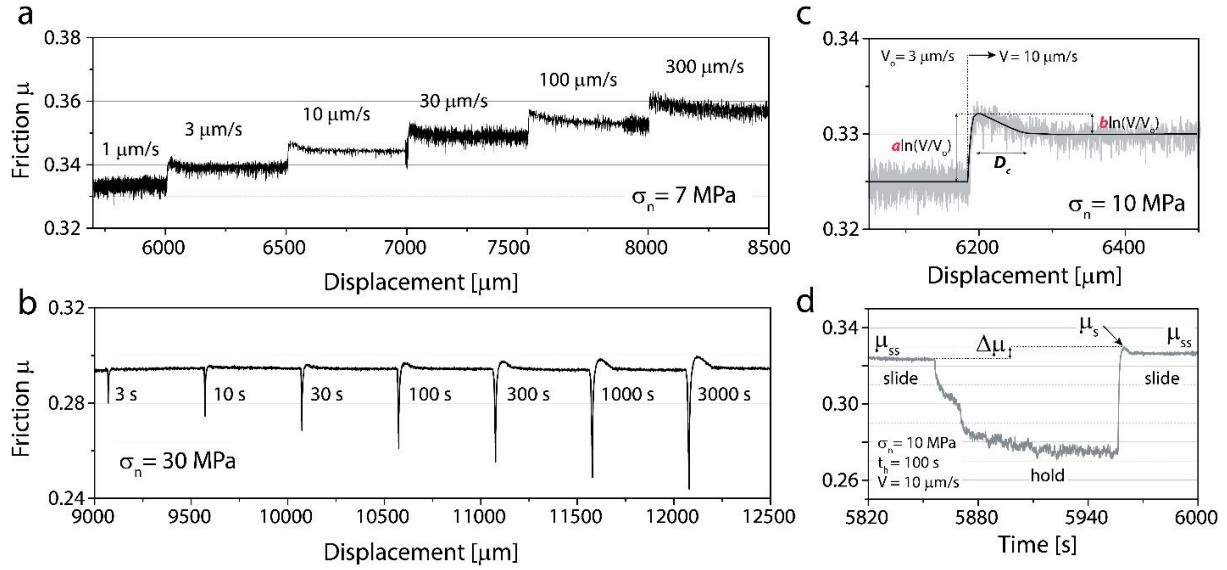


**Figure 3-5:** Friction parameter analysis. A) The coefficient of friction versus displacement during the velocity step sequence. B) The coefficient of friction versus displacement during the slide hold slide sequence. C) An example of frictional parameter ( $a - b$ ) measurement. The parameter  $a$ , also known as the direct effect, is proportional to the instantaneous change in friction. The friction parameter  $b$ , also known as the evolution effect, is proportional to the subsequent drop to a new steady-state. The black line shows the modelled output of Ruina's slip dependent evolution law. D) An example of frictional healing ( $\Delta\mu$ ) measurement for experiment i443 (normal stress equal to 10 MPa). The sequence corresponds to 100 s holding time. Frictional healing  $\Delta\mu$  is defined as the difference between peak static friction  $\mu_s$  and the pre-hold steady-state friction  $\mu_{ss}$ .

As first suggested by *Rabinowicz* (1951) and then by *Dieterich* (1979),  $\theta$  can be interpreted as the average lifetime of contacts, i.e. the average elapsed time since the contacts existing at a given time were first formed (Scholz, 2002). The critical slip distance  $D_c$ , at a constant velocity  $V$ , is defined as the distance over which friction evolves from a local peak to a steady-state. *Marone* (1998) has pointed out the standard interpretation for  $D_c$  as the slip necessary to renew the population of contacts, meaning that contacts are destroyed and replaced by an uncorrelated set (Scholz, 2002). The sliding stability is determined by the friction parameter ( $a-b$ ), defined as:

$$a - b = \frac{\Delta\mu_{ss}}{\ln\left(\frac{V}{V_o}\right)}$$

**Equation 3-5:** Frictional stability parameter

Where  $\Delta\mu_{ss}$  is the change in the steady-state friction upon an immediate change in sliding velocity from  $V_o$  to  $V$  (Marone, 1998). For neutral or positive rate dependence,  $(a-b) \geq 0$ , sliding will tend to be stable, and the material will be described as velocity-strengthening. Conversely, if the frictional strength decreases upon an increase in sliding velocity,  $(a-b) < 0$ , any perturbation on the fault will potentially promote slip acceleration. Thus, the system will be considered potentially unstable, and the material will be described as velocity- weakening (Scholz, 2002).



We have modeled our laboratory data using a fifth-order Runge-Kutta method. It corresponds to an iterative least square method (Reinen & Weeks, 1993; Saffer & Marone, 2003) that allows us to determine the best-fit parameters of the velocity-steps test, i.e. the critical slip distance  $D_c$ , the parameters  $a$  and  $b$ , and their respective variances derived from the goodness of the model fit to the experimental data.

Slide-hold-slide tests (Figure 3-5b) were performed to measure the amount of frictional healing ( $\Delta\mu$ ). During these tests, gouge layers were sheared at a constant velocity of 10  $\mu\text{m/s}$  followed by a hold period,  $t_h$ , during which the vertical ram is stopped and gouge layers were under quasi-stationary contact. In our tests, the hold period varied between 3 and 3000 seconds. After the hold period, the gouge was re-sheared at 10  $\mu\text{m/s}$ . As is shown in Figure 3-5c, we observe an increase (or eventually decrease) of friction upon re-shear, followed by a decay to the previous steady-state value (Figure 3-5d) (Scholz, 2002). The amount of frictional healing,  $\Delta\mu$ , was measured as the difference between the peak friction measured upon re-shear after each hold and the pre-hold steady-state friction (Marone, 1998). Frictional healing rates  $\beta$  were calculated as:

$$\beta = \frac{\Delta\mu}{\Delta \log_{10}(t_h)}$$

**Equation 3-6:** Frictional healing

### 3.3.3. MICROSTRUCTURAL ANALYSIS

At the end of each test, to obtain thin sections parallel to the direction of shear, we have recovered parts of the gouge samples, and we have embedded them in epoxy resin (London resin). The thin sections of about 30  $\mu\text{m}$  in thickness were prepared at the Dipartimento di Scienze della Terra, Università degli Studi La Sapienza (Rome, Italy). At the Swiss Federal Institute of Technology in Lausanne (EPFL), we have carried out microstructural observations on thin sections using Secondary Electron (SE) and Back-scattered Electron (BSE) images, detailed microstructural observations were performed using the Scanning Electron Microscopy (SEM) FEI XLF30-FEG installed at the Interdisciplinary Centre for Electron Microscopy (CIME, EPFL, Switzerland).

## 3.4. RESULTS

### 3.4.1. MECHANICAL DATA

#### 3.4.1.1. FRICTIONAL STRENGTH

We have measured the evolution of shear strength as a function of displacement for gouge samples as presented in Figure 3-4. Here, we report the friction  $\mu$  (Figure 3-6a), the inherent shear strength  $S_o$  (Figure 3-6b) and the coefficient of friction  $\mu_f$  (Figure 3-6c) values calculated according to Equation 3-1 and Equation 3-2 respectively.

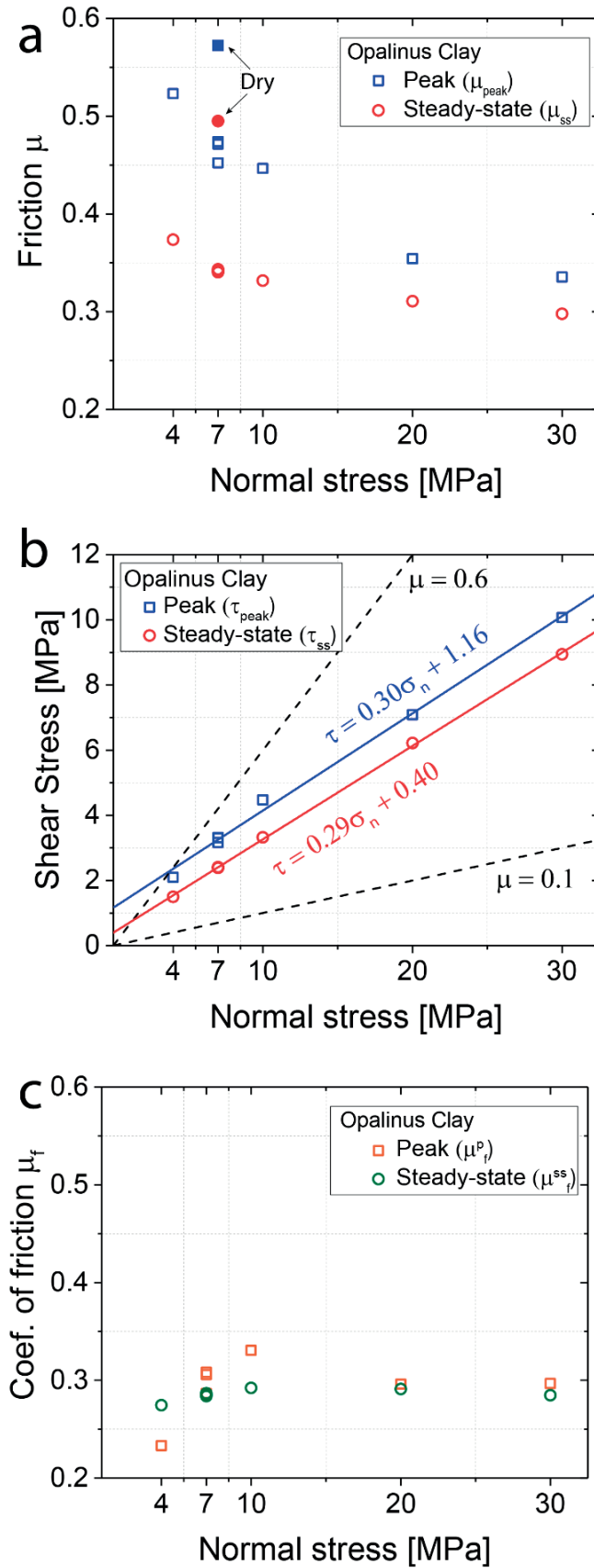


**Figure 3-6:** A) Amontons' friction  $\mu$  (Equation 3-1) versus normal stress. In black: peak friction  $\mu_{peak}$ . In red: steady-state friction  $\mu_{ss}$ . Filled symbols correspond to experiments performed on dry samples. B) Shear stress versus normal stress. We have linearized both peak and steady-state shear strength following the linear fit  $\tau = \mu_f' \sigma_n + S_o$  as shown in the graph. At the peak,  $\mu_f'_p = 0.30$  and  $S_o = 1.16$ . At steady state,  $\mu_f'_{ss} = 0.29$  and  $S_o = 0.40$ . For comparison, we display  $\tau = 0.6 \cdot \sigma_n$  and  $\tau = 0.1 \cdot \sigma_n$  on the chart. C) The coefficient of friction for coherent surfaces  $\mu_f$  (Equation 3-2) at both peak and steady state shear stress.

For all the saturated samples at 100% RH (hereafter saturated), the shear stress evolves quasi-linearly with displacement until a peak strength was reached (Figure 3-4). At that point, friction ( $\mu_{peak}$ ) ranges from 0.33 to 0.52 (Figure 3-6a, Table 3-2). As shearing continues, shear stress reaches a residual value corresponding to a steady-state. At the steady-state condition, achieved between 4 to 5 mm shear displacements, steady-state friction values ( $\mu_{ss}$ ) range from 0.29 to 0.37 (Figure 3-6a, Table 3-2).

The dry sample shows a peak friction equals to 0.57 and steady-state friction of 0.50. Figure 3-6a shows a decrease of both peak and steady-state friction when normal stress increases.

To calculate the coefficient of friction for cohesive surfaces  $\mu_f$  (Equation 3-2), we have first fitted the shear stress (Figure 3-6b) with  $\tau = \mu_f' \sigma_n + S_o$ , where  $\mu_f'$  is the linearized value of the coefficient of friction and  $S_o$  the inherent shear strength. While at the peak the inherent shear strength  $S_o$  is 1.16, at steady-state  $S_o$  is equal to 0.40 (Figure 3-6b). Then, we have calculated the coefficient of friction  $\mu_f$  (Figure 3-6c) for each samples following Equation 3-2: Coefficient of friction. Figure 3-6c shows that the coefficient of friction for cohesive surfaces measured at peak shear stress ( $\mu_f^p$ ) increases with normal stress from 0.23 at 4 MPa to 0.3 at 30 MPa. On the other hand, at steady-state shear stress, the steady-state coefficients of friction ( $\mu_f^{ss}$ ) were fairly constant over the range of normal stress.

#### 3.4.1.2. FRICTIONAL STABILITY

Velocity-dependence of friction tests on saturated gouge indicated ( $a-b$ ) values comprised between 0.0072 and 0.0012 (Table 3-2, Figure 3-7a), i.e. a velocity-strengthening regime, with no points in the potentially unstable regime at any sliding velocity. The dry sample sheared at 7 MPa shows a transition from velocity-weakening to velocity-strengthening at up-step velocity of 10  $\mu\text{m/s}$ .

For saturated gouges, the frictional parameter  $a$  take values of  $\sim 0.006$  and shows a non-dependent behavior with respect to normal stress. The parameter  $b$  exhibits an increase from 0.0015 (on average) at low normal stress (4 MPa) to values of about 0.003 at 10 MPa normal stress (Figure 3-7b). Thus, the resulting friction rate parameter ( $a-b$ ) decreases as normal stress increases (Figure 3-7a) and no transition to velocity-weakening is observed. At all normal stress, the frictional parameters ( $a-b$ ) do not show a correlation with up-step velocities. For the dry sample sheared at 7 MPa normal stress, the parameter  $a$  take values of  $\sim 0.003$ . On the other hand, the frictional parameter  $b$  shows a decrease from 0.004 to 0.001 with increasing up-step velocities from 3 to 300  $\mu\text{m/s}$ .

For saturated gouges, the critical slip distance  $D_c$  increases (on average) from 0.05 to 0.15 mm as normal stress increases (Figure 3-7c). At 4 MPa normal stress,  $D_c$  decreases with increasing displacement and up-step velocity (velocity-step tests were performed at the same up-step velocity sequence in each experiment). At 7 (saturated), 10, and 20 MPa normal stress,  $D_c$  slightly increases or remains constant with up-step velocity. At 30 MPa normal stress, there is no general trend. Finally, on the dry sample sheared at 7 MPa,  $D_c$  decreases with increasing displacement and up-step velocity.

## 3.4.1.3. FRICTIONAL HEALING

Figure 7d shows the healing values ( $\Delta\mu$ ) versus holding times ( $t_h$ ). Healing values ranged between -0.006 and 0.02 (Table 3-2, Figure 3-7d). Saturated gouge samples sheared at  $\sigma_n > 10$  MPa show positive healing values and positive healing rates ( $\beta$ ). For example, at  $\sigma_n = 20$  MPa,  $\beta \approx 0.0012$  and at  $\sigma_n = 30$  and  $\sigma_n = 10$  MPa, the frictional healing rate is equal to  $\beta \approx 0.0018$ . The dry sample shows positive healing values ranging from 0.002 to 0.006 and a positive healing rate of about  $\beta \approx 0.013$ .

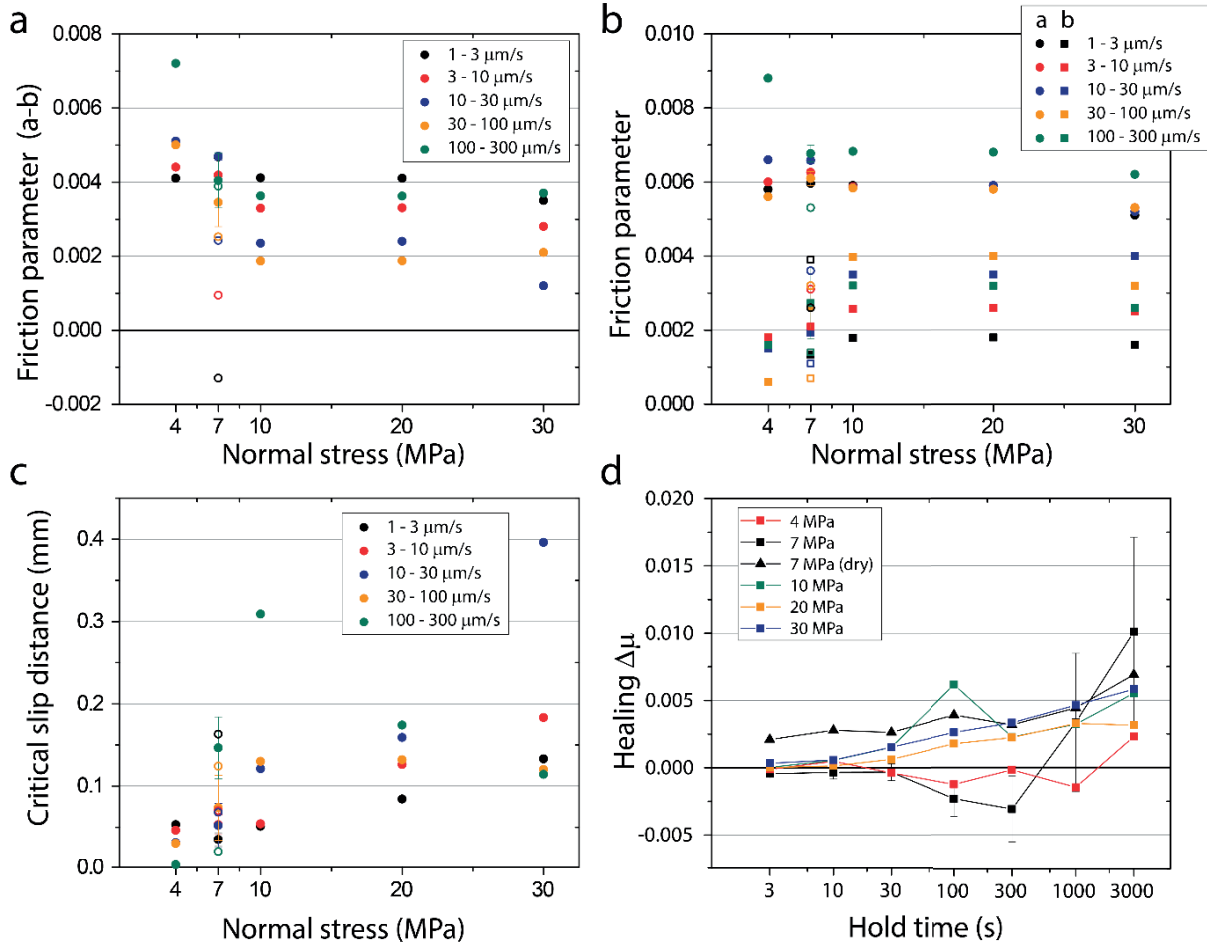


**Figure 3-7:** Friction rate parameters for simulated Opalinus clay gouge. A) Stability friction parameter ( $a - b$ ) versus normal stress. Gouge samples are characterized by a velocity-strengthening behavior meaning ( $a - b$ )  $> 0$ . The parameter ( $a - b$ ) decreased as normal stress increased and ( $a - b$ ) values are nearly close to 0. B) Evolution of the individual parameters  $a$  and  $b$  with normal stress. Parameters  $a$  and  $b$  are represented by a circle and a square respectively. Parameter  $b$  increased when normal stress increased. C) Critical slip distance  $D_c$  versus normal stress. D) The frictional healing parameter  $\Delta\mu$  versus hold time. Experiments were carried out at sliding velocity of 10  $\mu\text{m/s}$  and at different normal stress. Error bars denote the standard deviation of multiple tests and non-filled symbols referred to results on the dry sample.

Test	Moisture content	Normal Stress (MPa)	Pore pressure (MPa)	Initial porosities $\Phi$ (%)	Peak friction $\mu_{peak}$	Steady-state friction $\mu_{ss}$	Up-Step Velocity Steps (μm/s)	Friction parameter $a$	Friction parameter $b$	Friction parameter $(a - b)$	Critical Distance $D_c$ (mm)	Sequence of hold times (s)	Healing $\Delta\mu$
<b>i454</b>	Saturated at RH 100%	4	0	27.3	0.523	0.374	3	0.0058	0.0018	0.0041	0.053	3	-0.00013
							10	0.006	0.0018	0.0044	0.046	10	0.00049
							30	0.0066	0.0015	0.0051	0.031	30	-0.00039
							100	0.0056	0.0006	0.005	0.03	100	-0.00124
							300	0.0088	0.0016	0.0072	0.003	300	-0.00017
<b>i447</b>	Saturated at RH 100%	7	0	28.7	0.452	0.343						1000	-0.00146
												3000	0.0023
							3	0.006	0.0014	0.0047	0.043	3	-0.00021
							10	0.0063	0.0021	0.0042	0.065	10	-0.00011
							30	0.0065	0.002	0.0046	0.079	30	-0.00021
<b>i441</b>	Saturated at RH 100%	7	0	25.2	0.472	0.34	100	0.0059	0.0031	0.0028	0.113	100	-0.00126
							300	0.007	0.0037	0.0033	0.184	300	-0.00207
												1000	-0.00096
												3000	0.00549
							3	0.0059	0.0013	0.0047	0.027	3	-0.00058
<b>i442</b>	Saturated at RH 100%	7	0	27.0	0.474	0.342	10	0.0062	0.0020	0.0042	0.041	10	-0.00103
							30	0.0067	0.0019	0.0048	0.025	30	0.0004
							100	0.0063	0.0022	0.0041	0.034	100	-0.00153
							300	0.0065	0.0018	0.0048	0.109	300	-0.00072
												1000	0.01058
												3000	0.02003
							3	-	-	-	-	3	-0.00054
							10	-	-	-	-	10	0.00014
							30	-	-	-	-	30	-0.00115
							100	-	-	-	-	100	-0.00414
							300	-	-	-	-	300	-0.00644
												1000	0.00046
												3000	0.00475

Test	Moisture content	Normal Stress (MPa)	Pore pressure (MPa)	Initial porosities $\Phi$ (%)	Peak friction $\mu_{\text{peak}}$	Steady-state friction $\mu_{\text{ss}}$	Up-Step Velocity Steps ( $\mu\text{m/s}$ )	Friction parameter $a$	Friction parameter $b$	Friction parameter $(a - b)$	Critical Distance $D_c$ (mm)	Sequence of hold times (s)	Healing $\Delta\mu$
i440	Dry, RH 5%	7	0	27.5	0.572	0.502	3	0.0026	0.0039	-0.0013	0.163	3	0.0021
							10	0.0031	0.0021	0.0009	0.07	10	0.00278
							30	0.0036	0.0011	0.0024	0.068	30	0.00263
							100	0.0032	0.0007	0.0025	0.124	100	0.0039
							300	0.0053	0.0014	0.0039	0.02	300	0.00317
i443	Saturated at RH 100%	10	0	22.3	0.447	0.332						1000	0.00443
												3000	0.00691
							3	0.0059	0.0018	0.0041	0.0510	3	0.00003
							10	0.0059	0.0026	0.0033	0.0540	10	0.00055
							30	0.0058	0.0035	0.0023	0.1210	30	0.00152
i444	Saturated at RH 100%	20	0	23.0	0.354	0.311	100	0.0058	0.0040	0.0019	0.1300	100	0.00616
							300	0.0068	0.0032	0.0036	0.3090	300	0.00228
												1000	0.00323
												3000	0.00553
							3	0.0059	0.0018	0.0041	0.084	3	0.00002
i445	Saturated at RH 100%	30	0	22.9	0.335	0.298	10	0.0059	0.0026	0.0033	0.126	10	0.00014
							30	0.0059	0.0035	0.0024	0.159	30	0.00062
							100	0.0058	0.004	0.00187	0.132	100	0.00177
							300	0.0068	0.0032	0.00362	0.174	300	0.00222
												1000	0.00328
												3000	0.00314
							3	0.0051	0.0016	0.0035	0.133	3	0.00035
							10	0.0053	0.0025	0.0028	0.183	10	0.00058
							30	0.0052	0.004	0.0012	0.396	30	0.00152
							100	0.0053	0.0032	0.0021	0.12	100	0.00262
							300	0.0062	0.0026	0.0037	0.114	300	0.00333
												1000	0.00464
												3000	0.00582

Table 3-2: Frictional experiments parameters and data summary.



When normal stress is equal to 4 and 7 MPa, the healing value does not follow the classical log-linear fit but shows zero or negative healing values ( $\Delta\mu^-$ ) for hold times  $<300$  s and positive values ( $\Delta\mu^+$ ) for hold times  $>300$  s. To calculate the healing rate, we have separated the healing values into two regions considering a critical hold time  $t_h^*$  at 300 s. Then, we have computed a log-linear fit for the healing values contained in each region and we calculated two healing rates for the same experiment. For example, the sample sheared at 7 MPa shows a weakening rate  $\beta^{7\text{ MPa}}_1 \approx -0.00097$  for hold times  $< 300$  s and a positive healing rate of about  $\beta^{7\text{ MPa}}_2 \approx 0.007$  for hold times  $> 300$  s.

#### 3.4.1.4. EVOLUTION OF POROSITY AND SAMPLE THINNING.

Figure 3-8a shows the evolution of porosity ( $\phi_t$ ) during shearing. The initial porosity ( $\phi_o$ ) at the start of shearing is  $\sim 27\%$  for samples sheared at 4 and 7 MPa, and  $\sim 22\%$  for samples sheared at 10, 20, and 30 MPa. At the end of the experiments, porosity shows values of about 18% and 16% for the samples sheared at low (4,7 MPa) and high (10, 20, 30 MPa) normal stress, respectively. Accordingly, sample thinning ( $h$ ) is greater in samples sheared at 4 MPa ( $\Delta h_{4\text{ MPa}} \sim 1000 \mu\text{m}$ ) than in samples sheared at 30 MPa ( $\Delta h_{30\text{ MPa}} \sim 600 \mu\text{m}$ ) due to lower initial compaction of samples sheared at low normal stress.

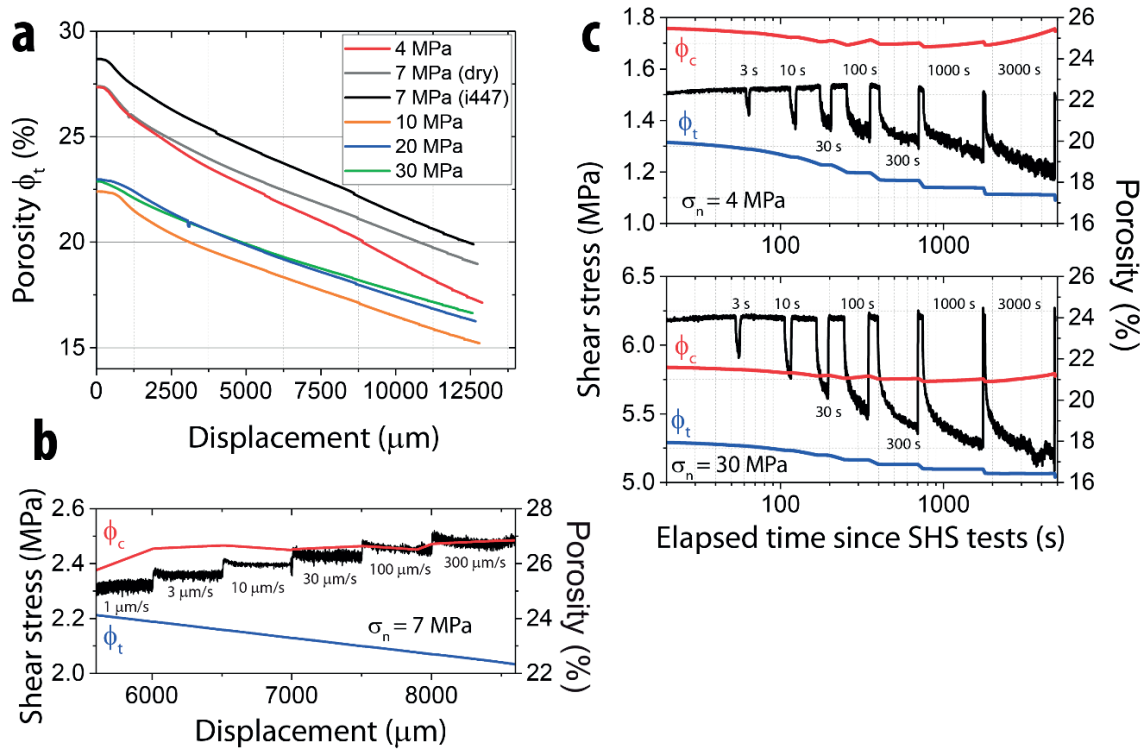


**Figure 3-8:** Evolution of porosity. A) Porosity ( $\phi_t$ ) versus shear displacement. On shearing,  $\phi_t$  monotonically decreases for all samples. The total porosity  $\phi_t$  decreases from  $\sim 27$  to  $\sim 17\%$  for sample sheared at 4 MPa, and from  $\sim 22\%$  to  $\sim 16\%$  for sample sheared at 30 MPa. B) Total and corrected porosity versus displacement during velocity-step tests for sample sheared at 7 MPa normal stress. C) Total and corrected porosity versus elapsed time since the beginning of slide-hold-slide tests (in logarithmic scale) for samples sheared at 4 and 30 MPa normal stress. Values of corrected porosity  $\phi_c$  were treated by removing the linear trend.

Following the procedure described in *Samuelson et al.*, (2009), we removed the linear thinning trend from the calculated gouge layer thickness and then, we determined a corrected value of porosity ( $\phi_c$ ). By doing so, we want to emphasize the instantaneous changes in porosity during shearing while analyzing dilation and consolidation during the tests.

During the velocity-step tests and based on the evolution of corrected porosity  $\phi_c$  (red curve), we observe either dilation or consolidation when increasing velocity, i.e. no correlation with the imposed sliding velocity (Figure 3-8b). During the slide-hold-slide tests and for all samples (Figure 3-8c), the porosity  $\phi_t$  (blue curve) shows consolidation during shearing and null dilation or consolidation during hold times. On the other hand, the corrected porosity  $\phi_c$  (red curve) slightly increases during hold times while it decreases during shearing. The latter is more evident for samples sheared at low normal stress (4 and 7 MPa), as the rate of the porosity changes (drop and recovery) is almost double.

### 3.4.2. MICROSTRUCTURAL OBSERVATIONS

In this section, we compare the microstructure of postmortem samples sheared at 7 MPa and 30 MPa (Figure 3-9) following the classification based on the scheme of *Logan et al.* (1992). The microstructure of the sample sheared at 7 MPa is characterized by the presence of R-shear planes and open cracks parallel to shear direction and orthogonal to the applied normal stress (Figure 3-9a). Within the Riedel shear bands, clays minerals surround calcite and quartz minerals and tend to be distributed sub-parallel to the R-shear planes (Figure 3-9c). In the same region, limited fracturing affects calcite grains (Figure 3-9e).

For experiments performed at 30 MPa normal stress, we observe pervasive R-shear planes, no apparent preferential orientation of cracks, and a grain-size reduction within the entire experimental fault (Figure 3-9b). Riedel shear planes are more numerous and tightly distributed at 30 MPa than at 7 MPa of normal stress (Logan et al., 1992). Here again, clay lamellae surrounds stronger grains, and they are also concentrated along R- shear planes (Figure 3-9d). The intragranular fracturing of calcite minerals is more pervasive in comparison to experiments at 7 MPa, and fractured grains are always surrounded by clay material (Figure 3-9f). We do not identify well-developed Y-planes in any of the tested samples.

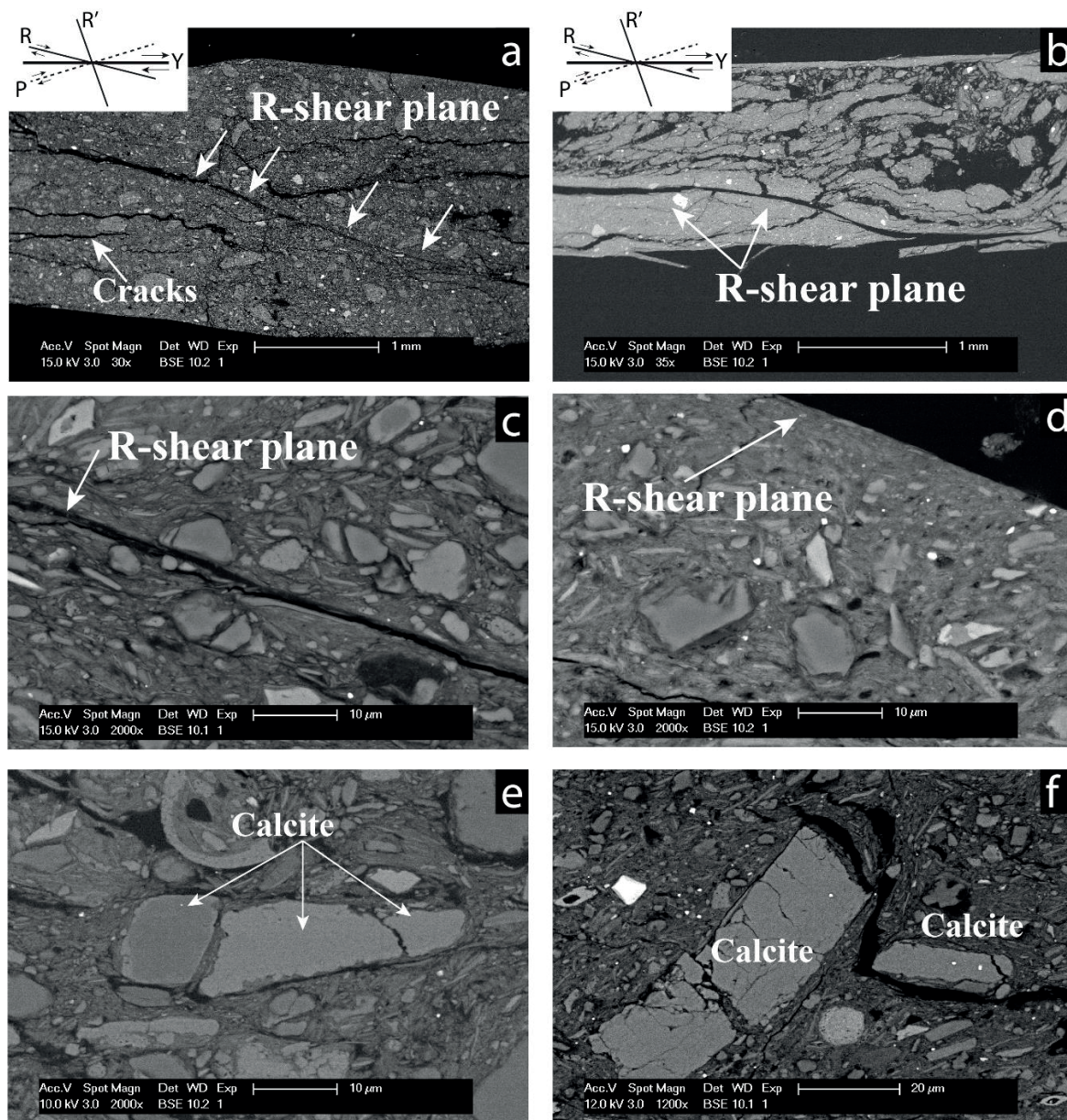


**Figure 3-9:** BSE images of post-mortem OPA samples. Shear direction is at the top of figures (a) and (b). The orientation of typical brittle fault zone is included. Images (a), (c), and (e) show sample sheared at 7 MPa normal stress. Images (b), (d), and (f) show sample sheared at 30 MPa normal stress. A) R-shear plane, weak foliation, development of cracks often aligned sub-parallel to the shear direction. B) R-shear plane on sample sheared at 30 MPa. Significant grain-size reduction within the entire experimental fault. C) Close-up of a Riedel shear plane. Note the clay alignment parallel to the R-shear plane. D) Detailed R-shear plane on sample sheared at 30 MPa. We observe a band of grain size reduction. Pictures (e) and (f) show intragranular cracks in calcite minerals. The penetrative clays in the cracks suggest that microcracking occurred during deformation. Photos also show how clays flow around stiffer fragments such as calcite and quartz.



## 3.5. DISCUSSION

### 3.5.1. FAULT STRENGTH

While the peak friction values ( $\mu_{peak}$ ) of OPA range from 0.33 to 0.52 (Figure 3-6a, Equation 3-1), the coefficients of peak friction for cohesive surfaces ( $\mu_f^p$ ) range from 0.23 to 0.30 (Figure 3-6c, Equation 3-2). In both cases, the results suggest the OPA fault gouges are weak compared to the Byerlee's rule (Byerlee, 1978).

Figure 3-10 shows a second comparison of peak friction values (calculated as  $\mu = \frac{\tau}{\sigma_n}$ ), where the values of frictional strength of OPA are in concordance with other kaolinite-rich samples that have similar clay content (Behnsen & Faulkner, 2012; Bos et al., 2000; Crawford et al., 2008).

In terms of fault reactivation, unfortunately, *Fang et al.*, (2017) have performed just one test, thus comparison is difficult. However, their results for Opalinus Clay at 3 MPa on intact material are in agreement with the trend of our results.

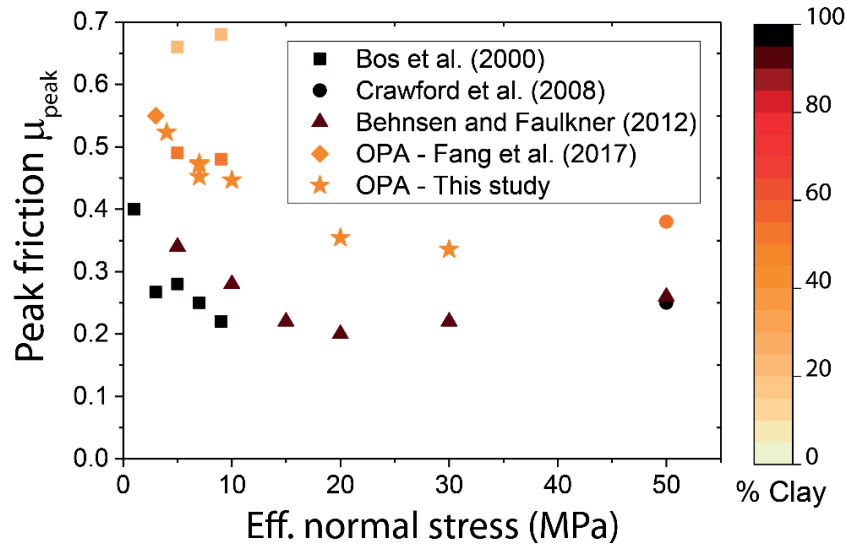


**Figure 3-10:** Comparison of the peak coefficient of friction as a function of effective normal stress for different kaolinite-rich clay gouges.

### 3.5.2. VARIATION OF FRICTION WITH NORMAL STRESS.

In our experiments, we observe a reduction in peak friction ( $\mu_{peak}$ ), from 0.52 to 0.34, and steady-state friction ( $\mu_{ss}$ ), from 0.37 to 0.29 with increasing normal stress from 4 to 30 MPa (Figure 3-6a). This similar behavior has already been observed in direct shear tests on other types of clay-rich samples, such as Ca-smectite and illite/smectite gouges (Ikari et al., 2007; Saffer et al., 2001; Saffer & Marone, 2003). In the same configuration, *Numelin et al.* (2007) reported a decrease of ~50 % of the peak friction coefficient from normal stress of 5

MPa to 100 MPa in samples containing >50% clay content (smectite/illite -32%, muscovite -25%). Similarly, *Behnken and Faulkner* (2012) have reported saw-cut tests where peak friction coefficients decrease with increasing normal stress for several phyllosilicates gouges. Among them, kaolinite-rich gouges experienced a reduction of peak friction from 0.35 to 0.25 when sheared at 5 and 50 MPa normal stress respectively (Figure 3-10).

Different processes have been evoked to explain the decrease of friction with increasing normal stress. For instance, *Saffer and Marone* (2003) have argued the possibility of water flowing into pore spaces resulting in undetected high pore pressures during the experiment. A second hypothesis presented by the same authors referred to a progressive increase of contact area between grains with increasing normal stress until a constant value of contact area at higher stress (> 40 MPa). *Behnken and Faulkner* (2012) have suggested consolidation and squeezing of water, promoting mineral to mineral contact due to a reduction in pore space. In addition, the same authors discussed about the role of gouge “cohesion” as a speculative explanation for an overestimation of friction at low normal stress ( $\sigma_n < 20$  MPa).

We have tested the “cohesion” hypothesis, so we have calculated both the friction coefficient ( $\mu$ ) and the friction coefficient for cohesive surface  $\mu_f$  (Figure 3-6c, Equation 3-2). The steady-state coefficients of friction  $\mu_f^{ss}$  do not vary with normal stress confirming that gouge “cohesion” produce an apparent increase in friction at low normal stress. However, the coefficients of friction at peak strength  $\mu_f^p$  depend on normal stress (Figure 3-6c). Therefore, gouge “cohesion” can only partially explain the decrease of the (Amonton’s) friction coefficient with increasing normal stress (Figure 3-6a).

Based on our results, we suggest that this dependency is the result of 1) the different initial porosities and 2) the amount of consolidation experienced during shearing (Figure 3-8a). Before shearing, saturated samples compacted at high normal stress (20 and 30 MPa) have lower porosity (low water content) compared with samples compacted at lower normal stresses (4, 7 MPa). Indeed, before shearing, samples had different initial thickness because of compaction at various normal stresses: ~2.7 mm on average for samples sheared at 4 and 7 MPa, and ~2.25 mm on average for samples sheared at > 10 MPa. Accordingly, initial porosities for samples sheared at 4 and 7 MPa are of about ~27, whilst ~22% for samples sheared at 10, 20, and 30 MPa. Our values are in agreement with oedometric tests of powdered Opalinus Clay (Favero et al., 2016). Moreover, Figure 3-4 shows different slopes during the quasi-linear loading of the samples, posing a correlation between stiffer samples, i.e. steeper slopes, and low porosity samples (Figure 3-8c).

High porosity samples (4 and 7 MPa) are less dense and grains more spaced and will therefore, deform to large strains without pervasive fracturing as shown in the microstructures (Figure 3-9a). Thus, grains will tend to easily slide over each other and rotate (Figure 3-9c). Moreover, limited grain size reduction will take place as observed in our microstructures. On the other hand, low porosity samples (>10 MPa) might have a smaller pore structure and the sample will have to dilate or grains will have to crack in order for movement to occur (Figure 3-9f). Thus,

pervasive cataclasis will take place, including grains size reduction, micro-cracking, a higher number and more well-developed Riedel planes as observed in sample sheared at 30 MPa normal stress (Figure 3-9b).

Finally, based on microstructures and mechanical data, we suggest a transition in the relative importance of the shear deformation mechanisms operating over the whole range of normal stress. The transition occurs at normal stresses higher than 10 MPa (Figure 3-6) as a result of a change in mechanical behavior from deformation, mainly accommodated by frictional sliding (grain sliding, rotation and translation of minerals) and minor fracturing within the clay matrix (at low normal stress < 10 MPa), to a combination of frictional sliding and strong fracturing (at high normal stress > 10 MPa).

### 3.5.3. INFLUENCE OF WATER ON FRICTIONAL STRENGTH

The peak friction coefficient for dry OPA is 0.57, while for the wet samples sheared at the same normal stress (7 MPa), it is about 0.47. Similarly, previous experiments comparing dry versus saturated friction show higher friction values for dry samples than for saturated samples (Behnsen & Faulkner, 2012; Crawford et al., 2008; Moore & Lockner, 2004). Because of the sheet-structure of clays minerals, platy phyllosilicates separated by water layers may allow shear to be concentrated within the water layers, which results in a substantial decrease of friction coefficient (Moore & Lockner, 2004). Thus, friction might increase with the total loss of water between mineral surfaces, and the upper limit of frictional strength of phyllosilicate gouges would be the strength of each mineral under dry conditions (Behnsen & Faulkner, 2012). The tendency to adsorb water has been attributed to 1) surface charge, i.e. hydrophilic versus hydrophobic surfaces, 2) the chemistry and pH of the water, and 3) pressure-temperature conditions (Morrow et al., 2000).

We have performed dry (5% RH) and saturated (100% RH) experiments at 7 MPa of normal stress at the same pressure and temperature conditions. Therefore, we suggest that the reduction of frictional strength can only be explained by the different surface charge capacities of the clays minerals of OPA (kaolinite, chlorite, mica, and illite/smectite). A detailed analysis of the contribution of each clay is out of the scope of this paper.

### 3.5.4. FAULT STABILITY

The frictional rate parameter ( $a-b$ ) of OPA, that ranges between 0.0012 to 0.0072, shows similar values when compared to other types of rocks with > 40 wt% clays (Ikari et al., 2009; Kohli & Zoback, 2013; Numelin et al., 2007; Tembe et al., 2010). At 25 MPa normal stress, experiments on natural samples containing kaolinite (25% chlorite + kaolinite) taken from the Northeast Boundary Fault (San Andres Fault), have shown a velocity-strengthening regime with values of ( $a-b$ ) of about 0.004 – 0.0055 (Carpenter et al., 2015). Similarly, the friction parameter ( $a-b$ ) of OPA indicates same velocity-strengthening regime but with slightly lower values ranging from 0.012 to 0.0041 at both 20 and 30 MPa.



The friction parameters ( $a$ - $b$ ) decrease as normal stress increases (Figure 3-7a). In particular, in our experiments, ( $a$ - $b$ ) decreases with increasing normal stress as result of the increase in the friction rate parameter  $b$  and constant values of friction parameter  $a$  (Figure 3-7b). On saturated samples, no transition from velocity strengthening to velocity weakening is observed as well as no clear dependency on sliding velocity.

The direct effect  $a$  is interpreted as the effect of loading rate on asperity strength with relatively constant contact area (Paterson & Wong, 2005). Despite difficulties to account for a physical interpretation of this value, dilation has been found to have a partial correlation to the magnitude of the parameter  $a$  (Scholz, 2002). In our experiments, the friction parameter  $a$  is constant with respect to normal stress (Figure 3-7b), and we do not observe an apparent dependency on the sliding velocities. Thus, we do not observe any apparent correlation between dilation and  $a$ .

The evolution of the parameter  $b$  can be interpreted as the changes in asperities contact sizes due to the changes in strength during the lifetime of an asperity i.e. a decrease in contact area upon a change (increase) in sliding velocity (Niemeijer et al., 2010; Paterson & Wong, 2005; Scholz, 2002). The critical slip distance  $D_c$  is the slip required to replace an entire population of asperity contacts; thus the memory of prior state is removed (Paterson & Wong, 2005).

At the same normal stress, we do not observe an explicit dependency of parameter  $b$  with increasing up-step sliding velocities (Figure 3-7b), suggesting that contact area does not strongly change after variations in a velocity step. On the other hand, the increase of  $b$  values with normal stress (<10 MPa) might be explained by the lower porosities and the lower state of localization in samples sheared at 4 and 7 MPa, as indicated by the values initial porosity (Figure 3-8a) and the microstructures of those samples (Figure 3-9). At normal stress higher than 10 MPa,  $b$  values are relatively constant (0.002 - 0.004) and do not change with increasing normal stress. This behavior is in agreement with the evolution of critical slip distance  $D_c$  (Figure 3-7c).

### 3.5.5. FAULT HEALING

Frictional healing is a time and slip-dependent mechanism related to fault strengthening between inter-seismic periods. Frictional healing depends on the mechanical and physicochemical processes at asperity contacts based on factors such as temperature, pressure, porosity, grain size distribution, and shape (Marone, 1998; Niemeijer et al., 2008; Renard et al., 2012; Yasuhara et al., 2005). Under quasi-stationary contact, the static coefficient of friction increases with time, and this time-dependent strengthening or ageing effect is characterized by the healing rate  $\beta$  (Equation 3-6) (Paterson & Wong, 2005).

Among fault rocks, phyllosilicates are characterized by their small healing values ( $\Delta\mu$ ) and healing rates ( $\beta$ ) (Bos et al., 2000; Carpenter et al., 2016; Haines et al., 2014) when compared to other granular materials such as quartz or calcite-rich rocks.

During our slide-hold-slide tests, we have calculated values of healing ( $\Delta\mu$ ) very close to zero (Figure 3-7d), i.e. a negligible re-strengthening after quasi-stationary contact (i.e. hold period) and small healing rates ( $\beta$ ). This lack fault re-strengthening has, indeed, important implications to the slip behavior of this fault. As the fault will not be able to regain its strength (or part of it) during the inter-seismic periods, the fault will not slide seismically, therefore resulting in long-term stable fault creeping. Our results are in concordance with the idea that clay minerals may act as inhibitors to contact strengthening (Bos & Spiers, 2000; Niemeijer & Spiers, 2006) and with previous work reported on clay-rich gouges (Carpenter et al., 2011; Chen et al., 2015; Tesei et al., 2012).

When samples were sheared at  $\sigma_n > 10$  MPa, frictional healing values remained constantly positive (Figure 3-7d) and are linearly proportional to the logarithm of time. However, samples sheared at 4 and 7 MPa normal stress reveals a “parabolic” frictional healing transition, from negative ( $\Delta\mu^-$ ) to positive ( $\Delta\mu^+$ ) healing values.

To better constrain our results, we have performed an additional experiment to explore the role of water in healing properties of Opalinus Clay gouge. We have carried out an additional test at 7 MPa normal stress, following the same experimental procedure described before, but under controlled dry conditions (5% RH). Contrary to wet samples, dry OPA shows only a positive frictional healing rate ( $\beta_{dry} \approx 0.0013$ ), revealing the importance of water on the healing behavior of OPA.

We therefore propose a mechanism where water-filling pores may experience local overpressure because of compaction of the gouges when sliding resumes after the short hold times ( $< 300$  s). Because there is no time for water diffusion to occur, probably helped by some low permeability of the material, undrained re-shearing will raise up pore pressure decreasing effective normal stress resulting in null or negative frictional healing.

For longer holding times ( $> 300$  s), water may be expelled, thus preventing the attainment of fluid overpressure and leading to re-strengthening (positive healing rates) as we observe. Because initial sample compaction is lower at low rather than at high normal stress (see Figure 3-8a), the expulsion of water might be stronger just in samples sheared at 4 and 7 MPa normal stress, as they are more likely to further compact during shearing.

Based on a simple form, we estimate the time constant (H. Wang, 2000) for water diffusion  $t_d \approx \frac{L^2}{4c}$ , where  $c$  ( $\frac{mm^2}{s}$ ) is the hydraulic diffusivity and  $L$  the maximum path length (mm). We deduced values of powdered Opalinus Clay, i.e. crushed and then molded, for the hydraulic diffusivity at different normal stress (Favero et al., 2016). We calculated  $t_d$  using  $L = 25$  mm, the maximum path length of diffusion (half length of the samples). Values of hydraulic diffusivity decreased from 0.23 to 0.12 mm<sup>2</sup>/s as long normal stresses increased. Then, we found  $t_d \approx 700$  s for samples sheared at 4 and 7 MPa normal stress (Figure 3-8b). The previous analysis is consistent with the hold times  $t_h^* = 300$ s presented in the results section. Since we used the maximum length of the fluid path, these values correspond to maximum

diffusion times during hold times. Considering the uncertainty in both diffusion coefficient and the actual diffusion path length, this calculation suggests that water diffusion promoting frictional strengthening is keen to play a role in the observed healing behavior.

However, if local overpressures played a role upon re-shearing during slide hold slide tests, it will also affect the results of the velocity steps. In particular, it will affect the results during sliding at faster up-step velocities ( $>30 \mu\text{m/s}$ ) when pore water has absolutely no time to diffuse ( $t \approx 2$  seconds for up-step velocity of  $300 \mu\text{m/s}$ ). However, we have not observed any correlation of the friction parameter ( $a-b$ ) with respect to up-step velocity (Figure 3-7a), suggesting that local fluid overpressure is not a very active process during velocity-steps and maybe it is not the only one acting during the frictional healing of OPA.

A second hypothesis we suggest is a competition between two mechanisms: consolidation and the creation of local swelling pressures. The global trend of porosity ( $\phi_t$ ) indicates that samples compacted on shearing (Figure 3-8a) during our experiments. In particular, during slide-hold-slide tests, samples experienced compaction on shearing and null dilation during hold times (Figure 3-8c). However, when we removed the linear trend from the total porosity calculations, we do observe a small influence of dilation. Despite dilation is minimum in our tests, it appears more marked in samples sheared at 4 and 7 MPa than in samples sheared at 10, 20, and 30 MPa. Indeed, the higher rate of porosity ( $\phi_c$ ) changes of sample sheared at low normal stress is in concordance with this observation (Figure 3-8c).

Following our argument, we assume that the dilation experienced by our samples may correspond to local swelling pressures of some clay minerals that operates at different rates with respect to normal stress. Because swelling pressures of OPA are up to  $\sim 6$  MPa (C. L. Zhang et al., 2010), its effect will be more significant for samples sheared at low normal stress, (4,7 MPa) than at high normal stress (10, 20, and 30 MPa). Thus at low normal stress, a strong competition between shear consolidation and swelling pressures takes place, but swelling pressures plays a more important role, being responsible for the reduction in frictional strength i.e. negative healing values, observed in our samples. For hold times  $> 300$  s, consolidation (as observed in the total porosity  $\phi_t$ ) leads to densification of the samples, requiring dilation upon re-shearing promoting the re-strengthening of the samples. For samples sheared at high normal stress, dilation is null, so if swelling pressures operate, their effect is negligible.

A third hypothesis we propose is that water has a mechanical lubricating effect preventing the re-strengthening of OPA (Behnsen & Faulkner, 2012; Moore & Lockner, 2004; Morrow et al., 2000; Renard et al., 2012). In the saturated gouges, water forms a thin film in proportion to the surface energy properties of the clays (Moore & Lockner, 2004), but also, as a function of contact normal stress, salinity, and temperature (Renard & Ortoleva, 1997). Indeed, the water film thickness at grain to grain contacts decreases with increasing normal load (Renard & Ortoleva, 1997), supporting the observations in our tests that the healing behavior is also function of normal stress. The latter is also consistent with the fact that samples sheared at low normal stress have a higher porosity than samples sheared at 10, 20, and 30 MPa. As in the

second hypothesis, for hold times  $> 300$  s, the increase of packing density controls the re-strengthening of the samples.

Although these weakening mechanism are a reasonable explanation for the healing behavior experienced by our samples, other mechanisms affecting friction are also possible. Some of them could be the relative electrochemical effect of the other clays (smectite, chlorite, illite) presented in OPA (Behnsen & Faulkner, 2012; Morrow et al., 2000), disjoining pressures (Gonçalvès et al., 2010), saturation of contact area (Ikari et al., 2009), pressure solution (Yasuhara et al., 2005; X. Zhang et al., 2010), thermal expansion by local temperature increase (even though room temperature was constant), a combination of two or more of the previous mechanism, etc. the future, dedicated experiments to understand this negative healing behavior will be performed by varying the viscosity and the chemistry of the fluid.

### 3.5.6. IMPLICATIONS FOR NUCLEAR WASTE STORAGE

Our experiments on fault gouge derived from the Opalinus Clay formation document a very low frictional strength at different normal stress (4 – 30 MPa). As normal stress increases, the associated mechanical deformation mechanism evolves from deformation mainly accommodated by frictional sliding and minor (at low normal stress  $< 10$  MPa) to major and pervasive fracturing (at high normal stress  $> 10$  MPa).

A key observation of this study is that upon fault reactivation, the velocity-strengthening behavior observed at different normal stress suggests stable sliding as the most likely fault slip-behavior. In addition, our results indicate that the healing behavior of the fault is dominated by a lack of re-strengthening during inter-seismic periods. Therefore, we propose that if a fault system within the Opalinus Clay formation re-activates (at the hypothetical boundary conditions for a nuclear waste repository: conditions imposed during experiments, i.e. crustal depth of 150-1000 m and no fluid pressure), it will re-activate within the aseismic regime and earthquakes might be difficult to nucleate. Moreover, the absence of long-term inter-seismic healing will prevent the fault from re-gaining fault strength, resulting in stable fault creeping. Even though our previous results suggest aseismic creep, departures from this behavior can be induced by 1) the attainment of fluid overpressure that can change the frictional rheology of the fault (Scuderi & Collettini, 2016), 2) co-seismic slip if a dynamic rupture from a large earthquake propagates onto saturated clay-rich faults (Bullock et al., 2015; Faulkner et al., 2011), and 3) an abrupt perturbation of the surrounding stress field caused by natural or anthropogenic operations (Perfettini & Ampuero, 2008).

## 3.6. CONCLUSIONS

We have systematically tested the frictional behavior of water saturated Opalinus Clay formation performing double-direct shear experiments at normal stress ranging from 4 to 30 MPa and sliding velocity between 1 and 300  $\mu\text{m/s}$ . Slide hold slide tests (1-3000 s) have been carried out to analyze the healing capacity of fault in OPA formation. Our results indicate:

- Very low peak and steady-state friction
- Moderate slip weakening at normal stress lower than 10 MPa.
- Velocity-strengthening behavior at all normal stresses, with the friction rate parameter ( $a-b$ ) that decreases increasing normal stress,
- Almost zero healing values at different hold periods and normal stresses

These results suggest that OPA faults are mechanically weak and due to the low frictional healing they remain weak in the long term. Moreover, our results suggest that faults within the Opalinus Clay formation, can be easily reactivated during stress and hydro mechanical perturbations, predominantly with aseismic creep as inferred by the velocity strengthening behavior of the fault rocks and the lack of re-strengthening during inter-seismic periods.

Our results also reveal conditions for potential frictional slip instability at very shallow depths (~150 m), as the mechanical behavior of the fault system presents moderate evidence of slip weakening behavior. In the framework of deep geological disposal in clay formations, the most promising option for deep geological nuclear waste storage, our results indicate that stable slip within the fault structure is the most likely slip behavior. However, the interaction of the fault behavior with anthropogenic operations put the long-term safety into question due to reactivation during stress and hydro-mechanical perturbations.

## 3.7. REFERENCES

- Behnsen, J., & Faulkner, D. (2012). The effect of mineralogy and effective normal stress on frictional strength of sheet silicates. *Journal of Structural Geology*, 42, 49–61. <https://doi.org/10.1016/j.jsg.2012.06.015>
- Bird, P. (1984). Hydration-phase diagrams and friction of montmorillonite under laboratory and geologic conditions, with implications for shale compaction, slope stability, and strength of fault gouge. *Tectonophysics*, 107(3–4), 235–260. [https://doi.org/10.1016/0040-1951\(84\)90253-1](https://doi.org/10.1016/0040-1951(84)90253-1)
- Bock, H., Dehandschutter, B., Martin, C. D., Mazurek, M., De Haller, A., Skoczylas, F., & Davy, C. (2010). *Seal-sealing of fractures in argillaceous formations in the context of geological disposal of radioactive waste: Review and Synthesis. Nuclear Waste Management*.
- Bos, B., & Spiers, C. (2000). Effect of phyllosilicates on fluid-assisted healing of gouge-bearing faults. *Earth and Planetary Science Letters*, 184(1), 199–210. [https://doi.org/10.1016/S0012-821X\(00\)00304-6](https://doi.org/10.1016/S0012-821X(00)00304-6)
- Bos, B., Peach, C. J., & Spiers, C. (2000). Frictional-viscous flow of simulated fault gouge caused by the combined effects of phyllosilicates and pressure solution. *Tectonophysics*, 327(3–4), 173–194. [https://doi.org/10.1016/S0040-1951\(00\)00168-2](https://doi.org/10.1016/S0040-1951(00)00168-2)
- Bossart, P., Bernier, F., Birkholzer, J., Bruggeman, C., Connolly, P., Dewonck, S., et al. (2017). Mont Terri rock laboratory, 20 years of research: introduction, site characteristics and overview of experiments. *Swiss Journal of Geosciences*, 110(1), 3–22. <https://doi.org/10.1007/s00015-016-0236-1>
- Brantut, N., Schubnel, A., Rouzaud, J. N., Brunet, F., & Shimamoto, T. (2008). High-velocity frictional properties of a clay-bearing fault gouge and implications for earthquake mechanics. *Journal of Geophysical Research: Solid Earth*, 113(10), 1–18. <https://doi.org/10.1029/2007JB005551>
- Bullock, R., De Paola, N., & Holdsworth, R. (2015). An experimental investigation into the role of phyllosilicate content on earthquake propagation during seismic slip in carbonate faults. *Journal of Geophysical Research: Solid Earth*, 120(5), 3187–3207. <https://doi.org/10.1002/2015JB011914>
- Byerlee, J. D. (1978). Friction of rocks. *Pure and Applied Geophysics*, 116(4–5), 615–626. <https://doi.org/10.1007/BF00876528>
- Carpenter, B., Marone, C., & Saffer, D. (2011). Weakness of the San Andreas Fault revealed by samples from the active fault zone. *Nature Geoscience*, 4(4), 251–254. <https://doi.org/10.1038/ngeo1089>
- Carpenter, B., Saffer, D., & Marone, C. (2015). Frictional properties of the active San Andreas Fault at SAFOD: Implications for fault strength and slip behavior. *Journal of Geophysical Research: Solid Earth*, 120(7), 5273–5289. <https://doi.org/10.1002/2015JB011963>
- Carpenter, B., Ikari, M. J., & Marone, C. (2016). Laboratory observations of time-dependent



- frictional strengthening and stress relaxation in natural and synthetic fault gouges. *Journal of Geophysical Research: Solid Earth*, 121(2), 1183–1201. <https://doi.org/10.1002/2015JB012136>
- Chen, J., Verberne, B., & Spiers, C. (2015). Effects of healing on the seismogenic potential of carbonate fault rocks: Experiments on samples from the Longmenshan Fault, Sichuan, China. *Journal of Geophysical Research: Solid Earth*, 120(8), 5479–5506. <https://doi.org/10.1002/2015JB012051>
- Collettini, C., Di Stefano, G., Carpenter, B., Scarlato, P., Tesei, T., Mollo, S., et al. (2014). A novel and versatile apparatus for brittle rock deformation. *International Journal of Rock Mechanics and Mining Sciences*, 66, 114–123. <https://doi.org/10.1016/j.ijrmms.2013.12.005>
- Crawford, B. R., Faulkner, D., & Rutter, E. (2008). Strength, porosity, and permeability development during hydrostatic and shear loading of synthetic quartz-clay fault gouge. *Journal of Geophysical Research: Solid Earth*, 113(3), 1–14. <https://doi.org/10.1029/2006JB004634>
- Dieterich, J. H. (1979). Modeling of rock friction: 1. Experimental results and constitutive equations. *Journal of Geophysical Research*, 84(9), 2161–2168. <https://doi.org/10.1007/BF00876539>
- Fang, Y., Elsworth, D., Wang, C., Ishibashi, T., & Fitts, J. P. (2017). Frictional stability-permeability relationships for fractures in shales. *Journal of Geophysical Research: Solid Earth*, 122(3), 1760–1776. <https://doi.org/10.1002/2016JB013435>
- Faulkner, D., Mitchell, T. M., Behnsen, J., Hirose, T., & Shimamoto, T. (2011). Stuck in the mud? Earthquake nucleation and propagation through accretionary forearcs. *Geophysical Research Letters*, 38(18), 1–5. <https://doi.org/10.1029/2011GL048552>
- Favero, V., Ferrari, A., & Laloui, L. (2016). On the hydro-mechanical behaviour of remoulded and natural Opalinus Clay shale. *Engineering Geology*, 208, 128–135. <https://doi.org/10.1016/j.enggeo.2016.04.030>
- Gonçalvès, J., Rousseau-Gueutin, P., De Marsily, G., Cosenza, P., & Violette, S. (2010). What is the significance of pore pressure in a saturated shale layer? *Water Resources Research*, 46(4), 1–16. <https://doi.org/10.1029/2009WR008090>
- Haines, S., Marone, C., & Saffer, D. (2014). Frictional properties of low-angle normal fault gouges and implications for low-angle normal fault slip. *Earth and Planetary Science Letters*, 408, 57–65. <https://doi.org/10.1016/j.epsl.2014.09.034>
- Hashash, Y. M. A., Hook, J. J., Schmidt, B., & I-Chiang Yao, J. (2001). Seismic design and analysis of underground structures. *Tunnelling and Underground Space Technology*, 16(4), 247–293. [https://doi.org/10.1016/S0886-7798\(01\)00051-7](https://doi.org/10.1016/S0886-7798(01)00051-7)
- Ikari, M. J., Saffer, D., & Marone, C. (2007). Effect of hydration state on the frictional properties of montmorillonite-based fault gouge. *Journal of Geophysical Research: Solid Earth*, 112(6), 1–12. <https://doi.org/10.1029/2006JB004748>
- Ikari, M. J., Saffer, D., & Marone, C. (2009). Frictional and hydrologic properties of clay-rich

- fault gouge. *Journal of Geophysical Research: Solid Earth*, 114(5), 1–18. <https://doi.org/10.1029/2008JB006089>
- Ikari, M. J., Marone, C., & Saffer, D. (2011). On the relation between fault strength and frictional stability. *Geology*, 39(1), 83–86. <https://doi.org/10.1130/G31416.1>
- Klinkenberg, M., Kaufhold, S., Dohrmann, R., & Siegesmund, S. (2009). Influence of carbonate microfabrics on the failure strength of claystones. *Engineering Geology*, 107(1–2), 42–54. <https://doi.org/10.1016/j.enggeo.2009.04.001>
- Kohli, A. H., & Zoback, M. D. (2013). Frictional properties of shale reservoir rocks. *Journal of Geophysical Research: Solid Earth*, 118(9), 5109–5125. <https://doi.org/10.1002/jgrb.50346>
- Kübler, B. (1987). Cristallinité de l'illite, méthodes normalisées de préparations, méthodes normalisées de mesures. In *Cahiers de l'Institut de Géologie de Neuchâtel, Série ADX* (Vol. 1, p. 13).
- Laurich, B., Urai, J. L., Desbois, G., Vollmer, C., & Nussbaum, C. (2014). Microstructural evolution of an incipient fault zone in Opalinus Clay: Insights from an optical and electron microscopic study of ion-beam polished samples from the Main Fault in the Mt-Terri Underground Research Laboratory. *Journal of Structural Geology*, 67(PA), 107–128. <https://doi.org/10.1016/j.jsg.2014.07.014>
- Lockner, D. A., & Beeler, N. M. (2002). *Rock failure and earthquakes. International Geophysics* (Vol. 81). [https://doi.org/10.1016/S0074-6142\(02\)80235-2](https://doi.org/10.1016/S0074-6142(02)80235-2)
- Logan, J. M., Dengo, C. A., Higgs, N. G., & Wang, Z. Z. (1992). Fabrics of Experimental Fault Zones: Their Development and Relationship to Mechanical Behavior. In *International Geophysics* (Vol. 51, pp. 33–67). [https://doi.org/10.1016/S0074-6142\(08\)62814-4](https://doi.org/10.1016/S0074-6142(08)62814-4)
- Marone, C. (1998). Laboratory-Derived Friction Laws and Their Application To Seismic Faulting. *Annual Review of Earth and Planetary Sciences*, 26(1), 643–696. <https://doi.org/10.1146/annurev.earth.26.1.643>
- Moore, D., & Lockner, D. A. (2004). Crystallographic controls on the frictional behavior of dry and water-saturated sheet structure minerals. *Journal of Geophysical Research*, 109(B3), B03401. <https://doi.org/10.1029/2003JB002582>
- Morrow, C., Moore, D., & Lockner, D. A. (2000). The effect of mineral bond strength and adsorbed water on fault gouge frictional strength. *Geophysical Research Letters*, 27(6), 815–818. <https://doi.org/10.1029/1999GL008401>
- Niemeijer, A., & Collettini, C. (2013). Frictional Properties of a Low-Angle Normal Fault Under In Situ Conditions: Thermally-Activated Velocity Weakening. *Pure and Applied Geophysics*, 171(10), 2641–2664. <https://doi.org/10.1007/s00024-013-0759-6>
- Niemeijer, A., & Spiers, C. (2006). Velocity dependence of strength and healing behaviour in simulated phyllosilicate-bearing fault gouge. *Tectonophysics*, 427(1–4), 231–253. <https://doi.org/10.1016/j.tecto.2006.03.048>
- Niemeijer, A., Marone, C., & Elsworth, D. (2008). Healing of simulated fault gouges aided by

- pressure solution: Results from rock analogue experiments. *Journal of Geophysical Research: Solid Earth*, 113(4), 1–15. <https://doi.org/10.1029/2007JB005376>
- Niemeijer, A., Marone, C., & Elsworth, D. (2010). Frictional strength and strain weakening in simulated fault gouge: Competition between geometrical weakening and chemical strengthening. *Journal of Geophysical Research: Solid Earth*, 115(10), 1–16. <https://doi.org/10.1029/2009JB000838>
- Numelin, T., Marone, C., & Kirby, E. (2007). Frictional properties of natural fault gouge from a low-angle normal fault, Panamint Valley, California. *Tectonics*, 26(2), n/a-n/a. <https://doi.org/10.1029/2005TC001916>
- Nussbaum, C., Bossart, P., Amann, F., & Aubourg, C. (2011). Analysis of tectonic structures and excavation induced fractures in the Opalinus Clay, Mont Terri underground rock laboratory (Switzerland). *Swiss Journal of Geosciences*, 104(2), 187–210. <https://doi.org/10.1007/s00015-011-0070-4>
- Passchier, C. W., & Trouw, R. R. A. J. (2005). *Microtectonics*. *Microtectonics*. <https://doi.org/10.1007/978-3-662-08734-3>
- Paterson, M. S., & Wong, T. F. (2005). *Experimental rock deformation - The brittle field* (2nd ed.). Springer-Verlag Berlin Heidelberg. <https://doi.org/10.1007/b137431>
- Perfettini, H., & Ampuero, J. P. (2008). Dynamics of a velocity strengthening fault region: Implications for slow earthquakes and postseismic slip. *Journal of Geophysical Research: Solid Earth*, 113(9), 1–22. <https://doi.org/10.1029/2007JB005398>
- Popp, T., Salzer, K., & Minkley, W. (2008). Influence of bedding planes to EDZ-evolution and the coupled HM properties of Opalinus Clay. *Physics and Chemistry of the Earth*, 33(SUPPL. 1), 374–387. <https://doi.org/10.1016/j.pce.2008.10.018>
- Rabinowicz, E. (1951). The nature of the static and kinetic coefficients of friction. *Journal of Applied Physics*, 22(11), 1373–1379. <https://doi.org/10.1063/1.1699869>
- Reinen, L. A., & Weeks, J. D. (1993). Determination of rock friction constitutive parameters using an iterative least squares inversion method. *Journal of Geophysical Research*, 98(B9), 15937. <https://doi.org/10.1029/93JB00780>
- Renard, F., & Ortoleva, P. (1997). Water films at grain-grain contacts: Debye-Hückel, osmotic model of stress, salinity, and mineralogy dependence. *Geochimica et Cosmochimica Acta*, 61(10), 1963–1970. [https://doi.org/10.1016/S0016-7037\(97\)00036-7](https://doi.org/10.1016/S0016-7037(97)00036-7)
- Renard, F., Beauprêtre, S., Voisin, C., Zigone, D., Candela, T., Dysthe, D. K., & Gratier, J. P. (2012). Strength evolution of a reactive frictional interface is controlled by the dynamics of contacts and chemical effects. *Earth and Planetary Science Letters*, 341–344, 20–34. <https://doi.org/10.1016/j.epsl.2012.04.048>
- Rice, J. R., & Ruina, A. (1983). Stability of Steady Frictional Slipping. *Journal of Applied Mechanics*, 50(2), 343. <https://doi.org/10.1115/1.3167042>
- Ruina, A. (1983). Slip instability and state variable friction laws. *Journal of Geophysical Research*, 88(B12), 10359. <https://doi.org/10.1029/JB088iB12p10359>

- Saffer, D., & Marone, C. (2003). Comparison of smectite- and illite-rich gouge frictional properties: Application to the updip limit of the seismogenic zone along subduction megathrusts. *Earth and Planetary Science Letters*, 215(1–2), 219–235. [https://doi.org/10.1016/S0012-821X\(03\)00424-2](https://doi.org/10.1016/S0012-821X(03)00424-2)
- Saffer, D., Frye, K. M., Marone, C., & Mair, K. (2001). Laboratory results indicating complex and potentially unstable frictional behavior of smectite clay. *Geophysical Research Letters*, 28(12), 2297–2300. <https://doi.org/10.1029/2001GL012869>
- Saffer, D., Lockner, D. A., & McKiernan, A. (2012). Effects of smectite to illite transformation on the frictional strength and sliding stability of intact marine mudstones. *Geophysical Research Letters*, 39(11), 2–7. <https://doi.org/10.1029/2012GL051761>
- Samuelson, J., Elsworth, D., & Marone, C. (2009). Shear-induced dilatancy of fluid-saturated faults: Experiment and theory. *Journal of Geophysical Research: Solid Earth*, 114(12), 1–15. <https://doi.org/10.1029/2008JB006273>
- Scholz, C. H. (1998). Earthquakes and friction laws. *Nature*, 391(6662), 37–42. <https://doi.org/10.1038/34097>
- Scholz, C. H. (2002). *The Mechanics of Earthquakes and Faulting*. Cambridge University Press. Retrieved from <https://books.google.ch/books?id=JL1VM5wMbrQC>
- Scuderi, M. M., & Collettini, C. (2016). The role of fluid pressure in induced vs. triggered seismicity: Insights from rock deformation experiments on carbonates. *Scientific Reports*, 6(January), 1–9. <https://doi.org/10.1038/srep24852>
- Shimamoto, T., & Logan, J. M. (1981). Effects of simulated clay gouges on the sliding behavior of Tennessee sandston. *Tectonophysics*, 75(3–4), 243–255. [https://doi.org/10.1016/0040-1951\(81\)90276-6](https://doi.org/10.1016/0040-1951(81)90276-6)
- Smith, S. A. F., & Faulkner, D. (2010). Laboratory measurements of the frictional properties of the Zuccale low-angle normal fault, Elba Island, Italy. *Journal of Geophysical Research: Solid Earth*, 115(2), 1–17. <https://doi.org/10.1029/2008JB006274>
- Tembe, S., Lockner, D. A., & Wong, T. F. (2010). Effect of clay content and mineralogy on frictional sliding behavior of simulated gouges: Binary and ternary mixtures of quartz, illite, and montmorillonite. *Journal of Geophysical Research: Solid Earth*, 115(3), 1–22. <https://doi.org/10.1029/2009JB006383>
- Tesei, T., Collettini, C., Carpenter, B., Viti, C., & Marone, C. (2012). Frictional strength and healing behavior of phyllosilicate-rich faults. *Journal of Geophysical Research: Solid Earth*, 117(9), 1–13. <https://doi.org/10.1029/2012JB009204>
- Tesei, T., Collettini, C., Barchi, M. R., Carpenter, B., & Di Stefano, G. (2014). Heterogeneous strength and fault zone complexity of carbonate-bearing thrusts with possible implications for seismicity. *Earth and Planetary Science Letters*, 408, 307–318. <https://doi.org/10.1016/j.epsl.2014.10.021>
- Tsang, C.-F., Barnichon, J. D., Birkholzer, J., Li, X. L., Liu, H. H., & Sillen, X. (2012). Coupled thermo-hydro-mechanical processes in the near field of a high-level radioactive waste repository in clay formations. *International Journal of Rock Mechanics and Mining*

- Sciences*, 49, 31–44. <https://doi.org/10.1016/j.ijrmms.2011.09.015>
- Tsutsumi, A., Fabbri, O., Karpoff, A. M., Ujiie, K., & Tsujimoto, A. (2011). Friction velocity dependence of clay-rich fault material along a megasplay fault in the Nankai subduction zone at intermediate to high velocities. *Geophysical Research Letters*, 38(19), 2–7. <https://doi.org/10.1029/2011GL049314>
- Wang, H. (2000). *Theory of Linear Poroelasticity with Applications to Geomechanics and Hydrogeology*. Princeton University Press. Retrieved from <https://books.google.ch/books?id=RauGOzaQBRUC>
- Wang, W. L., Wang, T. T., Su, J. J., Lin, C. H., Seng, C. R., & Huang, T. H. (2001). Assessment of damage in mountain tunnels due to the Taiwan Chi-Chi Earthquake. *Tunnelling and Underground Space Technology*, 16(3), 133–150. [https://doi.org/10.1016/S0886-7798\(01\)00047-5](https://doi.org/10.1016/S0886-7798(01)00047-5)
- Yasuhara, H., Marone, C., & Elsworth, D. (2005). Fault zone restrengthening and frictional healing: The role of pressure solution. *Journal of Geophysical Research: Solid Earth*, 110(6), 1–11. <https://doi.org/10.1029/2004JB003327>
- Zhang, C. L., Wiczorek, K., & Xie, M. L. (2010). Swelling experiments on mudstones. *Journal of Rock Mechanics and Geotechnical Engineering*, 2(1), 44–51. <https://doi.org/10.3724/SP.J.1235.2010.00044>
- Zhang, X., Spiers, C., & Peach, C. J. (2010). Compaction creep of wet granular calcite by pressure solution at 28°C to 150°C. *Journal of Geophysical Research: Solid Earth*, 115(9), 1–18. <https://doi.org/10.1029/2008JB005853>





## 4.

# FRictional PROPERTIES AND PERMEABILITY VARIATIONS OF FAULT ZONES IN THE OPALINUS CLAY FORMATION, A HOST-ROCK FOR DEEP NUCLEAR WASTE STORAGE

**Authors:** Luis Felipe Orellana<sup>1</sup>, Carolina Giorgetti<sup>1</sup>, and Marie Violay<sup>1</sup>

<sup>1</sup> Laboratory of Experimental Rock Mechanics (LEMR), ENAC, EPFL, Switzerland;

**Status:** A shorter version of this chapter has been submitted to *Geophysical Research Letters*

**Contributions:** L. F. Orellana has collected, prepared and characterized samples used in this study. L.F. Orellana has designed experimental setup. L.F. Orellana, C. Giorgetti and M. Violay have contributed to the testing strategy and methodology. L. F. Orellana has written the manuscript. C. Giorgetti and M. Violay have edited and guided discussions of the manuscript. M. Violay has acted as a supervisor and main responsible author of the publication.

### Highlights:

- Dry samples are weak and shift from unstable to stable fault slip behavior when increasing sliding velocity.
- Wet samples exhibit velocity-strengthening behavior, and water reduces the coefficient of friction to  $\sim 40\%$  of dry samples.
- Shear deformation is accompanied by shear dilatancy and enhanced permeability

## 4.1. ABSTRACT

The underground disposal of high-level nuclear waste (HLW) is a pressing issue for several countries. The Opalinus Clay (OPA) formation, a shale with favorable barrier properties, is the potential host-rock for disposal of HLW in Switzerland. However, small-to-large faults that intersect the formation bring the long-term integrity of the future repositories into question. Here, we present the first systematic laboratory study on the frictional strength, stability, dilatancy and permeability of simulated OPA gouge under typical repository conditions. Wet gouges exhibit an extremely low coefficient of friction ( $\mu_f \sim 0.16$ ), velocity-strengthening behavior, and shear-enhanced dilatancy at the onset of slip and permeability increase. Conversely, dry gouges are still weak ( $\mu_f \sim 0.36$ ) but exhibit a transition from unstable to stable sliding with increasing sliding velocity. Thus, we infer that faults hosted in OPA could be easily reactivated via aseismic creep, possibly acting as weak fluid conduits. However, if temporarily dried, they could become potentially unstable.

## 4.2. INTRODUCTION

Deep geological repositories (DGR) are one of the most promising solutions for the long-term confinement of high-level nuclear waste (HLW) (Kim et al., 2011). HLW, a waste product of nuclear energy production, needs to be safely stored for long-term periods to guarantee its isolation and thus to provide protection to the people and the environment (Ewing et al., 1995; Norris, 2017). In Switzerland, the concept for DGR is developed within the Mont Terri Laboratory (MTL) project (Bossart et al., 2017; Nussbaum et al., 2011). Situated to the northern Switzerland, the MTL is an underground laboratory that runs site characterization and testing activities in the Opalinus Clay (OPA) formation. The OPA formation corresponds to an indurated, hydro-mechanically anisotropic (bedding planes) shale that has favorable transport (e.g., low permeability) and geochemical barrier properties for the retention of radionuclides (Bossart et al., 2017).

At the MTL, the OPA formation is intersected by small-to-large tectonic fault systems. For instance, the “Main Fault” (MF) is a 1.0 to 4.2 m thick thrust fault that crosscuts the MTL at a depth of ~300 m (Figure 4-1a). Within the limits of the MF, various structural elements are recognizable such as fractures, secondary shear planes, non-deformed rock, scaly clays and fault gouge (Nussbaum et al., 2011). While there will not be any disposal of radioactive waste at the MTL, the presence of faults within the OPA formation poses questions about fault-related processes in other potential site regions. Faults, for instance, have the potential to damage the underground infrastructure (e.g. via sudden fault slip events) and to influence the migration of stored radionuclides through the geologic formations (e.g. as preferential drainage) (Tsang et al., 2015; Wang et al., 2001) (Figure 4-1b).

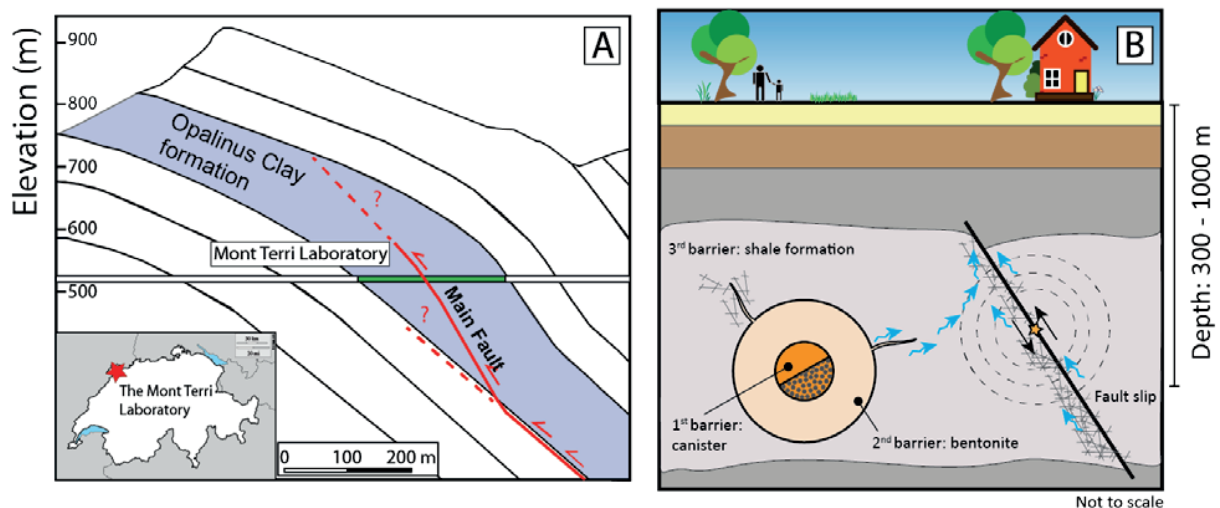


**Figure 4-1:** A) Cross-section of the Opalinus Clay formation showing the location of the Mont Terri Laboratory (MTL) and the Main Fault crosscutting the laboratory. Inlet shows the site of the MTL in the northern part of Switzerland. B) A schematic representation of nuclear waste storage risks including potential seismicity and creation of preferential fluid-flow paths.

In recent in-situ fluid-injection experiments at the MTL (Guglielmi et al., 2017; Jeanne et al., 2017, 2018), the MF was activated resulting in limited displacement accompanied by a sequence of seismic events within the fault zone. Moreover, permeability measurements coupled with fault displacement in the same experiments have revealed an increase in fault permeability associated with shear-enhanced dilation.

Furthermore, during the operation of the DGR, heating generated from HLW can affect the host-rock and adjacent fault systems. Indeed, temperature can exceed the 50 -70 °C for long periods of times (~ 10000 yr.) in the surroundings (~ 10 m) of the heating source (Heierli & Genoni, 2017; Yang & Yeh, 2009), leading to temperature gradients and dehydration processes (Buscheck et al., 2002), which will tend to dry the rock, create pore overpressures and change the natural permeability of the host-rock (Monfared et al., 2014; Tsang et al., 2012).

Despite recent efforts, how the evolution of fault slip on pre-existing faults in the OPA formation evolves (seismic or aseismic) and how fault permeability changes during shear deformation (enhancement or destruction) still are not well understood, yet they are crucial to the long-term integrity of the repositories. Thus, further investigations of the frictional properties, shear-enhanced dilatancy and the couplings governing slip stability in OPA fault-arrays are still needed.

At low temperature and pressure, deformation in faults occurs mostly in the brittle deformation domain and is controlled by fracturing and frictional sliding processes (Rutter et al., 2001). Frictional properties of OPA have been recently studied at laboratory scale (Fang et al., 2017, 2018; Orellana et al., 2018b) in the context of rate-and-state theory (Dieterich, 1978; Ruina, 1983). However, these laboratory studies were run in partially saturated conditions or with limited normal stress ranges. Nevertheless, these studies have shown a significant frictional weakness relative to Byerlee's rule (Byerlee, 1978) and, at low slip velocities (<1 mm/s), a velocity-strengthening behavior, i.e. aseismic, similar to other clay-rich rocks (e.g. Morrow et al., 2017; Tembe et al., 2010; Haines et al., 2014; Behnsen and Faulkner, 2012; Kohli and Zoback, 2013).

Once fault slip on pre-existing faults in shales occurs fault permeability can be either depleted or enhanced. Fluid permeability might decrease thank to shear-enhanced compaction (Crawford et al., 2008) and clay-fabric development (Ikari et al., 2009). Conversely, fluid permeability might increase due to deformation-induced dilatancy when sheared at low to moderate effective stresses (Lefèvre et al., 2016; Wu et al., 2017; Zhang & Cox, 2000). Furthermore, existing works on fracture permeability changes in OPA intact samples have shown that permeability decreases with displacement associated with the swelling of clays (Cuss et al., 2011; Fang et al., 2017, 2018).

The strategy of this study includes frictional sliding experiments in a triaxial saw-cut configuration at different effective normal stresses which are representative of future in-situ conditions. We have run tests at sliding velocities and different saturation conditions (dry and

wet) that have not been previously tested. Dry and wet conditions represent end-member environments of the operation of nuclear waste storage repositories. Further, we examine dilatancy and compaction behavior via volumetric pore fluid changes in the gouge layer, and we measure permeability before and after shearing. Here, we attempt to quantify the frictional strength, stability, dilatancy and permeability variations of the OPA formation and its implications for the nuclear waste storage concept in clay-rich formations. In this work, we substantially advance on previous studies by providing new insights on for fault weakness, unstable behavior, and shear-dilatancy in OPA fault arrays.

## 4.3. METHODS

### 4.3.1. SAMPLES

We have used simulated fault gouge samples that were prepared from non-deformed OPA. The simulated fault gouge samples were first crushed and then sieved to ensure grain sizes of less than 125  $\mu\text{m}$ . Using a Malvern Mastersizer S equipment (Powder Technology Laboratory, EPFL), we have measured an average particle diameter of about 7  $\mu\text{m}$  and maximum sizes of 125  $\mu\text{m}$ . The mineral composition of the simulated Opalinus clay fault gouge (Table 1A) consists of phyllosilicates ( $\sim 51\%$ ), quartz ( $\sim 23\%$ ), calcite ( $\sim 14\%$ ), and pyrite ( $\sim 1.4\%$ ). Among the phyllosilicates, kaolinite, mica, and chlorite are the main components comprising  $\sim 28\%$ ,  $\sim 10\%$ , and  $\sim 9\%$  of the total weight content respectively (See Chapter 3, Orellana et al., 2018b).

### 4.3.2. EXPERIMENTAL SETUP

The frictional sliding experiments have been performed in a servo-controlled triaxial apparatus using a saw-cut configuration (Figure 4-2a). The triaxial apparatus is controlled by a digital controller series PCS8000 integrated with PC running the testing software DION7 (Walter + Bai AG). Axial load up to 2000 kN (accuracy of 0.01 kN) can be controlled using a displacement or force feedback loop. The triaxial apparatus can control and produce confining pressures up to 1000 bar (maximum error 0.02%). Two digital transducers are used to control and measure displacement with an accuracy better than 0.003  $\mu\text{m}$ .

The saw-cut configuration comprises two cylindrical stainless steel pistons of 38 mm in diameter that were cut along a plane oriented at an angle of  $30^\circ$  to the cylindrical axis. The saw-cut surface of each piston has a roughness ( $R_a$ ) of 12.5  $\mu\text{m}$ . During testing, the pistons are separated by  $\sim 1$  mm-thick layer of dry or wet powdered gouge along the saw cut. Before inserting the piston assembly into the Hoek Cell, we have used a latex membrane (VJT/0554, Sols Mesures) and a rubber sealing sleeve (model 45-D0554/1, Controls Group) to act as an effective seal and to separate the specimen from the confining oil respectively. In between the latex membrane and the rubber sealing, we put anti-friction coating to reduce artificial frictional resistance. The contribution of the latex to the shear strength is found to be negligible for the 2.8 mm of total axial displacement.

At each end of the piston assembly, one sintered porous stainless steel filters of 3.8 mm in diameter (AISI 316L, GKN Sinter Metals) and 5 mm in height was placed to allow fluid flow. To measure the upstream ( $P_{p1}$ ) and downstream ( $P_{p2}$ ) pore fluid pressure, we have used two GDS pressure/volume controllers and the GDSLAB control and data acquisition software. Pressure and volume can go up to 16/32 MPa and 200.000 mm<sup>3</sup> respectively. Variations in pressure and volume were also measure using and additional sensors (Temposonics® R-Series V RP Profinet RT & IRT, resolution 0.5  $\mu$ m) connected to the pore fluid pumps, which are synchronized with the controlling PC of the triaxial apparatus. The stiffness of the press and the testing setup is 626.9 kN/mm.

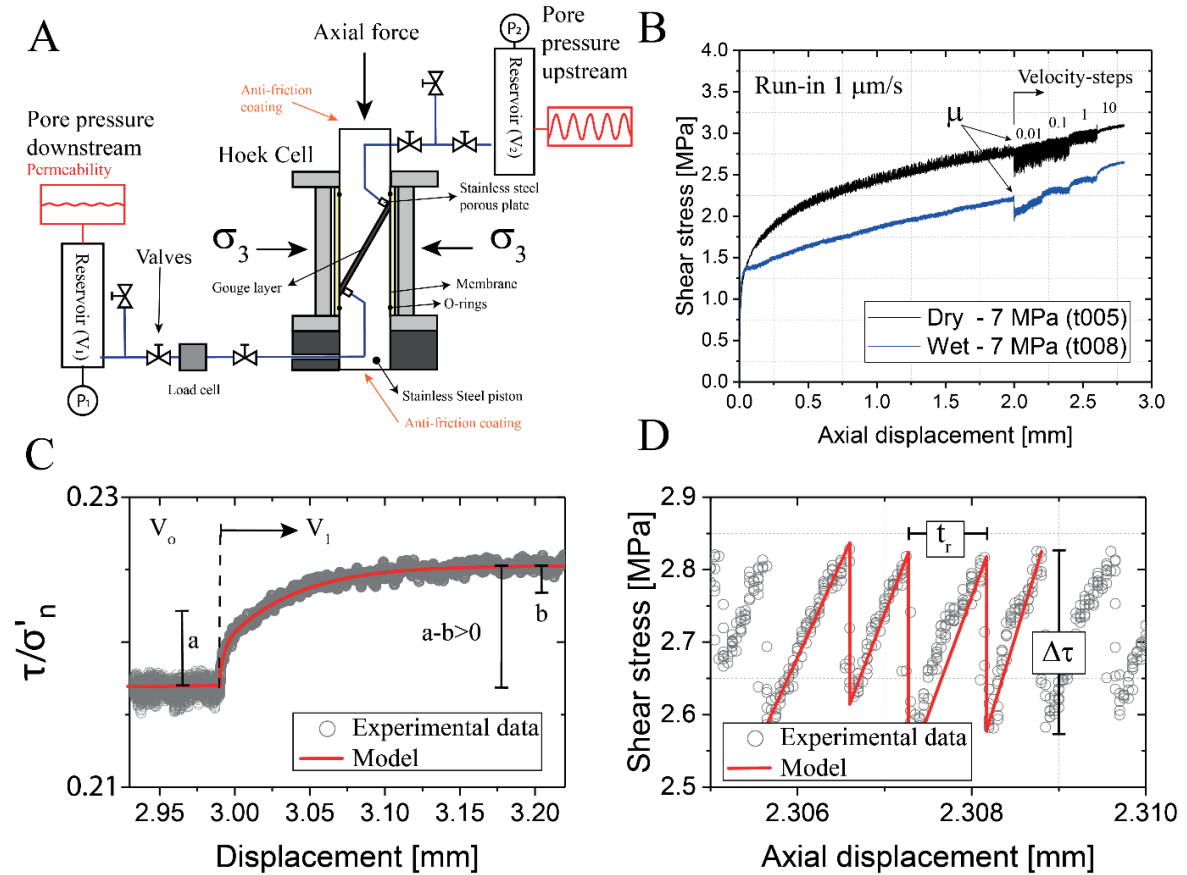


**Figure 4-2:** Experimental setup, frictional tests, and quantification of frictional properties. A) Saw-cut and pore pressure pumps configuration. B) Wet and dry test. Friction is calculated before velocity-steps started. Run-in velocity is of 1  $\mu$ m/s. Blue squares show the position of figures C) and D). C). Model inversion of the experimental data with slip law resulting in rate and state values of  $a$ ,  $b$ , and  $a-b$ . D) Stress drop and recurrence time of the stick-slip events.

#### 4.3.3. TESTING PROCEDURE

A series of experiments (19 in total) was designed to investigate the frictional properties of dry and wet Opalinus Clay, and the evolution of permeability with fault slip. We have performed the experiments as follows:



- i. We measured 5 g of dry powdered Opalinus clay that we have observed guaranteed a continuous ~1 mm-thick clay layer at the end of each experiment. For dry experiments, samples were first dried for 48 h at 50°. In this way, while some small fraction of interlayer water could still be present, in this study 1) we replicate dry conditions similar to those expected during the operation of the nuclear waste repository (Heierli & Genoni, 2017; Yang & Yeh, 2009) and 2) we have ensured that the and any thermal damage to the mineral grains was avoided (Rutter & Mecklenburgh, 2018).
- ii. For wet experiments, the dried powdered sample is mixed with ~2.5 ml of deionized water to make a paste (Lockner et al., 2011; Morrow et al., 1982; Tembe et al., 2010). The sample is then spread onto the saw cut surface of the lower piston and sandwiched by the upper stainless steel piston. Next, the sample/piston assembly is put into the membranes and Hoek Cell. Finally, we have emplaced the assembly in the triaxial apparatus and covered the top piston – triaxial apparatus contact with anti-friction coating (MoS<sub>2</sub>-based coating).
- iii. Frictional experiments on both wet and dry samples have been carried out at constant effective normal stress ( $\sigma'_n$ ) ranging from 4 to 20 MPa and at room temperature. To keep normal stress constant during sliding, we adjusted under computer control the confining pressure. For dry experiments, the assembly is loaded at 0.01 MPa/s to the target value in axial and confining pressure. Before shearing, dry samples were compacted for about 45 - 60 minutes to an initial steady-state thickness. For wet experiments, hydraulic circuits were saturated with deaerated and demineralized water. Then the sample was repeatedly loaded in axial and confining pressure at 0.01 MPa/s to the desire test value. We have increased pore pressure at a rate of 0.01 MPa/s and we fixed it to 10 MPa. Once target normal stress and pore pressure were achieved, we wait for consolidation, pore pressure and volume equilibrium in both controllers (Morrow et al., 2017). This stage has lasted for at least 48 h.
- iv. After pore pressures and water volume have reached equilibrium, the initial permeability parallel to shearing direction ( $k_{i, //}$ ) of each wet sample was measured using the oscillatory method (Bernabé et al., 2006) as a function of effective hydrostatic confining pressure (Crawford et al., 2008; Faulkner & Rutter, 2000; Rutter & Mecklenburgh, 2018; Sanchez-Roa et al., 2017). The permeability test lasted for about 10 to 12 h. Shearing did not start immediately as we have to wait for at least 12 h for re-establishing pore volumes equilibrium.
- v. Each experiment has followed a common displacement history (Figure 4-2b). The initial axial loading rate for the first 2.0 mm was 1  $\mu\text{m/s}$ , i.e., a sliding velocity of 1.14  $\mu\text{m/s}$  and a strain rate of  $\gamma \approx 0.001 \text{ s}^{-1}$  along the fault. After 2.0 mm of axial displacement, the samples were subjected to a sequence of increasing velocity-steps: 0.01-0.1, 0.1-1, and 1-10  $\mu\text{m/s}$  for 0.2 mm each. These rates are slow enough to ensure

controlled pore fluid pressure and, if applicable, acceptable overpressures (Faulkner et al., 2018; Morrow et al., 2017). Indeed, localization within clay-rich shear planes during deformation and the inherent low-permeability of the material can generate local fluid overpressures and non-drained conditions in the surroundings of the shear planes that are impossible to control. In each step, velocity was suddenly increase inducing an instantaneous reaction in friction followed by a decay over a critical slip distance ( $D_c$ ) to a new stable value of frictional strength (Scholz, 2002).

- vi. During wet experiments, while keeping  $Pp$  constant, we estimated shear-enhanced compaction or dilation by measuring the volume of water expelled or absorbed respectively (Behnsen & Faulkner, 2012; French et al., 2015). Leaks were not detected in the experiments reported here. The shearing stage last approximately 7 h.
- vii. Finally, once the shearing stage was finished, we have waited 12 h again to re-establish pore volumes equilibrium. Then, we have measured end permeability ( $k_{f, //}$ ) as described in point iv).

Full dry test lasts around 8 to 9 hours, including sample preparation and compaction. Each wet tests have lasted at least 120 hours (5 days).

### 4.3.4. DATA PROCESSING

#### 4.3.4.1. FRICTION AND COEFFICIENT OF FRICTION

We have calculated friction ( $\mu$ ) as:

$$\mu = \frac{\tau}{\sigma_n'} = \frac{\tau}{\sigma_n - Pp}$$

**Equation 4-1:** Friction

Where  $\tau$  corresponds to the shear strength parallel to the fault,  $\sigma_n$  the normal stress,  $Pp$  is the pore pressure, and  $\sigma_n'$  the effective normal stress. Shear strength ( $\tau$ ) was corrected for the decreasing contact area. Friction ( $\mu$ ) values were obtained at 2 mm of axial displacement, before velocity-steps started (Figure 4-2b). In addition, we have evaluated the coefficient of friction ( $\mu_f$ ) and an inherent shear strength or equivalent cohesion ( $S_o$ ) (Jaeger et al., 2007). Here  $\mu_f$  is the best-fit to the tangent of the  $\tau - \sigma_n'$  curve. The values of friction  $\mu$  and coefficient of friction  $\mu_f$  are related as:

$$\mu = \frac{\tau}{\sigma_n'} = \frac{\tau}{\sigma_n - Pp} = \frac{S_o}{\sigma_n - Pp} + \mu_f$$

**Equation 4-2:** Friction and coefficient of friction

#### 4.3.4.2. FRICTIONAL STABILITY

To understand fault stability, we have computed the velocity dependence of friction via the frictional stability parameter ( $a - b$ ). To do that, we modelled each velocity-step using the empirical Ruina's slip –dependent evolution law, also known as Slip law (Ruina, 1983), through a least square numerical fitting routine (Noda & Shimamoto, 2009):

$$\mu = \mu_o + a \cdot \ln\left(\frac{V}{V_o}\right) + b \cdot \ln\left(\frac{V_o \cdot \theta}{D_c}\right),$$

**Equation 4-3:** Rate and state constitutive empirical law

$$\frac{d\theta}{dt} = -\frac{V \cdot \theta}{D_c} \cdot \ln\left(\frac{V_o \cdot \theta}{D_c}\right)$$

**Equation 4-4:** Ruina's evolution law (Ruina, 1983)

Where  $\mu_o$  is a constant that represents friction at steady-state for a reference velocity  $V_o$ ,  $\mu$  is the friction at the new steady-state velocity  $V$ ,  $D_c$  the critical slip distance, and  $\theta$  the average lifetime of contacts (Dieterich, 1979; Rabinowicz, 1951; Ruina, 1983; Scholz, 2002). Ruina's empirical law allows the calculation of the direct ( $a$ ) and evolution ( $b$ ) dimensionless constants. Thus, the computation of the frictional parameter ( $a - b$ ) is as follows (Figure 4-2c):

$$a - b = \frac{\Delta\mu_{ss}}{\ln\left(\frac{V}{V_o}\right)}.$$

**Equation 4-5:** Frictional stability parameter

In Equation 4-5,  $\Delta\mu_{ss}$  is the change in the steady-state friction upon an immediate change in sliding velocity from  $V_o$  to  $V$  (Marone, 1998; Scholz, 2002). When  $(a - b) \geq 0$  fault slip occurs in a stable manner, i.e., velocity-strengthening behavior. If  $(a - b) < 0$  fault slip will potentially develop in an unstable fashion, i.e., velocity-weakening behavior (Jaeger et al., 2007; Scholz, 2002). If necessary, we have removed the linear strengthening assuming that the strengthening is independent of the velocity-dependence of friction (Samuelson et al., 2009). When stick-slip behavior occurs, magnitudes of  $(a - b)$  cannot be directly computed. Thus, we have implied velocity-weakening and calculated average stress drops ( $\Delta\tau$ ) (Figure 4-2d).

#### 4.3.4.3. PERMEABILITY

As indicated before, we have estimated permeability parallel to the shearing direction, before ( $k_{i, //}$ ) and after ( $k_{f, //}$ ) the shearing stage, using the oscillatory method (Fischer, 1992; Bernabé et al., 2006). Permeability was measured at a target normal stress before shearing after pore pressures and volumes were equilibrated. At the end of each shear test and to preserve the shear microstructures, we have removed shear stress and we have held normal stress constant

(Rutter & Mecklenburgh, 2018). The oscillatory permeability method has been previously used in the triaxial saw-cut configuration for low permeability clays materials (Crawford et al., 2008; Faulkner & Rutter, 1998, 2000; Rutter & Mecklenburgh, 2018; Sanchez-Roa et al., 2017).

The oscillatory method is based on the transmission of a pore pressure wave within the porous media. The method applies a sinusoidal pore-fluid pressure oscillation in the up-stream reservoir using a servo-controlled pump. The amplitude and period of the imposed oscillation were fixed to 1 MPa and 1800 s, respectively. The resulting pressure variations are recorded in the downstream reservoir in terms of phase shift  $\theta$  and amplitude ratio  $A$ . Two dimensionless parameters storativity ( $\xi$ ) and permeability ( $\eta$ ), are calculated as:

$$\xi = \frac{S \cdot L \cdot \beta}{\beta_d} \qquad \eta = \frac{A' \cdot t \cdot k}{\pi \cdot L \cdot \mu_{vis} \cdot \beta_d}$$

**Equation 4-6:** Dimensionless permeability ( $\eta$ ) and storativity ( $\xi$ ). Oscillatory method (Fischer, 1992; Bernabé et al., 2006)

Where  $A'$  is the cross-sectional area of the sample,  $L$  is the length or height of the sample,  $\beta$  is the unknown sample storage capacity,  $\beta_d$  is the downstream reservoir compressibility,  $t$  the period of the upstream excitation,  $k$  the permeability of the formation and  $\mu_{vis}$  the dynamic viscosity of the pore fluid. In various tests, the storage capacity of the samples could not be determined accurately across the whole pressure range by the oscillation method employed here. These data must be then interpreted with caution. The relation between parameters  $\xi$  and  $\eta$ , and the measured values of  $\theta$  and  $A$  is given by:

$$Ae^{-i\theta} = \left( \frac{1+i}{\sqrt{\xi\eta}} \sinh \left[ (1+i) \sqrt{\frac{\xi}{\eta}} \right] + \cosh \left[ (1+i) \sqrt{\frac{\xi}{\eta}} \right] \right)^{-1}$$

**Equation 4-7:** Relation between dimensionless permeability ( $\eta$ ) storativity ( $\xi$ ). Oscillatory method (Fischer, 1992; Bernabé et al., 2006)

## 4.4. RESULTS

At 1.14  $\mu\text{m/s}$  sliding velocity, our results show  $\mu$  values ranging from 0.18 to 0.41 for wet samples, and 0.33 to 0.45 for dry samples (Figure 4-3a). Wet and dry friction decreases with increasing  $\sigma'_n$ . Cohesion is then estimated giving  $\mu_f = 0.15$  and  $S_o = 0.79$  MPa for wet samples, and  $\mu_f = 0.36$  and  $S_o = 0.22$  for dry samples (Figure 4-3b).

Regarding fault stability, wet experiments show a consistent velocity-strengthening behavior with values of  $(a - b)$  between 0.002 and 0.013 at all up-step velocities (Figure 4-3c, Table 4-1). Dry experiments undergo a transition from unstable behavior, i.e. stick-slips, to stable behavior above slip rates of 10  $\mu\text{m/s}$ , with  $(a - b)$  values between 0.001 and 0.008 (Figure 4-3d, Table 4-2). When stick-slips occur, we record more than 50 events, with recurrence times

up to 145 s and average stress drops ranging from 0.05 to 0.56 MPa (Figure 4-3e). The stress drop release represents less than 5% of the initial shear stress. At low  $\sigma'_n$  and slow sliding velocities, stick-slip events have systematically smaller  $\Delta\tau$  and are less regular than their higher normal stress counterparts. For example, at the same axial velocity of 0.01  $\mu\text{m/s}$ , the average stress drop is 0.20 at  $\sigma'_n = 4$  MPa, while 0.33 at 20 MPa. Finally,  $\Delta\tau$  amplitudes decrease when increasing velocity for all tests. All results are presented in Table 4-1 and Table 4-2 for wet and dry samples respectively.

Test	Normal stress $\sigma_n$ [MPa]	Condition	Friction $\mu$ at 2 mm	Permeability $k$ [ $\text{m}^2$ ]		Axial Velocity [ $\mu\text{m/s}$ ]	a-b	$D_c$ [ $\mu\text{m}$ ]
				Before $k_i$	After $k_f$			
t006	4	wet	0.411	n/a	n/a	0.1	n/a	n/a
						1	0.009	10.3
						10	0.012	9.9
t010	4	wet	0.245	2.0E-20	2.7E-20	0.1	0.013	10.0
						1	0.011	33.4
						10	0.012	24.3
t008	7	wet	0.315	1.9E-20	3.9E-20	0.1	0.006	4.0
						1	0.008	38.7
						10	0.008	10.1
t024	7	wet	0.274	7.6E-21	3.3E-20	0.1	0.002	7.5
						1	0.005	10.5
						10	0.007	24.2
t007	10	wet	0.233	1.1E-20	2.4E-20	0.1	0.006	38.8
						1	0.007	44.1
						10	0.004	34.6
t016	10	wet	0.208	6.7E-21	2.0E-20	0.1	0.005	38.8
						1	0.005	21.7
						10	0.007	34.5
t009	20	wet	0.183	6.2E-21	1.8E-20	0.1	0.004	1.1
						1	0.005	15.1
						10	0.005	9.5
t025	20	wet	0.205	7.5E-21	1.7E-20	0.1	0.004	1.6
						1	0.005	31.1
						10	0.005	37.5

**Table 4-1:** Results for wet tests of the numerical fitting of the empirical constants  $a$ ,  $b$ , and  $D_c$ . Measurements of permeability before ( $k_i$ ) and after ( $k_f$ ) shearing.

In our tests, permeability increases from  $k_{i, //} = 2.02 \times 10^{-20}$  to  $k_{f, //} = 2.71 \times 10^{-20}$  when samples are sheared at  $\sigma'_n = 4$  MPa, and from  $6.15 \times 10^{-21}$  to  $1.78 \times 10^{-20}$  when  $\sigma'_n = 20$  MPa (Figure 4-4a). These measurements indicate that, after shearing, permeability increases by a factor of  $\sim 3$  and reaches values of  $\sim 10^{-20} \text{ m}^2$ . The pore volume evolution during shearing suggests a long-duration dilation during the first  $\sim 1.0$ - $1.5$  mm of axial displacement followed

by a slight compaction and/or a steady-state porosity until 2 mm of axial displacement is reached (Figure 4-4b). Once the velocity-steps sequence starts (0.01 to 0.1  $\mu\text{m/s}$ ), dilation or compaction occurs depending on the undergone velocity history and the acting normal stress.

Test	Normal stress $\sigma_n$ [MPa]	Condition	Friction $\mu$ at 2 mm	Axial Velocity [ $\mu\text{m/s}$ ]	a-b	$D_c$ [ $\mu\text{m}$ ]	# SS events	Average $\Delta\tau$ [Mpa]	Average $t_r$ [s]
t001	4	dry	0.399	0.01	-	-	170	0.24	113.59
				0.1	-	-	197	0.16	10.08
				1	-	-	191	0.05	1.02
				10	0.004	86.21	-	-	-
t015	4	dry	0.451	0.01	-	-	197	0.20	96.44
				0.1	-	-	236	0.15	8.44
				1	-	-	205	0.08	0.96
				10	0.001	28.63	-	-	-
t020	7	dry	0.417	0.01	-	-	189	0.26	101.87
				0.1	-	-	195	0.25	10.26
				1	-	-	134	0.17	1.46
				10	0.003	0.02	-	-	-
t005	7	dry	0.395	0.01	-	-	177	0.21	110.17
				0.1	-	-	226	0.18	8.86
				1	-	-	194	0.12	1.02
				10	0.008	168.53	-	-	-
t014	7	dry	0.401	0.01	-	-	196	0.23	103.93
				0.1	-	-	244	0.22	8.16
				1	-	-	208	0.14	0.95
				10	0.002	0.11	-	-	-
t021	10	dry	0.408	0.01	-	-	166	0.56	118.20
				0.1	-	-	129	0.27	15.31
				1	-	-	-	-	-
				10	0.003	2123.1	-	-	-
t002	10	dry	0.332	0.01	-	-	191	0.20	100.87
				0.1	-	-	215	0.19	9.19
				1	-	-	181	0.17	1.10
				10	0.003	10.71	-	-	-
t012	10	dry	0.375	0.01	-	-	184	0.25	105.57
				0.1	-	-	213	0.26	8.38
				1	-	-	165	0.21	1.21
				10	0.006	0.98	-	-	-
t018	10	dry	0.372	0.01	-	-	181	0.25	107.79
				0.1	-	-	225	0.24	8.86
				1	-	-	161	0.18	1.22
				10	n/a	n/a	-	-	-
t023	20	dry	0.382	0.01	-	-	126	0.33	145.22
				0.1	-	-	159	0.31	12.51
				1	-	-	117	0.18	1.69
				10	0.004	94.83	-	-	-
t017	20	dry	0.368	0.01	-	-	145	0.23	130.71
				0.1	-	-	206	0.33	9.64
				1	-	-	118	0.40	1.67
				10	0.005	1154.10	-	-	-

**Table 4-2:** Results for dry tests of the numerical fitting of the empirical constants  $a$ ,  $b$ , and  $D_c$ . Measurements of average stress drop  $\Delta\tau$  and recurrence time  $t_r$ , or all dry experiments



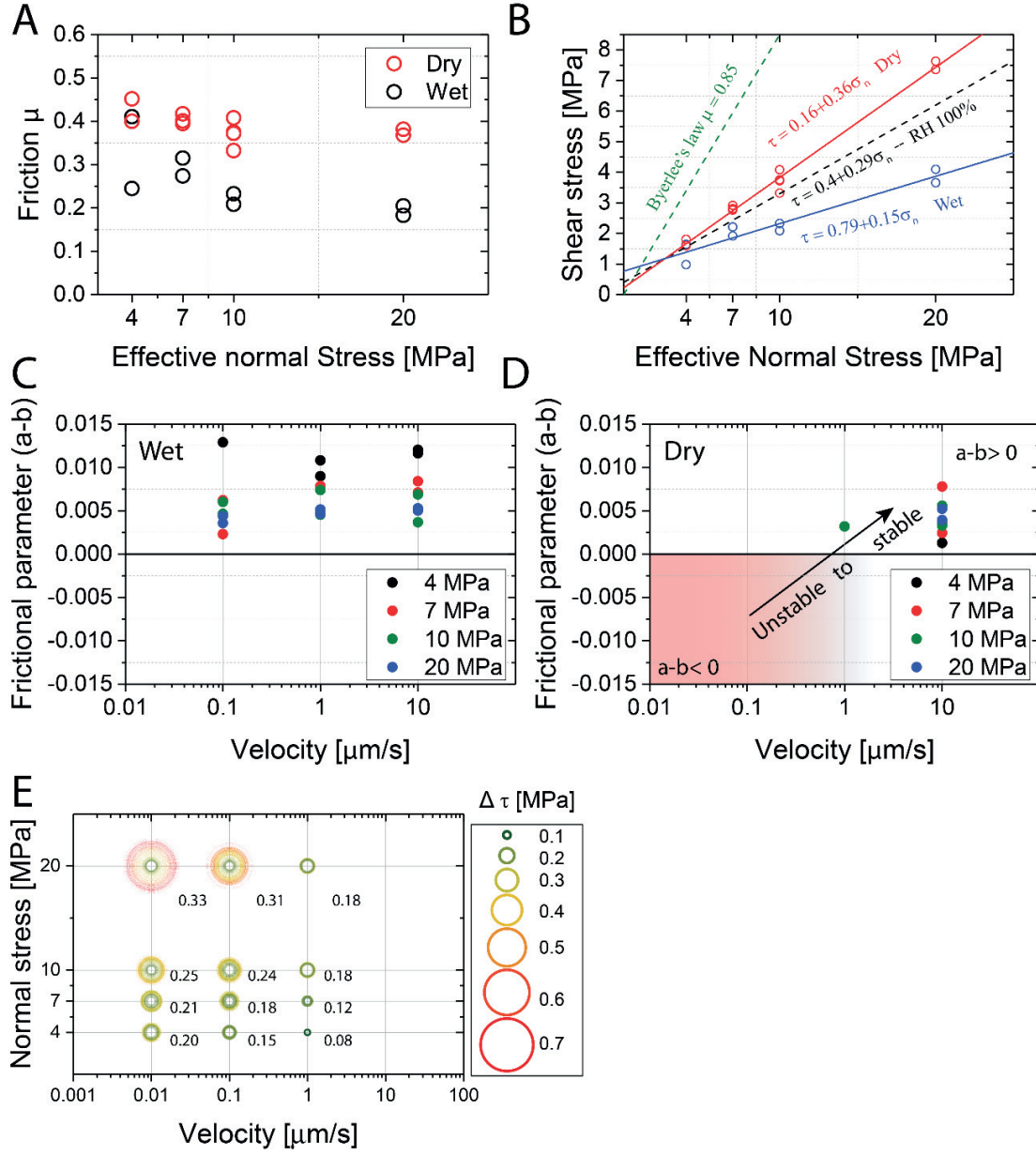


**Figure 4-3:** Frictional results. A) Friction at 2 mm displacement (axial) and B) Shear stress versus effective normal stress for wet and dry samples. For comparison, we have included the Byerlee's rule (Byerlee, 1978) and previous results of frictional experiments carried out at 100% room humidity condition (Orellana et al., 2018b). Frictional parameter versus axial velocity for C) wet and D) dry samples. E) Stress drops for selected experiments (t015, t005, t018, t023).

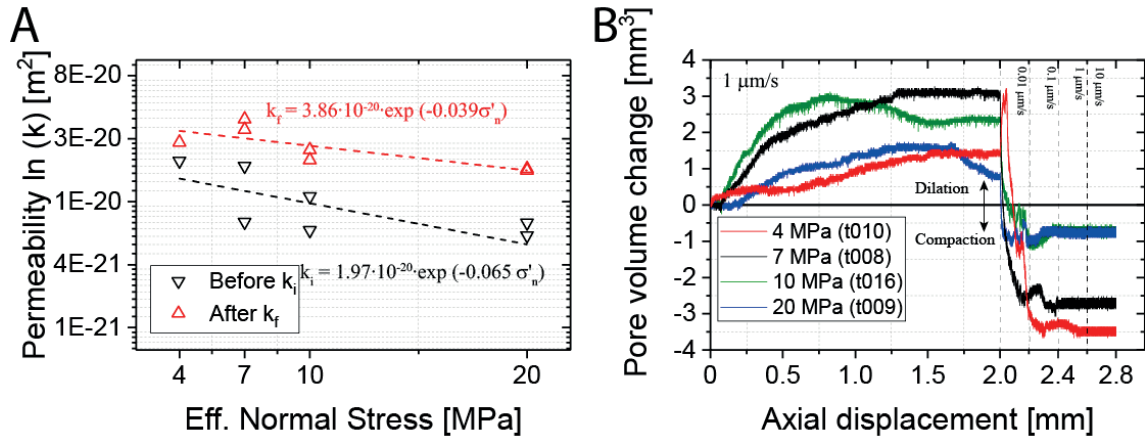


**Figure 4-4:** A) Permeability measurements parallel to the direction of shearing before and after shearing. B) The change in pore volume during shearing for selected samples (t010, t008, t016, t009). Compaction corresponds to negative pore volume change.

## 4.5. DISCUSSION

### 4.5.1. FRICTIONAL STRENGTH

Clays exert a remarkably strong control in reducing the frictional strength of fault rocks (Byerlee, 1978), in particular when the clay content is higher than ~15-30% (Ikari et al., 2007; Tembe et al., 2010). The presence of large amounts of clays in our samples (~50%) is sufficient to explain the overall strength reduction of the simulated fault gouge with respect to the Byerlee's rule ( $\mu \approx 0.85$ ) (Byerlee, 1978), and is also consistent with previous studies on clay-rich materials ( $\mu_f \approx 0.2 - 0.6$ ) (Behnsen & Faulkner, 2012; Crawford et al., 2008; Kohli & Zoback, 2013).

The frictional strength ( $\mu_f$ ) of OPA appears also strongly dependent on whether the sample is dry or wet for the full range of  $\sigma'_n$  tested (Ikari et al., 2007; Morrow et al., 2017). We show that dry samples are weak ( $\mu_f \approx 0.36$ ) and are weaker ( $\mu_f \approx 0.15$ ) when wet. The strong weakening enhanced by the presence of water may be, in addition to re-alignment of clay minerals and shear-localization (Chester & Logan, 1987; Numelin et al., 2007; Saffer et al., 2001), to the lubrication effect of water films within the clay-rich shear planes, as inferred by previous studies (Moore & Lockner, 2004, 2007; Morrow et al., 2000; Tembe et al., 2010).

Previous frictional experiments performed on OPA gouge at a 100% relative humidity (RH) i.e., partially saturated condition (Orellana et al., 2018b) exhibited  $\mu_f$  values between results of this study (Figure 4-3b), which were higher than our values of wet friction, i.e.  $\mu_{f,wet} < \mu_{f,100\%} < \mu_{f,dry}$ . Taken together, our results highlight the strong effect of pressurized water on the frictional weakness of faults hosting OPA, suggesting that small pore fluid or stress field perturbations could result in their activation.

### 4.5.2. FRICTIONAL STABILITY

Previous work on OPA gouge samples has shown velocity-strengthening behavior (Fang et al., 2017, 2018; Orellana et al., 2018b). Our wet sample data is consistent with those studies, and also with others in clay-rich samples (Numelin et al., 2007; Tembe et al., 2010; Morrow et al., 2017; Ikari et al., 2009). Interestingly, within the same range of low  $\sigma'_n$ , our dry gouges are velocity-weakening (stick-slip) at slow velocities ( $\leq 1 \mu\text{m/s}$ ) and experience a shift to velocity-strengthening when increasing sliding velocity ( $\geq 10 \mu\text{m/s}$ ). A few examples in the literature indicate that clay-rich materials are velocity-weakening at slow velocities ( $\leq 20 \mu\text{m/s}$ ). Unstable slip behavior has been observed 1) when clay content is less than 30% (Kohli & Zoback, 2013), 2) under dry conditions and low  $\sigma'_n$  in smectite (Ferri et al., 2011; Saffer et al., 2001; Saffer & Marone, 2003) and montmorillonite-bearing samples (Ikari et al., 2007; Logan & Rauen Zahn, 1987), and 3) due to clay-fabric (Orellana et al., 2018a).

In our tests, velocity-strengthening behavior dominates in wet samples and stick-slip events are observed only in dry gouges at slow sliding velocities. Then, the transition between unstable and stable frictional behavior might be explained in terms of deformation and frictional healing processes that occur depending upon the absence or presence of pore fluids. First, in clays, the re-orientation and preferential alignment of clay minerals along shear planes with shearing result in shear localization and foliation development (Chester & Logan, 1987; Numelin et al., 2007; Saffer et al., 2001). Under dry conditions, cataclastic deformation mechanisms, including frictional sliding, distributed and chaotic granular flow and grain fracturing, are dominant processes (Moore & Lockner, 2007). Thus, our dry samples possibly deform in a mainly distributed manner, resulting in relatively higher friction and cohesion (e.g. grain interlocking). Conversely, the presence of pore fluids in clays facilitates a lubricant effect between grains promoting shear-localization of strain along well defined clay rich-planes (Morrow et al., 2000; Shimamoto & Logan, 1981; Tembe et al., 2010) resulting in lower coefficient of friction and velocity strengthening behavior as observed in our wet gouges (Figure 4-3a, Figure 4-3b, Figure 4-3c). Unfortunately, we were not able to retrieve microstructures to confirm this hypothesis. Moreover, in dry samples, frictional healing processes could partially explain the transition from unstable (stick-slips) to stable sliding that occur at velocities smaller than a reference cut-off velocity  $v_*$  (i.e.,  $v < v_* \approx 10 \mu\text{m/s}$ ). We infer that this velocity-weakening behavior should be expected due to the potential aging of contacts i.e. fault re-strengthening, associated to friction healing processes with slip, namely ploughing, shear-enhanced indentation, shear-enhanced compaction or a combination of them (Marone & Saffer, 2015). When  $v > v_*$ , frictional healing is possibly negligible because it is no more effective at high sliding velocities (Bar-sinai et al., 2014; Kuwano et al., 2013). This observation is also supported by frictional healing rates ( $\beta$ ) previously measured in the same OPA gouge samples during slide-hold-slide tests (Chapter 3, Orellana et al., 2018b). This study shows higher values of  $\beta$  for dry samples than for partially saturated samples i.e.  $\beta_{100RH} < \beta_{dry}$ . In our wet samples, we expect even smaller values of  $\beta$  i.e.  $\beta_{wet} < \beta_{100RH} < \beta_{dry}$ , and therefore null frictional re-strengthening over time, in agreement with the velocity-strengthening behavior observed in our tests (Figure 4-3c). Furthermore, our results show that the magnitude of the  $\Delta\tau$  increases with increasing  $\sigma_n$  (Figure 4-3e). This effect is a consequence of the interplay

between the increase in fault stiffness with  $\sigma_n$  and the constant machine stiffness, as the rate-and-state friction theory predicts (Baumberger & Berthoud, 1999; Leeman et al., 2016)

The stick-slips behavior shown by dry samples, thought characterized by small stress drops ( $\Delta\tau \leq 0.35$  MPa,  $\Delta\tau/\tau \leq 5\%$ ), are manifestations of fault instability (Brace & Byerlee, 1966; Leeman et al., 2016). However, the conditions for instability do not persist as slip velocity increases ( $v_* \geq 10$   $\mu\text{m/s}$ ), as suggested by the transition to velocity-strengthening when increasing velocity, thus inhibiting the potential nucleation of large earthquakes. Additional work is needed to adequately quantify these observations.

Finally, and based on these observations, we infer that faults within the OPA formation under water-saturated conditions will tend to slip stably via aseismic creep. Nonetheless, our results illustrate the key role played by water in stabilizing fault slip, at least at extremely slow velocities.

### 4.5.3. PERMEABILITY EVOLUTION AND SHEAR-ENHANCED DILATION

Values of  $k_{i, //}$  and  $k_{f, //}$  ( $10^{-21} - 10^{-20}$ ) are in the same range as values previously reported for non-deformed rock (Senger et al., 2018; Yu et al., 2017). Our data suggest a shear-enhanced fault-parallel permeability at slow sliding velocities ( $<1$   $\mu\text{m/s}$ ) and at low  $\sigma'_n$  in agreement with previous tests on clay-rich samples (Wu et al., 2017; Zhang & Cox, 2000). This increase suggests that during slip events a fault within the OPA formation could act as a weak conduit with respect to the surrounding non-deformed rock.

Consistent with the permeability increase upon shear deformation, the evolution of pore-volumes during shearing suggests a predominant shear-enhanced dilatancy, during at least the first 2 mm of displacement (Figure 4-4b). When the sliding velocity suddenly decreases to 0.01  $\mu\text{m/s}$  at the beginning of the velocity-steps sequence, shear-enhanced compaction occurs under quasi-stationary contact for  $\sim 5.5$  h., indicating a rearrangement of the pore structure. The velocity- and stress-dependent dilation or compaction observed during the velocity sequences implies a competition between continuous creation and destruction of dilatant regions within the gouge sample related to its velocities history, which in turn will create and destroy fluid-flow pathways that affect permeability. In our tests, the initial dilatancy during the first 2 mm of displacement along with the measured permeability increase after shearing suggests that the shear deformation of the gouge results in the development of weak fluid pathways. More experiments are needed to fully understand the micromechanism governing this competition.

### 4.5.4. IMPLICATIONS FOR NUCLEAR WASTE REPOSITORY

While it is most likely that underground nuclear repositories will be placed far away from fault systems, the identification of these faults remains challenging in shale formations. Therefore, risks associated to fault re-activation and induced-seismicity may result, not only from well-known fault arrays, but also from pre-existing faults that were undetected during the

site characterization process of the project (Husen et al., 2012; Mazzoldi et al., 2012). Associated risks to fault activation persist as a major concern for deep geological repositories that cannot be neglected.

In this study, we have shown that the frictional properties of wet OPA fault gouge are different from the dry counterpart. The wet OPA gouges are extraordinarily weak ( $\mu_f \approx 0.15$ ) and exhibit stable, velocity-strengthening behavior at the different  $\sigma'_n$  that are of interest to possible emplacement depths of nuclear repositories in Switzerland. This extremely low friction suggests that faults in OPA tend to be activated mainly via aseismic creep. Thus, our results might help to explain the induced in-situ fault reactivation at the MTL, however they cannot explain the swarm of triggered seismic events (Guglielmi et al., 2017; Jeanne et al., 2018).

Pore volume changes during shearing indicates shear-enhanced dilation at the onset of fault sliding initiates, in agreement with field-scale experiments at the MT in the OPA formation (Guglielmi et al., 2017; Jeanne et al., 2018). However, small permeability increases are however within the same range of non-deformed rock values, suggesting that the fluid conduit potential for OPA fault-arrays is low.

Tests on dry gouges show a weak ( $\mu_f \approx 0.36$ ) and unstable behavior at slow sliding velocity that evolves to stable behavior as soon as a threshold sliding velocity is overcome ( $v_* \geq 10 \mu\text{m/s}$ ). Natural clay-rich faults in the earth are rarely dry. However, during the operation of the nuclear waste storage facility, near-field drying processes of the host-rock may occur during the early stages of the nuclear waste emplacement affecting the host-rock. Despite this scenario, our results suggest that conditions for a large earthquake are unlikely.

## 4.6. CONCLUSION

Our frictional tests were specifically designed to further understand the frictional and transport properties of fault arrays within the OPA formation under conditions relevant for nuclear waste repositories. Our study significantly expands upon previous work by exploring saturation conditions, permeability and dilatancy evolution during shearing. In this way, we have constrained conditions for fault weakness, unstable behavior, and shear-dilatancy. In summary, our primarily results indicate that:

- a) Dry gouges exhibit a transition from velocity-weakening to strengthening at sliding velocities  $\sim 10 \mu\text{m/s}$ . The magnitude of the stress drops increases with increasing normal stress and decreases with increasing sliding velocities. Since velocity-weakening behavior does not persist at high sliding velocities, unstable slip is restricted to extremely peculiar conditions, rarely met in natural faults, and therefore nucleation of large earthquakes is unlikely to occur.
- b) Experiments on wet gouges show an extremely low friction and an exclusive velocity-strengthening behavior at all sliding velocities and effective normal stresses tested in

this study. This suggests that fault activation may easily occurs within the repository, however fault gouges will slide slowly in an aseismic, stable fashion.

- c) Shear-enhanced dilation is dominant at the onset of shearing. Permeability measurements reveal a slightly higher permeability after shearing, yet partially overlapping values of non-deformed rock ( $10^{-20}$  m<sup>2</sup>). These observations suggest that OPA fault arrays can potentially act as weak conduits.

Further research is required to study chemo-mechanical and hydro-thermal process, and the effect of fault structure to constrain better the frictional behavior, stability and other physical interactions that can affect the long-term feasibility of nuclear waste repositories in the OPA formation.



## 4.7. REFERENCES

- Bar-sinai, Y., Spatschek, R., Brener, E. a, & Bouchbinder, E. (2014). On the velocity-strengthening behavior of dry friction. *Journal of Geophysical Research: Solid Earth*, 119(3), 1738–1748. <https://doi.org/https://doi.org/10.1002/2013JB010586>
- Behnsen, J., & Faulkner, D. (2012). The effect of mineralogy and effective normal stress on frictional strength of sheet silicates. *Journal of Structural Geology*, 42, 49–61. <https://doi.org/10.1016/j.jsg.2012.06.015>
- Bernabé, Y., Mok, U., & Evans, B. (2006). A note on the oscillating flow method for measuring rock permeability. *International Journal of Rock Mechanics and Mining Sciences*, 43(2), 311–316. <https://doi.org/10.1016/j.ijrmms.2005.04.013>
- Bossart, P., Bernier, F., Birkholzer, J., Bruggeman, C., Connolly, P., Dewonck, S., et al. (2017). Mont Terri rock laboratory, 20 years of research: introduction, site characteristics and overview of experiments. *Swiss Journal of Geosciences*, 110(1), 3–22. <https://doi.org/10.1007/s00015-016-0236-1>
- Brace, W. F., & Byerlee, J. D. (1966). Stick Slip as a Mechanism for Earthquakes. *Science*, 153(3739), 990–992.
- Byerlee, J. D. (1978). Friction of rocks. *Pure and Applied Geophysics*, 116(4–5), 615–626. <https://doi.org/10.1007/BF00876528>
- Chester, F. M., & Logan, J. M. (1987). Composite planar fabric of gouge from the Punchbowl Fault, California. *Journal of Structural Geology*, 9(5–6). [https://doi.org/10.1016/0191-8141\(87\)90147-7](https://doi.org/10.1016/0191-8141(87)90147-7)
- Crawford, B. R., Faulkner, D., & Rutter, E. (2008). Strength, porosity, and permeability development during hydrostatic and shear loading of synthetic quartz-clay fault gouge. *Journal of Geophysical Research: Solid Earth*, 113(3), 1–14. <https://doi.org/10.1029/2006JB004634>
- Cuss, R. J., Milodowski, A., & Harrington, J. F. (2011). Fracture transmissivity as a function of normal and shear stress: First results in Opalinus Clay. *Physics and Chemistry of the Earth*, 36(17–18), 1960–1971. <https://doi.org/10.1016/j.pce.2011.07.080>
- Dieterich, J. H. (1978). Time-dependent friction and the mechanics of stick-slip. *Pure and Applied Geophysics PAGEOPH*, 116(4–5), 790–806. <https://doi.org/10.1007/BF00876539>
- Dieterich, J. H. (1979). Modeling of rock friction: 1. Experimental results and constitutive equations. *Journal of Geophysical Research*, 84(9), 2161–2168. <https://doi.org/10.1007/BF00876539>
- Ewing, R. C., Weber, W. J., & Clinard, F. W. (1995). Radiation effects in nuclear waste forms for high-level radioactive waste. *Progress in Nuclear Energy*, 29(2), 63–127. [https://doi.org/10.1016/0149-1970\(94\)00016-Y](https://doi.org/10.1016/0149-1970(94)00016-Y)
- Fang, Y., Elsworth, D., Wang, C., Ishibashi, T., & Fitts, J. P. (2017). Frictional stability-

- permeability relationships for fractures in shales. *Journal of Geophysical Research: Solid Earth*, 122(3), 1760–1776. <https://doi.org/10.1002/2016JB013435>
- Fang, Y., Elsworth, D., Wang, C., & Jia, Y. (2018). Mineralogical Controls on Frictional Strength, Stability, and Shear Permeability Evolution of Fractures. *Journal of Geophysical Research: Solid Earth*, (2), 3549–3563. <https://doi.org/10.1029/2017JB015338>
- Faulkner, D., & Rutter, E. (1998). The gas permeability of clay-bearing fault gouge at 20°C. *Geological Society, London, Special Publications*, 147(1), 147–156. <https://doi.org/10.1144/GSL.SP.1998.147.01.10>
- Faulkner, D., & Rutter, E. (2000). Comparisons of water and argon permeability in natural clay-bearing fault gouge under high pressure at 20°C. *Journal of Geophysical Research*, 105(B7), 16415. <https://doi.org/10.1029/2000JB900134>
- Faulkner, D., Sanchez-Roa, C., Boulton, C., & Den Hartog, S. A. M. (2018). Pore Fluid Pressure Development in Compacting Fault Gouge in Theory, Experiments, and Nature. *Journal of Geophysical Research: Solid Earth*, 123(1), 226–241. <https://doi.org/10.1002/2017JB015130>
- Ferri, F., Di Toro, G., Hirose, T., Han, R., Noda, H., Shimamoto, T., et al. (2011). Low- to high-velocity frictional properties of the clay-rich gouges from the slipping zone of the 1963 Vaiont slide, northern Italy. *Journal of Geophysical Research: Solid Earth*, 116(9), 1–17. <https://doi.org/10.1029/2011JB008338>
- Fischer, G. J. (1992). The determination of permeability and storage capacity: Pore pressure oscillation method. In B. Evans & T.-F. Wong (Eds.), *Fault mechanics and transport properties of rocks* (pp. 187–212). New York: Academic Press.
- French, M. E., Chester, F. M., & Chester, J. S. (2015). Micromechanisms of creep in clay-rich gouge from the Central Deforming Zone of the San Andreas Fault. *Journal of Geophysical Research: Solid Earth*, 120(2), 827–849. <https://doi.org/10.1002/2014JB011496>
- Guglielmi, Y., Birkholzer, J., Rutqvist, J., Jeanne, P., & Nussbaum, C. (2017). Can Fault Leakage Occur before or Without Reactivation? Results from an in Situ Fault Reactivation Experiment at Mont Terri. *Energy Procedia*, 114(November 2016), 3167–3174. <https://doi.org/10.1016/j.egypro.2017.03.1445>
- Haines, S., Marone, C., & Saffer, D. (2014). Frictional properties of low-angle normal fault gouges and implications for low-angle normal fault slip. *Earth and Planetary Science Letters*, 408, 57–65. <https://doi.org/10.1016/j.epsl.2014.09.034>
- Husen, S., Kissling, E., & von Deschanden, A. (2012). Induced seismicity during the construction of the Gotthard Base Tunnel, Switzerland: Hypocenter locations and source dimensions. *Journal of Seismology*, 17(1), 63–81. <https://doi.org/10.1007/s10950-012-9313-8>
- Ikari, M. J., Saffer, D., & Marone, C. (2007). Effect of hydration state on the frictional properties of montmorillonite-based fault gouge. *Journal of Geophysical Research: Solid Earth*, 112(6), 1–12. <https://doi.org/10.1029/2006JB004748>

- Ikari, M. J., Saffer, D., & Marone, C. (2009). Frictional and hydrologic properties of clay-rich fault gouge. *Journal of Geophysical Research: Solid Earth*, 114(5), 1–18. <https://doi.org/10.1029/2008JB006089>
- Jaeger, J., Cook, N. G., & Zimmerman, R. (2007). *Fundamentals of Rock Mechanics*, 4th Edition (4th Editio). Blackwell Publishing.
- Jeanne, P., Guglielmi, Y., Rutqvist, J., Nussbaum, C., & Birkholzer, J. (2017). Field characterization of elastic properties across a fault zone reactivated by fluid injection. *Journal of Geophysical Research: Solid Earth*, 122(8), 6583–6598. <https://doi.org/10.1002/2017JB014384>
- Jeanne, P., Guglielmi, Y., Rutqvist, J., Nussbaum, C., & Birkholzer, J. (2018). Permeability Variations Associated With Fault Reactivation in a Claystone Formation Investigated by Field Experiments and Numerical Simulations. *Journal of Geophysical Research: Solid Earth*, 123(2), 1694–1710. <https://doi.org/10.1002/2017JB015149>
- Kim, J.-S., Kwon, S.-K., Sanchez, M., & Cho, G.-C. (2011). Geological storage of high level nuclear waste. *KSCE Journal of Civil Engineering*, 15(4), 721–737. <https://doi.org/10.1007/s12205-011-0012-8>
- Kohli, A. H., & Zoback, M. D. (2013). Frictional properties of shale reservoir rocks. *Journal of Geophysical Research: Solid Earth*, 118(9), 5109–5125. <https://doi.org/10.1002/jgrb.50346>
- Kuwano, O., Ando, R., & Hatano, T. (2013). Crossover from negative to positive shear rate dependence in granular friction. *Geophysical Research Letters*, 40(7), 1295–1299. <https://doi.org/10.1002/grl.50311>
- Leeman, J., Saffer, D., Scuderi, M. M., & Marone, C. (2016). Laboratory observations of slow earthquakes and the spectrum of tectonic fault slip modes. *Nature Communications*, 7, 1–6. <https://doi.org/10.1038/ncomms11104>
- Lefèvre, M., Guglielmi, Y., Henry, P., Dick, P., & Gout, C. (2016). Calcite veins as an indicator of fracture dilatancy and connectivity during strike-slip faulting in Toarcian shale (Tournemire tunnel, Southern France). *Journal of Structural Geology*, 83, 73–84. <https://doi.org/10.1016/j.jsg.2016.01.002>
- Lockner, D. A., Morrow, C., Moore, D., & Hickman, S. (2011). Low strength of deep San Andreas fault gouge from SAFOD core. *Nature*, 472(7341), 82–86. <https://doi.org/10.1038/nature09927>
- Logan, J. M., & Rauenzahn, K. A. (1987). Frictional dependence of gouge mixtures of quartz and montmorillonite on velocity, composition and fabric. *Tectonophysics*, 144(1–3), 87–108. [https://doi.org/10.1016/0040-1951\(87\)90010-2](https://doi.org/10.1016/0040-1951(87)90010-2)
- Marone, C. (1998). Laboratory-Derived Friction Laws and Their Application To Seismic Faulting. *Annual Review of Earth and Planetary Sciences*, 26(1), 643–696. <https://doi.org/10.1146/annurev.earth.26.1.643>
- Marone, C., & Saffer, D. (2015). *The Mechanics of Frictional Healing and Slip Instability*

- During the Seismic Cycle. Treatise on Geophysics: Second Edition* (Vol. 4). Elsevier B.V. <https://doi.org/10.1016/B978-0-444-53802-4.00092-0>
- Mazzoldi, A., Rinaldi, A. P., Borgia, A., & Rutqvist, J. (2012). Induced seismicity within geological carbon sequestration projects: Maximum earthquake magnitude and leakage potential from undetected faults. *International Journal of Greenhouse Gas Control*, 10, 434–442. <https://doi.org/10.1016/j.ijggc.2012.07.012>
- Moore, D., & Lockner, D. A. (2004). Crystallographic controls on the frictional behavior of dry and water-saturated sheet structure minerals. *Journal of Geophysical Research*, 109(B3), B03401. <https://doi.org/10.1029/2003JB002582>
- Moore, D., & Lockner, D. A. (2007). Friction of the smectite clay montmorillonite: A review and interpretation of data. In T. Dixon & C. Moore (Eds.), *The Seismogenic Zone of Subduction Thrust Faults* (pp. 317–345). Columbia University Press. <https://doi.org/10.7312/dixo13866-011>
- Morrow, C., Shi, L. Q., & Byerlee, J. D. (1982). Strain hardening and strength of clay-rich fault gouges. *Journal of Geophysical Research*, 87(B8), 6771–6780. <https://doi.org/10.1029/JB087iB08p06771>
- Morrow, C., Moore, D., & Lockner, D. A. (2000). The effect of mineral bond strength and adsorbed water on fault gouge frictional strength. *Geophysical Research Letters*, 27(6), 815–818. <https://doi.org/10.1029/1999GL008401>
- Morrow, C., Moore, D., & Lockner, D. A. (2017). Frictional strength of wet and dry montmorillonite. *Journal of Geophysical Research: Solid Earth*, 122(5), 3392–3409. <https://doi.org/10.1002/2016JB013658>
- Niemeijer, A., & Collettini, C. (2013). Frictional Properties of a Low-Angle Normal Fault Under In Situ Conditions: Thermally-Activated Velocity Weakening. *Pure and Applied Geophysics*, 171(10), 2641–2664. <https://doi.org/10.1007/s00024-013-0759-6>
- Niemeijer, A., & Vissers, R. L. M. (2014). Earthquake rupture propagation inferred from the spatial distribution of fault rock frictional properties. *Earth and Planetary Science Letters*, 396, 154–164. <https://doi.org/10.1016/j.epsl.2014.04.010>
- Noda, H., & Shimamoto, T. (2009). Constitutive properties of clayey fault gouge from the Hanaore fault zone, southwest Japan. *Journal of Geophysical Research: Solid Earth*, 114(4), 1–29. <https://doi.org/10.1029/2008JB005683>
- Norris, S. (2017). Radioactive waste confinement: Clays in natural and engineered barriers - introduction. *Geological Society Special Publication*, 443(1), 1–8. <https://doi.org/10.1144/SP443.26>
- Numelin, T., Marone, C., & Kirby, E. (2007). Frictional properties of natural fault gouge from a low-angle normal fault, Panamint Valley, California. *Tectonics*, 26(2), n/a-n/a. <https://doi.org/10.1029/2005TC001916>
- Nussbaum, C., Bossart, P., Amann, F., & Aubourg, C. (2011). Analysis of tectonic structures and excavation induced fractures in the Opalinus Clay, Mont Terri underground rock

- laboratory (Switzerland). *Swiss Journal of Geosciences*, 104(2), 187–210. <https://doi.org/10.1007/s00015-011-0070-4>
- Orellana, L. F., Scuderi, M. M., Collettini, C., & Violay, M. (2018a). Do scaly clays control seismicity on faulted shale rocks? *Earth and Planetary Science Letters*, 488, 59–67. <https://doi.org/10.1016/j.epsl.2018.01.027>
- Orellana, L. F., Scuderi, M. M., Collettini, C., & Violay, M. (2018b). Frictional Properties of Opalinus Clay: Implications for Nuclear Waste Storage. *Journal of Geophysical Research: Solid Earth*, 123(1), 157–175. <https://doi.org/10.1002/2017JB014931>
- Rabinowicz, E. (1951). The nature of the static and kinetic coefficients of friction. *Journal of Applied Physics*, 22(11), 1373–1379. <https://doi.org/10.1063/1.1699869>
- Ruina, A. (1983). Slip instability and state variable friction laws. *Journal of Geophysical Research*, 88(B12), 10359. <https://doi.org/10.1029/JB088iB12p10359>
- Rutter, E., & Mecklenburgh, J. (2018). Influence of Normal and Shear Stress on the Hydraulic Transmissivity of Thin Cracks in a Tight Quartz Sandstone, a Granite, and a Shale. *Journal of Geophysical Research: Solid Earth*, 123(2), 1262–1285. <https://doi.org/10.1002/2017JB014858>
- Rutter, E., Holdsworth, R., & Knipe, R. J. (2001). The nature and tectonic significance of fault-zone weakening: an introduction. *Geological Society, London, Special Publications*, 186(1), 1 LP-11. Retrieved from <http://sp.lyellcollection.org/content/186/1/1.abstract>
- Saffer, D., & Marone, C. (2003). Comparison of smectite- and illite-rich gouge frictional properties: Application to the updip limit of the seismogenic zone along subduction megathrusts. *Earth and Planetary Science Letters*, 215(1–2), 219–235. [https://doi.org/10.1016/S0012-821X\(03\)00424-2](https://doi.org/10.1016/S0012-821X(03)00424-2)
- Saffer, D., Frye, K. M., Marone, C., & Mair, K. (2001). Laboratory results indicating complex and potentially unstable frictional behavior of smectite clay. *Geophysical Research Letters*, 28(12), 2297–2300. <https://doi.org/10.1029/2001GL012869>
- Samuelson, J., Elsworth, D., & Marone, C. (2009). Shear-induced dilatancy of fluid-saturated faults: Experiment and theory. *Journal of Geophysical Research: Solid Earth*, 114(12), 1–15. <https://doi.org/10.1029/2008JB006273>
- Sanchez-Roa, C., Faulkner, D., Boulton, C., Jimenez-Millan, J., & Nieto, F. (2017). How phyllosilicate mineral structure affects fault strength in Mg-rich fault systems. *Geophysical Research Letters*, 44(11), 5457–5467. <https://doi.org/10.1002/2017GL073055>
- Scholz, C. H. (2002). *The Mechanics of Earthquakes and Faulting*. Cambridge University Press. Retrieved from <https://books.google.ch/books?id=JL1VM5wMbrQC>
- Senger, R., Romero, E., & Marschall, P. (2018). Modeling of Gas Migration Through Low-Permeability Clay Rock Using Information on Pressure and Deformation from Fast Air Injection Tests. *Transport in Porous Media*, 1–17. <https://doi.org/10.1007/s11242-017-0962-5>



- Shimamoto, T., & Logan, J. M. (1981). Effects of simulated clay gouges on the sliding behavior of Tennessee sandston. *Tectonophysics*, 75(3–4), 243–255. [https://doi.org/10.1016/0040-1951\(81\)90276-6](https://doi.org/10.1016/0040-1951(81)90276-6)
- Tembe, S., Lockner, D. A., & Wong, T. F. (2010). Effect of clay content and mineralogy on frictional sliding behavior of simulated gouges: Binary and ternary mixtures of quartz, illite, and montmorillonite. *Journal of Geophysical Research: Solid Earth*, 115(3), 1–22. <https://doi.org/10.1029/2009JB006383>
- Tsang, C.-F., Bernier, F., & Davies, C. (2005). Geohydromechanical processes in the Excavation Damaged Zone in crystalline rock, rock salt, and indurated and plastic clays - In the context of radioactive waste disposal. *International Journal of Rock Mechanics and Mining Sciences*, 42(1), 109–125. <https://doi.org/10.1016/j.ijrmms.2004.08.003>
- Tsang, C.-F., Neretnieks, I., & Tsang, Y. (2015). Hydrologic issues associated with nuclear waste repositories. *Water Resources Research*, 51(9), 6923–6972. <https://doi.org/10.1002/2015WR017641>
- Wang, W. L., Wang, T. T., Su, J. J., Lin, C. H., Seng, C. R., & Huang, T. H. (2001). Assessment of damage in mountain tunnels due to the Taiwan Chi-Chi Earthquake. *Tunnelling and Underground Space Technology*, 16(3), 133–150. [https://doi.org/10.1016/S0886-7798\(01\)00047-5](https://doi.org/10.1016/S0886-7798(01)00047-5)
- Wu, W., Reece, J. S., Gensterblum, Y., & Zoback, M. D. (2017). Permeability Evolution of Slowly Slipping Faults in Shale Reservoirs. *Geophysical Research Letters*, 44(22), 11,368–11,375. <https://doi.org/10.1002/2017GL075506>
- Yu, C., Matray, J. M., Gonçalves, J., Jaeggi, D., Gräsle, W., Wieczorek, K., et al. (2017). Comparative study of methods to estimate hydraulic parameters in the hydraulically undisturbed Opalinus Clay (Switzerland). *Swiss Journal of Geosciences*, 110(1), 85–104. <https://doi.org/10.1007/s00015-016-0257-9>
- Zhang, S., & Cox, S. F. (2000). Enhancement of fluid permeability during shear deformation of a synthetic mud. *Journal of Structural Geology*, 22(10), 1385–1393. [https://doi.org/10.1016/S0191-8141\(00\)00065-1](https://doi.org/10.1016/S0191-8141(00)00065-1)



## 5.

# DO SCALY CLAYS CONTROL SEISMICITY IN SHALES?

**Authors:** Luis Felipe Orellana<sup>1\*</sup>, Marco Maria Scuderi<sup>2, 3</sup>, Cristiano Collettini<sup>2, 3</sup>, and Marie Violay<sup>1</sup>

<sup>1</sup> Laboratory of Experimental Rock Mechanics (LEMR), ENAC, EPFL, Switzerland;

<sup>2</sup> Dipartimento di Scienze della Terra, Università degli Studi La Sapienza, Rome, Italy;

<sup>3</sup> Istituto Nazionale di Geofisica e Vulcanologia (INGV), Italy;

**Reference:** Orellana, L.F., Scuderi, M.M., Collettini, C., Violay, M., 2018. Do scaly clays control seismicity on faulted shale rocks? *Earth Planet. Sci. Lett.* 488, 59–67. doi: 10.1016/j.epsl.2018.01.027

**Contributions:** L. F. Orellana has collected, prepared and characterized samples used in this study. M.M. Scuderi and L. F. Orellana have run the experiments. All authors have contributed to the testing strategy and methodology. L. F. Orellana has carried out microstructural observations and modelled results. L. F. Orellana has written the manuscript. M. M. Scuderi, C. Collettini and M. Violay have edited and guided discussions of the manuscript. M. Violay has acted as a supervisor and main responsible author of the publication.

### Highlights:

- Frictional properties of the fault zone intersecting the Opalinus Clay formation.
- Scaly clays form from frictional sliding of experimental layered clay intact samples.
- Low frictional strength, near-zero healing values, and velocity weakening behaviour.
- Small, but rare nucleation of earthquakes within the scaly clays.

**Keywords:** Scaly clays, mirror-like surfaces, frictional behaviour of shales, anthropogenic seismicity, deep geological repositories.

## 5.1. ABSTRACT

One of the major challenges regarding the disposal of radioactive waste in geological formations is to ensure isolation of radioactive contamination from the environment and the population. Shales are suitable candidates as geological barriers. However, the presence of tectonic faults within clay formations put the long-term safety of geological repositories into question. In this study, we carry out frictional experiments on intact samples of Opalinus Clay, i.e. the host rock for nuclear waste storage in Switzerland. We report experimental evidence suggesting that scaly clays form at low normal stress ( $\leq 20$  MPa), at sub-seismic velocities ( $\leq 300$   $\mu\text{m/s}$ ) and is related to pre-existing bedding planes with an ongoing process where frictional sliding is the controlling deformation mechanism. We have found that scaly clays show a velocity-weakening and -strengthening behaviour, low frictional strength, and poor re-strengthening over time, conditions required to allow the potential nucleation and propagation of earthquakes within the scaly clays portion of the formation. The strong similarities between the microstructures of natural and experimental scaly clays suggest important implications for the slip behaviour of shallow faults in shales. If natural and anthropogenic perturbations modify the stress conditions of the fault zone, earthquakes might have the potential to nucleate within zones of scaly clays controlling the seismicity of the clay-rich tectonic system, thus, potentially compromising the long-term safeness of geological repositories situated in shales.

## 5.2. INTRODUCTION

In Switzerland, the Mont Terri Laboratory (MTL) is the research program for the study of deep geological repositories in shale rocks (Bossart et al., 2017; Nussbaum et al., 2011, 2017). The Mont Terri Laboratory (Figure 5-1a) is emplaced ~300 m underground within the Opalinus Clay (OPA) formation, an argillaceous rock located throughout the northern part of Switzerland.

Deep geological repositories are considered worldwide as a suitable solution for the safe storage of high-level nuclear waste. As geological barriers, hosting rocks need to be sufficiently thick and impermeable to minimise gas diffusion and radiation over geological timescales. Moreover, they need to be seismically safe to avoid hazards such as fault activation, induced seismicity, and contamination of aquifers due to the leakage of radionuclides through networks of fractures associated with fault zones (Tsang et al., 2012).

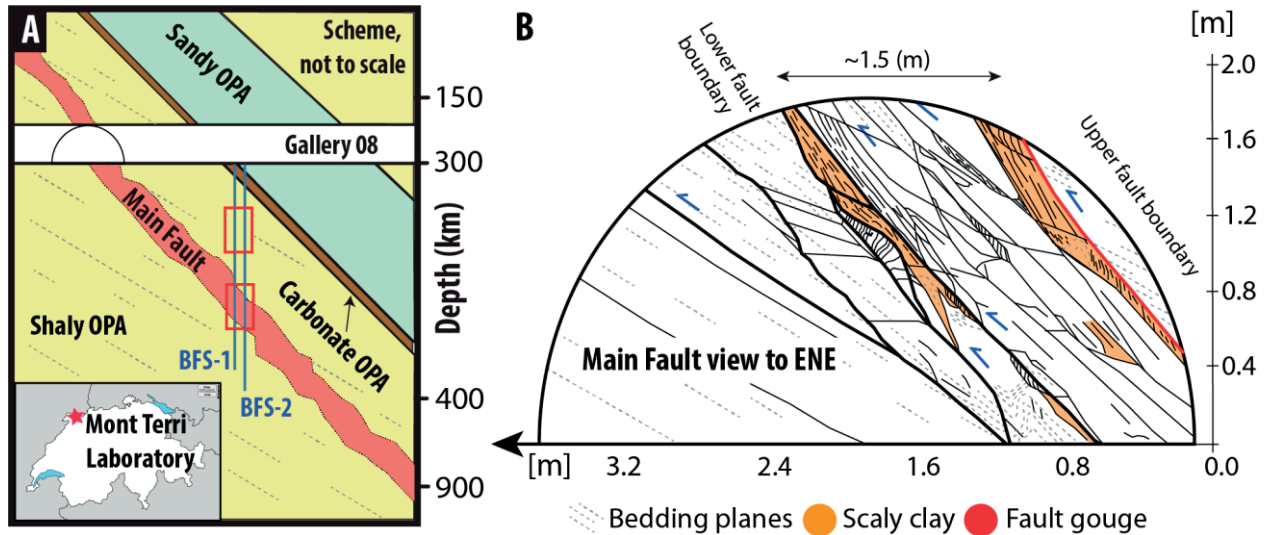


**Figure 5-1:** The Main Fault. A) A cross-section of the Main Fault that intersects the Mont Terri Laboratory (MTL) in the clay-rich facies of the OPA formation (shaly OPA). Gray lines are bedding planes oriented 15° on average from the fault zone. The red box indicates the position of the samples used in this study. Black semicircle in gallery 08 indicates the position of Figure 1B. The inset shows the location of the MTL, in the north part of Switzerland. B) Scheme of the Main Fault intersecting the gallery 08 at the MTL modified from Nussbaum et al., (2011).

Following the seismic hazard assessment map introduced by Giardini et al., (2014), Switzerland is characterised as a moderate to high- hazardous country. Indeed, the latest data published by the Swiss Seismological Service (SED) indicates that during 2014 a total of 977 earthquakes were recorded and 22 events had magnitude  $M_w \geq 2.3$  (Diehl et al., 2015). Moreover, the largest earthquake ever documented in Switzerland is the 1356 Basel earthquake with an estimated magnitude of 6.0 – 7.1 (Monecke et al., 2004). Recently, an earthquake of  $M_w$  4.5 (focal depth of 12 km) occurred in 2004 close to the location of the Mont Terri Laboratory (Baer et al., 2005; Nussbaum et al., 2011). Also, several others have been recorded near possible geological sites

areas (Diehl et al., 2014, 2015). Overall, these data support the view that earthquakes are an important source of risk for nuclear waste repositories.

At the Mont Terri Laboratory, the largest tectonic structure intersecting galleries is a thrust fault named the Main Fault (Figure 5-1b) (Nussbaum et al., 2011). Samples that were taken from boreholes BFS-1 and BFS-2 reveal that the Main Fault is characterised by a highly fractured zone that extends ~1.5 m and by a complex fault-core assemblage. From the fault damage zone to the fault core, we can find undisturbed rocks, ubiquitous fractures, calcite veins, scaly clays, and fault gouges.

An anisotropic mechanical behaviour characterises the undisturbed rock due to the presence of bedding planes (Bossart et al., 2017; Salager et al., 2013). Among the structural elements of the fault-core, the scaly clays are characterised by a scaly clay fabric consisting of an array of anastomosing, polished/mirror-like surfaces, commonly undulated, smooth, and striated (Laurich et al., 2014; Vannucchi et al., 2003). The fault gouge is an in-cohesive, dark, ultra-fine-grained partially continuous band of 8-12 mm thickness (Laurich et al., 2014; Nussbaum et al., 2011), frequently surrounded by scaly clays. This description of the boreholes is in agreement with previous characterisations of the Main Fault at the Gallery 08 of the Mont Terri Laboratory (Fig. 1B, Nussbaum et al., 2011; Laurich et al., 2014).

Because of its complex fault structure, the question of how the Main Fault can accommodate deformation is still unclear. Indeed, the fact that the Main Fault contains such different mixture of rock materials, and therefore a complex spatial distribution of physical properties, leads to the question of whether the shear displacement is accommodated by continuous aseismic creep, standard earthquakes or a combination of both (Fagereng & Sibson, 2010).

Numerous studies on the mechanical behavior of clay-rich gouges suggest that most of them are frictionally weak, they show a lack of re-strengthening over time, and they are inherently stable, velocity-strengthening materials (Haines et al., 2014; Ikari et al., 2009; Kohli & Zoback, 2013; Tesei et al., 2012). Similarly, recent experiments have been performed on fault gouge composed of Opalinus clay showing a low frictional strength, low healing rates, and a velocity-strengthening behaviour (Orellana et al., 2018, see Supp. material). Also, while clay-rich velocity-strengthening materials generally inhibit the nucleation of earthquakes, the propagation of co-seismic slip through clay-rich zones at shallow depths might still be possible if fracture energy conditions are favourable (Faulkner et al., 2011).

On the other hand, the mechanical behaviour of scaly clays is still poorly understood. Thin and interconnected layers of phyllosilicates may result in large weakness of natural fault rocks (Carpenter et al., 2011; Collettini et al., 2009; Schleicher et al., 2010), thus, enhancing co-seismic slip propagation during earthquakes as observed during the large co-seismic displacements

occurred in the slip zone of the 2011 Tohoku-Oki earthquake (Chester et al., 2013; Ujiie et al., 2013). Moreover, for different types of rocks, mirror-like surfaces (a distinctive feature of scaly clays) have been associated with seismic faulting (Chen et al., 2013; Evans et al., 2014; Fondriest et al., 2013; Green et al., 2015; Kuo et al., 2016; Siman-Tov et al., 2015). On the contrary, the scaly clays are related to the aseismic creep behaviour of major faults such as the San Andreas complex (Carpenter et al., 2011; Schleicher et al., 2010).

In this paper, we document the conditions for unstable sliding of the Main Fault associated with the velocity-weakening behaviour of the scaly clays develop after shearing intact samples of OPA at sub-surface conditions and sub-seismic velocities. After integrating the mechanical data with the microstructural observations, we suggest that the frictional behaviour of scaly clays is a key factor controlling the seismic behaviour of clay-bearing faults.

### 5.3. MATERIAL AND METHODS

To understand the frictional and stability behaviour of the scaly clays, we have performed laboratory experiments in a biaxial rock deformation apparatus (BRAVA, INGV Rome) using a double-direct shear configuration (Collettini et al., 2014) (Figure 5-2a). In this configuration, two wafers of intact rock were sandwiched in a three steel block assembly with a nominal contact area of 25 cm<sup>2</sup> (Figure 5-2b). In BRAVA, two servo-hydraulic rams were used to apply the horizontal and vertical forces. The loads were measured using strain gauge load cells (accuracy  $\pm 0.03$  kN), in contact with the sample assembly. Vertical and horizontal displacements were measured using Linear Variable Displacement Transformers (LVDTs) (accuracy of  $\pm 0.1$   $\mu$ m).

<b>Mineralogy</b>	<b>Scaly clay (Wt %)</b>	<b>Intact rock (Wt %)</b>
<b>Phyllosilicates</b>	49.3	50.8
<b>Quartz</b>	20.6	23.0
<b>Calcite</b>	17.5	14.2
<b>Pyrite</b>	1.4	1.4
<b>Others</b>	11.2	10.6

**Table 5-1:** Comparison of the mineralogical content (wt %) of the natural scaly clays and the intact rock of the Opalinus Clay formation (also in Chapter 2).

We have recovered intact (non-deformed) and natural scaly clay samples from the boreholes BFS-1 and BFS-2 that cross-cut the Main Fault zone (Figure 5-1a). The mineralogical composition of the samples was determined by X-Ray diffraction (XRD) analysis at the Geological Institute of the University of Lausanne (UNIL), Switzerland. The mineralogy of the intact and natural scaly clay samples (Table 5-1) reveals similar proportions of clay minerals (~50%), quartz (~22%), and calcite (~16%).

We have conducted experiments on intact samples. We carefully cut the intact samples ( $5 \times 5 \times 1 \text{ cm}^3$ ) to ensure shear parallel and perpendicular to the bedding planes, representing the two main directions of shear where we have hypothesised deformation might occur in the scaly clays. We have kept the samples under *in-situ* saturation conditions before, and during the experiments (using water at chemical equilibrium with the rock), however, local pore pressures within the samples were not controlled during tests due to experimental constraints.

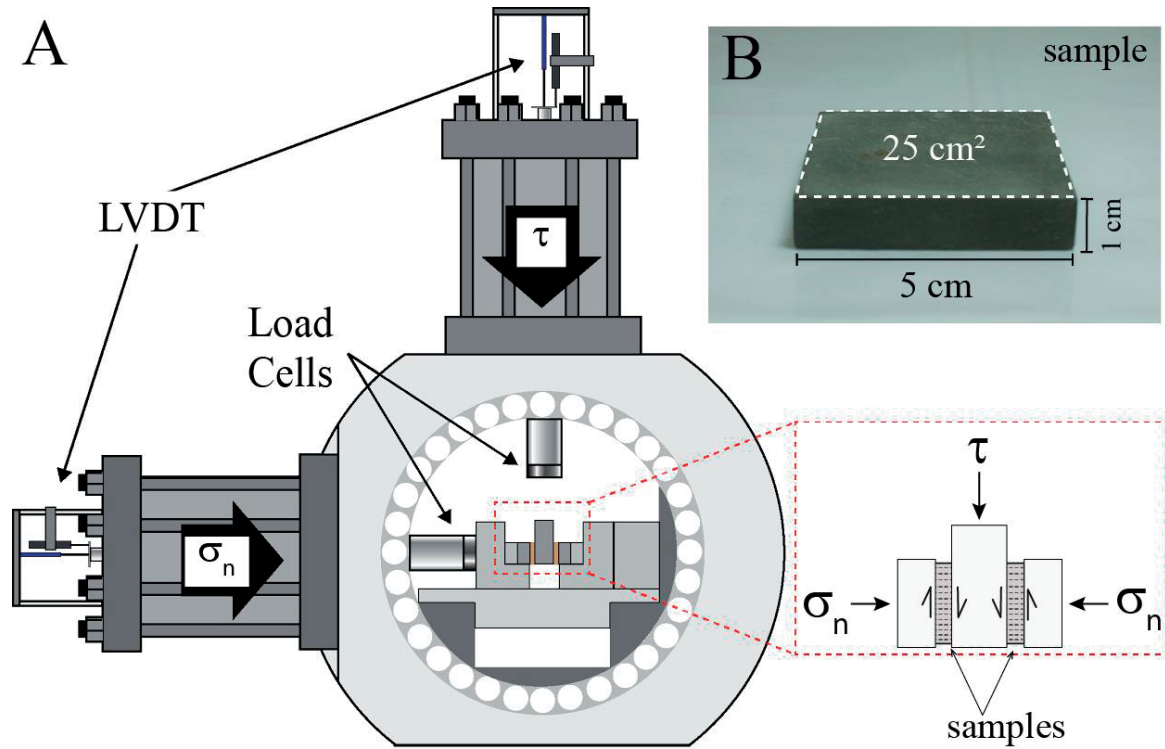


**Figure 5-2:** Experimental setup. A) The double-direct shear configuration in BRAVA modified after Collettini et al. (2014). Dashed red box shows the position of the samples and orientation of stresses. B) Experimental samples. Samples have a nominal contact area of  $\sim 25 \text{ cm}^2$  and are 1 cm thick.

We have performed friction experiments at different normal stresses ( $\sigma_n$ ), from 4 to 20 MPa and at room temperature (Figure 5-3a, Table 5-2). At the beginning of each test, the normal load was applied and maintained constant throughout the experiments. When sample thickness reached a quasi-steady state, the samples were sheared at a constant displacement rate of  $10 \text{ } \mu\text{m/s}$ , following a common computer-controlled displacement history.

We have calculated frictional strength ( $\mu$ ), defined as the ratio of shear stress ( $\tau$ ) to normal stress ( $\sigma_n$ ) and assuming no cohesion. During shearing, the samples were deformed quasi-elastically



with increasing displacement until a peak strength ( $\mu_{peak}$ ) followed by an evolution to a steady state sliding friction ( $\mu_{ss}$ ). The steady state friction was calculated after the experimental fault accumulated between 5 to 6 mm of shear displacement (Figure 5-3a).

Experiment	Bedding orientation	Normal stress (MPa)	Velocity-step tests (μm/s)	Slide-hold-slide (s)
b537	Parallel	4	1, 3, 10, 30, 100, 300	3,10,30,100,300,1000,3000,10000
i451		7		
b614		10		
b533		20		
b731		7	Experiment stopped after 0.5 cm displacement.	
b732		10		
b539	Perpendicular	4	1, 3, 10, 30, 100, 300	3,10,30,100,300,1000,3000,10000
i446		7		
b538		10		
b536		20		

**Table 5-2:** List of experiments. Slide-hold-slide tests of experiments i451 and i446 have been carried out until hold time 3000 s.

At this stage (except for experiments b732 and b731) we have conducted velocity step tests, with velocities ranging from 1 to 300  $\mu\text{m/s}$  (Table 5-2), to study the velocity-dependence of friction (e.g. Marone, 1998; Scholz, 2002). Each velocity-step (Figure 5-3b) was then modelled using an inversion algorithm (Reinen & Weeks, 1993) following the Ruina's slip dependent empirical evolution law (Ruina, 1983):

$$\mu = \mu_o + a \cdot \ln\left(\frac{V}{V_o}\right) + b \cdot \ln\left(\frac{V_o \cdot \theta}{D_c}\right)$$

**Equation 5-1:** Rate and state constitutive empirical law

$$\frac{d\theta}{dt} = -\frac{V \cdot \theta}{D_c} \cdot \ln\left(\frac{V_o \cdot \theta}{D_c}\right)$$

**Equation 5-2:** Ruina's evolution law (Ruina, 1983)

Where  $\mu_o$  is a reference friction value at slip velocity  $V_o$ ,  $\mu$  is the friction at the new steady state velocity  $V$ ,  $\theta$  can be interpreted as the average lifetime of contacts, and  $a$  and  $b$  are empirical parameters (Dieterich, 1979; Rabinowicz, 1951; Scholz, 2002). The critical slip distance  $D_c$  is interpreted as the slip necessary to renew the asperities on the surface contacts at a constant velocity  $V$  (Marone, 1998).

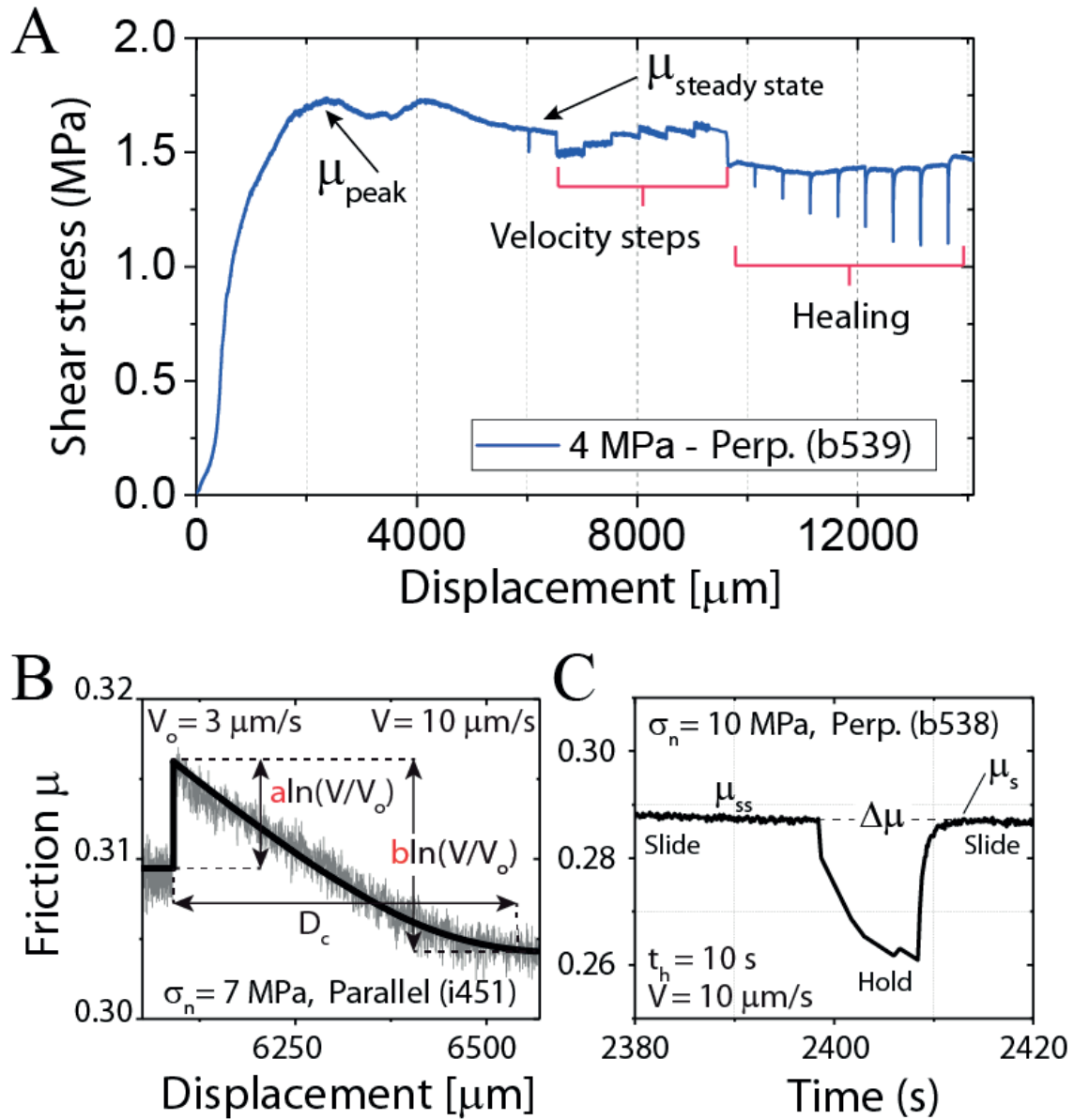


**Figure 5-3:** A) Representative friction experiment (sample sheared perpendicular to bedding at 4 MPa normal stress). The curve shows the evolution of shear stress with displacement, the velocity-step, and the slide-hold-tests. During shearing, friction reaches a peak value ( $\mu_{\text{peak}}$ ) and then evolves to a steady-state ( $\mu_{\text{ss}}$ ) condition. B) Example of frictional parameter (a-b) modelling using the Ruina's empirical law in sample sheared parallel to bedding at 20 MPa. C) Example of frictional healing during hold time of 10 s in sample sheared perpendicular to bedding at 10 MPa normal stress indicating almost null re-strengthening on time.

We have used the friction rate parameter  $(a - b) = \frac{\Delta\mu_{ss}}{\ln(\frac{V}{V_0})}$  to determine the velocity dependence of friction, where  $\Delta\mu_{ss}$  is the change in the steady-state friction coefficient upon an instantaneous change in sliding velocity from  $V_0$  to  $V$  (Marone, 1998; Scholz, 2002). If  $(a - b)$  is positive, it indicates a velocity-strengthening behavior, i.e. stable slip, whilst a negative value of  $(a - b)$ , indicates a velocity-weakening behavior, i.e. potentially unstable slip.

Following the velocity-step sequence, we have performed slide-hold-slide tests to study the time-dependent healing properties of the samples. The test consists of alternating stages where the sample is sheared at constant displacement rate of  $10\mu\text{m/s}$  (slide) with hold periods ( $t_h$ ) where the vertical ram is stopped for a prescribed amount of time. This time in our experiments varied between 3 to 10000 s (Table 5-2). We have calculated the rate of frictional healing  $\beta = \frac{\Delta\mu}{\Delta \log_{10}(t_h)}$  from the slide-hold-slide tests where  $\Delta\mu$  is measured as the difference between the peak friction measured upon re-shear after each hold period  $t_h$  (3 to 10000 seconds) and the pre-hold steady-state friction (Figure 5-3c). Positive healing rates imply fault strengthening between inter-seismic periods (Marone, 1998; Scholz, 2002).

To gain insight into the deformation mechanisms that govern deformation, we have performed detailed microstructural observations at the optical, secondary electron (SE), and backscattered (BSE) microscope. To constrain the roughness of the post-mortem samples, we have measured the root mean square height parameter ( $Sq$ ) of the slip surfaces using an optical contactless profilometer (UBM) following the norm ISO 25178.

## 5.4. RESULTS

### 5.4.1. MECHANICAL RESULTS

All results are presented in Table 5-3 and Table 5-4 for samples sheared parallel and perpendicular to bedding respectively. We document that peak ( $\mu_{peak}$ ) and steady-state ( $\mu_{ss}$ ) friction decreases as normal stress ( $\sigma_n$ ) increases for both sample orientations i.e. perpendicular and parallel to the bedding (Figure 5-4a). Values of  $\mu_{peak}$  range between 0.21 and 0.45 for samples sheared parallel and perpendicular to bedding and they do not substantially differ from each other. Values of  $\mu_{ss}$  are higher ( $\sim 30\%$  in average) for samples sheared perpendicular to the bedding ( $0.22 < \mu_{ss} < 0.40$ ) with respect to samples sheared parallel ( $0.15 < \mu_{ss} < 0.33$ ) to the bedding.

Regarding frictional stability (Figure 5-4b), samples exhibit both velocity-weakening and -strengthening behaviour, with values of the parameter  $(a-b)$  ranging from -0.004 to 0.010 for samples sheared parallel to bedding, and -0.024 to 0.013 for samples sheared perpendicular to bedding. The values of the critical slip distance  $D_c$  range from 0.01 to 1.35 mm for the samples

sheared parallel to the bedding planes, and 0.18 to 10.51 mm for samples sheared perpendicular to bedding (Figure 5-4c). They do not follow a clear trend with respect to normal stress or sliding velocity.

Finally, frictional healing values ( $\Delta\mu$ ) range from -0.0362 to 0.015 for samples sheared parallel to bedding, and from -0.0039 to 0.0093 for samples sheared perpendicular to bedding (Figure 5-4d). For all samples, the frictional healing values ( $\Delta\mu$ ) evolve from almost zero to positive healing values as the hold times increase and they are independent of both the orientation of shearing with respect to the bedding and the applied normal stress.

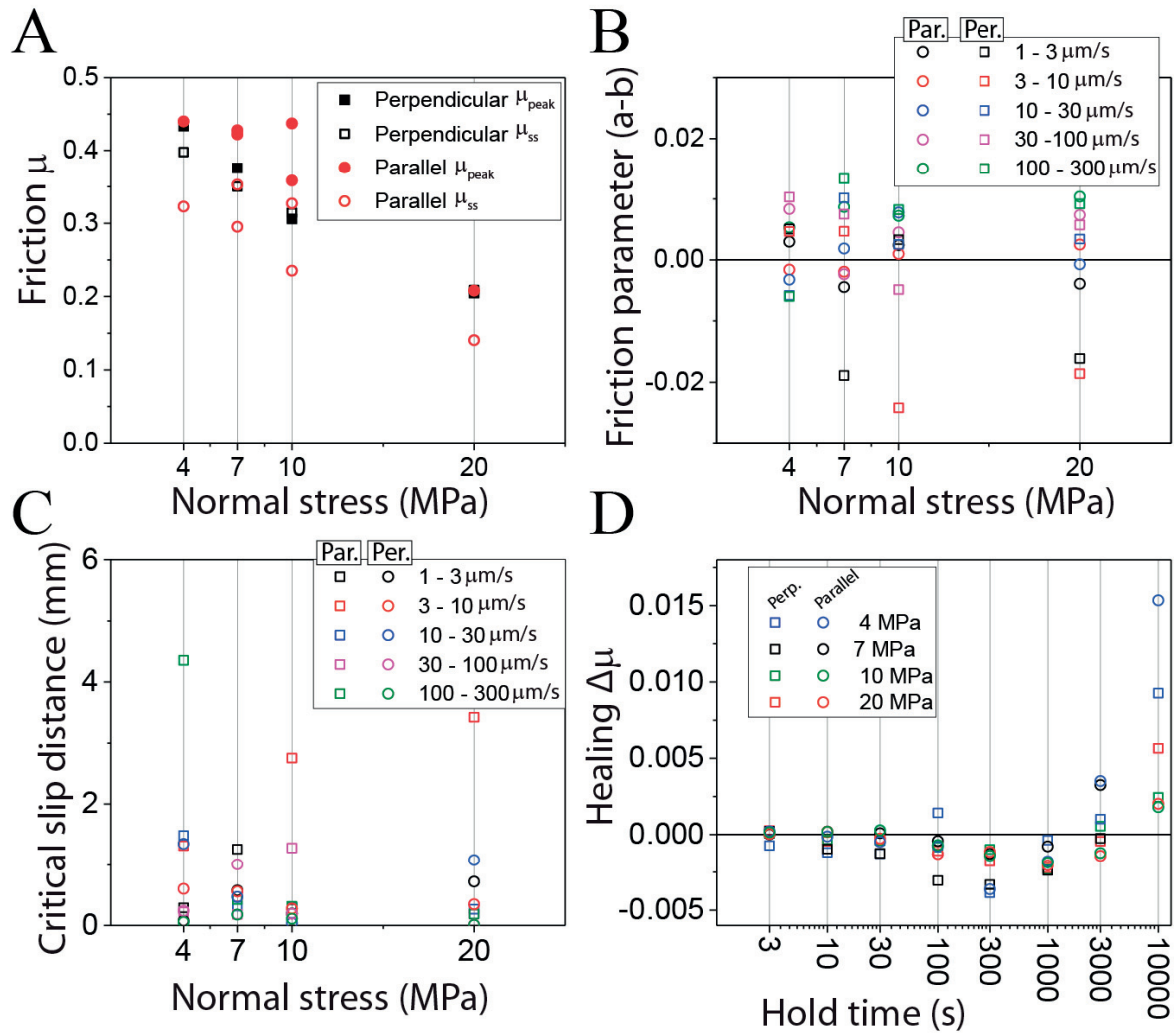


**Figure 5-4:** Results. A) Friction versus normal stress. B) Frictional parameter ( $a-b$ ) versus normal stress (MPa). C) Critical slip distance (mm) versus normal stress (MPa). D) Frictional healing values versus hold time (s).

Bedding	Test	Normal Stress (MPa)	Peak friction $\mu_{peak}$	Steady-state friction $\mu_{ss}$	Up-Step Velocity Steps ( $\mu\text{m/s}$ )	Friction parameter $a$	Friction parameter $b$	Friction parameter $a - b$	Critical Distance $D_c$ (mm)	Sequence of Hold Times (s)	Healing $\Delta\mu$
Parallel	i537	4	0.44	0.32	3	0.005	0.002	0.003	0.075	3	0.000
					10	0.004	0.006	-0.002	0.600	10	0.000
					30	0.005	0.008	-0.003	1.345	30	0.000
					100	0.005	-0.003	0.008	0.239	100	-0.001
					300	0.008	0.003	0.005	0.053	300	-0.004
										1000	-0.002
										3000	0.004
										10000	0.015
	i451	7	0.42	0.3	3	0.005	0.010	-0.004	0.575	3	0.000
					10	0.005	0.007	-0.002	0.558	10	0.000
					30	0.006	0.004	0.002	0.469	30	0.000
					100	0.006	0.008	-0.002	1.006	100	0.000
					300	0.007	-0.002	0.009	0.176	300	-0.001
										1000	-0.001
										3000	0.003
										10000	-
	i614	10	0.36	0.24	3	0.005	0.003	0.002	0.194	3	0.000
					10	0.005	0.004	0.001	0.275	10	0.000
					30	0.000	-0.008	0.008	0.039	30	0.000
					100	0.006	0.002	0.005	0.189	100	-0.001
					300	0.008	0.001	0.007	0.109	300	-0.001
										1000	-0.002
										3000	-0.001
										10000	0.002
	i533	20	0.21	0.14	3	0.006	0.010	-0.004	0.719	3	0.000
					10	0.006	0.003	0.003	0.348	10	0.000
					30	0.006	0.007	-0.001	1.076	30	0.000
					100	0.007	-0.001	0.007	0.012	100	-0.001
					300	0.003	-0.007	0.010	0.006	300	-0.001
										1000	-0.002
										3000	-0.001
										10000	0.002
	b731	7	0.43	0.35	-	-	-	-	-	-	-
	b732	10	0.44	0.33	-	-	-	-	-	-	-

Table 5-3: Results for samples sheared parallel to bedding.

Bedding	Test	Normal Stress (MPa)	Peak friction $\mu_{peak}$	Steady-state friction $\mu_{ss}$	Up-Step Velocity Steps ( $\mu\text{m/s}$ )	Friction parameter $a$	Friction parameter $b$	Friction parameter $a - b$	Critical Distance $D_c$ (mm)	Sequence of Hold Times (s)	Healing $\Delta\mu$
Perpendicular	i539	4	0.43	0.40	3	0.007	0.002	0.005	0.287	3	-0.001
					10	0.008	0.004	0.005	1.313	10	-0.001
					30	0.009	0.015	-0.006	1.485	30	-0.001
					100	0.009	-0.002	0.010	0.221	100	0.001
					300	0.010	0.016	-0.006	4.354	300	-0.004
										1000	0.000
										3000	0.001
										10000	0.009
	i446	7	0.38	0.35	3	0.006	0.025	-0.019	1.257	3	0.000
					10	0.007	0.002	0.005	0.467	10	-0.001
					30	0.008	-0.002	0.010	0.317	30	-0.001
					100	0.009	0.001	0.008	0.181	100	-0.003
					300	0.010	-0.003	0.013	0.420	300	-0.003
										1000	-0.002
										3000	0.000
										10000	-
	i538	10	0.31	0.32	3	0.007	0.003	0.003	0.271	3	0.000
					10	0.007	0.031	-0.024	2.755	10	0.000
					30	0.007	0.005	0.003	0.306	30	0.000
					100	0.007	0.012	-0.005	1.276	100	-0.001
					300	0.009	0.001	0.008	0.314	300	-0.001
										1000	-0.002
										3000	0.001
										10000	0.002
	i536	20	0.21	0.21	3	0.007	0.023	-0.016	10.505	3	0.000
					10	0.006	0.025	-0.019	3.423	10	0.000
					30	0.006	0.003	0.003	0.265	30	0.000
					100	0.007	0.002	0.006	0.183	100	-0.001
					300	0.009	0.000	0.009	0.186	300	-0.002
										1000	-0.002
										3000	0.000
										10000	0.006

**Table 5-4:** Results for samples sheared perpendicular to bedding.



### 5.4.2. MICROSTRUCTURAL RESULTS

In Figure 5-5 we report the macroscopic features along with SEM microstructural observations and roughness measurements of natural (non-deformed and scaly clays) and experimental samples. We include post-mortem samples of experiments sheared for 0.5 and 1.5 cm of displacement at 10 MPa of normal stress.

At cm- to mm-scale, the non-deformed samples (i.e. bedding planes) show irregular, rough, and non-polished surfaces (Figure 5-5a, Figure 5-5b) and the mean surface roughness ( $Sq$ ) is equal to  $\sim 24 \mu\text{m}$  (Figure 5-5c). In samples sheared parallel and perpendicular to bedding, we observe patches of polished shear or mirror-like surfaces (outlined in red in Figure 5-5d, Figure 5-5g). These patches are rather evident in samples sheared parallel to bedding planes and at higher normal stresses (from 7 to 20 MPa).

At the very early stage of deformation, i.e. 0.5 cm displacement, we detected mm-scale patches of polished surfaces (Figure 5-5d), and they become more pervasive in samples sheared after 1.5 cm of displacement (Figure 5-5g). At the microscale, the polished surfaces appear as relatively uniform areas with parallel slickenlines or striations (grooves) (Figure 5-5e, Figure 5-5h). The mean surface roughness ( $Sq$ ) for these patches of mirror-like surfaces ranges between  $\sim 10 \mu\text{m}$  and  $\sim 15 \mu\text{m}$  (Figure 5-5f, Figure 5-5i) for samples sheared after 0.5 and 1.5 cm of displacement. Finally, samples of natural scaly clays are characterised by anastomosing mirror-like and very smooth surfaces (Figure 5-5j, Figure 5-5k), and a mean surface roughness ( $Sq$ ) that approximates  $\sim 7.5 \mu\text{m}$  (Figure 5-5l).

To get insights on the deformation mechanism, we have performed optical and SEM-BSE microstructural analysis on thin sections from samples sheared parallel and perpendicular to bedding planes at 7 MPa, 10 MPa and 20 MPa normal stress (Figure 5-6). The sample sheared parallel to bedding planes (Figure 5-6a) shows the formation of incipient R-shear planes and ubiquitous micro-fractures parallel to the R direction. As shown in Figure 5-6b, we observe a zone of intense but gradual grain size reduction (e.g. intergranular fracturing of calcite minerals) where deformation is localised (R-planes). We also recognise clay minerals that appear re-orientated parallel to the R-direction, clay lamellae surrounding stronger grains, and few truncated carbonate clasts (Figure 5-6c).

In the matrix, we do not observe strong markers of shearing. However, we recognise some intergranular cracking, rotation of calcite and quartz minerals, and clays flowing around rigid minerals. Diffuse deformation, i.e., a global flowing of the matrix, is difficult to recognise because of the influence of the pre-existing fabric. The latter evidence that deformation is mainly accommodated by both frictional sliding and moderate to strong cataclastic flow along interconnected clay-rich horizons.

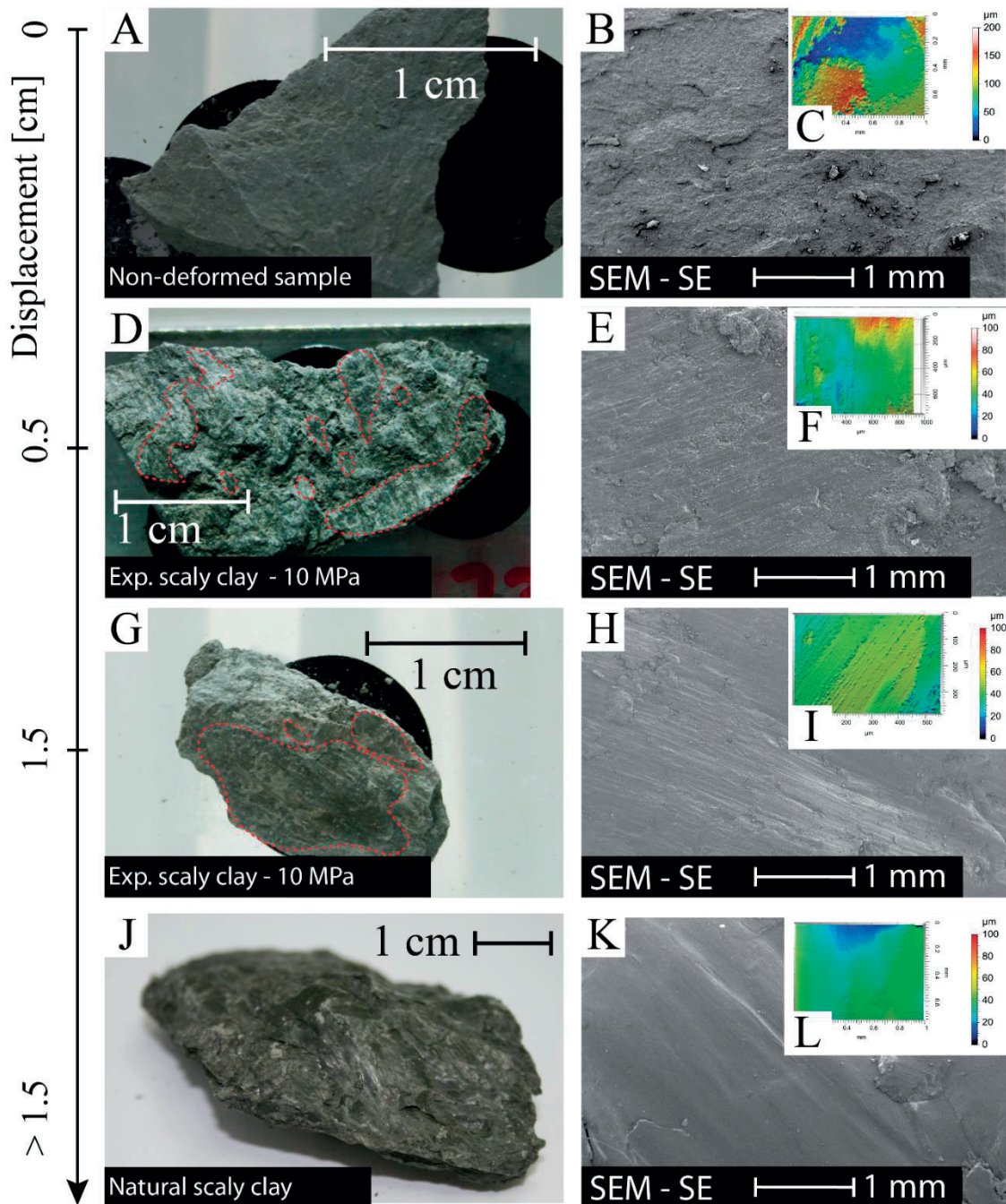


**Figure 5-5:** Natural and experimental samples. Photographs of A) non-deformed sample, B) experimental samples sheared parallel to bedding after 0.5 cm and C) 1.5 cm of displacement showing mirror-like slip surfaces under natural light, and D) a deformed hand sample exhibiting natural scaly clays. Scanning electron microscope images of E) a non-deformed, F) experimental samples sheared parallel to bedding after 0.5 cm and G) 1.5 cm of displacement, and H) natural scaly clays. Optical contactless profilometer model (area of 0.7 mm<sup>2</sup>) showing mean roughness amplitude of about I) ~24 μm for non-deformed samples and L) ~7.5 μm for natural scaly clays. For samples sheared after J) 0.5 and H) 1.5 cm, the mean surface roughness range between ~10 μm and ~15 μm.



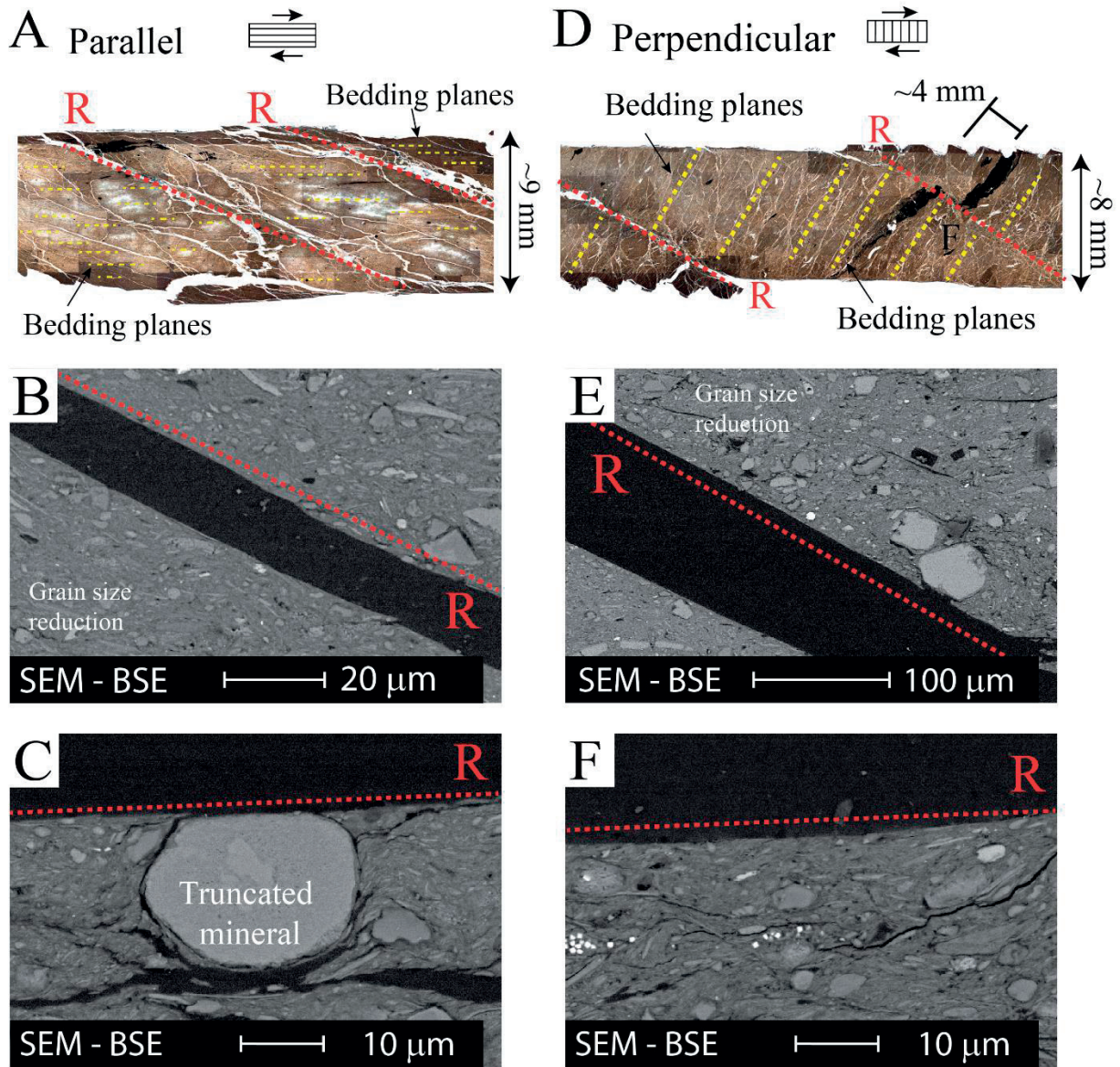


**Figure 5-6:** Microstructures of experimental samples tested at 7 MPa, 10 MPa and 20 MPa normal stress. A) Optical image of sample sheared parallel to bedding at 7 MPa showing incipient R-shear planes, microfractures parallel to the R-direction, and the accommodation of shearing within bedding planes (yellow dashed lines). B) BSE image of sample sheared parallel to bedding at 10 MPa showing a smooth surface associated with a zone of intense grain size reduction in which deformation is localised (R-plane). C) BSE image of sample sheared parallel to bedding at 10 MPa showing a truncated carbonate mineral. D) Optical image of sample sheared perpendicular to bedding at 7 MPa reveals the formation of R-shear planes (red dashed lines) and rotation of the bedding planes ( $\sim 45^\circ$ ) parallel to the P-direction (yellow dashed lines). E) BSE image of sample sheared perpendicular to bedding at 20 MPa and F) showing mirror-like surface associated with a zone of intense grain size reduction where deformation is localised.

The sample sheared perpendicular to bedding planes (Figure 5-6d) shows a domino structure underlined by a clockwise rotation ( $\sim 45^\circ$ ) of the initial fabric. Shear movement is emphasised by a  $\sim 4$  mm offset as is revealed by the displacement of framboid pyrites that act as markers. We observe that deformation is localised along two well-defined R-shear planes and is characterised by a pervasive cataclastic zone bounded by these shear planes. We distinguish several sub-parallel micro-fractures inherited from bedding planes oriented parallel to P-direction. We also notice strong grain comminution of calcite minerals that takes place within the shear zones and the matrix. Again, we observe polished or smooth surfaces associated with areas of intense grain size reduction and re-alignment of clay minerals in which deformation is localised (Figure 5-6e, Figure 5-6vf). The previous information favours frictional sliding, but also strong micro-fracturing, and strong cataclastic flow, as the main rock deformation mechanisms.

## 5.5. DISCUSSION

The microstructural analyses evidence the creation of polished, smooth surfaces forming mirror-like surfaces resembling the natural scaly clays (Figure 5-5). Indeed, the experimental and natural samples share similar characteristics including very low roughness, shiny surfaces, and evidence of slickensides. Based on our observations, we relate these experimental mirror-like surfaces to 1) a decrease of surface roughness thanks to strong grain size reduction (Fondriest et al., 2013; Siman-Tov et al., 2015), and 2) to the re-orientation of clay minerals parallel to the R-shear orientation within the principal slipping zones (Vannucchi et al., 2003). Moreover, our study suggests that the scaly clays start to form in the very early stages of the fault activity (i.e. slip  $\leq 0.5$  cm) and continue to develop with cumulative slip. Indeed, natural scaly presents lower roughness values than sample sheared up to 1.5 cm of slip.

The conditions that allow the formation of these mirror-like surfaces, as observed in samples sheared parallel and perpendicular to bedding, are sub-seismic velocities ( $\leq 300$   $\mu\text{m/s}$ ), shallow conditions ( $\leq 20$  MPa), low temperatures ( $\sim 20$   $^\circ\text{C}$ ), and in zones of shear localisation (R-Planes). Most of the previous studies have shown that mirror-like surfaces form at co-seismic slip velocities and are commonly associated with high temperatures mechanisms (Evans et al., 2014; Green et al., 2015; Kuo et al., 2016; Siman-Tov et al., 2015). However, our experimental evidence suggests, similarly to Verberne et al., (2014) and Sagy et al., (2017), that they can also form under shallow conditions, sub-seismic slip velocities, and low temperatures. In our case, the genesis of the scaly-clays has frictional sliding and cataclastic flow as the most likely deformation mechanisms.

Based on the similarity between the natural and experimental scaly fabric it is, therefore, possible to hypothesise that our laboratory tests might be a good approximation of the frictional behaviour of the natural scaly clays within the Main Fault of the Mount Terri Laboratory. Thus, the links between the frictional strength, stability, and healing might have important implications for the slip behaviour of the Main Fault.

When considering the mechanical data, previous studies have shown that uniaxial and triaxial experiments on OPA show that elastic properties vary with the orientation of the bedding, i.e. mechanical anisotropy (Bossart et al., 2017). In our experiments, the orientation of the bedding with respect to shear does not have a major control on the peak strength ( $\mu_{peak}^{parallel} \cong \mu_{peak}^{perp}$ ), but parallel samples show lower steady-state friction ( $\mu_{ss}$ ) values than samples sheared perpendicular to bedding ( $\mu_{ss}^{parallel} < \mu_{ss}^{perp}$ ). During deformation strong micro-fracturing and cataclastic flow, rather than distributed frictional sliding along clay, would make the samples sheared perpendicular to bedding stronger.

Following these observations, we posit that shearing within scaly clays will initiate simultaneously on multiple shear surfaces, regardless of orientation, but strongly depending on the stress state of the fault surroundings (the higher the normal stress, the lower the frictional strength). Then, frictional sliding, micro-fracturing, and cataclastic flow will coexist, leading to a dynamic creation and destruction of multiple shearing surfaces, i.e. generation of new scaly clays, with ongoing deformation. However, because of lower  $\mu_{ss}^{parallel}$ , slip will mostly occur on the pre-existing parallel scaly clays, being frictional sliding the main controlling deformation mechanism. These observations are in agreement with the orientation of the Main Fault where scaly clays, secondary fractures, and shear planes observed at the Mont Terri Laboratory are sub-parallel to the orientation of the bedding planes (Fig 1B.). To note that despite the same mineralogical composition, the frictional strength of OPA powdered gouges (Orellana et al., 2018, Chapter 3) is higher than frictional strength of experimental scaly clays ( $\mu_{scaly} < \mu_{gouge}$ ), highlighting the role of fault fabric in controlling fault strength (Collettini et al., 2009; Ikari et al., 2015) (Figure 5-7).

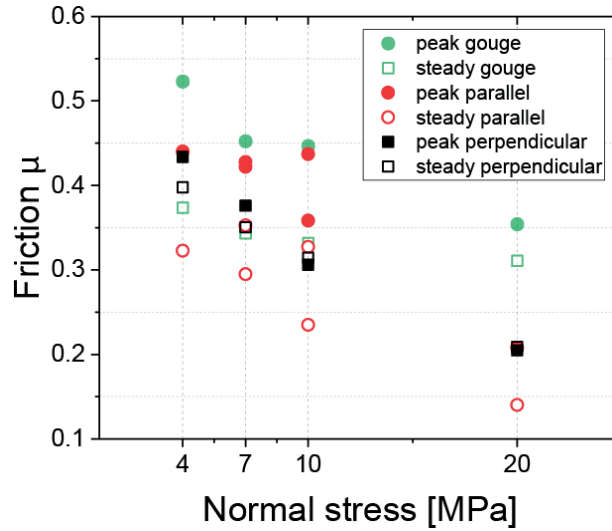


**Figure 5-7:** Friction  $\mu = \tau/\sigma_n$  values for intact samples sheared parallel and perpendicular to bedding, and simulated fault gouges samples from Chapter 3.

On the question of frictional healing, this study found that the experimental scaly clays have near-zero healing values. The latter has an important implication for the fault behaviour. Indeed, the lack of re-strengthening during inter-seismic cycles indicates that contact strength does not increase with hold times (Bos & Spiers, 2000; Carpenter et al., 2011). In this respect, the null healing should contribute to the overall weakness of the clay-rich Main Fault, but also to the long-term stability of the fault.

Another important finding is that scaly clays show a velocity-weakening and –strengthening behaviour. This outcome is contrary to the velocity-strengthening behaviour observed in previous clay-rich samples (Haines et al., 2014; Ikari et al., 2009; Kohli & Zoback, 2013), including research on Opalinus clay gouges (Orellana et al., 2018, see Chapter 3) (Figure 5-8). Previous studies have shown that the velocity-weakening regime is often associated with the cataclastic flow regime and a strong localisation along narrow shear planes (Niemeijer & Spiers, 2007; Tsutsumi et al., 2011). On the other hand, the velocity-strengthening regime has often been associated with an anastomosing creation of foliation and homogenous distribution of deformation (Niemeijer & Spiers, 2007). In our samples, we have not recognised strong evidence of foliation within the matrix. However, as strong pervasive cataclastic flow, strong localisation, and re-alignment of clay minerals are recognisable in the microstructures (Figure 5-6). We suggest the latter as a possible mechanism controlling the velocity-weakening behaviour.

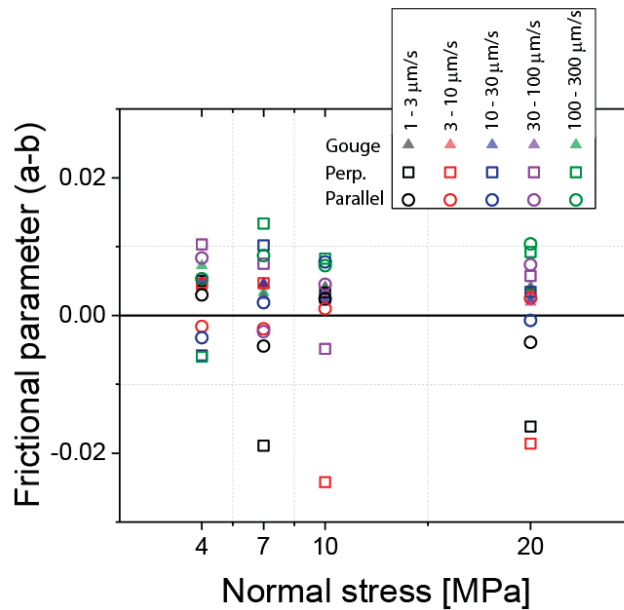


**Figure 5-8:** Friction parameter (a-b) for intact samples sheared parallel and perpendicular to bedding, and simulated fault gouges samples from Chapter 3. Figure is showing that simulated fault gouges have a velocity-strengthening behaviour (Orellana et al., 2018), while on the other hand, intact samples sheared parallel and perpendicular to bedding planes exhibit both velocity-weakening and -strengthening behaviour at the same range of normal stresses (up to 20 MPa)



Moreover, in our study, the mean surfaces roughness decreases with fault slip (Figure 5-5). It is thus also possible to hypothesise that if critical conditions are fulfilled, such as seismic velocities and greater fault displacements, the progressive surface smoothing of scaly clays might control the velocity-weakening behaviour in our samples (Chen et al., 2013; Proctor et al., 2014). Further research should be undertaken to investigate both the mechanisms behind the velocity-weakening behaviour by surface smoothing.

To better understand these velocity-weakening results in the context of geological repositories, we now present a synoptic model (Figure 5-9) through the frictional stability parameter  $\xi = (a - b) \cdot \sigma_n$  (Scholz, 1998). We consider the typical depths for deep geological repositories; usually bellow 300 m and up to 1000 m. The model is presented separately for samples sheared parallel and perpendicular to bedding defining stable (blue) or unstable (red) based on  $\xi$ . Our results reveal a potentially unstable regime for whole a range of prospective depths ( $< 700$  m) where deep geological repositories are planned to be constructed. We also observe a quasi-stable zone around  $\sim 300$  m, but only when sliding velocities are higher than  $100 \mu\text{m/s}$ . At higher depths ( $> 700$  m) and higher slip velocities ( $> 100 \mu\text{m/s}$ ), the frictional behavior transitions to stable.

As earthquakes might only nucleate within unstable regimes, i.e. frictional parameter  $(a-b) < 0$ , we now estimate the earthquake magnitudes that might impact the nuclear repositories associated with the potentially unstable sliding of the Main Fault described before.

To do that, we first calculate the critical lengths. The critical lengths ( $l_c$ ) indicate the required size of the fault patch to transit from stable sliding to unstable sliding in a nucleation stage (Scholz, 1998, 2002). Thus, if  $r \geq l_c$ , being  $r$  the size of the fault, we should expect earthquakes to be able to nucleate and propagate within the fault system. If the fault patch is considered as an elliptical crack, the critical length can be defined as  $l_c = \frac{ED_c}{2\sigma_n \cdot (1-v^2)(b-a)}$ , where,  $E$  is the Young modulus,  $v$  the Poisson's ratio, and  $\sigma_n$  the normal stress. Because of the mechanical anisotropy of the hosting rock (Bossart et al., 2017), to calculate  $l_c$ , we use different Young's modulus ( $E_{//} = 7200 \text{ MPa}$ ,  $E_{\perp} = 2800 \text{ MPa}$ ) and Poisson's ratios ( $v_{//} = 0.24$ ,  $v_{\perp} = 0.33$ ) upon bedding orientation. We find values of  $l_c$  between 35 and 397 m for samples sheared parallel to bedding, and between 14 and 285 for samples sheared perpendicular to bedding (Figure 5-9).

Second, following the Brune's model approach (Brune, 1970), the scalar seismic moment  $M_0$  can be written in terms of a stress drop ( $\Delta\sigma$ ) and the radius  $r$  of a circular fault. Thus, the seismic moment is now given by  $M_0 \approx A \cdot \Delta\sigma r^3$  (Brune, 1970; Madariaga & Ruiz, 2016), where  $A$  is a geometrical factor.

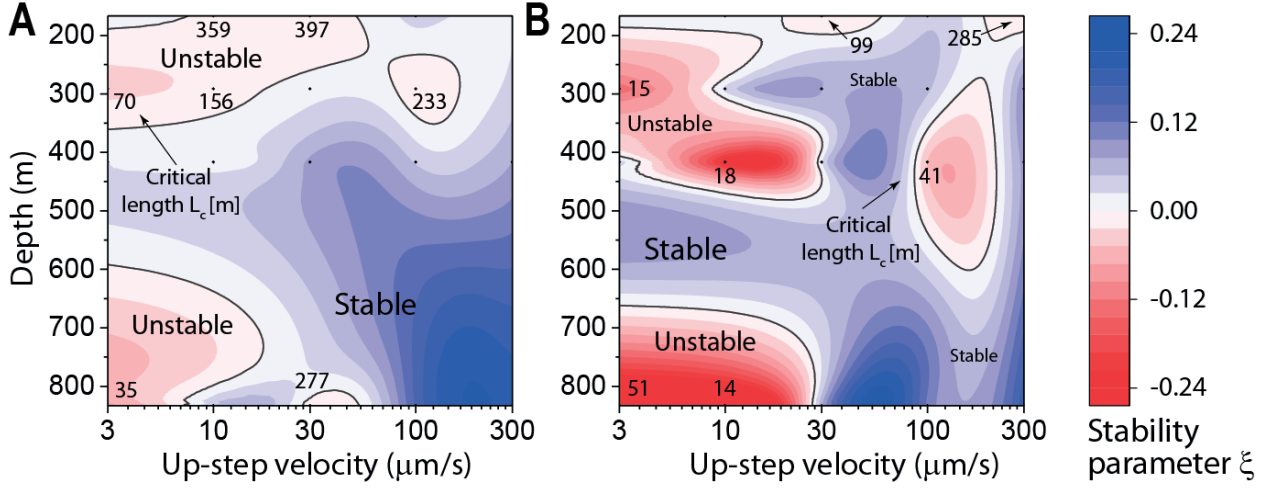


**Figure 5-9:** Contour plot of the stability parameter  $\xi = \sigma_n \cdot (a - b)$  (Scholz, 1998) as a function of depth and sliding velocity for samples sheared A) parallel and B) perpendicular to bedding planes. Parameter  $\xi$  is obtained from experimental values of  $(a-b)$  and assuming a gradient in vertical stress of 24 MPa/km (corresponding to the lithostatic pressure at the MTL). The critical nucleation length  $L_c$  (m) is calculated based on the elliptical crack approach (Scholz, 2002). In the figure, the numbers within the unstable areas represent the values of  $L_c$  (m).  $L_c$  has not been estimated for velocity strengthening regions.

Finally, as the earthquake magnitudes ( $M_w$ ) are related to the earthquakes momentum ( $M_o$ ) through the empirical relationship  $M_w = \frac{2}{3} \log M_o - 6.07$  (Scholz, 2002), we can compute the minimum earthquake magnitudes ( $M_w$ ) that might occur within the clay-bearing fault. Indeed, if we consider that earthquakes have typical stress drops ( $\Delta\sigma$ ) between 0.1 and 10 MPa (Madariaga & Ruiz, 2016), we find that, theoretically, the scaly clays within the fault system might hold earthquakes of magnitudes  $M_w > 1$ .

As mentioned before, earthquake magnitudes are controlled by the fault size  $r$ , that in the particular case of the secondary faults within the scaly clays, it is often very limited (Figure 5-1b) i.e. lower than tens of centimeters (Nussbaum et al., 2011). Thus, the critical length for earthquake nucleation can be higher than the dimension of the fault size, implying that, even though the friction parameter  $(a-b)$  is negative i.e. velocity-weakening, the nucleation of earthquakes is probably difficult. This difficulty for earthquake nucleation is also accentuated by 1) the near-zero healing values (Figure 5-4d) and 2) the co-existence of velocity-weakening and -strengthening behavior (Figure 5-4b).

While the near-zero healing values should prevent the fault system from re-strengthening and therefore, preclude large stress drops, the co-existence of velocity-weakening and -strengthening behaviour suggests that discontinuous localisation of the seismic and aseismic slip will co-exist in different parts of the faults (Fagereng & Sibson, 2010). Then, if earthquake nucleates, it is likely that the regions of velocity-strengthening rock will play an arresting role in the slip rupture dynamics. However, if this is not the case, i.e., the propagation of earthquake ruptures is not

inhibited by the velocity-strengthening portions of the fault, the clay-bearing fault might also be capable of hosting large ruptures (Faulkner et al., 2011; Noda & Lapusta, 2013). The capability of clay-bearing faults of hosting large earthquakes is of particular importance since larger earthquakes have been recorded within the near-region of the Mont Terri Laboratory (Baer et al., 2005; Diehl et al., 2014, 2015). A note of caution is due here since our experiments have been conducted under shallow conditions and slow slip velocities, and hence these results do not rule out the influence of other factors. Further research should be undertaken to investigate the influence of variables and processes such as the role of fluid pressures, saturation, consolidation, temperatures and depth-dependent processes, and others.

In summary, our results show that OPA exhibit a low frictional strength, a velocity-weakening and –strengthening behaviour, a large critical nucleation length, and a near-zero healing values. Taken together, we suggest that if earthquakes nucleate within the scaly clays in clay-bearing faults, they will be probably small and rare over time, and they will localise at a depth below 300 m in the repository.

## 5.6. CONCLUSIONS

Our observations indicate that the scaly clays are the weakest point within the fault core of clay-bearing fault tectonic systems. Our data also suggests that the possibility of earthquake nucleation exists, being the scaly clays the most suitable candidates to host them throughout the fault system. However, if earthquakes nucleate within the clay-bearing fault, they might be small and rare over time, as suggested by the low frictional strength, the velocity-strengthening and –weakening behaviour, the large critical nucleation length, and the near-zero healing values. This evidence carries out significant implications for nuclear waste repositories. If anthropogenic and natural perturbations trigger unstable sliding, it will most probably initiate on the scaly clays portions of the clay-bearing fault and at near depths where nuclear repositories are planned to be emplaced.

## 5.7. REFERENCES

- Baer, M., Deichmann, N., Braunmiller, J., Husen, S., Fäh, D., Giardini, D., et al. (2005). Earthquakes in Switzerland and surrounding regions during 2004. *Eclogae Geologicae Helvetiae*, 98(3), 407–418. <https://doi.org/10.1007/s00015-005-1168-3>
- Bos, B., & Spiers, C. (2000). Effect of phyllosilicates on fluid-assisted healing of gouge-bearing faults. *Earth and Planetary Science Letters*, 184(1), 199–210. [https://doi.org/10.1016/S0012-821X\(00\)00304-6](https://doi.org/10.1016/S0012-821X(00)00304-6)
- Bossart, P., Bernier, F., Birkholzer, J., Bruggeman, C., Connolly, P., Dewonck, S., et al. (2017). Mont Terri rock laboratory, 20 years of research: introduction, site characteristics and overview of experiments. *Swiss Journal of Geosciences*, 110(1), 3–22. <https://doi.org/10.1007/s00015-016-0236-1>
- Brune, J. (1970). Tectonic stress and the spectra of seismic shear waves from Earthquakes. *Journal of Geophysical Research : Solid Earth*, 75(26).
- Carpenter, B., Marone, C., & Saffer, D. (2011). Weakness of the San Andreas Fault revealed by samples from the active fault zone. *Nature Geoscience*, 4(4), 251–254. <https://doi.org/10.1038/ngeo1089>
- Chen, X., Madden, A. S., Bickmore, B. R., & Reches, Z. (2013). Dynamic weakening by nanoscale smoothing during high-velocity fault slip. *Geology*, 41(7), 739–742. <https://doi.org/10.1130/G34169.1>
- Chester, F. M., Rowe, C., Ujiie, K., Kirkpatrick, J. D., Regalla, C., Remitti, F., et al. (2013). Structure and Composition of the Plate-Boundary Slip Zone for the 2011 Tohoku-Oki Earthquake. *Science*, 342, 1208–1211.
- Collettini, C., Niemeijer, A., Viti, C., & Marone, C. (2009). Fault zone fabric and fault weakness. *Nature*, 462(7275), 907–910. <https://doi.org/10.1038/nature08585>
- Collettini, C., Di Stefano, G., Carpenter, B., Scarlato, P., Tesei, T., Mollo, S., et al. (2014). A novel and versatile apparatus for brittle rock deformation. *International Journal of Rock Mechanics and Mining Sciences*, 66, 114–123. <https://doi.org/10.1016/j.ijrmms.2013.12.005>
- Diehl, T., Clinton, J., Kraft, T., Husen, S., Plenkens, K., Guilhelm, A., et al. (2014). Earthquakes in Switzerland and surrounding regions during 2013. *Swiss Journal of Geosciences*, 107(2), 359–375. <https://doi.org/10.1007/s00015-014-0171-y>
- Diehl, T., Deichmann, N., Clinton, J., Kästli, P., Cauzzi, C., Kraft, T., et al. (2015). Earthquakes in Switzerland and surrounding regions during 2014. *Swiss Journal of Geosciences*, 108(2–3), 425–443. <https://doi.org/10.1007/s00015-015-0204-1>
- Dieterich, J. H. (1979). Modeling of rock friction: 1. Experimental results and constitutive equations. *Journal of Geophysical Research*, 84(9), 2161–2168.

<https://doi.org/10.1007/BF00876539>

- Evans, J. P., Prante, M. R., Janecke, S. U., Ault, A. K., & Newell, D. L. (2014). Hot faults: Iridescent slip surfaces with metallic luster document high-temperature ancient seismicity in the Wasatch fault zone, Utah, USA. *Geology*, 42(7), 623–626. <https://doi.org/10.1130/G35617.1>
- Fagereng, Å., & Sibson, R. H. (2010). Mélange rheology and seismic style. *Geology*, 38(8), 751–754. <https://doi.org/10.1130/G30868.1>
- Faulkner, D., Mitchell, T. M., Behnsen, J., Hirose, T., & Shimamoto, T. (2011). Stuck in the mud? Earthquake nucleation and propagation through accretionary forearcs. *Geophysical Research Letters*, 38(18), 1–5. <https://doi.org/10.1029/2011GL048552>
- Fondriest, M., Smith, S. A. F., Candela, T., Nielsen, S., Mair, K., & Toro, G. Di. (2013). Mirror-like faults and power dissipation during earthquakes. *Geology*, 41(11), 1175–1178. <https://doi.org/10.1130/G34641.1>
- Giardini, D., Wössner, J., & Danciu, L. (2014). Mapping Europe’s seismic hazard. *Eos*, 95(29), 261–262. <https://doi.org/10.1002/2014EO290001>
- Green, H. W., Shi, F., Bozhilov, K., Xia, G., & Reches, Z. (2015). Phase transformation and nanometric flow cause extreme weakening during fault slip. *Nature Geoscience*, 8(6), 448–489. <https://doi.org/10.1038/NGEO2436>
- Haines, S., Marone, C., & Saffer, D. (2014). Frictional properties of low-angle normal fault gouges and implications for low-angle normal fault slip. *Earth and Planetary Science Letters*, 408, 57–65. <https://doi.org/10.1016/j.epsl.2014.09.034>
- Ikari, M. J., Saffer, D., & Marone, C. (2009). Frictional and hydrologic properties of clay-rich fault gouge. *Journal of Geophysical Research: Solid Earth*, 114(5), 1–18. <https://doi.org/10.1029/2008JB006089>
- Ikari, M. J., Niemeijer, A., & Marone, C. (2015). Experimental investigation of incipient shear failure in foliated rock. *Journal of Structural Geology*, 77, 82–91. <https://doi.org/10.1016/j.jsg.2015.05.012>
- Kohli, A. H., & Zoback, M. D. (2013). Frictional properties of shale reservoir rocks. *Journal of Geophysical Research: Solid Earth*, 118(9), 5109–5125. <https://doi.org/10.1002/jgrb.50346>
- Kuo, L.-W., Song, S.-R., Suppe, J., & Yeh, E. C. (2016). Fault mirrors in seismically active fault zones: A fossil of small earthquakes at shallow depths. *Geophysical Research Letters*, 43(5), 1950–1959. <https://doi.org/10.1002/2015GL066882>
- Laurich, B., Urai, J. L., Desbois, G., Vollmer, C., & Nussbaum, C. (2014). Microstructural evolution of an incipient fault zone in Opalinus Clay: Insights from an optical and electron microscopic study of ion-beam polished samples from the Main Fault in the Mt-Terri Underground Research Laboratory. *Journal of Structural Geology*, 67(PA), 107–128.

<https://doi.org/10.1016/j.jsg.2014.07.014>

- Madariaga, R., & Ruiz, S. (2016). Earthquake dynamics on circular faults: a review 1970–2015. *Journal of Seismology*, 20(4), 1235–1252. <https://doi.org/10.1007/s10950-016-9590-8>
- Marone, C. (1998). Laboratory-Derived Friction Laws and Their Application To Seismic Faulting. *Annual Review of Earth and Planetary Sciences*, 26(1), 643–696. <https://doi.org/10.1146/annurev.earth.26.1.643>
- Monecke, K., Anselmetti, F. S., Becker, A., Sturm, M., & Giardini, D. (2004). The record of historic earthquakes in lake sediments of Central Switzerland. *Tectonophysics*, 394(1–2), 21–40. <https://doi.org/10.1016/j.tecto.2004.07.053>
- Niemeijer, A. R., & Spiers, C. J. (2007). A microphysical model for strong velocity weakening in phyllosilicate-bearing fault gouges. *Journal of Geophysical Research: Solid Earth*, 112(10), 1–12. <https://doi.org/10.1029/2007JB005008>
- Noda, H., & Lapusta, N. (2013). Stable creeping fault segments can become destructive as a result of dynamic weakening. *Nature*, 493(7433), 518–521. <https://doi.org/10.1038/nature11703>
- Nussbaum, C., Bossart, P., Amann, F., & Aubourg, C. (2011). Analysis of tectonic structures and excavation induced fractures in the Opalinus Clay, Mont Terri underground rock laboratory (Switzerland). *Swiss Journal of Geosciences*, 104(2), 187–210. <https://doi.org/10.1007/s00015-011-0070-4>
- Nussbaum, C., Kloppenburg, A., Caër, T., & Bossart, P. (2017). Tectonic evolution around the Mont Terri rock laboratory, northwestern Swiss Jura: constraints from kinematic forward modelling. *Swiss Journal of Geosciences*, 110(1), 39–66. <https://doi.org/10.1007/s00015-016-0248-x>
- Orellana, L. F., Scuderi, M. M., Collettini, C., & Violay, M. (2018). Frictional Properties of Opalinus Clay: Implications for Nuclear Waste Storage. *Journal of Geophysical Research: Solid Earth*, 123(1), 157–175. <https://doi.org/10.1002/2017JB014931>
- Proctor, B. P., Mitchell, T. M., Hirth, G., Goldsby, D., Zorzi, F., Platt, D. J., & Di Toro, G. (2014). Dynamic weakening of serpentinite gouges and bare surfaces at seismic slip rates. *Journal of Geophysical Research: Solid Earth*, 119(11), 8107–8131. <https://doi.org/10.1002/2014JB011057>
- Rabinowicz, E. (1951). The nature of the static and kinetic coefficients of friction. *Journal of Applied Physics*, 22(11), 1373–1379. <https://doi.org/10.1063/1.1699869>
- Reinen, L. A., & Weeks, J. D. (1993). Determination of rock friction constitutive parameters using an iterative least squares inversion method. *Journal of Geophysical Research*, 98(B9), 15937. <https://doi.org/10.1029/93JB00780>
- Ruina, A. (1983). Slip instability and state variable friction laws. *Journal of Geophysical Research*, 88(B12), 10359. <https://doi.org/10.1029/JB088iB12p10359>



- Sagy, A., Tesei, T., & Collettini, C. (2017). Fault-surface geometry controlled by faulting mechanisms: Experimental observations in limestone faults. *Geology*, 45(9), 851–854. <https://doi.org/10.1130/G39076.1>
- Salager, S., François, B., Nuth, M., & Laloui, L. (2013). Constitutive analysis of the mechanical anisotropy of Opalinus Clay. *Acta Geotechnica*, 8(2), 137–154. <https://doi.org/10.1007/s11440-012-0187-2>
- Schleicher, A., Van der Pluijm, B., & Warr, L. N. (2010). Nanocoatings of clay and creep of the San Andreas fault at Parkfield, California. *Geology*, 38(7), 667–670. <https://doi.org/10.1130/G31091.1>
- Scholz, C. H. (1998). Earthquakes and friction laws. *Nature*, 391(6662), 37–42. <https://doi.org/10.1038/34097>
- Scholz, C. H. (2002). *The Mechanics of Earthquakes and Faulting*. Cambridge University Press. Retrieved from <https://books.google.ch/books?id=JL1VM5wMbrQC>
- Siman-Tov, S., Aharonov, E., Boneh, Y., & Reches, Z. (2015). Fault mirrors along carbonate faults: Formation and destruction during shear experiments. *Earth and Planetary Science Letters*, 430, 367–376. <https://doi.org/10.1016/j.epsl.2015.08.031>
- Tesei, T., Collettini, C., Carpenter, B., Viti, C., & Marone, C. (2012). Frictional strength and healing behavior of phyllosilicate-rich faults. *Journal of Geophysical Research: Solid Earth*, 117(9), 1–13. <https://doi.org/10.1029/2012JB009204>
- Tsang, C.-F., Barnichon, J. D., Birkholzer, J., Li, X. L., Liu, H. H., & Sillen, X. (2012). Coupled thermo-hydro-mechanical processes in the near field of a high-level radioactive waste repository in clay formations. *International Journal of Rock Mechanics and Mining Sciences*, 49, 31–44. <https://doi.org/10.1016/j.ijrmms.2011.09.015>
- Tsutsumi, A., Fabbri, O., Karpoff, A. M., Ujiie, K., & Tsujimoto, A. (2011). Friction velocity dependence of clay-rich fault material along a megasplay fault in the Nankai subduction zone at intermediate to high velocities. *Geophysical Research Letters*, 38(19), 2–7. <https://doi.org/10.1029/2011GL049314>
- Ujiie, K., Tanaka, H., Saito, T., Tsutsumi, A., Mori, J., & Toczko, S. (2013). Low Coseismic Shear Stress on the Tohoku-Oki Megathrust Determined from Laboratory Experiments. *Science*, 342(December), 1211–1214. <https://doi.org/10.1126/science.1243485>
- Vannucchi, P., Maltman, A., Bettelli, G., & Clennell, B. (2003). On the nature of scaly fabric and scaly clay. *Journal of Structural Geology*, 25(5), 673–688. [https://doi.org/10.1016/S0191-8141\(02\)00066-4](https://doi.org/10.1016/S0191-8141(02)00066-4)
- Verberne, B., Spiers, C., Plümpner, O., & Matthijs de Winter, D. A. (2014). Superplastic nanofibrous slip zones control seismogenic fault friction. *Science*, 346(6215), 1342 LP-1344. Retrieved from <http://science.sciencemag.org/content/346/6215/1342.abstract>



## 6.

## CONCLUSIONS AND PERSPECTIVES

## 6.1. SUMMARY AND MAIN FINDINGS

In this Ph.D. thesis, we have investigated the frictional and the transport properties of fault systems within the Opalinus Clay (OPA) formation at relevant conditions for nuclear waste storage in the subsurface. This study focused primarily on the potential risks associated with the presence of faults near geological siting regions where potential underground repositories might be emplaced in Switzerland.

During this study, we were able to integrate datasets of microstructural observations, petrophysical measurements, and mechanical and frictional results to provide a qualitative and quantitative characterization of the clay-bearing fault systems within the Opalinus Clay formation. The objective of the thesis was 1) to characterize the pore structure and fluid transport properties of the fault gouge, 2) to study the frictional properties of the OPA fault-rocks: fault gouge and scaly clays, under conditions relevant for nuclear storage, and 3) to investigate the evolution of dilatancy and permeability during shear deformation of the Opalinus Clay fault gouge.

Using these different experimental approaches, we have illustrated that the spatial heterogeneities of the fault rock properties and that changes in the water saturation condition exert a significant influence on the frictional and transport properties of the formation. The major findings and results of this study are summarized as follows:

## 6.1.1. TRANSPORT PROPERTIES OF THE FAULT GOUGE

We have performed laboratory porosity measurements and microstructural and mineralogical analysis to quantify and describe the pore network structure, mineralogy, permeability and connected porosity with a primary focus on the fault gouge (Chapter 2). A total of 60 samples were analyzed to estimate porosity across the borehole BFS-2 using two different techniques: the helium picnometry and fluid displacement methods. A group of samples was also collected to analyze the pore throat size distribution using mercury injection porosimetry. The focused ion beam (FIB) integrated into secondary electron microscopy (SEM) has allowed us to characterize the pore structure of the fault gouge. Average porosity was  $\phi \approx 21\%$  for the fault gouge,  $\phi \approx 14\%$  for the non-deformed rock, and  $\phi \approx 13\%$  for the scaly clay samples. Pore throats of less than 10 nm exert an important control of the pore structure of the fault gouges, while for scaly clays and non-deformed rock, the dominant pore throat spectrum range between  $\sim 12$  and  $\sim 20$  nm.

Permeability was measured in two samples cored parallel to the bedding using the steady-state and pulse decay methods. Because of the current experimental complexities for direct measuring permeability on OPA fault-rocks, different permeability models were used to evaluate their fluid permeability. Depending on the permeability model, fault gouge permeability was estimated to  $\sim 10^{-18} - 10^{-20}$ , which was found to be up to 3 times higher than the modeled permeability of the non-deformed rock. Furthermore, mineralogical analyses show a strong reduction in calcite content within the fault gouge, in agreement with recent evidence suggesting pore fluids flowing throughout it. Thus, we have concluded that the Main Fault does not act as a barrier to fluid. Further, it might act as a localized, narrow and discontinuous preferential fluid conduit.

### 6.1.2. FRICTIONAL PROPERTIES OF SIMULATED FAULT GOUGE

Frictional experiments have been performed under dry, partially saturated (RH 100%) and pressurized water conditions, hereafter wet samples, on simulated fault gouges of Opalinus Clay (Chapter 3 and Chapter 4). We have performed experiments in a biaxial (Collettini et al., 2014) and triaxial (LEMUR, EPFL) apparatus under effective normal stresses ranging from 4 to 30 MPa and slow sliding velocities ( $< 300 \mu\text{m/s}$ ). In total, 27 frictional experiments have been carried out. The objective was to assess the frictional strength, frictional stability, and frictional healing of simulated fault gouge.

The frictional strength of simulated OPA fault gouge exhibited a generally weak frictional strength relative to the Byerlee's rule, i.e.  $\mu \approx 0.85$  (Byerlee, 1978). Average friction (steady state)  $\mu = \tau/\sigma'_n$  for was  $\mu \approx 0.4$  for dry,  $\mu \approx 0.33$  for partially saturated, and  $\mu \approx 0.1$  for wet samples. When the coefficient of friction  $\mu_f = (\tau - S_o)/\sigma'_n$  and an equivalent cohesion ( $S_o$ ) is computed, the coefficient for friction is equal to  $\mu_f = 0.36$  for dry,  $\mu_f = 0.29$  for partially saturated, and  $\mu_f = 0.15$  for wet samples. Cohesion is  $S_o = 0.16$  for dry,  $S_o = 0.4$  for partially saturated, and  $S_o = 0.79$  for wet samples. Fault samples under wet conditions (pressurized water) suppress any contribution from cohesion to the overall strength of the fault. Wet samples are extremely weak and represents less than 50% of the dry friction.

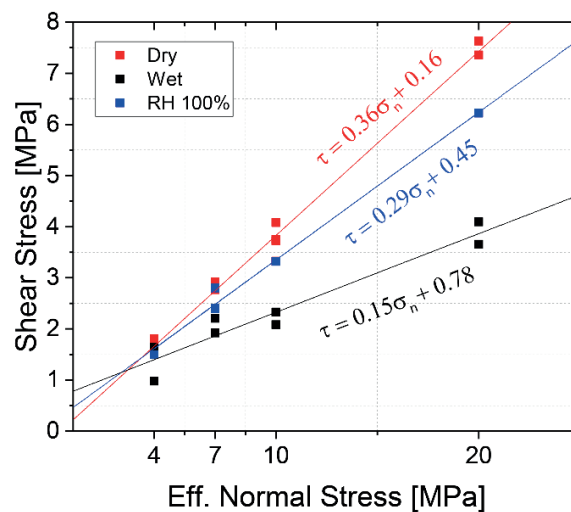


**Figure 6-1:** Shear stress versus effective normal stress for the simulated fault gouge.

The frictional stability of the simulated fault was addressed through the rate and state frictional approach, in particular using the empirical Ruina's slip law (Ruina, 1983). When samples are wet or partially saturated (RH 100%) the fault gouge experience exclusively velocity-strengthening behavior ( $a - b > 0$ ) i.e., stable slip different up-step sliding velocities ranging from 1 to 300  $\mu\text{m/s}$ . Dry gouge however showed a transition from velocity-weakening ( $a - b < 0$ ) to velocity strengthening behavior ( $a - b > 0$ ) when sliding velocities are higher than a cut-off velocity equal to 10  $\mu\text{m/s}$ .

We studied the frictional healing behavior of the simulated fault gouge only at partially saturated conditions. Results show that OPA fault exhibit near-zero healing values at different hold times (3 to 3000s) with average healing rates of about  $\beta \approx 0.0007$  at different normal stress. The latter implies that OPA faults exhibit a lack of re-strengthening during interseismic periods.

These experimental results taken together indicate that if OPA faults reactivate, which under wet conditions can easily occur, faults will slide in an aseismic stable fashion thus making the nucleation of earthquakes difficult. Note that OPA dehydration can favor seismic reactivation rather than a stable creep. Moreover, the almost null fault- re-strengthening during interseismic periods will favor a long-term weakness, promoting stable fault creep over geological times.

### 6.1.3. FRICTIONAL PROPERTIES OF SIMULATED SCALY CLAYS

We have carried out frictional experiments on intact (wafer-shaped) samples cut parallel and perpendicular to bedding (Chapter 5). The objective was to address the frictional behavior of scaly clays, which formation was hypothesized occur after shearing of intact material. Tests were carried out in the biaxial apparatus BRAVA (Collettini et al., 2014) under normal stresses ranging from 4 to 20 MPa and slow sliding velocities ( $< 300 \mu\text{m/s}$ ). Pore pressures were not controlled.

Similar to the results on fault gouge, the frictional strength of our intact samples exhibited a generally weak frictional strength relative to the Byerlee's rule i.e.,  $\mu \approx 0.85$ . Average values of friction (steady state) were  $\mu \approx 0.25$  for samples sheared parallel to the bedding planes, and  $\mu \approx 0.32$  for samples sheared perpendicular to the bedding planes. The coefficient for friction is equal to  $\mu_f = 0.1$  for samples sheared parallel to bedding, and  $\mu_f = 0.15$  for samples sheared perpendicular to bedding. Cohesion is  $S_o = 1.3$  for samples sheared parallel to bedding, and  $S_o = 1.27$  for samples sheared perpendicular to bedding.

When we compared the results from gouge and intact samples at similar water saturation condition (Chapter 3 and Chapter 5), we noted that the frictional strength of Opalinus fault gouges is higher than the frictional strength of intact samples. Thus suggesting a strong influence of the scaly fabric on the frictional behavior of the fault structural elements within the Main Fault, even though they share the same mineralogical content.

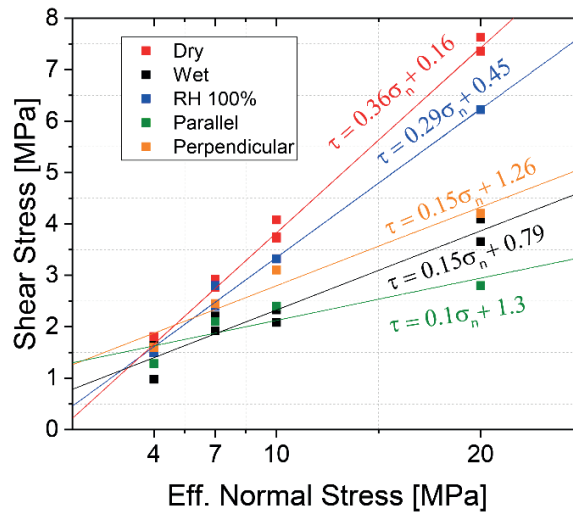


**Figure 6-2:** Shear stress versus effective normal stress for the simulated fault gouge and scaly clays.

The intact samples showed both velocity-strengthening ( $a - b > 0$ ) and -weakening ( $a - b < 0$ ) suggesting unstable sliding may be possible within the fault zone of the Main Fault. A more detailed analysis of the data estimated the magnitudes of the potential earthquakes if unstable sliding occurred. If we considered the Brune's model approach (Brune, 1970; Madariaga & Ruiz, 2016), the minimum magnitudes of the earthquakes that can be hold within the OPA fault zone were of  $M_w > 1$ .

Similar to the experimental gouges, the intact samples of OPA showed similar near-zero healing values ( $\Delta\mu$ ) at different hold times. Average healing values was  $\Delta\mu \approx 0.0002$  for samples sheared parallel to bedding, and  $\Delta\mu \approx 0$  for sample sheared perpendicular to bedding. Accordingly, healing rates are very small,  $\beta \approx 0.0004$  and  $\beta \approx 0.0003$  for samples sheared parallel and perpendicular to bedding respectively. The latter suggests that, even though contact re-strengthening increased with holding times, it occurred at an extremely slow rate.

The mechanical data presented here, in addition to microstructural observations that will be described below (see 6.1.4.) suggests that during the exploitation of shale formations, scaly clays are potential candidates fir induced-earthquakes nucleation, thus controlling the overall seismicity of clay-rich tectonic systems. However, if earthquakes nucleate, they might small and rare over time as suggested by the low frictional strength, the co-existence of velocity-strengthening and weakening slip patches, and the near zero healing values.

#### 6.1.4. DEFORMATION MECHANISM OF SIMULATED FAULT GOUGES AND SCALY CLAYS

Various set of microstructural analyses were performed through backscattered electron (BSE) and secondary electron (SE) mode a using secondary electron microscopy (SEM) at EPFL. In addition, mosaics of photographs using an optical microscope were built. The two groups of analysis were done to better understand the deformation mechanism behind the frictional properties of the simulated fault gouge and scaly clays. These analyses revealed that deformation was mainly accommodated by cataclastic processes, including:



- Frictional sliding characterized by the formation of several Riedel shear planes,
- Distributed and chaotic granular flow i.e., rotation and translation of minerals,
- Minor to strong fracturing within the clay matrix,
- Cataclasis of minerals via intragranular and intergranular cracking. This was particularly observed in calcite and the collapse of framboid pyrites,

Micro-cracking, intergranular, and intragranular cracking was especially strong for intact samples sheared perpendicular to bedding. Overprinting of shearing markers was also a common characteristic observed in experimental gouges, and intact samples sheared parallel to bedding.

In addition, microstructural analyses shown significant similarities between the experimental and natural scaly clay samples, notably the formation of mirror-like surfaces at sub-seismic velocities, low temperature and low normal stresses.

### 6.1.5. DILATANCY AND PERMEABILITY EVOLUTION OF FAULT GOUGE

Wet experiments performed in a triaxial configuration (Chapter 3) reveals, all normal stress, a dominant shear-enhanced dilation at deformation occurring at effective normal stress less than 20 MPa. Changes in the velocity history of our tests unveil competition between continuous creation and destruction of dilatant regions within the gouge, which in turn create and destroy fluid-flow pathways affecting permeability. In our experiments, the shear history leads to permeability enhancement. These results are in agreement with field observations (Guglielmi et al., 2017; Jeanne et al., 2017, 2018).

Our tests show that the permeability of all fault gouge samples is progressively reduced with increasing normal stress after. Moreover, permeability increases after shearing for all experiments at all tested normal stress. However, the higher permeability is within the same order of magnitude of non-deformed rock ( $10^{-20}$  m<sup>2</sup>). These results are in agreement with the laboratory data and permeability models presented in Chapter 2, suggesting that fault gouge can potentially act as a limited conduit for fluid migration.

## 6.2. Future research

Although this work has answered many of the questions initially posed, others have remained unanswered, and new ones were brought up and needed to be addressed in the future. Here, some unsolved questions and suggestions for further research are described:

### Scaling of the laboratory results

We have shown that laboratory experiments can provide relevant information to understand the complex earthquake faulting phenomenon in the Opalinus Clay formation. Some important aspects have been addressed as frictional strength, stability, and healing. However, there are several factors or characteristics of natural fault zones we have not, or we cannot reproduce. For instance, total displacements, fault roughness or fault structure (Marone, 1998; Scholz, 2002). In consequences,

some limitations can be argued about the representability of the rate and state parameters  $a - b$  or  $D_c$ . Following the fault injection tests performed at the MTL (Guglielmi et al., 2017; Jeanne et al., 2017, 2018), scaling rules might be adopted to link both the field and laboratory observations. Size-effects could be identified which might help to explain the frictional phenomena of the OPA fault arrays over different scales. The combined studies might then provide a complete, both theoretical and experimental framework of the stability of the Main Fault at Mont Terri.

## Frictional healing

It was shown in Chapter 3 and 5 that the simulated fault gouge and scaly clays exhibit an extremely low frictional healing. Moreover, it appears that healing transits from negative values to positive as time increases. We have shown in Chapter 3 that water plays an important role in this behavior and we have provided a different hypothesis to explain the observations, including local pore overpressures, swelling, or a lubrication effect (Moore & Lockner, 2007; Morrow et al., 2000, 2017). To adequately describe the frictional healing behavior more frictional experiments must be performed. New experiments may study the role of the sliding velocity and fluid viscosity and chemistry which can influence the different possible healing mechanisms.

## Frictional parameter $b$

In this study, negative values of  $b$  have been found at different experimental conditions. Negative values of the evolution effect  $b$  have been in previous frictional experiments with clay-rich natural and experimental samples. Yet, physical interpretations of this parameter are still not clear (Dieterich, 1978; Niemeijer & Collettini, 2013; Niemeijer & Vissers, 2014). More experiments where physical properties and experimental conditions are changed and then correlated to the evolution parameter might be helpful to better understand how the contact area evolves upon a change in velocity in clay-rich materials.

## High-speed friction

The recent development of high-speed rotary shear apparatus have allowed the study of fault strength at seismic velocities and fault displacements comparable to those of natural earthquake during rupture propagations [e.g. Shimamoto, 1994; Di Toro et al., 2010; Ma et al., 2014]. These studies have shown that at seismic rates  $> 0.01$  m/s, the frictional strength of fault-rocks significantly decreases from the Byerlee's estimate  $\mu_{ss} \approx 0.85$ , to values of  $\mu_{ss} = 0.1 - 0.3$  regardless the fault rock composition (Faulkner et al., 2010; Di Toro et al., 2011). In this thesis, we have shown that OPA fault gouge exhibit, in general, a velocity-strengthening behavior at sub-seismic slip velocities ( $< 300\mu\text{m/s}$ ) (Chapter 3). However, the deformation mechanism of OPA during co-seismic slip are still not well constrain nor under dry or wet conditions. This experiments may also help to understand fault propagation and slip-rate weakening processes in clay rich shallow regions (Brantut et al., 2008; Faulkner et al., 2011; Ferri et al., 2011; Oohashi et al., 2015; Ujiie et al., 2013)

## **Temperature effects on the long-term stability of clay-rich faults**

During the operation of nuclear waste laboratories, the near-field of repositories will experience a thermal perturbation due to the heat coming from radioactive waste. The increase of the temperature gradient will necessarily create pore-pressures changes leading to changes in the effective stress state. Dedicated experiments to study how this temperature increase may affect the frictional properties would be a valuable contribution to better understand the long-term safety of the repositories. Moreover, this experiments can also contribute to the characterization of the Opalinus clay formation as a CO<sub>2</sub> reservoir (e.g. Bakker et al., 2016; Samuelson & Spiers, 2012).

## **Frictional and transport properties of the quartz- and carbonate-rich facies of the Opalinus Clay formation**

In the Opalinus Clay formation, different lithological facies coexist which can be categorized according to their different mineralogical compositions (see Chapter 1). Shaly facies, which we have studied here, is characterized by a high content in clays (~50%). The clay content of the quartz – (~27%) and the carbonate-rich (~18%) facies is much lower. Mineralogical composition is key parameter on the understating of frictional and transport properties of faults (Behnsen & Faulkner, 2012; Fang et al., 2018; Kohli & Zoback, 2013). Frictional experiments on the carbonate-rich and quartz-rich facies are therefore needed to have a more complete view of the potential scenarios within the whole Opalinus Clay formation. The additional experiments will broaden the spectrum of potential slip behavior of fault arrays within the formation. This work was already initiated on the master thesis of Ms. Chaymae Samir.

## 6.3. REFERENCES

- Bakker, E., Hangx, S. J. T., Niemeijer, A., & Spiers, C. (2016). Frictional behaviour and transport properties of simulated fault gouges derived from a natural CO<sub>2</sub> reservoir. *International Journal of Greenhouse Gas Control*, 54, 70–83. <https://doi.org/10.1016/j.ijggc.2016.08.029>
- Behnsen, J., & Faulkner, D. (2012). The effect of mineralogy and effective normal stress on frictional strength of sheet silicates. *Journal of Structural Geology*, 42, 49–61. <https://doi.org/10.1016/j.jsg.2012.06.015>
- Brantut, N., Schubnel, A., Rouzaud, J. N., Brunet, F., & Shimamoto, T. (2008). High-velocity frictional properties of a clay-bearing fault gouge and implications for earthquake mechanics. *Journal of Geophysical Research: Solid Earth*, 113(10), 1–18. <https://doi.org/10.1029/2007JB005551>
- Brune, J. (1970). Tectonic stress and the spectra of seismic shear waves from Earthquakes. *Journal of Geophysical Research : Solid Earth*, 75(26).
- Byerlee, J. D. (1978). Friction of rocks. *Pure and Applied Geophysics*, 116(4–5), 615–626. <https://doi.org/10.1007/BF00876528>
- Collettini, C., Di Stefano, G., Carpenter, B., Scarlato, P., Tesei, T., Mollo, S., et al. (2014). A novel and versatile apparatus for brittle rock deformation. *International Journal of Rock Mechanics and Mining Sciences*, 66, 114–123. <https://doi.org/10.1016/j.ijrmms.2013.12.005>
- Dieterich, J. H. (1978). Time-dependent friction and the mechanics of stick-slip. *Pure and Applied Geophysics PAGEOPH*, 116(4–5), 790–806. <https://doi.org/10.1007/BF00876539>
- Fang, Y., Elsworth, D., Wang, C., & Jia, Y. (2018). Mineralogical Controls on Frictional Strength, Stability, and Shear Permeability Evolution of Fractures. *Journal of Geophysical Research: Solid Earth*, (2), 3549–3563. <https://doi.org/10.1029/2017JB015338>
- Faulkner, D., Jackson, C. A. L., Lunn, R. J., Schlische, R. W., Shipton, Z. K., Wibberley, C. A. J., & Withjack, M. O. (2010). A review of recent developments concerning the structure, mechanics and fluid flow properties of fault zones. *Journal of Structural Geology*, 32(11), 1557–1575. <https://doi.org/10.1016/j.jsg.2010.06.009>
- Faulkner, D., Mitchell, T. M., Behnsen, J., Hirose, T., & Shimamoto, T. (2011). Stuck in the mud? Earthquake nucleation and propagation through accretionary forearcs. *Geophysical Research Letters*, 38(18), 1–5. <https://doi.org/10.1029/2011GL048552>
- Ferri, F., Di Toro, G., Hirose, T., Han, R., Noda, H., Shimamoto, T., et al. (2011). Low- to high-velocity frictional properties of the clay-rich gouges from the slipping zone of the 1963 Vajont slide, northern Italy. *Journal of Geophysical Research: Solid Earth*, 116(9), 1–17. <https://doi.org/10.1029/2011JB008338>
- Guglielmi, Y., Birkholzer, J., Rutqvist, J., Jeanne, P., & Nussbaum, C. (2017). Can Fault Leakage Occur before or Without Reactivation? Results from an in Situ Fault Reactivation Experiment at Mont Terri. *Energy Procedia*, 114(November 2016), 3167–3174. <https://doi.org/10.1016/j.egypro.2017.03.1445>
- Jeanne, P., Guglielmi, Y., Rutqvist, J., Nussbaum, C., & Birkholzer, J. (2017). Field characterization

- of elastic properties across a fault zone reactivated by fluid injection. *Journal of Geophysical Research: Solid Earth*, 122(8), 6583–6598. <https://doi.org/10.1002/2017JB014384>
- Jeanne, P., Guglielmi, Y., Rutqvist, J., Nussbaum, C., & Birkholzer, J. (2018). Permeability Variations Associated With Fault Reactivation in a Claystone Formation Investigated by Field Experiments and Numerical Simulations. *Journal of Geophysical Research: Solid Earth*, 123(2), 1694–1710. <https://doi.org/10.1002/2017JB015149>
- Kohli, A. H., & Zoback, M. D. (2013). Frictional properties of shale reservoir rocks. *Journal of Geophysical Research: Solid Earth*, 118(9), 5109–5125. <https://doi.org/10.1002/jgrb.50346>
- Ma, S., Shimamoto, T., Yao, L., Togo, T., & Kitajima, H. (2014). A rotary-shear low to high-velocity friction apparatus in Beijing to study rock friction at plate to seismic slip rates. *Earthquake Science*, 27(5), 469–497. <https://doi.org/10.1007/s11589-014-0097-5>
- Madariaga, R., & Ruiz, S. (2016). Earthquake dynamics on circular faults: a review 1970–2015. *Journal of Seismology*, 20(4), 1235–1252. <https://doi.org/10.1007/s10950-016-9590-8>
- Marone, C. (1998). Laboratory-Derived Friction Laws and Their Application To Seismic Faulting. *Annual Review of Earth and Planetary Sciences*, 26(1), 643–696. <https://doi.org/10.1146/annurev.earth.26.1.643>
- Moore, D., & Lockner, D. A. (2007). Friction of the smectite clay montmorillonite: A review and interpretation of data. In T. Dixon & C. Moore (Eds.), *The Seismogenic Zone of Subduction Thrust Faults* (pp. 317–345). Columbia University Press. <https://doi.org/10.7312/dixo13866-011>
- Morrow, C., Moore, D., & Lockner, D. A. (2000). The effect of mineral bond strength and adsorbed water on fault gouge frictional strength. *Geophysical Research Letters*, 27(6), 815–818. <https://doi.org/10.1029/1999GL008401>
- Morrow, C., Moore, D., & Lockner, D. A. (2017). Frictional strength of wet and dry montmorillonite. *Journal of Geophysical Research: Solid Earth*, 122(5), 3392–3409. <https://doi.org/10.1002/2016JB013658>
- Niemeijer, A., & Collettini, C. (2013). Frictional Properties of a Low-Angle Normal Fault Under In Situ Conditions: Thermally-Activated Velocity Weakening. *Pure and Applied Geophysics*, 171(10), 2641–2664. <https://doi.org/10.1007/s00024-013-0759-6>
- Niemeijer, A., & Vissers, R. L. M. (2014). Earthquake rupture propagation inferred from the spatial distribution of fault rock frictional properties. *Earth and Planetary Science Letters*, 396, 154–164. <https://doi.org/10.1016/j.epsl.2014.04.010>
- Oohashi, K., Hirose, T., Takahashi, M., & Tanikawa, W. (2015). Dynamic weakening of smectite-bearing faults at intermediate velocities: Implications for subduction zone earthquakes. *Journal of Geophysical Research: Solid Earth*, 120(3), 1572–1586. <https://doi.org/10.1002/2015JB011881>
- Ruina, A. (1983). Slip instability and state variable friction laws. *Journal of Geophysical Research*, 88(B12), 10359. <https://doi.org/10.1029/JB088iB12p10359>
- Samuelson, J., & Spiers, C. J. (2012). Fault friction and slip stability not affected by CO<sub>2</sub> storage: Evidence from short-term laboratory experiments on North Sea reservoir sandstones and

- caprocks. *International Journal of Greenhouse Gas Control*, 11(SUPPL), 78–90. <https://doi.org/10.1016/j.ijggc.2012.09.018>
- Scholz, C. H. (2002). *The Mechanics of Earthquakes and Faulting*. Cambridge University Press. Retrieved from <https://books.google.ch/books?id=JL1VM5wMbrQC>
- Shimamoto, T. (1994). A new rotary-shear high-speed frictional testing machine : its basic design and scope of research. *Jour. Tectonic Res. Group of Japan*, 39, 65–78. Retrieved from <https://ci.nii.ac.jp/naid/80008741644/en/>
- Di Toro, G., Niemeijer, A., Tripoli, A., Nielsen, S., Di Felice, F., Scarlato, P., et al. (2010). From field geology to earthquake simulation: A new state-of-The-art tool to investigate rock friction during the seismic cycle (SHIVA). *Rendiconti Lincei*, 21(SUPPL. 1), 95–114. <https://doi.org/10.1007/s12210-010-0097-x>
- Di Toro, G., Han, R., Hirose, T., De Paola, N., Nielsen, S., Mizoguchi, K., et al. (2011). Fault lubrication during earthquakes. *Nature*, 471(7339), 494–499. <https://doi.org/10.1038/nature09838>
- Ujiie, K., Tanaka, H., Saito, T., Tsutsumi, A., Mori, J., & Toczko, S. (2013). Low Coseismic Shear Stress on the Tohoku-Oki Megathrust Determined from Laboratory Experiments. *Science*, 342(December), 1211–1214. <https://doi.org/10.1126/science.1243485>



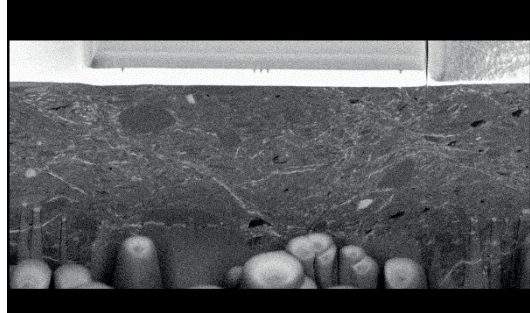
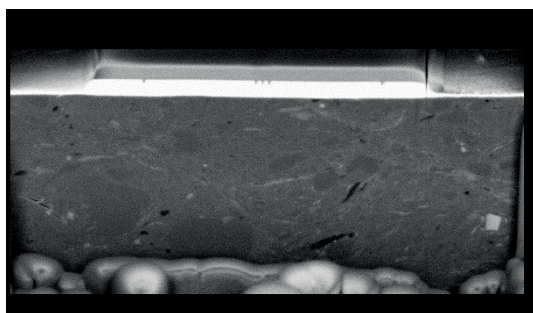
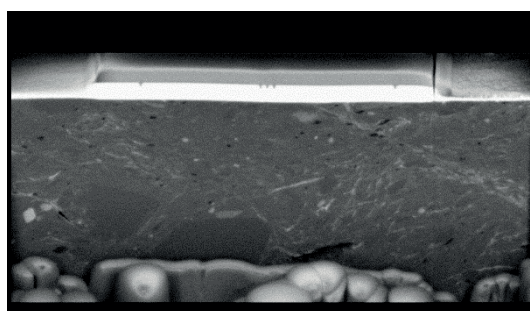
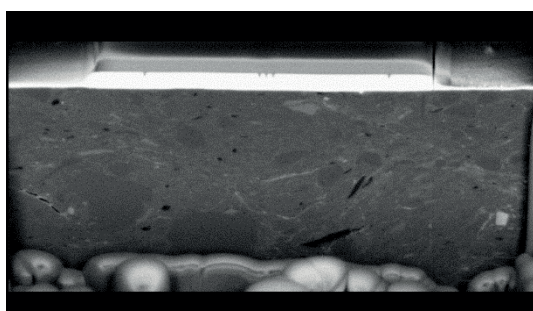
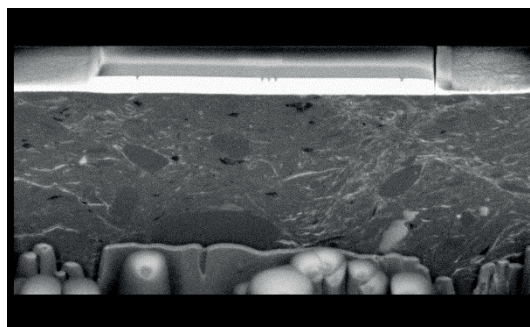
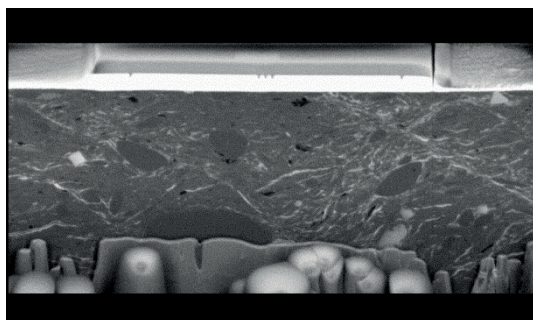
## APPENDIX A: CHAPTER 2

**Fault gouge sample collected from borehole BFS-2**



## FIB-SEM images of the fault gouge

Additional FIB-SEM photographs of the OPA fault gouge.





## A mosaic of optical images of a fault gouge thin section



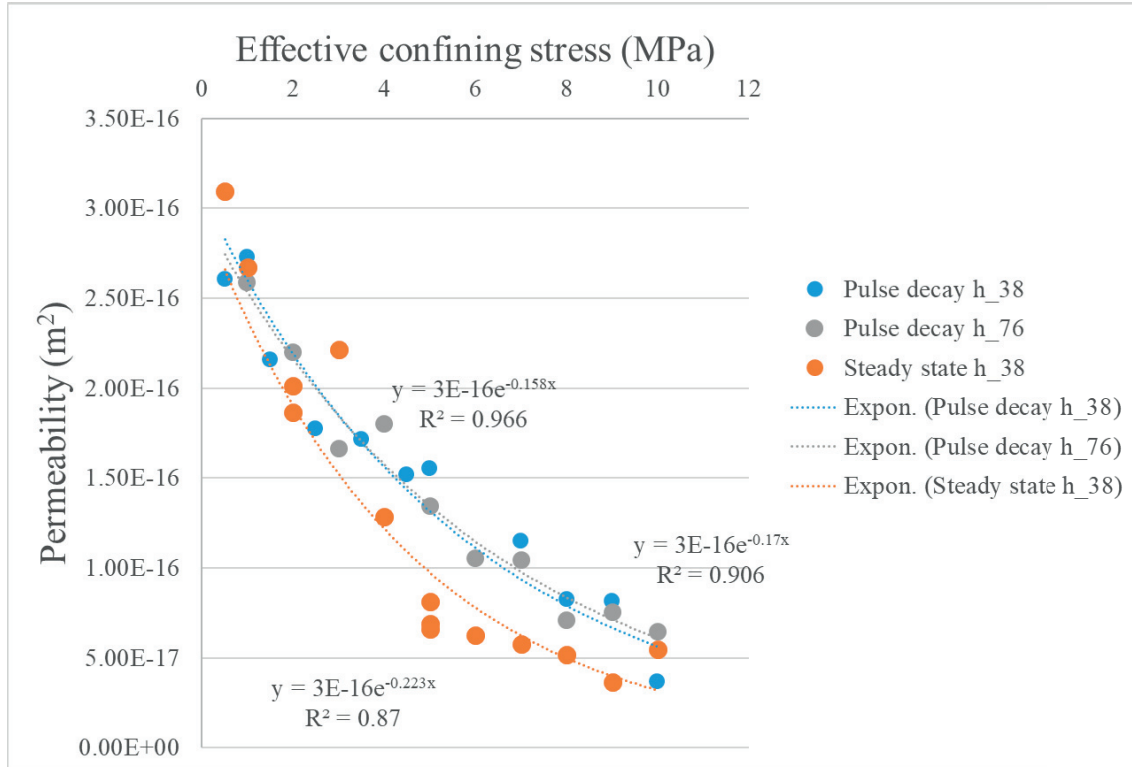
Scaly gouge

Gouge

Scaly gouge

## Calibration of permeability setup

Permeability of 3 granite samples (38 mm diameter) was measured at different effective confining stress using the pulse decay method and steady state. Pulse decay method was measured for two samples of 38 and 76 mm in height. All results show good agreement.



## Model of Yang & Aplin, (2010) based on an exponential law

$$\ln(k[m^2]) = a_{CF} + b_{CF} \cdot \frac{\phi}{1 - \phi} + c_{CF} \cdot \left(\frac{\phi}{1 - \phi}\right)^{0.5}$$

Where the coefficients  $a_{CF}$ ,  $b_{CF}$ , and  $c_{CF}$  are defined as:

$$a_{CF} = -69.59 - 26.79 \cdot CF + 44.07 \cdot CF^{0.5}$$

$$b_{CF} = -53.61 - 80.03 \cdot CF + 132.78 \cdot CF^{0.5}$$

$$c_{CF} = 86.61 + 81.91 \cdot CF - 163.61 \cdot CF^{0.5}$$

And  $CF$  is the clay content (in fraction) and  $\phi$  the related porosity.

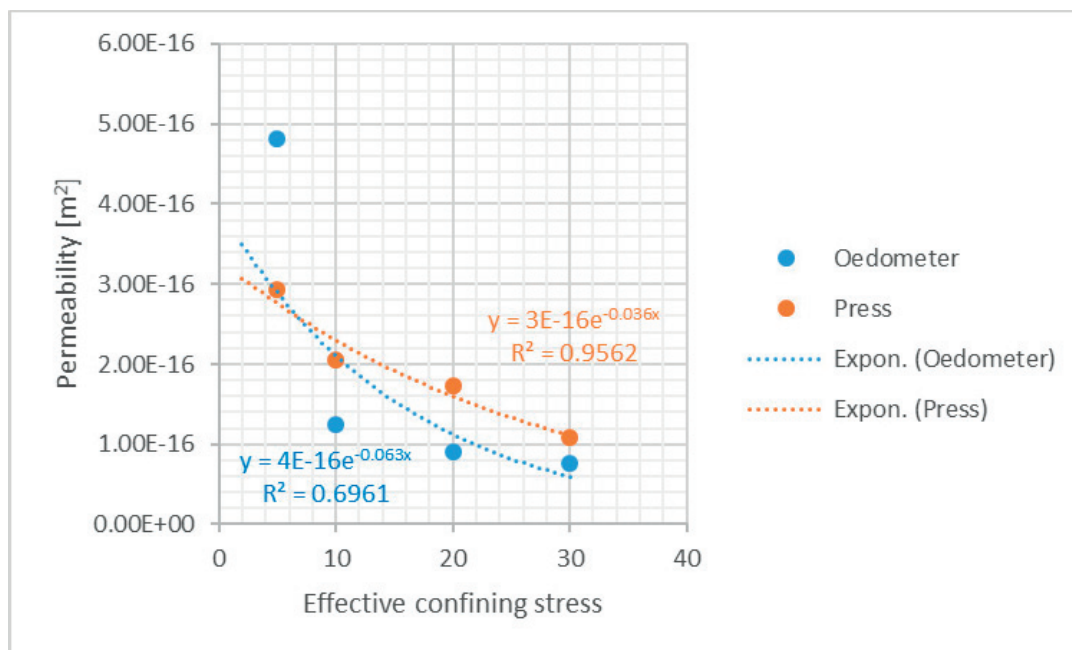
### Reference:

Yang, Y., & Aplin, A. C. (2010). A permeability-porosity relationship for mudstones. *Marine and Petroleum Geology*, 27(8), 1692–1697.  
<https://doi.org/10.1016/j.marpetgeo.2009.07.001>

## APPENDIX B: CHAPTER 4

### Calibration of permeability

We measured the permeability of powdered Carrara marble in a oedometer setup and in the saw-cut configuration used in Chapter 4. We have used the steady-state method. All results show good agreement.





# CURRICULUM VITAE



# Luis Felipe Orellana E.

[luisfelipe.orellana@ing.uchile.cl](mailto:luisfelipe.orellana@ing.uchile.cl)

Laboratory of Experimental Rock Mechanics – [www.lemr.epfl.ch](http://www.lemr.epfl.ch)  
School of Architecture, Civil and Environmental Engineering  
GC D1413 (Bâtiment GC)  
Station 18  
CH-1015 Lausanne, Switzerland  
Phone (+41) 0 788 75 72 71

## CURRENT POSITION

Since July 2015, **Ph. D. student** at the Laboratory of Experimental Rock Mechanics, Ecole Polytechnique Fédérale de Lausanne (EPFL), Switzerland.

## EDUCATION

July 2015 – Oct. 2018	<b>PhD Mechanics (Geomechanics)</b> Laboratory of Experimental Rock Mechanics, Ecole Polytechnique Fédérale de Lausanne, EPFL Provisional title of thesis: <i>Frictional properties of Opalinus Clay</i> Supervisor: Prof. Marie Violay
2010 - 2012	<b>Master degree in Mining Engineering</b> Universidad de Chile
2005 - 2012	<b>Bachelor degree in Mining and Extractive Metallurgy sciences</b> Universidad de Chile

## HONORS AND AWARDS

2011	Advanced Mining Technology Center – Block Caving Laboratory scholarship.
2010	Outstanding student (Mining Engineer) award - Universidad de Chile
2008 - 2010	Anglo American Chile “Mining of Excellence” scholarship
2008 - 2009	ENAEX scholarship – Moises Mellado Foundation and ENAEX.

## RESEARCH INTERESTS

Rock friction, the mechanics of faults and earthquakes  
Rock mechanics and rock engineering  
Underground mining, deep geological repositories and geothermal energy

## PUBLICATIONS, CONFERENCES & SEMINARS

### Publication in Journals ISI – WOS

1. **Orellana, L.F.**, Giorgetti, C., Violay, M., (under review) Frictional properties and permeability variations of fault zones in the Opalinus Clay formation, a host rock for deep nuclear waste storage.
2. **Orellana, L.F.**, Nussbaum, C., Grafulha L., Henry P., Violay, M., (under review) Clay-rich fault gouges can potentially act as discrete fluid-flow channels: the case of the Opalinus Clay formation.
3. **Orellana, L.F.**, Scuderi, M.M., Collettini, C., Violay, M., 2018a. Frictional Properties of Opalinus Clay: Implications for nuclear waste storage. **J. Geophys. Res. Solid Earth** 123, 157–175. <https://doi.org/10.1002/2017JB014931>
4. **Orellana, L.F.**, Scuderi, M.M., Collettini, C., Violay, M., 2018b. Do scaly clays control seismicity on faulted shale rocks? **Earth Planet. Sci. Lett.** 488, 59–67. <https://doi.org/10.1016/j.epsl.2018.01.027>
5. **Orellana, L.F.**, Castro, R., Hekmat, A., Arancibia, E., 2017. Productivity of a Continuous Mining System for Block Caving Mines. **Rock Mech. Rock Eng.** 50, 657–663. <https://doi.org/10.1007/s00603-016-1107-9>
6. Rotta Loria, A.F., **Orellana, L.F.**, Minardi, A., Fürbringer, J.-M., Laloui, L., 2015. Predicting the axial capacity of piles in sand. **Comput. Geotech.** 69, 485–495. <https://doi.org/10.1016/j.compgeo.2015.06.013>

### Conferences talks (T), posters (P) & papers (C)

1. **Fluid-flow control in clay-bearing faults** (T). **L. F. Orellana**, P. Henry, Y. Guglielmi, C. Nussbaum, L. Grafulha, M. Violay. European Geoscience Meeting (EGU), April 2018, Vienna, Austria.
2. **Petro-physical characterization of the Main Fault at the Mont Terri Laboratory** (P). **L.F. Orellana**, M. Violay, P. Henry, Y. Guglielmi and C. Nussbaum. 7th Clay Conference, Davos, Switzerland, 2017.
3. **On the stability of clay-bearing faults** (P). **Orellana, L.F.**, Violay, M., Scuderi M., Collettini. American Geoscience Meeting (AGU), December 2016, San Francisco, USA.
4. **Petro-physical properties of the Main Fault at the Mont Terri Laboratory** (P). **L.F. Orellana**, M. Violay, E. Gramajo, P. Henry, Y. Guglielmi, F. Amann, C. Nussbaum. 14<sup>th</sup> Swiss Geoscience Meeting (SGM), November 2016, Geneva, Switzerland. (P)
5. **Frictional Properties of Opalinus Clay** (P), **Orellana, L.F.**, Violay, M., Scuderi M., Collettini. Gordon Research Conference: Rock deformation, August 2016, Andover, New Hampshire, USA.
6. **Fault Frictional Stability in a Nuclear Waste Repository** (T). **Orellana L.F.**, Violay M., Scuderi M., Collettini C. European Geoscience Meeting (EGU), April 2016, Vienna, Austria.
7. **Frictional Properties of Opalinus Clay** (P). **L.F. Orellana** & M. Violay, 13<sup>th</sup> Swiss Geoscience Meeting (SGM), November 2015, Basel, Switzerland.
8. **A hollow cylinder testing device to study at small scale the damaged zone around underground openings in porous rocks** (T, C). V. Labiouse and **F. Orellana**, 13th International Symposium on Rock Mechanics, May 2015, Montreal, Canada.

9. **Physical Modelling as an Engineering Tool for Mining** (T, C). Castro, R., Orellana, L., Pineda, M., 2012. In Proceeding of the 6th Mass Mining and Exhibition Conference MassMin 2012, 10-14 June, Sudbury, Canada.

#### Invited seminars

1. Orellana L.F. Brown Bag seminar, **Swiss Seismological Service (SED), ETH Zürich**, April, 19<sup>th</sup> 2018. Frictional and transport properties of clay-bearing faults: The case of the Opalinus Clay formation.

### RESEARCH EXPERIENCE

- |                              |   |
|------------------------------|---|
| <b>July 2015 - present</b>   | <b>Ph. D student</b> , Laboratory of Experimental Rock Mechanics, Ecole Polytechnique Fédérale de Lausanne (EPFL), Switzerland.<br>Supervisor: Prof. Marie Violay |
| <b>Nov. 2013 – June 2015</b> | <b>Research Assistant</b> , Laboratory of Rock Mechanics, Ecole Polytechnique Fédérale de Lausanne (EPFL), Switzerland.<br>Supervisor: Dr. Vincent Labiouse.      |
| <b>2010 – Jan. 2012</b>      | <b>Master student (research)</b> , Block Caving Laboratory, Advanced Mining Technology Center, Universidad de Chile, Chile.<br>Supervisor: Prof. Raul Castro      |

### PROFESIONAL EXPERIENCE

- |                              |  |
|------------------------------|--|
| <b>June 2012 – Aug. 2013</b> | <b>Junior researcher</b> , Mining and Metallurgy Innovation Institute (IM2) – CODELCO, Chile.<br>Supervisor: Dr. Mauricio Telias |
| <b>Feb. 2012 – July 2013</b> | <b>Mining Engineer</b> , Hatch Ingenieros y Consultores  |

### TEACHING EXPERIENCE

- |                            |   |
|----------------------------|---|
| <b>Feb. 2014 - present</b> | <b>Teaching assistant</b><br>Laboratory of Experimental Rock Mechanics,<br>Ecole Polytechnique Fédérale de Lausanne, EPFL <ul style="list-style-type: none"><li>• Bachelor courses:<ul style="list-style-type: none"><li>○ Rock Mechanics and Tunnelling Engineering (Spring 2014, Spring 2015, Autumn 2015, Autumn 2016, Autumn 2017),</li><li>○ Management of territories affected by natural hazards in mountain areas (Spring 2014), and</li><li>○ Geotechnical Engineering (Autumn 2014)</li></ul></li><li>• Master courses<ul style="list-style-type: none"><li>○ Geophysics for Engineers (Spring 2017, Spring 2018), and</li><li>○ Underground construction technology (Spring 2016),</li></ul></li></ul> |
|----------------------------|---|

Feb. 2014 - present

**Co- supervisor**

Laboratory of Experimental Rock Mechanics, Ecole Polytechnique Fédérale de Lausanne, EPFL

- Bachelor and master projects:
  - Jesus Diaz (2014),
  - Grégoire Aguetant (2014),
  - Arabelle de Saussure (2015),
  - Julien Lepine (2016),
  - Lea Kaufmann (2016),
  - Ray Harran (2017),
  - Matthias Wojnarowicz (2017),
  - Heloïse Fuselier (2017),
  - Michela Casanova (2017),
  - Lisa Cassina (2018),
  - Tristan Liardon (2018).
- Master thesis:
  - Samuel Kivell (2015),
  - Eduardo Gramajo (2016),
  - Chaymae Samir (2017) \*. Chaymae Samir was awarded the best master thesis of the Civil Engineering Institute at EPFL in 2017.

## OUTREACH ACTIVITIES

2017 - 2018

**President**, Association of Chilean researchers in Switzerland.

2014 - 2017

**Secretary**, Association of Chilean researchers in Switzerland.

2011

**Member**, project EOLIAN 2, Universidad de Chile.

2009

**President**, Mining engineer students' union (Universidad de Chile).

2008

**Vice-President**, Mining engineer students' union (Universidad de Chile).

## ADDITIONAL TRAINING

**Languages**

**Spanish** – Native;

**English** – Full professional proficiency;

**French** – Basic proficiency

**Equipment**

**Secondary Electron Microscope (2016)**. Interdisciplinary Centre for Electron Microscopy (CIME), EPFL, Switzerland.

**Optical contactless profilometer (2016)**. Laboratory of Tribology, EPFL, Switzerland.

**Mercury intrusion porosimetry (2015)**. Laboratory of Construction materials, EPFL, Switzerland.

